TU Delft

Delft University of Technology

Document Version
Final published version

Citation (APA)
Al-Kutubi, H. A. A. (2026). *Lithium Ion Transport in Argyrodite-Based Solid Electrolytes: From Structural Disorder to Interfacial Effects*. [Dissertation (TU Delft), Delft University of Technology]. https://doi.org/10.4233/uuid:418fa443-c065-4cb8-b4ac-530e8acebfec

Important note
To cite this publication, please use the final published version (if applicable).
Please check the document version above.

Copyright
In case the licence states “Dutch Copyright Act (Article 25fa)”, this publication was made available Green Open Access via the TU Delft Institutional Repository pursuant to Dutch Copyright Act (Article 25fa, the Taverne amendment). This provision does not affect copyright ownership.
Unless copyright is transferred by contract or statute, it remains with the copyright holder.

Sharing and reuse
Other than for strictly personal use, it is not permitted to download, forward or distribute the text or part of it, without the consent of the author(s) and/or copyright holder(s), unless the work is under an open content license such as Creative Commons.

Takedown policy
Please contact us and provide details if you believe this document breaches copyrights.
We will remove access to the work immediately and investigate your claim.

This work is downloaded from Delft University of Technology.

Lithium Ion Transport in Argyrodite-Based Solid Electrolytes

From Structural Disorder to Interfacial Effects

Hanan Al-Kutubi

Lithium Ion Transport in Argyrodite-Based Solid Electrolytes
From Structural Disorder to Interfacial Effects

Lithium Ion Transport in Argyrodite-Based Solid Electrolytes From Structural Disorder to Interfacial Effects

Proefschrift

ter verkrijging van de graad van doctor
aan de Technische Universiteit Delft,
op gezag van de Rector Magnificus Prof. dr. ir. H. Bijl,
voorzitter van het College voor Promoties,
in het openbaar te verdedigen
op dinsdag 17 november 2026 12:30 uur

door

Hanan Ala Abdelamir AL-KUTUBI

Dit proefschrift is goedgekeurd door de (co)promotoren.

Samenstelling promotiecommissie:

Rector Magnificus,	voorzitter
Prof. Dr. Ir. M. Wagemaker,	Technische Universiteit Delft
Dr. S. Ganapathy,	Technische Universiteit Delft
Onafhankelijke leden:	
Prof. Dr. F.M Mulder,	Technische Universiteit Delft
Dr. E.M. Kelder,	Technische Universiteit Delft
Prof. Dr. Ir. M. Huijben,	Twente Universiteit
Dr. E.R.H. van Eck,	Radbound Universiteit
Prof. Dr. Ir. J.L. Kloosterman,	Technische Universiteit Delft, *reservelid*

Kernwoorden: Solid-state batteries, Solid electrolytes, Argyrodites, Solid-state NMR, Space charge layer, Electrochemical impedance spectroscopy
Omslag: Hanan Ala Abdelamir Al-Kutubi

Een elektronische versie van dit proefschrift is verkrijgbaar op
http://repository.tudelft.nl/.

With them the Seed of Wisdom did I sow
And with my own hand labour'd it to grow:
And this was all the Harvest that I reap'd
"I came like Water and like Wind I go."

Omar Khayyam

Contents

1 Introduction **1**
1.1 Motivation and Background . . . 2
1.2 Thesis Outline and Research Objectives . . . 4
Bibliography . . . 6

2 Theory **7**
2.1 Diffraction . . . 8
2.1.1 X-ray Diffraction . . . 8
2.1.2 Neutron Diffraction . . . 8
2.1.3 Rietveld Refinement . . . 9
2.2 Solid State Nuclear Magnetic Resonance . . . 9
2.2.1 Interactions in NMR . . . 10
2.2.2 Relaxation and Diffusion . . . 13
2.3 Electrochemical Impedance Spectroscopy . . . 16
2.3.1 Deviation from Ideality . . . 18
2.3.2 The Kramers Kronig Test . . . 19
Bibliography . . . 20

3 The Relationship Between Halide Substitution, Structural Disorder and Lithium Distribution in $Li_{6-x}PS_{5-x}Br_{1+x}$ **23**
3.1 Introduction . . . 24
3.2 Materials and Methods . . . 26
3.2.1 Mechanochemical Milling and Post-annealing . . . 26
3.2.2 X-ray Diffraction . . . 27
3.2.3 Neutron Powder Diffraction . . . 27
3.2.4 Bond Valence Site Energy (BVSE) . . . 27
3.2.5 Electrochemical Impedance Spectroscopy . . . 28
3.2.6 Rietveld Refinement . . . 28
3.2.7 Solid State NMR . . . 28
3.3 Results and discussion . . . 29
3.3.1 Structural Changes . . . 29
3.3.2 Lithium Substructure . . . 31
3.3.3 Ionic Transport . . . 34
3.3.4 Structure-Property Relationship . . . 35
3.4 Conclusion . . . 37
Bibliography . . . 38

4 Disentangling the Roles of Site Disorder and Chemical Composition in $Li_{6-x}PS_{5-x}Br_{1+x}$ 47
4.1 Introduction . . . 48
4.2 Materials and Methods . . . 50
4.3 Results and Discussion . . . 51
4.3.1 Ion Dynamics and Energetics . . . 53
4.3.2 Structure–Property Relationship . . . 56
4.3.3 The Prefactor from EIS and NMR . . . 61
4.4 Conclusion . . . 65
Bibliography . . . 65

5 Probing Lithium Diffusion in $Li_{6-x}PS_{5-x}Br_{1+x}$ through ^{31}P and ^{7}Li Relaxometry 77
5.1 Introduction . . . 78
5.2 Materials and Methods . . . 80
5.3 Results and discussion . . . 81
5.3.1 An Overview . . . 81
5.3.2 The BPP-model . . . 81
5.3.3 Sources of Relaxation . . . 84
5.3.4 Approach . . . 87
5.3.5 Fitting ^{7}Li $T_{1\rho}$ . . . 89
5.3.6 Fitting ^{31}P $T_{1\rho}$ . . . 92
5.3.7 Fitting ^{31}P T_1 . . . 98
5.3.8 Tying Everything Together . . . 103
5.4 Conclusion . . . 106
Bibliography . . . 107

6 Probing Space–Charge Layer Formation in Solid Electrolyte – Ionic Liquid Systems 113
6.1 Introduction . . . 114
6.2 Materials and Methods . . . 115
6.3 Results and Discussion . . . 116
6.3.1 The Chemical Environment . . . 116
6.3.2 Lithium Mobility . . . 121
6.3.3 Electrochemical Cycling . . . 127
6.4 Conclusion . . . 135
Bibliography . . . 137

Summary 141

Samenvatting 145

A Appendix Chapter 3 147

B Appendix Chapter 4 157

C Appendix Chapter 5 171

D Appendix Chapter 6 203

Acknowledgments **213**

Curriculum Vitæ **215**

1

Introduction

"The truth isn't easily pinned to a page. In the bathtub of history the truth is harder to hold than the soap and much more difficult to find."

Terry Pratchett, Sourcery

1

1.1 Motivation and Background

The transition toward sustainable energy technologies has intensified the demand for high-performance, safe and durable electrical energy storage systems. Among the most promising candidates are solid-state batteries, which replace flammable liquid electrolytes with solid materials capable of conducting lithium ions.[1] Solid-state electrolytes are crystalline, glassy or composite materials that are conductive to lithium ions. Within a solid-state battery, the electrolyte forms a layer separating the anode and cathode, where it provides lithium-ion transport between the electrodes. Furthermore, it is also incorporated within the electrode where it provides lithium-ion transport between cathode and anode particles within the electrode. To function effectively, solid electrolytes must posses high ionic conductivity at room temperature. This is essential for efficient ionic transport but also allows the electrolyte layer to occupy a smaller fraction of the electrode composition, allowing for higher energy density.[2] Solid electrolytes require good mechanical properties such as mechanical durability and compressibility, which allow for the formation of thin layers. Finally, they require good chemically and electrochemically stability during battery operation. However, despite extensive research, widespread implementation of solid-state batteries remains constrained by persistent challenges.

Sulphide-based electrolytes are one of the most prominent classes of solid-state electrolytes and offer high ionic conductivity and, due to their mechanical softness, good compressibility and low grain boundary resistance.

Argyrodites are crystalline sulphide-based electrolytes possessing the structure given in Figure 1.1. The backbone consists of PS_4^{3-}–tetrahedral units, shown in blue and orange and labeled 4*b* and 16*e*, respectively, referring to their crystallographic sites. The remaining sulphur and the halide anions occupy the 4*a* and 4*d* crystallographic sites, while lithium ions reside in a network of partially occupied tetrahedral sites (T1–T5a). Most lithium ions occupy the T5-site, which forms a cage-like structure around the 4*d* site. The degree of site disorder, defined in this thesis as the degree to which the 4*d* site is occupied by a halogen atom as opposed to sulphur atom, is known to play an important role in the overall ionic conductivity of the material.

The ability to alter the argyrodite chemical composition and synthesis conditions enables systematic control over site disorder as well as crystal distortion and subsequent lattice dynamics and ionic transport pathways.[3, 4] This tuneability makes argyrodites ideal candidates for understanding the complex relationship between composition and ionic transport in solid state electrolytes as well as expanding upon the theoretical models underpinning the techniques used to study such systems. This thesis aims to exploit this tuneablity to explore the effect of site disorder on lithium ion transport using diffraction methods, electrochemical impedance spectroscopy and solid-state nuclear magnetic resonance spectroscopy. Specifically, it aims to disentangle the effects of chemical composition and site-disorder on both long-range and short-range lithium transport. It further aims to combine the results obtained from different characterization methods to provide a more complete picture of lithium transport and expand upon the theory underpinning these techniques.

Whereas sulphide-based electrolytes, such as argyrodites, are known for their conductivity and compressibility, they also suffer from low chemical stability, making them highly sensitive to water and air. Furthermore, they are often also electrochemically unsta-

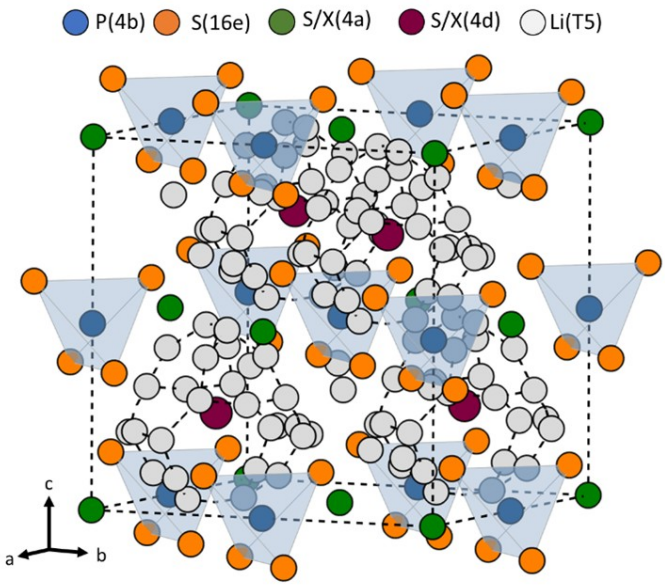

Figure 1.1: Illustrated crystal structure of Li_6PS_5X (X = Cl, Br, I) showing the PS_4^{3-}–tetrahedra, consisting of P on the 4*b* site and S on the 16*e* site, lithium on the T5 site and the remaining S and halogen on the 4*a*– and 4*d*–sites.

ble, resulting in degradation during battery cycling. Both cases result in the formation of resistive layers upon degradation and deterioration in battery performance. Oxide-based electrolytes, like the lithium lanthanum zirconium oxides ($Li_7La_3Zr_2O_{12}$ or LLZO) and lithium aluminium germanium phosphates ($Li_{1.5}Al_{0.5}Ge_{1.5}(PO_4)_3$ or LAGP) offer superior chemical and electrochemical stability. However, these electrolytes are mechanically hard, resulting in high grain boundary resistance and the need for very high stack pressure.[5]

One of the methods to reduce grain boundary resistance has been through the incorporation of a liquid electrolyte, resulting in a so-called "hybrid electrolyte". Besides the traditional, flammable electrolytes, ionic liquids can be used for this purpose.[6] Ionic liquids are molten salts that are liquid at room temperature, possessing low volatility and flammability and often good chemical and electrochemical stability. Conventionally, a lithium salt is dissolved into the ionic liquid used in hybrid system to impart lithium conductivity. However, in this thesis, salt-less ionic liquids are used to create a space charge layer.

Space charge layers have been theorized to result in an additional barrier for interfacial lithium movement, specifically at the interphase between the solid electrolyte and the cathode material.[7, 8] A schematic of the formation of a space charge layer is given in Figure 1.2a. When two materials with different chemical potentials come into contact, atoms migrate across the surface to establish thermodynamic equilibrium and equalize the chemical potential across the interphase. In solid-state electrolytes, which can conduct the lithium cation but not the electron counter-charge, something interesting can occur. The lithium ion moves across the electrode-electrolyte interphase, but the electron

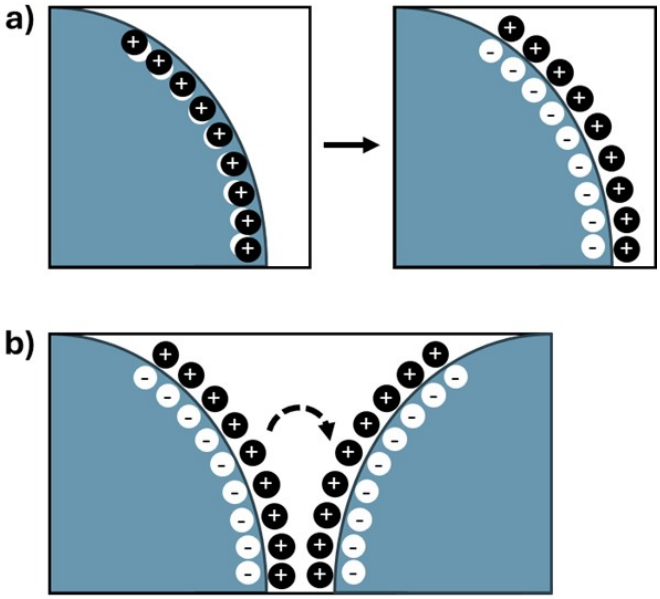

Figure 1.2: Schematic of the formation of a space charge layer at the interphase between the solid electrolyte and the ionic liquid (a) and movement of lithium ions between two electrolyte particles in ionic liquid (b).

cannot, resulting in excess charge at the interface. The lithium ion, unable to return to its original material due to thermodynamics, is now unable to dissipate into the new material due to electrostatics. The result is a thin, charged layer across the interface. Whereas its size is thought to only be a few nanometres, the (negative) influence of a space charge layer could be very large as it can act as barrier for lithium transport across the surface. Yet experimental evidence of the existence of space charge layers in batteries is rare and investigation of its behaviour even more so as the space charge between two materials is very thin and chemically almost identical to the bulk. This thesis aims to create a space charge layer through the use of an ionic liquid containing no additional lithium salt and utilize this space charge layer to reduce grain boundary resistance. At the solid electrolyte-ionic liquid interphase, the same mechanism should form a space charge layer, with the lithium being at the side of the ionic liquid, resulting in a distinct chemical environment. Furthermore, the thin layer of lithium ions at the interphase of the solid electrolyte should result in a "bridge" for lithium ions, thereby increasing interfacial transport across electrolyte particles and a reduction in grain boundary resistance (see Figure 1.2b).

1.2 Thesis Outline and Research Objectives

The main objective of this thesis is to advance the understanding of lithium diffusion mechanisms in argyrodite-based solid electrolytes, spanning both bulk and interfacial regimes. Furthermore, the thesis aims to explore the effect of synthesis conditions on structure and resultant lithium-ion motion, explore the beneficial use of space charge layers and expand

upon the theoretical frameworks used to interpret NMR and EIS data. The thesis is organized into six chapters. Following this introduction, Chapter 2 provides an overview of the fundamentals of nuclear magnetic resonance (NMR) and electrochemical impedance spectroscopy (EIS), the two main methods used to probe ion dynamics. The rest of the thesis can be divided into two parts. The first part, consisting of Chapters 3,4 and 5 explores the effect of bromine-content and synthesis conditions on the structural disorder and ionic conductivity of bromine-rich argyrodites ($Li_{6-x}PS_{5-x}Br)_{1+x}$). In Chapter 3, multinuclear solid-state nuclear magnetic resonance spectroscopy is combined with complementary techniques including X-ray- and neutron diffraction and EIS, providing a multiscale perspective and linking the local microscopic environment to dynamic processes and macroscopic conductivity. Chapter 4 uses ^{31}P and ^{7}Li NMR to link configurational entropy to structural changes in the lattice. Furthermore, it explores the Neldel-Meyer pre-factor and the migrational entropy and derives these not just from the traditional long-range EIS-based method but also from the relatively short-range spin-lattice relaxation NMR, allowing for a comparison of different length scales. Chapter 5 explores the Bloembergen-Purcel-Pound (BPP) model, used extensively to fit ^{7}Li relaxation data in the field of lithium-ion batteries, to fit ^{31}P relaxation. The chapter expands on the choice of appropriate models for the dipolar interactions that dominate relaxation, allowing for the extraction of structural data as well as energetic information. The second part, consisting of Chapter 6, examines the formation of space charge layers by employing compositions consisting of nano-sized argyrodite and ionic liquids. Nano-sized argyrodite allows for the formation of a large surface area, maximizing the amount of space charge layer formed, whereas ionic liquids allow for the formation of the space charge layer as a stable and chemically distinct environment. This allows for a new way to study space charges and utilize them to improve interfacial conductivity, not just for argyrodites, but also for LAGP-based electrolytes. Finally, Chapter 6.4 integrates the insights obtained, emphasizing the central role of synthesis, structural disorder, and interfacial chemistry in governing lithium diffusion across scales.

1

Bibliography

[1] John Christopher Bachman, Sokseiha Muy, Alexis Grimaud, Hao-Hsun Chang, Nir Pour, Simon F. Lux, Odysseas Paschos, Filippo Maglia, Saskia Lupart, Peter Lamp, Livia Giordano, and Yang Shao-Horn. Inorganic solid-state electrolytes for lithium batteries: Mechanisms and properties governing ion conduction. *Chemical Reviews*, 116(1):140–162, 2016. ISSN 0009-2665. doi: 10.1021/acs.chemrev.5b00563.

[2] Lv Hu, Jinzhu Wang, Kai Wang, Zhenqi Gu, Zhiwei Xi, Hui Li, Fang Chen, Youxi Wang, Zhenyu Li, and Cheng Ma. A cost-effective, ionically conductive and compressible oxychloride solid-state electrolyte for stable all-solid-state lithium-based batteries. *Nature Communications*, 14(1), 2023. ISSN 2041-1723. doi: 10.1038/s41467-023-39522-1.

[3] Ajay Gautam, Marcel Sadowski, Nils Prinz, Henrik Eickhoff, Nicolò Minafra, Michael Ghidiu, Sean P. Culver, Karsten Albe, Thomas F. Fässler, Mirijam Zobel, and Wolfgang G. Zeier. Rapid crystallization and kinetic freezing of site-disorder in the lithium superionic argyrodite li6ps5br. *Chemistry of Materials*, 31(24):10178–10185, 2019. ISSN 0897-4756. doi: 10.1021/acs.chemmater.9b03852.

[4] Ajay Gautam, Marcel Sadowski, Michael Ghidiu, Nicolò Minafra, Anatoliy Senyshyn, Karsten Albe, and Wolfgang G. Zeier. Engineering the site-disorder and lithium distribution in the lithium superionic argyrodite li6ps5br. *Advanced Energy Materials*, 11 (5), 2021. ISSN 1614-6832. doi: 10.1002/aenm.202003369.

[5] Abhik Banerjee, Xuefeng Wang, Chengcheng Fang, Erik A. Wu, and Ying Shirley Meng. Interfaces and interphases in all-solid-state batteries with inorganic solid electrolytes. *Chemical Reviews*, 120(14):6878–6933, 2020. ISSN 0009-2665. doi: 10.1021/acs.chemrev.0c00101.

[6] Chen-Zi Zhao, Bo-Chen Zhao, Chong Yan, Xue-Qiang Zhang, Jia-Qi Huang, Yifei Mo, Xiaoxiong Xu, Hong Li, and Qiang Zhang. Liquid phase therapy to solid electrolyte–electrode interface in solid-state li metal batteries: A review. *Energy Storage Materials*, 24:75–84, 2020. ISSN 2405-8297. doi: 10.1016/j.ensm.2019.07.026.

[7] Niek J. J. de Klerk and Marnix Wagemaker. Space-charge layers in all-solid-state batteries; important or negligible? *ACS Applied Energy Materials*, 2018. ISSN 2574-0962. doi: 10.1021/acsaem.8b01141.

[8] Jun Haruyama, Keitaro Sodeyama, Liyuan Han, Kazunori Takada, and Yoshitaka Tateyama. Space–charge layer effect at interface between oxide cathode and sulfide electrolyte in all-solid-state lithium-ion battery. *Chemistry of Materials*, 26(14):4248–4255, 2014. ISSN 0897-4756. doi: 10.1021/cm5016959.

2

Theory

"Meten is weten"

Dutch proverb

2.1 Diffraction

Diffraction techniques are fundamental for characterization of crystalline solid-state electrolytes. Because lithium transport depends on the arrangement of framework atoms, the distribution of lithium ions, and the degree of structural disorder, X-ray and neutron diffraction play a central role in establishing the structural basis for ionic conduction.

When a crystalline material is irradiated with monochromatic X-rays or neutrons, their periodic lattice causes constructive interference at specific angles, producing a diffraction pattern characteristic of the underlying structure.

Bragg's law defines the condition for constructive interference:

$$n\lambda = 2d_{hkl}\sin\theta \tag{2.1}$$

where λ is the wavelength of the incident radiation, d_{hkl} is the spacing between crystallographic planes indexed by (hkl), and θ is the scattering angle. The locations of the diffracted peaks provide information about the unit-cell geometry and symmetry, while their intensities reflect the scattering power and positions of the atoms in the structure.

2.1.1 X-ray Diffraction

In X-ray diffraction (XRD), scattering arises from the interaction between X-rays and the electron clouds surrounding atomic nuclei. Because the scattering amplitude increases with electron density, heavy elements dominate the diffracted intensity. As a result, XRD is highly effective at identifying crystalline compounds and resolving structural parameters such as the occupancy of sulphur and bromine at their respective sites.

In addition, X-ray diffraction can be used to estimate the average size of coherently scattering domains, commonly interpreted as crystallite size. Finite crystallite dimensions lead to peak broadening in the diffraction pattern, an effect that can be quantified using the Scherrer equation. Assuming that broadening arises primarily from size effects and that instrumental contributions are known or subtracted, the crystallite size D is given by

$$D = \frac{K\lambda}{\beta\cos\theta} \tag{2.2}$$

where K is the shape factor (typically taken as 0.9), λ is the X-ray wavelength, β is the full width at half maximum (FWHM) of the diffraction peak corrected for instrumental broadening, and θ is the Bragg angle of the peak.

The Scherrer equation provides an estimate of the lower bound of crystallite size and is most accurate for crystallites smaller than ~ 100 nm.

The weak scattering from light elements such as lithium limits the ability of XRD to directly resolve the lithium sublattice. Complimentary techniques can help resolve this issue.

2.1.2 Neutron Diffraction

Neutron diffraction provides a complementary perspective as neutrons scatter from atomic nuclei rather than electron clouds. Nuclear scattering lengths vary irregularly across the periodic table and do not scale with atomic number. Light atoms, including lithium, can scatter neutrons as effectively as, and in some cases more effectively than, heavier atoms.

This makes neutron diffraction well-suited for studying lithium occupancies and the structure of the lithium sub-lattice. It also makes it easier to distinguish between elements that are close to each other on the periodic table.

2.1.3 Rietveld Refinement

The quantitative extraction of structural information from diffraction data is typically accomplished through Rietveld refinement. Rather than analysing individual peak positions, Rietveld refinement optimizes a structural model by minimizing the difference between the observed diffraction pattern and a calculated one based on the model.

In the study of lithium argyrodites, Rietveld refinement is essential for quantifying the degree of halide/sulfide disorder, determining the distribution of lithium across multiple tetrahedral sites (T1–T5), and identifying small lattice distortions that influence ionic mobility. When X-ray and neutron data are refined in combination, the strengths of both techniques are fully exploited: XRD resolves the heavy-atom framework with high precision, while neutron diffraction constrains lithium positions and occupancies. This combined approach yields a robust and internally consistent structural model that forms the basis for interpreting NMR, impedance spectroscopy, and other techniques probing ionic diffusion.

2.2 Solid State Nuclear Magnetic Resonance

NMR probes the interaction between atoms with a non-zero spin and an applied magnetic field. The spin is defined by the spin number I and is non-zero when the number of neutrons and protons is both odd (integer I) or when their sum is odd (1/2 integer I). Non-zero spin nuclei possess (2I+1) possible spin configurations, each with a corresponding energy level. When no magnetic field is present, these levels are degenerate. However, when these nuclei are placed in a magnetic field, the spin energy levels split, with the population of each level being described by a Boltzmann distribution (2.3). This is the referred to as the Zeeman effect.

$$\frac{M_+}{M_-} = exp\left(\frac{-\Delta E_m}{k_B T}\right) \tag{2.3}$$

The energy difference between these levels is given by (2.4) and depends on the strength of the field (B_0), the gyromagnetic ratio of the nucleus (γ) and the reduced Planck's constant($\hbar$). This equation can be rewritten to give the characteristic Larmor frequency (ω_0).

$$\begin{aligned} \Delta E_m &= \hbar \gamma B_0 \\ &= \hbar \omega_0 \end{aligned} \tag{2.4}$$

The Larmor frequency is in the radio wave frequency regime. The energy levels for a I=1/2 is shown in Figure 2.1a, with each level representing the alignment of the spin with regards to the field. Under a static field, nuclei with a positive γ will display a preference for the low-energy state, which corresponds to a net magnetization along the direction of the applied field (the Z-direction). Nuclei with a negative γ will show the opposite. NMR relies on application of a radio frequency pulse to shift the Boltzmann population distribution. After pulse application, the net magnetization will precess in the XY-plane around the Z-axis and slowly return to equilibrium. Simply stated, by placing a coil in the

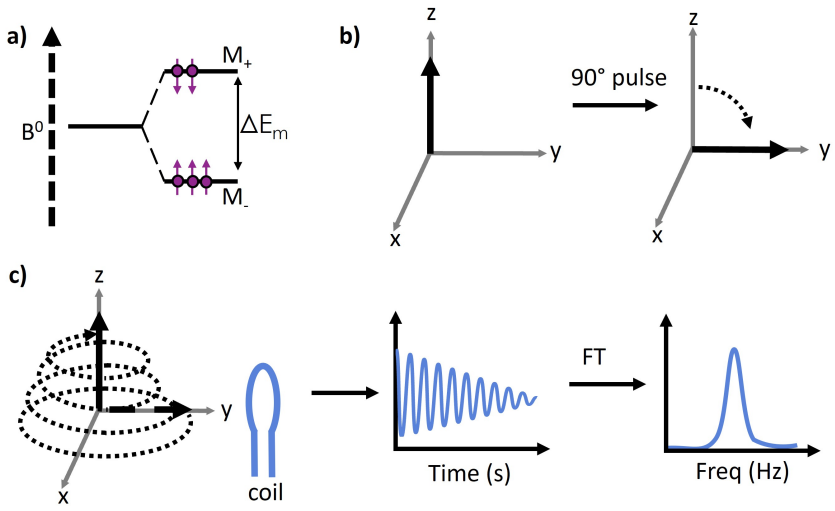

Figure 2.1: (a)The splitting nuclear energy levels of a spin $I = 1/2$ nucleus in the presence of a magnetic field B_0 in the z-direction, (b)the effect of a 90° radio frequency pulse causing the net magnetization to flip to the XY-plane and (c) the magnetization precessing in the XY-plane while returning to equilibrium, causing a signal measured by a coil which is Fourier transformed (FT) to yield a signal.

XY-plane we are able to capture the frequency of precession as well as the time needed for the magnetization to return to its equilibrium state. The frequency of precession is equal to the Larmor frequency of the nucleus and provides information about the chemical environment. The rate of relaxation can be used to investigate diffusion. To understand how this works, we need to understand the different interactions that NMR is sensitive to.

2.2.1 Interactions in NMR

Equation (2.4) describes an isolated spin and in an ideal case, where the experimentally obtained frequency would be equal to the theoretical Larmor frequency. In reality, the obtained frequency is always slightly different, reflecting the properties of the nucleus and its chemical environment. This change is due to the various interactions between the nucleus and its environment. The main interactions discussed in this thesis are:

- Zeeman interactions
- Chemical shift interactions
- Dipole-dipole interactions
- Quadrupolar interactions

For other interactions, such as J-coupling and paramagnetic interactions, the reader is referred to a series of excellent books and reviews on the subject. [1, 2, 11, 13]

Zeeman Interactions

The nuclear Zeeman interaction is the largest NMR interaction and occurs when a nucleus with a non-zero spin experiences a magnetic field. The interaction between spin j and a static field is described by the Hamiltonian:

$$\hat{H}_j^{static} = -\gamma_j B_0 \hat{I}_{jz} \tag{2.5}$$

with $\hat{I}_{jz}$ denoting the spin angular momentum of spin j in the Z-direction and $-\gamma_j B_0$ the Larmor frequency. Due to the size of this interaction, it can be assumed to mask the time-dependent fluctuations of the other interactions mentioned (the Secular Approximation).

Chemical Shift

In response to the applied magnetic field (B_0), electrons within the material will generate their own local magnetic fields ($B_j^{induced}$). The strength of this field depends on the strength of the static field as well as the electron density in the vicinity of the nucleus. Whereas $B_j^{induced}$ is only 10^{-4} times as large as B_0, it is strong enough to change the local magnetic field of the nucleus (Equation (2.6)).

$$\mathbf{B_j^{local}} = \mathbf{B_0} + \mathbf{B_j^{induced}} \tag{2.6}$$

The measured frequency will therefore shift, depending on the electron density and hence local chemical environment of a nucleus. The Hamiltonian therefore becomes:

$$\hat{H}_j^0 = \hat{H}_j^{static} + \hat{H}_j^{CS} \tag{2.7}$$

The shift depends on the orientation of the molecule relative to the applied field and can vary significantly. This effect is called the chemical shift anisotropy (CSA). $B_j^{induced}$ can be written as a function of the applied field and the chemical shift tensor $\boldsymbol{\delta}^j$.

$$\mathbf{B_j^{induced}} = \boldsymbol{\delta}^j \cdot \mathbf{B_0} \tag{2.8}$$

The $\boldsymbol{\delta}^j$ is an orientation-dependent 3x3 matrix. Additionally, each nuclear site possesses three directions which are perpendicular to each other and termed the principal axes of the chemical shift tensor, denoted X, Y and Z. The corresponding numbers (δ_{XX}, δ_{YY} and δ_{ZZ}) termed the principal values, determine the magnitude of the induced field when the external field is applied along the corresponding axis.

$$\hat{H}_j^{CS} = \gamma_j \hat{I}_j \cdot \boldsymbol{\delta}^j \cdot \mathbf{B_j^{induced}} \tag{2.9}$$

$$\mathbf{B_j^{induced}} = \delta zz \cdot B_0 \tag{2.10}$$

This leads to the Hamiltonian given by Eq. (2.9) which, where $\mathbf{B_j^{induced}}$ can be reduced to Eq. (2.10) when B_0 is along the z-axis. Here δ_{zz} depends on the orientation of the principal axis szstem of the chemical shift tensor with respect to the lab axis system as well as the values of the principal components of the CSA tensor (δ_{XX},δ_{YY} and δ_{ZZ})

In liquids, molecular movement results in an averaging of the chemical shift interaction, reducing δ^j to an average of these principal values, namely:

$$\delta_j^{iso} = \left(\delta_{XX}^j + \delta_{YY}^j + \delta_{ZZ}^j\right)/3 \tag{2.11}$$

and

$$\hat{H}_j^{CS} = -\gamma_j B_0 \delta_{iso}^j \hat{I}_{jz} \tag{2.12}$$

This results in an NMR spectrum with one sharp peak whose shift depends on δ_j^{iso}.

In solids, movement is restricted, resulting in an orientation-dependent Hamiltonian:

$$\hat{H}_j^{CS} = -\gamma_j B_0 \delta_{zz}^j \left(\Theta, \phi\right) \hat{I}_{jz} \tag{2.13}$$

with Θ being the angle between the principal Z-axis of the nucleus and the applied magnetic field and ϕ being the angle between the principal X-axis and the projection of the external field onto the principal XY-plane. Each crystallite orientation will have its own unique shift, resulting in a broadened NMR spectrum consisting of a superposition of these shifts.

Dipole-Dipole Interaction

Unlike chemical shifts, dipole-dipole interactions refer to interactions between neighboring nuclear spins. Nuclei are sensitive to neighboring fields and experience mutual interactions. These interactions do not involve the electron cloud and can be divided into homonuclear (between nuclei of the same isotope) and heteronuclear (between nuclei of different isotopes). In case of a large magnetic field, the Hamiltonian for the homonuclear dipolar interaction between spins i and j is given by:

$$\hat{H}_{II}^D = \left(\frac{\mu_0}{4\pi}\right) \frac{\hbar \gamma_I \gamma_I I(I+1)}{r_{ij}^3} \left(3cos^2\theta - 1\right) \left[\hat{I}_{iz} \cdot \hat{I}_{jz} - \frac{1}{4}\left(\hat{I}_i^+ \hat{I}_j^- + \hat{I}_i^- \hat{I}_j^+\right)\right] \tag{2.14}$$

and the Hamiltonian for heteronuclear interaction between spins **I** and **S** is:

$$\hat{H}_{IS}^D = \left(\frac{\mu_0}{4\pi}\right) \frac{\hbar \gamma_I \gamma_S S(S+1)}{r_{ij}^3} \left(3cos^2\theta_{ij} - 1\right) \hat{I}_{iz} \cdot \hat{I}_{jz} \tag{2.15}$$

Dipole-dipole interactions result in a broadening of NMR spectral peaks and can be removed by placing the sample at $\theta_m = \cos^{-1}(1/3) = 54.74^\circ$ relative to the magnetic field, also referred to as the *magic angle*.

Quadrupolar Interaction

Atomic nuclei are charged as they contain both protons and neutrons. For nuclei with spin $I = \mp 1/2$, this charge has a spherical symmetric distribution. In the presence of an electric field gradient, the interaction between the nucleus and the field will not depend on the orientation of the nucleus. A quadrupolar nucleus ($I > 1/2$) possess a non-spherically symmetric charge distribution. Interactions with an electric field gradient will be orientation-dependent. Essentially, quadrupolar nuclei are sensitive to the presence of an electric

field gradient and hence the symmetry of their environment. The Hamiltonian for the full quadrupolar interaction is:

$$\hat{H}^Q = \frac{eQ}{2I(2I-1)\hbar}\hat{\mathbf{I}}\cdot\mathbf{V}\cdot\hat{\mathbf{I}} \tag{2.16}$$

with $\mathbf{V}$ representing the electric field gradient tensor at the site of the nucleus, $\hat{\mathbf{I}}$ being the nuclear spin vector, Q the quadrupolar constant of the nucleus and the spin number. Equation(2.16) shows that the size of the quadrupolar interaction depends on Q and the asymmetry of the environment ($\mathbf{V}$).

The main quadrupolar nucleus in this thesis is ^{7}Li with I = 3/2, possessing $2I + 1 = 4$ nuclear energy levels (+3/2, +1/2, -1/2 and -3/2). In the absence of an electric field gradient, the difference between these levels is the same, $\Delta E_m = \hbar\omega_0$. When the quadrupolar interaction is small, the Hamiltonian can be solved with a first order perturbation. The result is a shifting of the energy levels by ω_Q^1, defined as (2.17) for I = 3/2 and a uniaxial electric field gradient tensor, with C_Q being the quadrupolar coupling constant, θ_Q the angle between the major principal axis of the electric field gradient tensor and the magnetic field and I the spin number.

$$\begin{aligned}\omega_Q^1 &= \frac{3\pi C_Q}{2I(2I-1)}\left(3\cos^2\theta_Q - 1\right)\\ &= \pi C_Q \times \frac{1}{2}\left(3\cos^2\theta_Q - 1\right)\end{aligned} \tag{2.17}$$

The coupling constant C_Q is defined as (2.18) with h being Planck's constant and eq the largest principal value of the electric field gradient tensor.

$$C_Q = \frac{e^2qQ}{h} \tag{2.18}$$

The resulting spectrum for a powder with I = 3/2 is given in 2.2c and consists of a *central transition*, similar to those seen for spin I = 1/2 nuclei, and two *satellite peaks* on either side displaying a characteristic Pake pattern. The distance between the satellite transition peaks is equal to $C_Q/2$. When C_Q, the satellite peaks become too broad to observe clearly or excite properly. In this case, a solid echo can be used. Like bipolar interactions, placing the sample at the magic angle removes the effect of first order quadrupolar interaction from the spectrum.

When C_Q is large, first order perturbation is not sufficient to describe the effect of quadrupolar interaction and second order effects become apparent. These are complex and affect the shape of the central transition, causing it to widen and distort. These effects will not be discussed here and readers are referred to texts on the subject. [13, 15]

2.2.2 Relaxation and Diffusion

After application of a radio frequency pulse, the system strives to return to thermodynamic equilibrium. This can occur when spins encounter a fluctuating magnetic field with the same frequency as their own Larmor frequency. There are two relaxation mechanisms, each with their own characteristic time (see Figure 2.3). Longitudinal relaxation, characterized by T_1, describes the return of net magnetization from the XY-plane to the Z-direction.

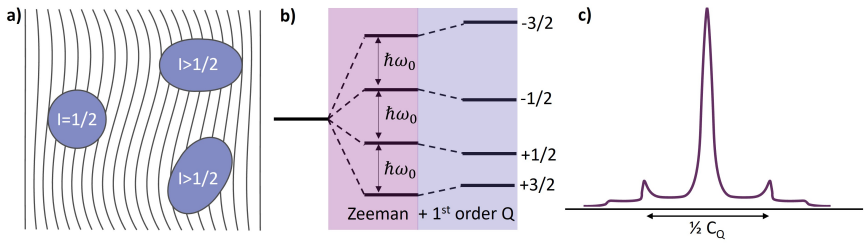

Figure 2.2: Illustration showing the non-spherical axially symmetric charge distribution of quadrupolar nuclei in a magnetic field (a), the change in Zeeman levels as a result of 1st order quadrupolar interactions (b) and a powder spectrum consisting of a central transition and satellite peaks (c)

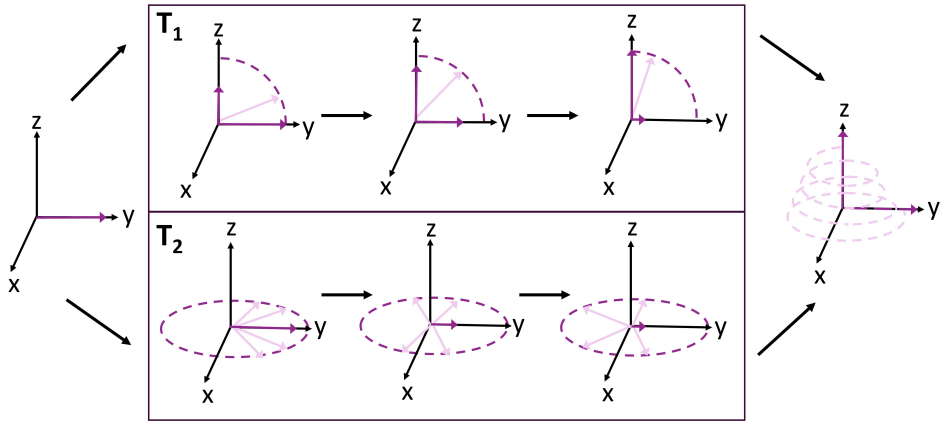

Figure 2.3: Relaxation to equilibrium after a 90 ° pulse through the longitudinal (T_1) and transversal (T_2) – pathways which occur simultaneously.

Transversal relaxation, characterized by T_2, describes the dephasing of net magnetization in the XY-plane. Nuclei experience field fluctuations through the interactions mentioned in Section 2.2.1. For spin $I = 1/2$ nuclei in solids, relaxation mainly occurs through dipolar interactions, whereas for spin $I > 1/2$ nuclei, quadrupolar interactions can also play a significant role.[4, 13]

The nuclear magnetization relaxation rate as a function of relaxation times T_1 and T_2 are given by the Bloch equations, where M_x, M_y, and M_z are the x,y and z-components of the nuclear magnetization, respectively, B_x, B_y and B_z are the x,y and z-components of the magnetic field experienced by the nuclei, respectively and M_0 is the magnetization at $t \longrightarrow \infty$ in the z-direction.

$$\frac{dM_x(t)}{dt} = \gamma\left(M_y(t)B_z(t) - M_z(t)B_y(t)\right) - \frac{M_x(t)}{T_2} \tag{2.19}$$

$$\frac{dM_y(t)}{dt} = \gamma\left(M_z(t)B_x(t) - M_x(t)B_z(t)\right) - \frac{M_y(t)}{T_2} \tag{2.20}$$

$$\frac{dM_z(t)}{dt} = \gamma\left(M_x(t)B_y(t) - M_y(t)B_x(t)\right) - \frac{M_z(t) - M_0}{T_1} \tag{2.21}$$

The seminal work of Bloembergen, Purcell and Pound relates the rates of relaxation to the thermally activated motion of nuclei.[6] Fluctuations in the surrounding magnetic field are due to the thermal motions of atoms in the vicinity of the nuclei studied. Diffusion causes a change in the atomic environment and hence the fluctuations The speed of this change can be defined by the autocorrelation function of the magnetic field experienced by the nuclei along the x-axis $G(\tau)$ and is assumed to be exponential in form (Eq. (2.22)), with $\langle B_x^2 \rangle$ being the mean square of the fluctuating field along the x-axis and τ_c the correlation time.

$$G(\tau) = \langle B_x^2 \rangle e^{\frac{-|\tau|}{\tau_c}} \tag{2.22}$$

The τ_c characterizes the speed of the decay of the autocorrelation and hence the speed at which the nuclei change environment. It is thought to follow an Arhennius equation:

$$\tau_c = \tau_0 e^{\frac{\Delta E}{k_B}} \tag{2.23}$$

The spectral density of an exponentially decaying autocorrelation function is a Lorentzian and shows the spectral contribution of each frequency.

$$J(\omega) = \frac{2\tau_c}{1 + \omega^2 \tau_c^2} \langle B_x^2 \rangle \tag{2.24}$$

In this thesis, T_1 is mainly used for the determination of lithium dynamics. The final formula for T_1 depends on the relaxation mechanism [1]. Dipolar interactions are the most common relaxation source, especially for spin I=1/2 nuclei such as ^{31}P. The formula for homonuclear dipolar interaction is:

$$\frac{1}{T_1} = \frac{2}{5}\left(\frac{\mu_0}{4\pi}\right)^2 \frac{\gamma_I^4 \hbar^2}{r^6} I(I+1)\left[J(\omega_0) + J(2\omega_0)\right] \tag{2.25}$$

Heteronuclear dipolar interactions occur between two unlike spins I and S, resulting in the formula:

$$\frac{1}{T_1} = \frac{2}{5}\left(\frac{\mu_0}{4\pi}\right)^2 \frac{\gamma_I^2 \gamma_S^2 \hbar^2}{r^6} S(S+1)\left[J\left(\omega_0^I\right) + 2J\left(\omega_0^I + \omega_0^S\right) + \frac{1}{3}J\left(\omega_0^I - \omega_0^S\right)\right] \tag{2.26}$$

Here, ω_0^I and ω_0^S and γ_I and γ_S are the Larmor frequencies and gyromagnetic ratios of spins I and S, respectively. Furthermore, r is the distance between two nuclei and μ_0 is the magnetic vacuum permittivity.

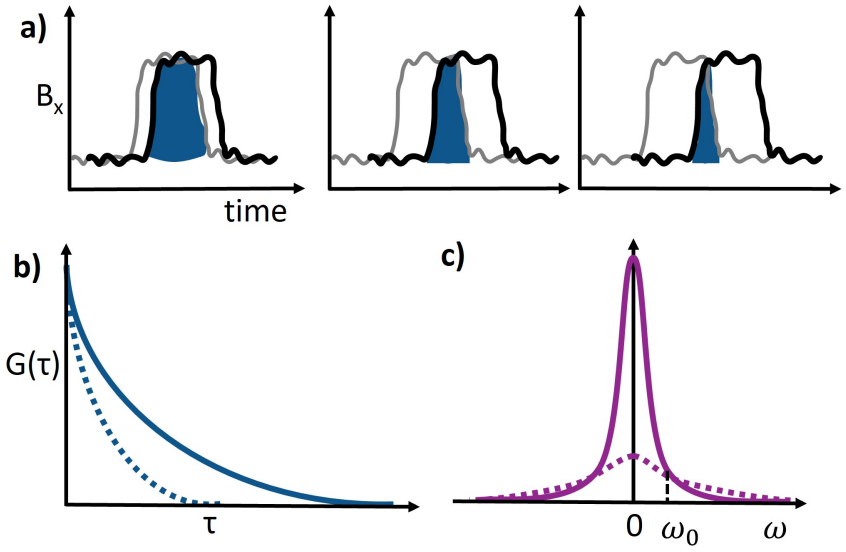

Figure 2.4: a)Illustration of the magnetic field experienced by a nucleus, which shifts with time. The area of overlap represents the magnitude of autocorrelation, b) an exponentially decaying autocorrelation function for different values of tau_c and c) the spectral density of an exponentially decaying autocorrelation function.

For spin I>1/2 nuclei, relaxation can also occur via quadrupolar interactions. For ^{7}Li (I=3/2), relaxation is thought to occur via a mixture of dipolar and quadrupolar interactions.[3, 4]

Finally, relaxation can occur via anisotropy in the chemical shift. As explained previously, variation in the chemical shift arises due to differences in the local degree of shielding experienced by a nucleus. Besides broadening of the NMR spectrum, the CSA can induce relaxation.[1, 5]

$$\frac{1}{T_1} = \frac{2}{15}\Delta\sigma^2\left(1+\frac{\eta^2}{3}\right)\omega_0^2 J(\omega_0) \tag{2.27}$$

Here, the $\Delta\sigma$ is defined as

$$\Delta\sigma = \sigma_{zz} - \left(\frac{\sigma_{xz}+\sigma_{yz}}{2}\right) \tag{2.28}$$

and the assymmetry η is:

$$\eta = \frac{\sigma_{yz}-\sigma_{xz}}{\sigma_{zz}-\sigma_{iso}} \tag{2.29}$$

2.3 Electrochemical Impedance Spectroscopy

Electrochemical impedance spectroscopy (EIS)is a powerful technique used for the determination of resistances within a system. In battery science, it is heavily relied on for the determination of ionic conductivities, charge transfer kinetics and battery degradation, making it the subject of many reviews and tutorials.[12, 16–18]

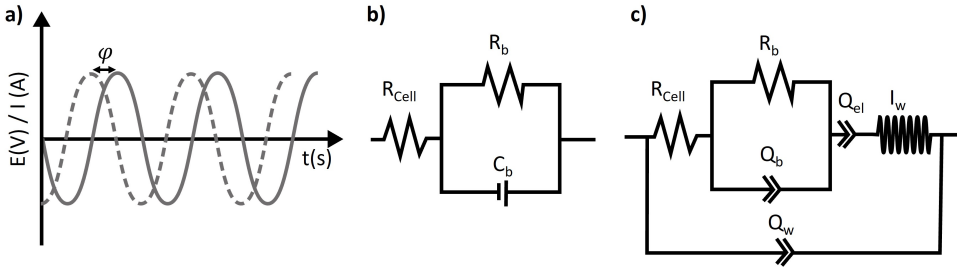

Figure 2.5: a)Illustration of the applied potential (solid line) and the resultant current response (dashed line) as a function of time, resulting in a phase shift ϕ, b) a common equivalent circuit used to fit solid electrolyte impedance spectra and c) a modified version of the equivalent circuit taking into account wire capacitance (Q_W), inductance (I_W) and electrode capacitance (Q_{el}).

Impedance spectroscopy relies on the application of a sinusoidal perturbation, usually in the applied potential across the cell with frequency ω and the measurement of the sinusoidal current response. For an ideal resistor, the resistance (Ω) is defined by Ohm's law (2.30) and is independent of time and frequency. The resistance is therefore only characterized by the magnitude of the potential applied (V) and current response (I).

$$\Omega = \frac{E}{I} \tag{2.30}$$

Impedance is the time-dependent equivalent to resistance and can be defined as:

$$Z(t) = \frac{E(t)}{I(t)} \tag{2.31}$$

Due to this time-dependence, impedance is not only characterized by the magnitude of I relative to V, but also by the shift in phase of I relative to V. Equation (2.31) can be written as (2.32) with Z_0 being the magnitude of the impedance and ϕ being the phase shift. Using the Euler relationship $e^{i\phi} = \cos\phi + i\sin\phi$, the impedance can also be written as a complex function with a real and imaginary part.

$$\begin{aligned} Z(t) &= \frac{E_0 \sin(\omega t)}{I_0 \sin(\omega t + \phi)} \\ &= Z_0 \frac{\sin(\omega t)}{\sin(\omega t + \phi)} \\ &= Z_0 \frac{e^{i\omega t}}{e^{i\omega t - \phi}} \\ &= Z_0 (\cos\phi + i\sin\phi) \end{aligned} \tag{2.32}$$

The phase shift depends on the elements present. For instance, for an ideal Ohmic resistor ϕ=0 ^{o} whereas for an ideal capacitor ϕ=90 ^{o}. Typically, different elements will be present in the system, resulting in a complex signal. Furthermore, when elements are

present in parallel, the degree to which they contribute to the signal can depend on ω. To unravel the various elements, ω is swept over a certain range (usually 0.1 Hz to 1 MHz), resulting in an impedance spectrum. This spectrum can be presented in either a Bode plot, where the magnitude and phase are given as separate data points, or a Nyquist plot, where the real and imaginary components of the impedance define the x- and y-values respectively with: $Z_{Re} = Z_0 \cos\phi$ and $Z_{Re} = Z_0 \sin\phi$.

To identify and quantify the elements present, the impedance spectrum obtained is fit by comparing it to a computed spectrum from a model circuit of elements. A common model used to model an ideal solid electrolyte is given in 2.5b. Here, the resistor R_{cell} represents the resistance of the cell and wires while the resistor R_b and capacitor C_b in parallel represent the resistance and capacitance of the solid electrolyte, respectively.

2.3.1 Deviation from Ideality

In reality, an ideal capacitor is often replaced by a constant phase element to account for non-ideality. The departure from ideality results in a $\phi < 90\ ^o$, quantified by an α-value (2.33). Various theories exist regarding the origin of the constant phase element, such as surface roughness and a distribution in capacitance.[9, 10]

$$\alpha = \frac{\theta}{90^\circ} \tag{2.33}$$

Furthermore, the measurement setup used is not invisible in the EIS-measurement and needs to be taken into account. A traditional electrochemical setup consists of three electrodes in contact with the system under study, namely the working-, counter- and reference electrode. Simply put, during a measurement, charge flows between the working electrode and the counter electrode, while the potential of the working electrode is monitored with respect to the reference electrode. This system is difficult to achieve for solid-state electrolytes, mainly due to challenges regarding the reference electrode. [18]

A two-electrode configuration is often used instead, combining the reference- and counter electrode into one electrode. The sample is sandwiched between this electrode and the working electrode, allowing measurement of current and potential across the cell. The electrode material can be either ion blocking or active. Ion blocking electrodes block the flow of ions while allowing electrons to pass and are typically made of stainless steel or other redox-inert materials. During an EIS-measurement, they appear as a (non-ideal) capacitor in series with the system. Non-blocking electrodes allow both ions and electrons to pass and typically consist of either lithium metal or a lithium-indium alloy in the case of lithium solid-state electrolytes. During an EIS-measurement, these electrodes show up as a resistor and (non-ideal) capacitor in parallel. Due to the inherent chemical instability of sulfide electrolytes, blocking electrodes are most often used to asses ionic conductivity. Besides the electrodes, the cell and wires can also appear in the EIS-spectrum obtained. Whereas this can sometimes be neglected, it is good practice to determine these values beforehand, especially when dealing with a home-built setup. When the wires leading to the cell are not shielded properly, the can act as antennas, picking up stray signals and

resulting in additional noise. Proper shielding of the wires as well as use of a Faraday cage can prevent this. Furthermore, long wires can lead to inductances and stray capacitances. Whereas inductances can easily be recognized, stray capacitances can obscure the authentic sample signal and result in erroneous interpretation of the data. For this reason, it is important to measure these capacitances and take them into account when fitting the data.

2.3.2 The Kramers Kronig Test

Equation (2.32) forms the basis of EIS and its analysis and is only valid if three requirements are met:

1. The response is linear, meaning that the ratio of V_0 and I_0 is constant, regardless of the size of the perturbation. A system loses linearity when Faradaic reactions occur and care must be taken to prevent this. This is often done by selecting inert electrodes and a small voltage perturbation.

2. The response is casual, meaning that it arises as a result of the perturbation. This is not the case when a signal is due to noise.

3. The response is stable and does not change over time. Factors such as degradation of the material and fluctuations in temperature can affect the stability.

To test whether a system meets the three requirements mentioned, a Kramers-Kronig Test (KKT) can be applied. This test relies on the Kramers-Kronig relations ((2.34) and (2.35)), which predict the real component of the signal (Z_{Re}) from the imaginary component (Z_{Im}) or vica versa, provided that the signal meets the three requirements given.

$$Z_{Re}(\omega) = \frac{2}{\pi}\int_0^\infty \frac{\omega' \cdot Z_{Im}(\omega')}{\omega^2 - \omega'^2}\, d\omega' \tag{2.34}$$

$$Z_{Im}(\omega) = \frac{-2}{\pi}\int_0^\infty \frac{\omega \cdot Z_{Re}(\omega')}{\omega^2 - \omega'^2}\, d\omega' \tag{2.35}$$

The equations require the measurement frequency ω to stretch from zero to infinity, which is not possible. The solution is to use a Linear Kramers-Kronig approach, pioneered by Boukamp.[7, 8] Here, a Voight-circuit, consisting of sets of a resistor and capacitor in parallel is used. Each set represents a datapoint k, from the total number of datapoints N and is defined by its own time constant $\tau_k = R_k C_k$. By taking $\tau_k = \omega_k^{-1}$, the real and imaginary components of the circuit impedance can be defined as:

$$\hat{Z}_{Re}(\omega_i) = R_\infty + \sum_{k=1}^{M} \frac{R_k}{1 + (\omega_i \tau_k)^2} \tag{2.36}$$

$$\hat{Z}_{Im}(\omega_i) = -\sum_{k=1}^{M} \frac{R_k \omega_i \tau_k}{1 + (\omega_i \tau_i)^2} \tag{2.37}$$

Equations (2.36) and (2.37) serve a dual purpose. As explained before, each measurement point has a corresponding Z_{Re} and Z_{Im}. By using the Z_{Re} and Z_{Im} obtained from the measurement, two sets of R_k-values can be obtained from equations (2.36) and (2.37). The values obtained from Z_{Re} can be used in equation (2.37) to calculate $\hat{Z}_{Im}$. As these $\hat{Z}_{Im}$-values are obtained using a theoretical circuit, it should comply with the three requirements listed above. By comparing the calculated $\hat{Z}_{Im}$-values to the experimentally obtained Z_{Im}-values for each point, a residual can be obtained to quantify the reliability of the point (2.38).[14] This procedure can also be done for $\hat{Z}_{Re}$ and Z_{Re}.

$$\Delta_{Im}(\omega) = \frac{Z_{Im}(\omega) - \hat{Z}_{Im}(\omega)}{|Z(\omega)|} \tag{2.38}$$

Bibliography

[1] A. Abragam. *The Principles of Nuclear Magnetism*. Clarendon Press, 1961.

[2] D. C. Apperley, R. K. Harris, and P. Hodgkinson. *Solid-state NMR: Basic principles and practice*. Momentum Press, 2012.

[3] K. Arbi, M. Tabellout, M. G. Lazarraga, J. M. Rojo, and J. Sanz. Non-Arrhenius conductivity in the fast lithium conductor li1.2ti1.8al0.2(po4)3 A 7li nmr and electric impedance study. *Physical Review B*, 72(9):094302, Sept. 2005. Publisher: American Physical Society.

[4] R. Bertermann and W. Müller-Warmuth. Universality of NMR results in LISICON systems and other solid lithium conductors. *Zeitschrift fur Naturforschung - Section A Journal of Physical Sciences*, 53(10-11):863–873, Nov. 1998. Publisher: Verlag der Zeitschrift fur Naturforschung.

[5] J. Blicharski. Nuclear Magnetic Relaxation by Anisotropy of the Chemical Shift. *Zeitschrift für Naturforschung A*, 27(10):1456–1458, Oct. 1972. Publisher: De Gruyter.

[6] N. Bloembergen, E. M. Purcell, and R. V. Pound. Relaxation Effects in Nuclear Magnetic Resonance Absorption. *Physical Review*, 73(7):679, Apr. 1948. Publisher: American Physical Society.

[7] B. A. Boukamp. A nonlinear least squares fit procedure for analysis of immittance data of electrochemical systems. *Solid state ionics*, 20(1):31–44, 1986.

[8] B. A. Boukamp. A linear kronig-kramers transform test for immittance data validation. *Journal of the electrochemical society*, 142(6):1885, 1995.

[9] G. Brug, A. van den Eeden, M. Sluyters-Rehbach, and J. Sluyters. The analysis of electrode impedances complicated by the presence of a constant phase element. *Journal of Electroanalytical Chemistry and Interfacial Electrochemistry*, 176(1-2):275–295, Sept. 1984. Publisher: Elsevier.

[10] A. Lasia. The Origin of the Constant Phase Element. *The Journal of Physical Chemistry Letters*, 13(2):580–589, Jan. 2022. Publisher: American Chemical Society.

[11] D. D. Laws, H.-M. L. Bitter, and A. Jerschow. Solid-state nmr spectroscopic methods in chemistry. *Angewandte Chemie International Edition*, 41(17):3096–3129, 2002.

[12] A. C. Lazanas and M. I. Prodromidis. Electrochemical Impedance Spectroscopy□A Tutorial. *ACS Measurement Science Au*, 3(3):162–193, June 2023. Publisher: American Chemical Society.

[13] M. H. Levitt. *Spin Dynamics: Basics of Nuclear Magnetic Resonance*. Wiley, Chichester, England ; Hoboken, NJ, 2008.

[14] M. Schönleber, D. Klotz, and E. Ivers-Tiffée. A Method for Improving the Robustness of linear Kramers-Kronig Validity Tests. *Electrochimica Acta*, 131:20–27, June 2014.

[15] J. Smith. Nuclear quadrupole interactions in solids. *Chemical Society Reviews*, 15(2):225–260, 1986.

2

[16] S. D. Talian, S. Brutti, M. A. Navarra, J. Moškon, and M. Gaberscek. Impedance spectroscopy applied to lithium battery materials: Good practices in measurements and analyses. *Energy Storage Materials*, 69:103413, May 2024.

[17] P. Vadhva, J. Hu, M. J. Johnson, R. Stocker, M. Braglia, D. J. Brett, and A. J. Rettie. Electrochemical impedance spectroscopy for all-solid-state batteries: theory, methods and future outlook. *ChemElectroChem*, 8(11):1930–1947, 2021.

[18] L. Zhang, Y. Dai, C. Li, Y. Dang, R. Zheng, Z. Wang, Y. Wang, Y. Cui, H. Arandiyan, Z. Shao, et al. Recent advances in electrochemical impedance spectroscopy for solid-state batteries. *Energy Storage Materials*, 69:103378, 2024.

3

The Relationship Between Halide Substitution, Structural Disorder and Lithium Distribution in $Li_{6-x}PS_{5-x}Br_{1+x}$

"The presence of those seeking the truth is infinitely to be preferred to the presence of those who think they've found it."

Terry Pratchett, Monstrous Regiment

This chapter has been published as: Gautam, Ajay, Al-Kutubi, H et al. "Exploring the Relationship Between Halide Substitution, Structural Disorder, and Lithium Distribution in Lithium Argyrodites ($Li_{6-x}PS_{5-x}Br_{1+x}$)" Chemistry of Materials 35.19 (2023): 8081-8091.

3.1 Introduction

Lithium-ion batteries are the leading battery technology used in portable electronics and electric vehicles, demonstrating constant enhancement/improvement in electrochemical performance resulting from both materials and engineering development. [1–3] However, lithium-ion batteries utilize organic liquid electrolytes with a high flammability risk and limited energy density due to their incompatibility with the lithium metal anode. [4, 5] All solid state batteries (ASSBs) replace liquid electrolytes with solid electrolytes and may enable the use of a lithium/silicon metal anode, which could offer a higher energy density and improved safety. [5–9] A crucial component of ASSBs is an ionically conductive solid electrolyte that can provide stable interfaces with the positive and negative electrodes. [9] To achieve this, various solid electrolytes have been developed so far including oxides, [10–12] phosphates, [13] lithium halides, [14–20] and lithium (halide-enriched) argyrodites ($Li_{6-x}PS_{5-x}Hal_{1+x}$, Hal = Cl and Br). [21–26] Among all of them, lithium argyrodites have gained relatively large interest because of their higher ionic conductivity, favourable mechanical properties, and ease of processing. [27, 28] High conductivities are required for fast charging and high power applications and generally allow more efficient use of the energy stored in the battery. Further, improving conductivity and developing effective synthesis routes demand a better understanding of the conduction mechanism and its correlation to the structure. The halide-based argyrodite family is considered one of the most promising classes of solid electrolytes exhibiting very high ionic conductivities at room temperature. [26] Figure 3.1a shows the ideal crystal structure of Li_6PS_5Hal argyrodite in the ordered state having the cubic $F\bar{4}3m$ space group. In the face-centered cubic lattice, halide ions occupy the tetrahedral Wyckoff 4*a* sites and S^{2-} not bonded to P occupies half of the tetrahedral sites (Wyckoff 4*d*). The argyrodite cubic phase anion framework forms 136 interstitial tetrahedral voids per unit cell available for cation occupancy. [11, 29] Four voids are occupied by P^{5+} cations on the Wyckoff 4*d* site, forming PS_4^{3-} tetrahedra, together with S on the Wyckoff 16*e* site. The remaining 132 voids can be occupied by the lithium sites and categorized according to how many S ions (16*e*) are shared (face, edge, corner) with the PS_4^{3-}-tetrahedra. [11, 30] Thus, the tetrahedral site can be split into five distinct tetrahedral types (types 1-5), as shown in Figure 3.1b, that were described by Deiseroth et al. [29, 31, 32] The type 1 (T1) and type 2 (T2) sites share faces and edges with PS_4^{3-}. The type 3 (T3) and type 4 (T4) tetrahedral sites share 4 and 3 corners with PS_4^{3-}, respectively. [11, 29, 31–33] The type 5 (T5) sites share 2 corners with PS_4^{3-} and the type 5a (T5a) sites lie in between the faces of 2 neighbouring T5 sites in a trigonal bipyramidal environment [11] because of their close proximity, as shown in Figure 3.1b. The T5, T2, T4, and T5a sites form a cage-like substructure around the free sulphur anions (4*d* site), as shown in Figure 3.1c, which form the 3D Li^+ network throughout the structure.

De Klerk et al [35] proposed three different jump processes for lithium-ion conduction pathways: intra-cage and doublet jumps (within the cage), and inter-cage jump (between the cages). In these DFT simulations T5- and T5a- Li-sites were considered, whereas a recent study has suggested additional lithium sites to be involved that impact the diffusion pathway and mechanism [36, 37]. Minafra et.al, recently re-investigated the lithium argyrodites substructure for $Li_{6-x}PS_{5-x}Hal_{1+x}$ (Hal= Cl, Br, I), revealing additional T2 lithium occupancies and suggested new lithium conduction pathways [37]. In other sul-

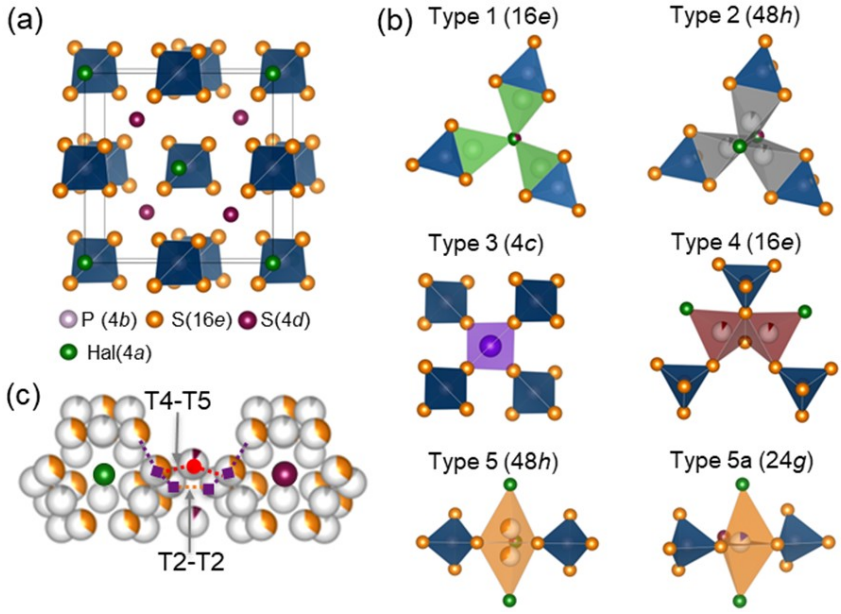

Figure 3.1: (a) Crystal structure of $Li_{6-x}PS_{5-x}Hal_{1+x}$, Hal = Cl, Br, and I, with ordered state. Hal– located on the Wyckoff 4*a* site and the sulfide anion (S^{2-}–) on the Wyckoff 4*d* site; S^{2-} anions are tetrahedrally close-packed on Wyckoff positions (4*d*, 16e), forming 136 tetrahedral voids; four are occupied by P5+ on the 4b site, forming tetrahedral PS43–. The lithium site is not shown for clarity. (b) Panels showing the trigonally coordinated type 5a site and the five tetrahedral interstitial sites (Types T1-T5) that can accommodate lithium ion(proposed in [34]). (c) Lithium (T5, T2, T5a, and T4 sites) form the cages around the S^{2-}/Hal^{-} anions (4*d* site); T2–T2 and T5–T4–T5 offer the shortest inter-cage jump distance (orange dot line and red dot line, respectively).

phide argyrodite compositions, partial occupancy of additional (T2, T3, or T4) lithium sites was discovered. [38–40] For instance, partial substitution of Ge4+ in the P5+ site in $Li_{6+x}P_{1-x}Ge_xS_5I$ leads to partial occupancy of interstitial T2 and T4 sites [41], which provides shorter and more favourable paths for the Li^+ diffusion, thereby increasing the ionic conductivity from 10^{-3} to 10 mS/cm [41]. Another argyrodite series, the Sn-substituted thioantimonate argyrodites, exhibited partial occupancy of the T2 and T3 sites, and the partial occupancy of the T4 sites was also observed in $Li_{6.15}Al_{0.15}Si_{1.35}S_{5.4}O_{0.6}$. [42] Anion site disorder refers to the random arrangement of various anions within the same crystallographic site (in this case Br occupancy on the 4*d* site) [43]. The iodide version represents the ordered arrangement where the 4*a* site is fully occupied by I^- (I^- (Wyckoff 4*a*) = 1), while the 4*d*-site is exclusively occupied by S^{2-}, a result of the large difference in ionic radii. In this case poor ion diffusion between the Li-ion cages presents the rate-limiting step for long rage diffusion [35]. Following the decreasing difference in ionic radii, the site disorder increases for bromide, followed by the chloride version having the highest site disorder of S^{2-}/Hal^- on the 4*d* site (Br^- (4*d*) = 20 % , Cl^- (4*d*) = 60 %) [43]. DFT simulations predict that the maximum conductivity may be achieved with around 75% site disorder, where the jump rate frequency of the three jump processes, doublet, intra and inter cage is similar [35]. Halide substitution is also shown to increase conductivity. Adeli et al. [26] investigated the higher chloride substitution in $Li_{6-x}PS_{5-x}Cl_{1+x}$ ($x \leq 0.5$;) with a conductivity of 9 mS/cm achieved at x = 0.5. In addition to different halides, Yu et al. [44] reported an ionic conductivity of 4.13 mS/cm for the higher bromide substituted $Li_{6-x}PS_{5-x}Br_{1+x}$ ($x \leq 0.5$) [44]. Despite these significant advances, the relationships between long-range diffusion and structure, especially with regard to sublattice disorder is still not well understood. In this study, we investigate the effect of halide substitution ($Li_{6-x}PS_{5-x}Cl_{1+x}$, in the range $0.0 \leq x \leq 0.5$) on lithium argyrodite and engineer the structural disorder by changing the synthesis protocol. First, an argyrodite precursor is prepared via mechanical milling, followed by heat treatment at a particular temperature to obtain the crystalline argyrodite. Two different cooling methods were employed to influence the extent of structural disorder. Rietveld refinement against the neutron diffraction patterns was performed, demonstrating that this preparation method influences the structural disorder. We find that higher ionic conductivity is correlated with a less negative charge on the 4*d* site, as replacing the S^{2-} with Br^- leads to a lowered average charge on the 4*d* site and weaker interactions within the Li^+ "cage", promoting a diffusion pathway for Li^+ ions across the unit cell. We also identify an additional T4 Li^+ site in bromide-based argyrodite, which enables an alternative jump route (T5–T4–T5) with a lower migration energy barrier. The resulting expansion of the Li^+ cages and the increased connections between the cages leads to a maximum ionic conductivity of 8.55 mS/cm. Overall, this work provides a deeper understanding to further improve the ionic conductivity of lithium argyrodites and other solid electrolytes.

3.2 Materials and Methods

3.2.1 Mechanochemical Milling and Post-annealing

$Li_{6-x}PS_{5-x}Br_{1+x}$ syntheses were performed under an argon atmosphere to prevent contamination of oxygen (O2 < 2 ppm) and water (H2O < 1 ppm). $Li_{6-x}PS_{5-x}Br_{1+x}$ was syn-

thesized using mechanochemical milling (Fritsch Pulverisette 7 premium line). The initial precursors; lithium sulfide (Li_2S, 99.98%), lithium bromide (LiBr, 99.99%), and phosphorus pentasulfide (P_4S_{10}, 99%) were purchased from Merck and Sigma Aldrich. All precursors were mixed in an appropriate stoichiometric ratio using a mortar and pestle. The obtained 1.0 g of the precursor was then mechanochemically milled (30:1 mass ratio of milling media to precursors) using 10-mm-diameter zirconia balls at 510 rpm for 25 h (every 10 min milling followed by 10 min rest time). After each cycle of milling the direction of rotation was reversed to achieve better mixing of the precursors. The obtained powder was manually pressed into a 1-cm-diameter pellet and then placed inside a quartz ampoule. Before filling, the quartz ampoules were heated in a dynamic vacuum at 473 K for 12 h to remove traces of water. The quartz ampoules were sealed under a vacuum (<10-3 mbar). The sealed quartz ampoules were placed inside a furnace for crystallization, where a ramping rate of 100 K h^{-1} was applied to reach a temperature of 550 °C for x = 0.0 and 430 °C; for x = 0.3 and 0.5 ($Li_{6-x}PS_{5-x}Br_{1+x}$). After a reaction time of 2 h, two different cooling methods were applied: (1) Fast cooling by quenching in liquid nitrogen or (2) slow cooling using a cooling rate of 4 K h^{-1} during 5-6 days. The final obtained powder was hand-ground, and stored in an argon atmosphere glove box. The phase purity, lithium substructure, and ionic transport of the argyrodite series were analyzed by X-ray diffraction, neutron powder diffraction, electrochemical impedance spectroscopy and NMR spectroscopy.

3.2.2 X-ray Diffraction

X-ray diffraction was carried out to determine the phase purities and relevant structural parameters with a X'Pert Pro X-ray diffraction (PaNalytical) in Bragg-Brentano θ-θ geometry with Cu Kα radiation (λ_1 = 1.540598 Å and λ_2 =1.544426 Å, at 45 kV and 40 mA). Measurements were taken in the 2θ range between 10° and 90°. All powders were placed in airtight sample holder with a Kapton lid under an argon atmosphere to prevent air exposure.

3.2.3 Neutron Powder Diffraction

Neutron powder diffraction data were collected on a PEARL neutron powder diffractometer at the research reactor of the TU Delft [45], operating at room temperature with the 533 reflections of the germanium monochromator (neutron wavelength of λ = 1.667 Å). For each sample approximately 1.5 g was loaded into a 6-mm-diameter cylindrical vanadium can under an argon atmosphere and then sealed using indium wire to prevent air exposure during transport. The sample was measured for 6–18 h from 10° <2θ ≤ 160°, under vacuum. A reference measurement of the empty sample can was subtracted from each of the reported diffractograms.

3.2.4 Bond Valence Site Energy (BVSE)

BVSE analysis was performed using softBV software tool combined with a grid size of 0.1 Å [46–48]. The Crystallographic Information File (CIF) obtained from the Rietveld refinement of the neutron diffraction data of $Li_{6-x}PS_{5-x}Br_{1+x}$ argyrodites series, was used to obtain the energy landscape. An input file (.cube) was generated in softBV, and the BVSE landscape was plotted in VESTA 50 to visualize the iso-surface of Li-ion migration paths across unit cell. More details of the BVSE model can be found in ref [47–49].

3.2.5 Electrochemical Impedance Spectroscopy

Temperature-dependent electrochemical impedance spectroscopy was performed using an Autolab PGSTAT with EC10M impedance analyser using 0.01V amplitude and frequency ranging from 10 MHz to 1 Hz to determine the ionic conductivity and activation energy of the samples. Approximately 200 mg powders were pressed into pellets with 10 mm diameter using the 300 MPa of pressure for 1 min. Stainless steel disks were attached on both sides of the pellet [49]. The temperature range was −40 to 10 °C with a step size of 10 °C (Fryka Climate Chamber). Analyses of the obtained spectra were performed using the RelaxIS 3–Impedance Spectrum Analysis software.

3.2.6 Rietveld Refinement

The TOPAS software [50] was used to perform Rietveld refinements of X-ray diffraction and neutron diffraction data. As a starting point for this study, the structural information obtained by the neutron power diffraction of Li_6PS_5Br from [39] was used. The quality of the fits was determined using the goodness-of-fit (GOF) fit indicator and Rwp. The following parameters were refined: (1) 15 coefficients for a Chebyshev function were used to fit the background and peak shape modelled by the modified Thomson–Cox–Hasting pseudo-Voigt function, (2) scale factor, zero error, (3) lattice parameter, isotropic atomic displacement parameter, (4) atomic occupancies of the free S^{2-} (Wyckoff 4*d*) and Br^- (Wyckoff 4*a*) anions, since these two anions can be exchanged. The occupancies of total occupancies of Br^- and S^{2-} on the Wyckoff 4*a* site Wyckoff 4*d* site were constrained to one (occupancies of Br^- (4*a*) + S^{2-} (4*a*) = 1, occupancies of S^{2-} (4*d*) + Br^- (4*d*) = 1) assuming full occupancy of these sites by S^{2-} and Br^-. The stability of the refinements was ensured by allowing the refinement of multiple correlated parameters simultaneously. Finally, lithium occupancies on the possible interstitial sites were determined. All lithium positions and occupancy was probed during the Rietveld refinement, Starting conditions from Gautam et al. [39] were used as a reference for both lithium position and occupancy. When the negative or unphysical value for thermal displacement parameter or occupancies occurred, the lithium occupancy was assumed to be below the resolution limit and was not included in the refinement model. The Fourier difference map was also performed to identify visible indications of Li occupation at particular sites. The overall Li^+ content was constrained to obtain a charge balance with the refined Br content. The constraints on individual anion/cation occupancies are available in supporting information (Table A.1 -A.7).

3.2.7 Solid State NMR

Solid state ^{6}Li NMR spectra were obtained on a Bruker Ascend 500 magnet with a static magnetic field B0=11.7 T equipped with a NEO console, corresponding to a ^{6}Li Larmor frequency of 73.6 MHz. Sample powders were packed into zirconia rotors of 4 mm diameter and a MAS speed of 5 kHz was used. The spin-lattice relaxation time (T1) was determined using a saturation-recovery pulse program [51]. The 90 degree pulse and T1 were determined for each sample individually. A recycle delay of 5 times the T1 was used for the single pulse spectra to ensure full relaxation. All spectra are referenced against LiCl in water at 0 ppm.

3.3 Results and discussion

3.3.1 Structural Changes

Lithium argyrodite Li_6PS_5Hal, where Hal represents Cl, Br, or I, exhibits structural disorder between the Hal^- and S^{2-} on 4*d* positions, where higher disorder has been shown to result in higher Li-ion conductivities [37, 44]. Recently, it was discovered that structural disorder can be tuned in single composition Li_6PS_5Br via the synthesis method. [39] Furthermore, replacing the S^{2-} with Br^- has been shown to increase ionic conductivity. However, the effects of this substitution on the lithium substructure and structural disorder are not well understood. In order to fully understand the influence of Br-substitutions in lithium argyrodites and the role of the Br^-/S^{2-} disorder, a mechanochemical synthesis method was used to synthesize a series of $Li_{6-x}PS_{5-x}Br_{1+x}$ materials ($x \leq 0.5$), where the precursors Li2S, P4S10, and LiBr were mechanically milled to ensure uniform mixing as reported previously, [52] and subsequently heated at different temperatures (550°C for x = 0.0, or 430°C for x = 0.3, and 0.5) for 2h, which was sufficient to achieve crystalline lithium argyrodite. In order to control site disorder (in this case the 4*d* Br occupancy), two distinct cooling methods were applied: (1) The material was slowly cooled at a rate of 4 °C per h over several days to minimize Br occupancy on 4*d* site in each composition, (2) The material was quenched in liquid nitrogen (fast cooling) to achieve higher Br occupancy on 4*d* site. The quenching was expected to "freeze in" the higher Br occupancy on 4*d* site that was achieved at higher (synthesis) temperatures. Rietveld refinement of the neutron diffraction patterns was used to determine the structure, especially aiming to reveal the lithium substructure and the Br site disorder. The lattice parameter, occupancies (Br and S, Wyckoff 4*d* and 4*a*), sites (S, Wyckoff 16*e*), and thermal parameters (S, P, and Br) were refined. Figure 3.2a shows a Rietveld refinement of slow-cooled Li_6PS_5Br as an example: all refinements and structural information can be found in the supporting information (Table A.1 -A.7). Samples (see Figure A.1) contained minor impurity phases of Li_3PO_4 and LiBr (less than 1.0 wt%), but these were assumed to have negligible impact on ionic transport or structural analysis. While increasing the Br content up to x = 0.5, the cubic polymorphs are maintained. Wang et al [21] showed that increasing Br content in $Li_{6-x}PS_{5-x}Br_{1+x}$ (x = 0.7 and 0.8) led to the increase LiBr and Li_3PS_4 impurities, indicating a solubility limit. Therefore, the analysis focused on the cubic polymorphs within the solubility limit ($x \leq 0.5$). The Pawley-fit-refined lattice parameter of slow-cooled Li_6PS_5Br results in a = 9.98356 (7) Å, consistent with previous studies [39]. Figure 3.2b shows the lattice parameter as a function of Br-content. As the Br content increases (higher x), the lattice parameter decreases for the slow cooling method and increases for the fast cooling method. The difference in the systematic change in the lattice parameter as a function of Br content and two cooling methods is noteworthy and unexpected. Figure 3.2c shows the lattice parameter as a function of the Br distributed across the Wyckoff 4*a* site. Variation in Br occupancy on 4*d* site in Li_6PS_5Br can affect the lattice parameter due to the difference in ionic radii between bromide (196 pm) and sulfur (184 pm) [53] anions occupying 4*a* sites and changes in the Li^+ occupancy around the 4*d*/4*a* sites as divalent sulphur is replaced by monovalent bromine [39]. For the slow cooling method, increasing the Br content does not affect the Br occupancy at the 4*a* site significantly (Figure A.3). Hence the decrease in lattice parameter with increasing Br content may be due to the increase in Li^+ vacancies and/or differences in Li^+ distribution. In the quenched sample, a clear

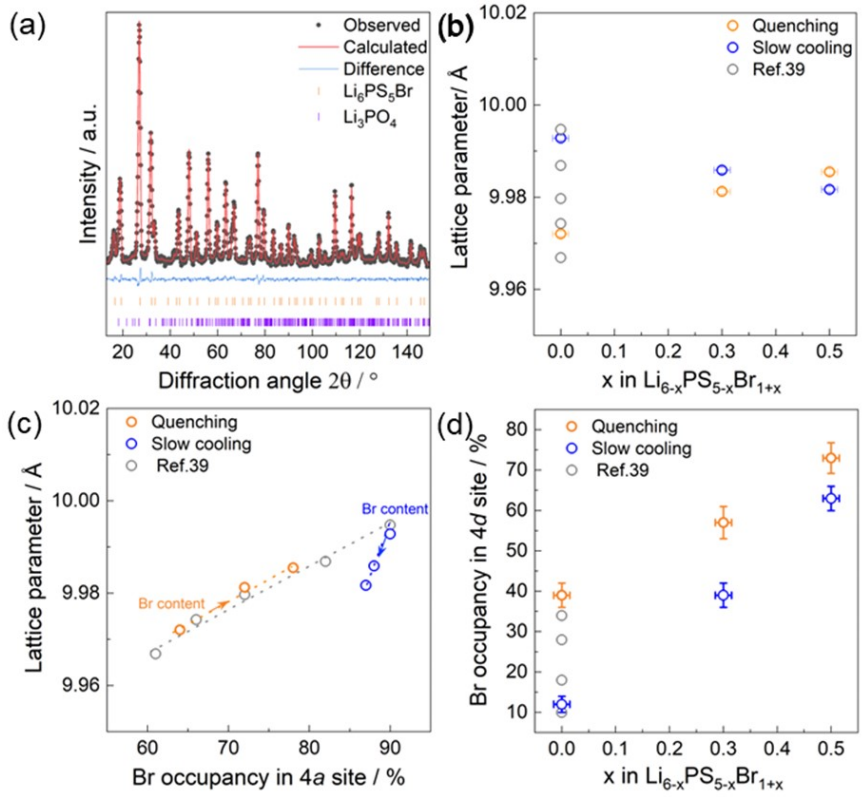

Figure 3.2: (a) Rietveld refinement analysis of neutron diffraction data of slow-cooled Li_6PS_5Br (x = 0), showing a small fraction (0.5 wt%) of the impurity phase Li_3PO_4. (b) Lattice parameters as a function of Br content. (c) Lattice parameters as a function of Br distributed across the Wyckoff 4*a* site, and (d) Percentage of Br occupancy on the Wyckoff 4*d* site as a function of total Br content. The data for Li_6PS_5Br in (b)-(d) are taken from [39]

trend was shown between the lattice parameter and Br occupancy in the 4*a* site. As the Br content increases, Br occupancy in the 4*a* site also increases (Figure A.3), resulting in a larger lattice parameter. This trend is consistent with the previous studies [39].

The Br occupancy on the 4*d* site can be tuned in a single composition by adjusting the synthesis method [39, 52]. In this work, we have employed a similar approach while increasing the Br content in lithium argyrodites. As the Br content (x) is increased, Br is distributed across the Wyckoff 4*a* and 4*d* sites in the crystal structure. Figure 3.2d shows the percentage of Br in 4*d* site obtained by the two different cooling methods as a function of total Br content. Slow-cooled sample have a lower Br 4*d* site occupancy, as determined by Rietveld refinements against neutron diffraction patterns. As the total Br content increases, the Br in 4*d* site increases, starting from 12% at x = 0.0 and reaching 63% at x = 0.5 for the slow-cooled method. The quenched method has an even higher Br in 4*d* site, starting from 39% at x = 0.0 to 72% at x = 0.5, most likely because fast cooling "freezes in" the higher Br occupancy of the 4*d* site that is achieved at higher temperatures.

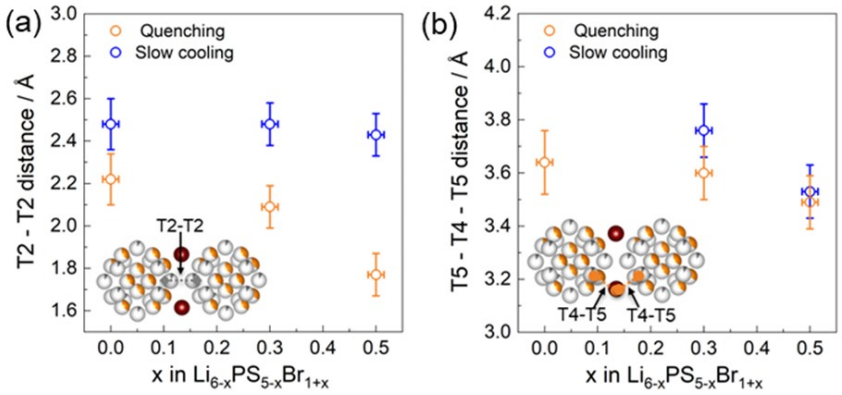

Figure 3.3: (a) T2–T2 distance and (b) T5–T4–T5 distance of $Li_{6-x}PS_{5-x}Br_{1+x}$ as a function of the Br content. The inset shows a visual representation of lithium cages in which the T5–T4–T5 (orange dot line) and T2–T2 (gray dot line) jump distance offer a shorter distance between the lithium cages. The T2–T2 distance and 2 times of (T5–T4) distance decrease with increasing Br content, indicating greater connectivity between cages and increasing ionic conductivity.

3.3.2 Lithium Substructure

As mentioned above, in the lithium argyrodite structure, the anion framework creates six different types of tetrahedral interstices, five of which can potentially accommodate lithium. [29, 31–33] These tetrahedra are classified based on the number of shared corners, edges, or faces with adjacent PS_4^{3-} units, and are referred to as types 1 through 5 (T1–T5). [37] The Li^+ occupies only type 5 and type 2 (T5, T2, and T5a) positions in Li_6PS_5Hal, (Hal = Cl, Br, and I), [37, 38, 43], forming cage-like structures around central anion (Wyckoff 4*d*) as shown in Figure 3.1b. However, recent reports have indicated that Li^+ can partially occupy the T4 site (Wyckoff 16*e*, Figure 3.1b) in $Li_{6.15}Al_{0.15}Si_{1.35}S_{5.4}O_{0.6}$ and related Li_2S-SnS_2-SiS_2-P_2S_5 sulfides. [42] Additionally, other argyrodites showed Li^+ occupancy of T2 and T4 sites in "Li-deficient" materials with stoichiometries of < 6.0 Li per formula unit 40. [40] In order to study the lithium substructure in the $Li_{6-x}PS_{5-x}Br_{1+x}$ series, we conducted a detailed investigation using neutron powder diffraction, analyzed by Rietveld refinement in the cubic $F\bar{4}3m$ space group. Figure A.2 shows the occupancy of various Li sites in the argyrodite series by both the quenching and slow cooling methods as a function of bromide content. Rietveld refinement revealed four Li^+ sites that are occupied depending on the composition of $Li_{6-x}PS_{5-x}Br_{1+x}$: T5, T2, T5a, and T4. The overall Li^+ content was constrained to obtain a charge balance with the refined Br content. For compositions x = 0.0–0.5 (quenching and slow cooling), the refined thermal displacement parameters of the T2 sites were relatively large compared to other Li^+ sites in the structure (B_{iso} values of ~9 Å2 for the T2 site) indicating a de-localization of the local motion of Li^+ around the T2 site. This high value is consistent with literature [11, 37, 39]. The refined thermal displacement parameters of the T4 site were unphysical negative values for the slow-cooled x = 0.0 compositions. Additionally, an FDM showed no visible evidence of Li occupation on the T4 site. When the Br content increases in slow-cooled compositions up to x ≥ 0.3, additional T4 lithium sites were found occupied as shown in Figure A.2. These

sites lead to a stable, and improved fit (for example, when T4 sites are excluded in x = 0.3, this leads to an increase in Rwp from 6.4 to 7.0%).

The T4 sites has previously been identified in Cu and Ag argyrodites. [54, 55] Masuda et al. have reported on their occupation in mixed-halide argyrodite systems. [40] The occupation of the T4 site, located between two cages has been suggested to improve Li-ion diffusion in argyrodites. There are two inter-cage pathways, which are important for long-range Li^+ diffusion as suggested in the literature [35, 56]: one pathway through two neighbouring T2 sites (T2–T2) and another pathway between two T5 sites via the T4 site (T5–T4–T5) as shown in Figure 3.1c. Figure A.4 shows that the T2, T5, and T4 polyhedral volumes are barely affected by change in Br content. BVSE landscapes of $Li_{6-x}PS_{5-x}Br_{1+x}$ series reveal that cage-to-cage Li^+ diffusion pathways are more connected for higher Br content (Figures S8-9). Figure 3.3a shows the T2–T2 and T5–T4–T5 distance as a function of bromide content using both slow-cooling and quenching methods. The slow-cooled Li_6PS_5Br composition only allows for lithium-ion diffusion through T2–T2 pathways, where no occupancy of the T4 site is observed. As the bromine content increases, the T2–T2 distance remains constant for the slow-cooled method, however, it decreases for the quenching method. The T5–T4–T5 distances decrease with increasing bromide content in both synthesis methods, as depicted in Figure 3.3b. With increasing bromide content in the slow-cooled method, the T5–T4–T5 distance decreases from 3.76 (10) Å at x = 0.3 (composition) to 3.6 (9) Å at x = 0.5. In the quenched method, the T5–T4–T5 distance decreases from 3.64 (12) Å at x = 0.0 to 3.49 (8) Å at x = 0.5 as seen in Figure 3.3b. Summarizing, upon increasing the bromide content the T5–T4–T5 inter-cage distance decreases for both slow and quenched cooled materials and the T2–T2 inter-cage distance reduces only for the quenched cooling. This can potentially promote long-range diffusion, especially for the quenched cooled materials.

The average charge on the Wyckoff 4*a* and 4*d* sites will vary based on their occupancy due to the different charges of Br^- and S^{2-}. This can be anticipated to change the average surrounding Li^+ substructure (occupancies). To quantify how Br^- impacts the arrangement of Li^+, the average lithium distribution (denoted as R_{mean}) in the structure was determined by calculating the average distance between the 4*d* site (central anion, S^{2-}) and Li^+ located at different sites (T2, T5, and T5a), weighed by the occupancy of each site within a single cage, as previously introduced. [37, 39] Previously, only the T5, T2, and T5a sites were considered [39], but at present the additional T4 site is included in the R_{mean} calculations. The visual representation of R_{mean} can be seen in Figure 3.4a. For the different total Br content and 4*d* Br^- occupancy, significant changes of R_{mean} are observed (see Figure 3.4b). This result is supported by room temperature ^{6}Li NMR spectra of $Li_{6-x}PS_{5-x}Br_{1+x}$ (Figure 3.4c). The spectrum for slow-cooled Li_6PS_5Br displays an intense resonance at 1.62 ppm assigned to Li^+ atom occupying the T2, T5, and T5a sites. We observed that with increasing Br content, the ^{6}Li resonance shifts towards lower ppm values (Figure 3.4d), as previously observed for a similar system. [21] This shift to lower ppm values indicates that Li-atoms are experiencing a more electron-rich environment. As the amount of Br^- on the 4*d* site increases, either through increasing the Br content, the average negative charge on the 4*d* site decreases as the divalent sulfide is replaced by monovalent Br. This results in reduced electrostatic interactions between the electronegative 4*d* site and the electropositive Li-atoms. Li-atoms move away, causing R_{mean} to

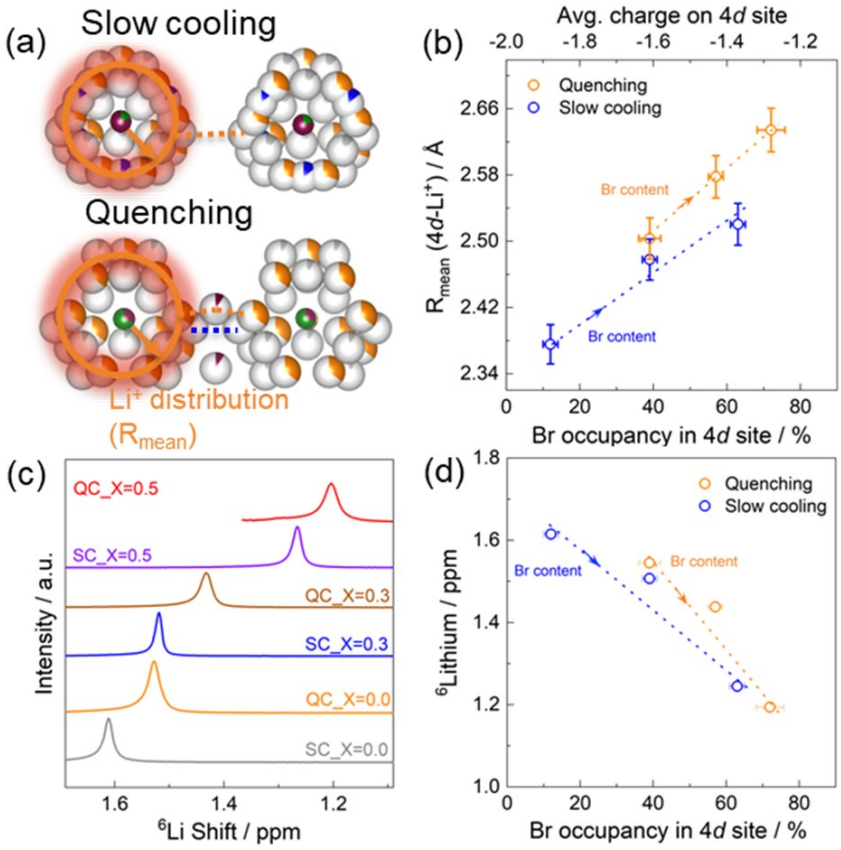

Figure 3.4: (a) The visual representation of R_{mean}. (b) the average Li^+ distribution, R_{mean}, representing the radius of the sphere formed by Li positions centered around the anion position (Wyckoff 4*d*, free sulfide anion site). As the Br content increases or the Br occupancy on 4*d* site increases, the average charge on the 4*d* anion decreases as the divalent S is replaced by monovalent Br. This causes R_{mean} to increase, representing an expansion of the distance between Li^+ cages. (c) ^{6}Li NMR spectra and (d) ^{6}Li shift ppm value of $Li_{6-x}PS_{5-x}Br_{1+x}$ as a function of the Br content, the shift ppm values decrease with increasing Br content, further indicating a change in the local Li^+ environment around the center of the anion (Wyckoff 4*d*, free sulfide anion site).

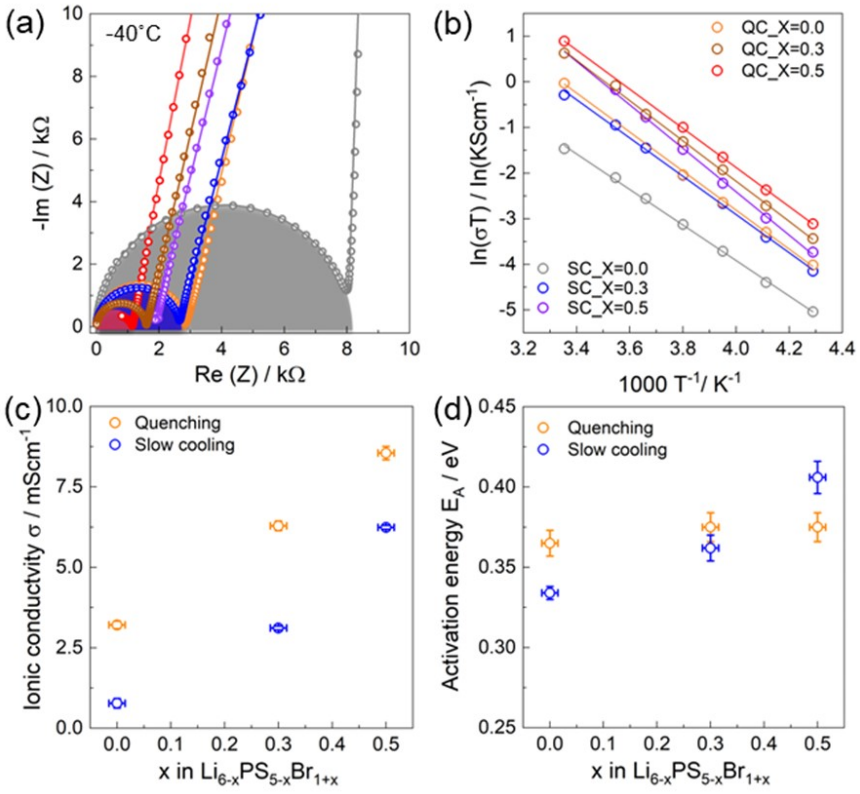

Figure 3.5: (a) Illustrates the impedance response of the $Li_{6-x}PS_{5-x}Br_{1+x}$ series at a temperature of -40℃. The open circles indicate the impedance response and exhibited capacitances of around 1 to 8 $\times 10^{-10}$ F cm^{-2}, and an α-value of 0.89–0.97, corresponding to bulk transport. (b) Represents Arrhenius plots of the $Li_{6-x}PS_{5-x}Br_{1+x}$ series, obtained from temperature-dependent impedance spectroscopy. (c) Shows the ionic conductivities at room temperature, and (d) activation energy E_A of $Li_{6-x}PS_{5-x}Br_{1+x}$ as a function of the Br content.

increase. More charge is maintained on the Li-atom as its electrons experience less interaction with the 4*d* site, causing the ^{6}Li shift to move to lower ppm value. [57] The increased Li cage radius is the origin of the reduced T2–T2 and T5–T4–T5 distances, effectively the result of the Br distribution over the 4*a* and 4*d* sites, which can be expected to result in better cage connectivity, and thus higher overall conductivity. [39, 40]

3.3.3 Ionic Transport

De Klerk et al. [35]suggested that both a higher site disorder, up to 75%, and a higher halide content in argyrodites can enhance ionic conductivity by facilitating inter-cage diffusion and by providing a more optimal Li-vacancy distribution. To examine the effect of varying total Br content and Br 4*d* occupancy on the ionic conductivity of $Li_{6-x}PS_{5-x}Br_{1+x}$, we performed temperature-dependent impedance spectroscopy to measure the ionic conductivity and activation energy. Figure 3.5a shows the Nyquist plots of quenched and

slow-cooled $Li_{6-x}PS_{5-x}Br_{1+x}$ at -40 ° C and other temperatures can be found in the supporting information (Figure A.5). The impedance data at lower temperatures (-40 to 0° C) were fitted with a resistor and constant phase element (CPE) in parallel; another CPE in the series represents the blocking electrode. The resistor represents the overall ionic conductivity. At higher temperatures (10 and 25° C), the response for the CPE/resistor shifts to higher frequencies and is difficult to resolve within the measured frequency range. In this case, only the tails of the blocking electrodes were used for the fit. The CPE in parallel exhibited a capacitance of around 1 to 8 $\times 10^{-10}$ F cm^{-2} indicating bulk transport. The impedance Z of CPE is given by:

$$Z = \frac{1}{Q(j\omega)^{\alpha}}$$

where, ω is the angular frequency, j is the imaginary unit, and Q is a parameter related to the magnitude of the impedance. The α-value represent the ideality of the semicircle, with an α value of 1 indicating an ideal capacitor. An α value of 0.89–0.97 is observed, indicating bulk transport. Figure 3.5c shows the ionic conductivities at room temperature as a function of Br content. The ionic conductivity increases with Br content for both cooling methods. As previously shown, higher site disorder (4*d* Br occupancy) leads to an improvement of the ionic conductivity [39]. In this work, the conductivity of slow-cooled Li_6PS_5Br sample (12% Br occupancy on 4*d* site) is 0.78 mS cm^{-1}. The conductivity of the slow-cooled samples increases from 0.78 mS cm^{-1} to 6.2 mS cm^{-1} with increasing Br content, while the conductivity of quenched samples increases from 3.21 mS cm^{-1} to 8.55 mS cm^{-1} with increasing Br content. Figure 3.5b shows that the temperature-dependence of the ionic conductivities, exhibits a linear Arrhenius behaviour from which an activation energy can be obtained. As shown in Figure 3.5d, the activation energy increases slightly with increasing Br content in both the slow-cooled and quenched samples. The observed increase in activation barrier, concurrent with an increase in conductivity, may seem paradoxical at first. However, this behaviour can be explained by the enthalpy-entropy compensation rule, also referred to as the Meyer-Neldel rule. [57–60] This rule states that an increase in the Arrhenius pre-factor can lead to an increase in the activation barrier, as demonstrated in Figure A.6-A.7, effectively meaning that more jumps occur, presumably because of the more optimal Li^+ distribution over the sites, providing a higher conductivity.

3.3.4 Structure-Property Relationship

Increasing the 4*d* Br occupancies through the synthesis method can significantly improve the ionic conductivity in lithium argyrodites. The occupancy and diffusion pathway and kinetics of lithium, within the Li cage, and between the Li cages, is dictated by the halogen content and distribution over the 4*d* and 4*a* sites. In this study we were able to tune the Br occupancies in the 4*d* site and lithium substructure in each composition, leading to the following observations:

- The slow-cooling method leads to a decrease in the lattice parameter while the fast-cooling method leads to an increase in the lattice parameter as the bromide content increases. The slow-cooling method does not affect the Br occupancy at the 4*a* site, but decreasing the Li content and differences in Li^+ distribution, leads to a decrease in the lattice parameter. As the Br content increases in the quenched sample, the Br occupancy at the 4*a* site increases, which leads to a larger lattice parameter.

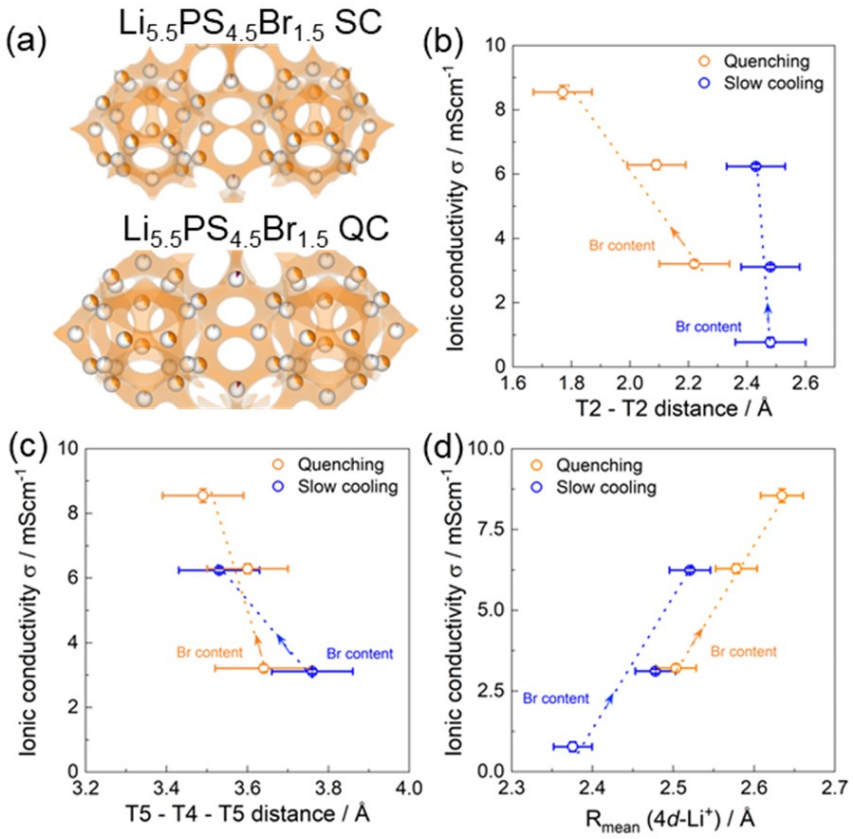

Figure 3.6: (a) Lithium diffusion pathways were analyzed using BVSE of slow cooled $Li_{5.5}PS_{4.5}Br_{1.5}$ and quenched $Li_{5.5}PS_{4.5}Br_{1.5}$ compositions. The room temperature ionic conductivity is shown as a (b) function of T2–T2 distance, (c) T2–T2 distance, and (d) R_{mean} distance. As the R_{mean} value increases, it indicates an expansion of the Li cage away from its center, which supports more connections between the cages through the T2–T2 and T5–T4–T5 distances. BVSE analyses show that cage-to-cage Li^+ diffusion pathways are more connected with higher Br content. For the slow cooled method, the T2–T2 distance remains constant, the T5–T4–T5 distances decrease and T4 Li occupancy increases, leading to more connections between cages and an increase in ionic conductivity from 0.78 to 6.20 mS cm-1. In the quenched method, both the T5–T4–T5 and T2–T2 distances decrease with increasing Br content. Additionally, T4 Li occupancy increases, resulting in an increase in connections between lithium cages and an increase in ionic conductivity from 3.21 to 8.55 mS cm-1.

- As the total Br content increases, the 4*d* Br occupancies also increase, starting from 12% to 63% for the slow-cooled method. The 4*d* Br occupancy is larger at higher temperatures and quenching "freezes in" the higher 4*d* Br occupancies at room temperature53. The quench method therefore results in even higher 4*d* Br occupancies, ranging from 39% to 72%. Overall, this work highlights the importance of the synthesis methods as a tool control the 4*d* Br occupancies in lithium argyrodites, which plays a key factor in the Li-ion conductivity.
- In the lithium substructure, the observation of non-zero T4 occupation implies activation of a new pathway for Li-ion diffusion, consisting of shorter inter-cage Li^+ jumps through face-sharing tetrahedral environments. This alternative pathway is in addition to the T2–T2 jumps that are observed in most lithium argyrodites. The inter-cage distance, which is connecting neighbouring lithium cages via T5–T4–T5 or T2–T2 distance, appears crucial to increase the ionic conductivity. Consistently, BVSE analyses shows that cage-to-cage Li^+ diffusion pathways are more connected for higher Br content (Figure 3.6a, Figure A.8 and Figure A.9).
- While the 4*d* Br occupancy increase for both cooling methods (see above section), the average negative charge on the 4*d* site decreases as the divalent sulphide is replaced by the monovalent bromide ion. This reduces the electrostatic interaction between the electronegative 4*d* site and the electropositive Li-ions. The Li ions move away, causing R_{mean} to increase and subsequent more charge is maintained on the Li-ion causing the observed ^{6}Li shift to move to lower ppm values. The increased Li cage radius (Figure 3.6d) is the origin of the reduced T2–T2 and T5–T4–T5 distances, and effectively the result of the difference Br distribution over the 4*d* sites, which is held responsible for the better connectivity between the cages, resulting in the larger overall conductivity observed.
- As the bromide content increases for the slow-cooled samples, the T2–T2 distance remains constant. The T5–T4–T5 distances decreases as the T4 Li occupancy increases (Figure 3.6b,c), resulting in higher connectivity between cages and increasing the ionic conductivity from 0.78 to 6.20 mS cm^{-1}.
- For quenched samples, the T5–T4–T5 and T2–T2 distances both decrease with increasing the Br content. Additionally, the T4 Li occupancy increases, leading to an increase in the diffusion pathways between the lithium cages and in a reduced inter-cage jump distance (T2–T2 and T5–T4–T5), resulting in an increase in ionic conductivity from 3.21 to 8.55 mS cm^{-1}. Hereby we highlight how the bromide content and sublattice occupancy affects the Li-cage expansion and the Li occupancies, which can be used to improve the diffusion pathway and Li-ion mobility and thus the Li-ion conductivity. We anticipate that understanding these structure-conductivity relationships further enhances the application potential of lithium argyrodites in solid-state lithium-ion batteries.

3.4 Conclusion

In this study, we synthesized bromide-enriched lithium argyrodites $Li_{6-x}PS_{5-x}Br_{1+x}$ with compositions ranging from x = 0.0 to 0.5 using two cooling methods. It is found that the

cooling method controls the Br occupancy on the 4*d* site in the $Li_{6-x}PS_{5-x}Br_{1+x}$ series. Rietveld refinement of neutron diffraction patterns reveals how this affects the 4*d*, 4*a* site occupancies and lithium substructure. As the Br content increased, the Li^+ ions move away from the center of the cage (4*d* site), as captured by the mean radius of the Li cage R_{mean}. Additionally, this induces T4 site occupancy, which opens up an alternative Li-ion diffusion pathway with a lower activation energy. The average negative charge on the 4*d* site decreases due to the increase in 4*d* Br^- occupancy, resulting in an increased Li cage radius and reduced T2–T2 and T5–T4–T5 distances, leading to a better-connected Li^+ landscape. The slow-cooled method results in an increase in ionic conductivity from 0.78 mS cm^{-1} at x = 0.0 to 6.2 mS cm^{-1} at x = 0.5, while the quenched method shows an increase from 3.21 mS cm^{-1} at x = 0.0 to 8.55 mS cm^{-1} at x = 0.5. These findings demonstrate the importance of understanding how chemical changes and synthesis conditions affect the lithium substructure in order to tailor the transport properties of these materials and raise their potential for solid state batteries.

Bibliography

[1] Akira Yoshino. The Birth of the Lithium-Ion Battery. *Angewandte Chemie International Edition*, 51(24):5798–5800, 2012. ISSN 1521-3773. doi: 10.1002/anie.201105006. URL https://onlinelibrary.wiley.com/doi/abs/10.1002/anie.201105006.

[2] Yangtao Liu, Ruihan Zhang, Jun Wang, and Yan Wang. Current and future lithium-ion battery manufacturing. *iScience*, 24(4):102332, April 2021. ISSN 2589-0042. doi: 10.1016/j.isci.2021.102332. URL https://www.sciencedirect.com/science/article/pii/S258900422100300X.

[3] Arumugam Manthiram. A reflection on lithium-ion battery cathode chemistry. *Nature Communications*, 11(1):1550, March 2020. ISSN 2041-1723. doi: 10.1038/s41467-020-15355-0. URL https://www.nature.com/articles/s41467-020-15355-0. Number: 1 Publisher: Nature Publishing Group.

[4] Wu Xu, Jiulin Wang, Fei Ding, Xilin Chen, Eduard Nasybulin, Yaohui Zhang, and Ji-Guang Zhang. Lithium metal anodes for rechargeable batteries. *Energy & Environmental Science*, 7(2):513–537, January 2014. ISSN 1754-5706. doi: 10.1039/C3EE40795K. URL https://pubs.rsc.org/en/content/articlelanding/2014/ee/c3ee40795k.

[5] Kelsey B. Hatzell, Xi Chelsea Chen, Corie L. Cobb, Neil P. Dasgupta, Marm B. Dixit, Lauren E. Marbella, Matthew T. McDowell, Partha P. Mukherjee, Ankit Verma, Venkatasubramanian Viswanathan, Andrew S. Westover, and Wolfgang G. Zeier. Challenges in Lithium Metal Anodes for Solid-State Batteries. *ACS Energy Letters*, 5(3):922–934, March 2020. doi: 10.1021/acsenergylett.9b02668. URL https://doi.org/10.1021/acsenergylett.9b02668.

[6] Jürgen Janek and Wolfgang G. Zeier. A solid future for battery development. *Nature Energy*, 1(9):1–4, September 2016. ISSN 2058-7546. doi: 10.1038/nenergy.2016.141. URL https://www.nature.com/articles/nenergy2016141.

[7] Thorben Krauskopf, Felix H. Richter, Wolfgang G. Zeier, and Jürgen Janek. Physicochemical Concepts of the Lithium Metal Anode in Solid-State Batteries. *Chemical Reviews*, 120(15):7745–7794, August 2020. ISSN 0009-2665. doi: 10.1021/acs.chemrev.0c00431. URL https://doi.org/10.1021/acs.chemrev.0c00431.

[8] Theodosios Famprikis, Pieremanuele Canepa, James A. Dawson, M. Saiful Islam, and Christian Masquelier. Fundamentals of inorganic solid-state electrolytes for batteries. *Nature Materials*, 18(12):1278–1291, December 2019. ISSN 1476-4660. doi: 10.1038/s41563-019-0431-3. URL https://www.nature.com/articles/s41563-019-0431-3.

[9] Kazunori Takada, Takahisa Ohno, Narumi Ohta, Tsuyoshi Ohnishi, and Yoshinori Tanaka. Positive and Negative Aspects of Interfaces in Solid-State Batteries. *ACS Energy Letters*, 3(1):98–103, January 2018. ISSN 23808195. doi: 10.1021/acsenergylett.7b01105. URL https://pubs.acs.org/doi/10.1021/acsenergylett.7b01105.

[10] John B. Goodenough. Oxide-Ion Electrolytes. *Annual Review of Materials Research*, 33 (1):91–128, 2003. doi: 10.1146/annurev.matsci.33.022802.091651. URL https://doi.org/10.1146/annurev.matsci.33.022802.091651.

[11] Alexandra Morscher, Benjamin B. Duff, Guopeng Han, Luke M. Daniels, Yun Dang, Marco Zanella, Manel Sonni, Ahmad Malik, Matthew S. Dyer, Ruiyong Chen, Frédéric Blanc, John B. Claridge, and Matthew J. Rosseinsky. Control of Ionic Conductivity by Lithium Distribution in Cubic Oxide Argyrodites Li6+xP1?xSixO5Cl. *Journal of the American Chemical Society*, 144(48):22178–22192, December 2022. ISSN 0002-7863. doi: 10.1021/jacs.2c09863. URL https://doi.org/10.1021/jacs.2c09863.

[12] Mogalahalli V. Reddy, Christian M. Julien, Alain Mauger, and Karim Zaghib. Sulfide and Oxide Inorganic Solid Electrolytes for All-Solid-State Li Batteries: A Review. *Nanomaterials*, 10(8):1606, August 2020. ISSN 2079-4991. doi: 10.3390/nano10081606. URL https://www.mdpi.com/2079-4991/10/8/1606.

[13] Takahiro Yoshinari, Raimund Koerver, Patrick Hofmann, Yoshiharu Uchimoto, Wolfgang G. Zeier, and Jürgen Janek. Interfacial Stability of Phosphate-NASICON Solid Electrolytes in Ni-Rich NCM Cathode-Based Solid-State Batteries. *ACS applied materials & interfaces*, 11(26):23244–23253, July 2019. ISSN 1944-8252. doi: 10.1021/acsami.9b05995.

[14] Bianca Helm, Roman Schlem, Björn Wankmiller, Ananya Banik, Ajay Gautam, Justine Ruhl, Cheng Li, Michael Ryan Hansen, and Wolfgang G. Zeier. Exploring Aliovalent Substitutions in the Lithium Halide Superionic Conductor Li3?xIn1?xZrxCl6 (0 ? x ? 0.5). *Chemistry of Materials*, 33(12):4773–4782, June 2021. ISSN 0897-4756. doi: 10.1021/acs.chemmater.1c01348. URL https://doi.org/10.1021/acs.chemmater.1c01348. Publisher: American Chemical Society.

[15] Roman Schlem, Sokseiha Muy, Nils Prinz, Ananya Banik, Yang Shao-Horn, Mirijam Zobel, and Wolfgang G. Zeier. Mechanochemical Synthesis: A Tool to Tune Cation Site Disorder and Ionic Transport Properties of Li3MCl6 (M = Y, Er) Superionic Conductors. *Advanced Energy Materials*, 10(6): 1903719, 2020. ISSN 1614-6840. doi: 10.1002/aenm.201903719. URL https://onlinelibrary.wiley.com/doi/abs/10.1002/aenm.201903719. _eprint: https://onlinelibrary.wiley.com/doi/pdf/10.1002/aenm.201903719.

[16] A. Bohnsack and G. Meyer. Ternary halides of the A3MX6 type V Synthesis, crystal structures, and sodium ionic conductivity of the ternary iodides Na3MI6 (M=Sm,Gd-Dy) and of the solid solution halides Na3GdBr6-xIx. *Zeitschrift fuer Anorganische und Allgemeine Chemie (1950)*, 623(5):837–843, 1997. ISSN 0044-2313. Place: Germany INIS Reference Number: 28048230.

[17] Se Young Kim, Kavish Kaup, Kern-Ho Park, Abdeljalil Assoud, Laidong Zhou, Jue Liu, Xiaohan Wu, and Linda F. Nazar. Lithium Ytterbium-Based Halide Solid Electrolytes for High Voltage All-Solid-State Batteries. *ACS Materials Letters*, 3(7):930–938, July 2021. doi: 10.1021/acsmaterialslett.1c00142. URL https://doi.org/10.1021/acsmaterialslett.1c00142. Publisher: American Chemical Society.

[18] Nicolás Flores-González, Nicolò Minafra, Georg Dewald, Hazel Reardon, Ronald I. Smith, Stefan Adams, Wolfgang G. Zeier, and Duncan H. Gregory. Mechanochemical Synthesis and Structure of Lithium Tetrahaloaluminates, LiAlX4 (X = Cl, Br, I): A Family of Li-Ion Conducting Ternary Halides. *ACS Materials Letters*, 3(5):652–657, May 2021. doi: 10.1021/acsmaterialslett.1c00055. URL https://doi.org/10.1021/acsmaterialslett.1c00055. Publisher: American Chemical Society.

[19] Zhantao Liu, Shuan Ma, Jue Liu, Shan Xiong, Yifan Ma, and Hailong Chen. High Ionic Conductivity Achieved in Li3Y(Br3Cl3) Mixed Halide Solid Electrolyte via Promoted Diffusion Pathways and Enhanced Grain Boundary. *ACS Energy Letters*, 6(1):298–304, January 2021. doi: 10.1021/acsenergylett.0c01690. URL https://doi.org/10.1021/acsenergylett.0c01690. Publisher: American Chemical Society.

[20] Tetsuya Asano, Akihiro Sakai, Satoru Ouchi, Masashi Sakaida, Akinobu Miyazaki, and Shinya Hasegawa. Solid Halide Electrolytes with High Lithium-Ion Conductivity for Application in 4 V Class Bulk-Type All-Solid-State Batteries. *Advanced Materials*, 30(44):1803075, 2018. ISSN 1521-4095. doi: 10.1002/adma.201803075. URL https://onlinelibrary.wiley.com/doi/abs/10.1002/adma.201803075. _eprint: https://onlinelibrary.wiley.com/doi/pdf/10.1002/adma.201803075.

[21] Pengbo Wang, Haoyu Liu, Sawankumar Patel, Xuyong Feng, Po Hsiu Chien, Yan Wang, and Yan Yan Hu. Fast Ion Conduction and Its Origin in Li6- xPS5- xBr1+ x. *Chemistry of Materials*, 32(9):3833–3840, May 2020. ISSN 15205002. doi: 10.1021/ACS.CHEMMATER.9B05331/ASSET/IMAGES/LARGE/CM9B05331_0008.JPEG. URL https://pubs.acs.org/doi/full/10.1021/acs.chemmater.9b05331. Publisher: American Chemical Society.

[22] Sawankumar V. Patel, Swastika Banerjee, Haoyu Liu, Pengbo Wang, Po Hsiu Chien, Xuyong Feng, Jue Liu, Shyue Ping Ong, and Yan Yan Hu. Tunable Lithium-Ion Transport in Mixed-Halide Argyrodites Li6- xPS5- xClBrx: An Unusual Compositional Space. *Chemistry of Materials*, 33(4):1435–1443, February 2021. ISSN 15205002. doi: 10.1021/ACS.CHEMMATER.0C04650/ASSET/IMAGES/LARGE/CM0C04650_0009.JPEG. URL https://pubs.acs.org/doi/full/10.1021/acs.chemmater.0c04650. Publisher: American Chemical Society.

[23] Laidong Zhou, Nicolò Minafra, Wolfgang G. Zeier, and Linda F. Nazar. Innovative Approaches to Li-Argyrodite Solid Electrolytes for All-Solid-State Lithium Batteries. *Accounts of Chemical Research*, 54(12):2717–2728, June 2021. ISSN 15204898. doi: 10.1021/ACS.ACCOUNTS.0C00874/ASSET/IMAGES/LARGE/AR0C00874_0006.JPEG. URL https://pubs-acs-org.tudelft.idm.oclc.org/doi/full/10.1021/acs.accounts.0c00874. Publisher: American Chemical Society.

[24] Laidong Zhou, Abdeljalil Assoud, Qiang Zhang, Xiaohan Wu, and Linda F. Nazar. New Family of Argyrodite Thioantimonate Lithium Superionic Conductors. *Journal of the American Chemical Society*, 141(48):19002–19013, December 2019. ISSN 0002-7863. doi: 10.1021/jacs.9b08357. URL https://doi.org/10.1021/jacs.9b08357. Publisher: American Chemical Society.

[25] Laidong Zhou, Kern-Ho Park, Xiaoqi Sun, Fabien Lalère, Torben Adermann, Pascal Hartmann, and Linda F. Nazar. Solvent-Engineered Design of Argyrodite Li $_6$ PS $_5$ X (X = Cl, Br, I) Solid Electrolytes with High Ionic Conductivity. *ACS Energy Letters*, 4 (1):265–270, January 2019. ISSN 2380-8195. doi: 10.1021/acsenergylett.8b01997. URL https://pubs.acs.org/doi/10.1021/acsenergylett.8b01997. Publisher: American Chemical Society.

[26] Parvin Adeli, J. David Bazak, Kern Ho Park, Ivan Kochetkov, Ashfia Huq, Gillian R. Goward, and Linda F. Nazar. Boosting Solid-State Diffusivity and Conductivity in Lithium Superionic Argyrodites by Halide Substitution. *Angewandte Chemie International Edition*, 58(26):8681–8686, 2019. ISSN 1521-3773. doi: 10.1002/anie.201814222. URL https://onlinelibrary.wiley.com/doi/abs/10.1002/anie.201814222.

[27] Eliana Quartarone and Piercarlo Mustarelli. Electrolytes for solid-state lithium rechargeable batteries: recent advances and perspectives. *Chemical Society Reviews*, 40(5):2525–2540, April 2011. ISSN 1460-4744. doi: 10.1039/C0CS00081G. URL https://pubs.rsc.org/en/content/articlelanding/2011/cs/c0cs00081g. Publisher: The Royal Society of Chemistry.

[28] Ananya Banik, Theodosios Famprikis, Michael Ghidiu, Saneyuki Ohno, Marvin A. Kraft, and Wolfgang G. Zeier. On the underestimated influence of synthetic conditions in solid ionic conductors. *Chemical Science*, 12(18):6238–6263, May 2021. ISSN 2041-6539. doi: 10.1039/D0SC06553F. URL https://pubs.rsc.org/en/content/articlelanding/2021/sc/d0sc06553f. Publisher: The Royal Society of Chemistry.

[29] Hans-Jörg Deiseroth, Joachim Maier, Katja Weichert, Vera Nickel, Shiao-Tong Kong, and Christof Reiner. Li7PS6 and Li6PS5X (X: Cl, Br, I): Possible Three-dimensional Diffusion Pathways for Lithium Ions and Temperature Dependence of the Ionic Conductivity by Impedance Measurements. *Zeitschrift für anorganische und allgemeine Chemie*, 637(10):1287–1294, August 2011. ISSN 1521-3749. doi: 10.1002/zaac.201100158. URL http://www.onlinelibrary.wiley.com/doi/abs/10.1002/zaac.201100158.

[30] Hans-Jörg Deiseroth, Shiao-Tong Kong, Hellmut Eckert, Julia Vannahme, Christof Reiner, Torsten Zaiß, and Marc Schlosser. Li6PS5X: A Class of Crystalline Li-Rich Solids With an Unusually High Li+ Mobility. *Angewandte Chemie*, 120(4): 767–770, January 2008. ISSN 1521-3757. doi: 10.1002/ange.200703900. URL https://onlinelibrary.wiley.com/doi/abs/10.1002/ange.200703900.

[31] S. T. Kong, C. Reiner, and H. J. Deiseroth. Synthesis and Characterization of Lithium Argyrodite, Li7PS6. *Zeitschrift für anorganische und allgemeine Chemie*, 632(12-13):2100–2100, 2006. ISSN 1521-3749. doi: 10.1002/zaac.200670048. URL https://onlinelibrary.wiley.com/doi/abs/10.1002/zaac.200670048. _eprint: https://onlinelibrary.wiley.com/doi/pdf/10.1002/zaac.200670048.

[32] Shiao Tong Kong, Özgül Gün, Barbara Koch, Hans Jörg Deiseroth, Hellmut Eckert, and Christof Reiner. Structural Characterisation of the Li Argyrodites Li7PS6 and Li7PSe6 and their Solid Solutions: Quantification of Site Preferences by MAS-NMR

Spectroscopy. *Chemistry ? A European Journal*, 16(17):5138–5147, May 2010. ISSN 1521-3765. doi: 10.1002/chem.200903023. URL http://onlinelibrary.wiley.com/doi/abs/10.1002/chem.200903023.

[33] Viktor Epp, Özgül Gün, Hans-Jörg Deiseroth, and Martin Wilkening. Highly Mobile Ions: Low-Temperature NMR Directly Probes Extremely Fast Li+ Hopping in Argyrodite-Type Li6PS5Br. *The Journal of Physical Chemistry Letters*, 4(13):2118–2123, July 2013. ISSN 1948-7185. doi: 10.1021/jz401003a. URL https://doi.org/10.1021/jz401003a.

[34] Shiao-Tong Kong, Hans-Jörg Deiseroth, Christof Reiner, Özgül Gün, Elmar Neumann, Clemens Ritter, and Dirk Zahn. Lithium Argyrodites with Phosphorus and Arsenic: Order and Disorder of Lithium Atoms, Crystal Chemistry, and Phase Transitions. *Chemistry ? A European Journal*, 16(7):2198–2206, February 2010. ISSN 1521-3765. doi: 10.1002/chem.200902470. URL http://onlinelibrary.wiley.com/doi/abs/10.1002/chem.200902470.

[35] Niek J. J. de Klerk, Irek Ros?o?, and Marnix Wagemaker. Diffusion Mechanism of Li Argyrodite Solid Electrolytes for Li-Ion Batteries and Prediction of Optimized Halogen Doping: The Effect of Li Vacancies, Halogens, and Halogen Disorder. *Chemistry of Materials*, 28(21):7955–7963, November 2016. ISSN 0897-4756. doi: 10.1021/acs.chemmater.6b03630. URL https://doi.org/10.1021/acs.chemmater.6b03630.

[36] Benjamin J. Morgan. Mechanistic Origin of Superionic Lithium Diffusion in Anion-Disordered Li6PS5X Argyrodites. *Chemistry of Materials*, 33(6):2004–2018, March 2021. ISSN 15205002. doi: 10.1021/ACS.CHEMMATER.0C03738/SUPPL_FILE/CM0C03738_SI_001.PDF. URL https://pubs.acs.org/doi/full/10.1021/acs.chemmater.0c03738. Publisher: American Chemical Society.

[37] Nicolò Minafra, Marvin A. Kraft, Tim Bernges, Cheng Li, Roman Schlem, Benjamin J. Morgan, and Wolfgang G. Zeier. Local Charge Inhomogeneity and Lithium Distribution in the Superionic Argyrodites Li6PS5X (X = Cl, Br, I). *Inorganic Chemistry*, 59 (15):11009–11019, August 2020. ISSN 1520510X. doi: 10.1021/ACS.INORGCHEM.0C01504/ASSET/IMAGES/LARGE/IC0C01504_0008.JPEG. URL https://pubs.acs.org/doi/full/10.1021/acs.inorgchem.0c01504. Publisher: American Chemical Society.

[38] Ajay Gautam, Michael Ghidiu, Emmanuelle Suard, Marvin A. Kraft, and Wolfgang G. Zeier. On the Lithium Distribution in Halide Superionic Argyrodites by Halide Incorporation in Li7-xPS6-xClx. *ACS Applied Energy Materials*, 4(7):7309–7315, July 2021. ISSN 25740962. doi: 10.1021/ACSAEM.1C01417/SUPPL_FILE/AE1C01417_SI_002.ZIP. URL https://pubs.acs.org/doi/full/10.1021/acsaem.1c01417. Publisher: American Chemical Society.

[39] Ajay Gautam, Marcel Sadowski, Michael Ghidiu, Nicolò Minafra, Anatoliy Senyshyn, Karsten Albe, Wolfgang G. Zeier, Ajay Gautam, Michael Ghidiu, Marcel Sadowski, Karsten Albe, Nicolò Minafra, Wolfgang G. Zeier, and A Senyshyn Heinz Maier-Leibnitz Zentrum. Engineering the Site-Disorder and Lithium Distribution in the

Lithium Superionic Argyrodite Li6PS5Br. *Advanced Energy Materials*, 11(5):2003369, February 2021. doi: 10.1002/AENM.202003369. URL https://onlinelibrary.wiley.com/doi/full/10.1002/aenm.202003369.

[40] Naoya Masuda, Kiyoshi Kobayashi, Futoshi Utsuno, Tetsuo Uchikoshi, and Naoaki Kuwata. Effects of Halogen and Sulfur Mixing on Lithium-Ion Conductivity in Li7-x-y(PS4)(S2-x-yClxBry) Argyrodite and the Mechanism for Enhanced Lithium Conduction. *Journal of Physical Chemistry C*, 126(33):14067–14074, August 2022. ISSN 19327455. doi: 10.1021/ACS.JPCC.2C03780/SUPPL_FILE/JP2C03780_SI_002.CIF. URL https://pubs.acs.org/doi/full/10.1021/acs.jpcc.2c03780. Publisher: American Chemical Society.

[41] Katharina Hogrefe, Nicolò Minafra, Isabel Hanghofer, Ananya Banik, Wolfgang G. Zeier, and H. Martin R. Wilkening. Opening Diffusion Pathways through Site Disorder: The Interplay of Local Structure and Ion Dynamics in the Solid Electrolyte Li6+xP1-xGexS5I as Probed by Neutron Diffraction and NMR. *Journal of the American Chemical Society*, 144(4):1795–1812, February 2022. ISSN 1520-5126. doi: 10.1021/jacs.1c11571. URL https://pubs.acs.org/doi/full/10.1021/jacs.1c11571.

[42] Wenze Huang, Lindong Cheng, Satoshi Hori, Kota Suzuki, Masao Yonemura, Masaaki Hirayama, and Ryoji Kanno. Ionic conduction mechanism of a lithium superionic argyrodite in the Li?Al?Si?S?O system. *Materials Advances*, 1(3):334–340, June 2020. ISSN 2633-5409. doi: 10.1039/D0MA00115E. URL https://pubs.rsc.org/en/content/articlehtml/2020/ma/d0ma00115e. Publisher: RSC.

[43] Marvin A. Kraft, Sean P. Culver, Mario Calderon, Felix Böcher, Thorben Krauskopf, Anatoliy Senyshyn, Christian Dietrich, Alexandra Zevalkink, Jürgen Janek, and Wolfgang G. Zeier. Influence of Lattice Polarizability on the Ionic Conductivity in the Lithium Superionic Argyrodites Li6PS5X (X = Cl, Br, I). *Journal of the American Chemical Society*, 139(31):10909–10918, August 2017. ISSN 0002-7863. doi: 10.1021/jacs.7b06327. URL https://doi.org/10.1021/jacs.7b06327.

[44] Chuang Yu, Yong Li, Weihan Li, Keegan R. Adair, Feipeng Zhao, Mathew Willans, Jianwen Liang, Yang Zhao, Changhong Wang, Sixu Deng, Ruying Li, Huan Huang, Shigang Lu, Tsun-Kong Sham, Yining Huang, and Xueliang Sun. Enabling ultrafast ionic conductivity in Br-based lithium argyrodite electrolytes for solid-state batteries with different anodes. *Energy Storage Materials*, 30:238–249, September 2020. ISSN 24058297. doi: 10.1016/j.ensm.2020.04.014. URL https://linkinghub.elsevier.com/retrieve/pii/S2405829720301343. Publisher: Elsevier.

[45] L. van Eijck, L. D. Cussen, G. J. Sykora, E. M. Schooneveld, N. J. Rhodes, A. A. van Well, and C. Pappas. Design and performance of a novel neutron powder diffractometer: PEARL at TU Delft. *Journal of Applied Crystallography*, 49(5):1398–1401, October 2016. ISSN 1600-5767. doi: 10.1107/S160057671601089X. URL //scripts.iucr.org/cgi-bin/paper?fs5138. Publisher: International Union of Crystallography.

[46] Stefan Adams. Bond valence analysis of structure-property relationships in solid electrolytes. *Journal of Power Sources*, 159(1):200–204, September 2006. ISSN 0378-

7753. doi: 10.1016/j.jpowsour.2006.04.085. URL https://www.sciencedirect.com/science/article/pii/S0378775306007154.

[47] S. Adams, A. Preusser, and J. Swenson. Modeling conduction pathways in ionic conductors. In *Superionic Conductor Physics*, pages 67–72. WORLD SCIENTIFIC, January 2007. ISBN 978-981-270-565-5. doi: 10.1142/9789812706904_0013. URL https://www.worldscientific.com/doi/abs/10.1142/9789812706904_0013.

[48] H. Chen, L. L. Wong, and S. Adams. SoftBV a software tool for screening the materials genome of inorganic fast ion conductors. *Acta Crystallographica Section B: Structural Science, Crystal Engineering and Materials*, 75(1):18–33, February 2019. ISSN 2052-5206. doi: 10.1107/S2052520618015718. URL https://journals.iucr.org/b/issues/2019/01/00/bm5104/. Number: 1 Publisher: International Union of Crystallography.

[49] Chuang Yu, Swapna Ganapathy, Jart Hageman, Lambert van Eijck, Ernst R. H. van Eck, Long Zhang, Tammo Schwietert, Shibabrata Basak, Erik M. Kelder, and Marnix Wagemaker. Facile Synthesis toward the Optimal Structure-Conductivity Characteristics of the Argyrodite Li6PS5Cl Solid-State Electrolyte. *ACS Applied Materials & Interfaces*, 10(39):33296–33306, October 2018. ISSN 1944-8244. doi: 10.1021/acsami.8b07476. URL https://doi.org/10.1021/acsami.8b07476.

[50] A. A. Coelho. TOPAS and TOPAS-Academic: an optimization program integrating computer algebra and crystallographic objects written in C++. *Journal of Applied Crystallography*, 51(1):210–218, February 2018. ISSN 1600-5767. doi: 10.1107/S1600576718000183. URL https://journals.iucr.org/j/issues/2018/01/00/jo5037/. Number: 1 Publisher: International Union of Crystallography.

[51] Eiichi Fukushima. *Experimental pulse NMR: a nuts and bolts approach*. CRC Press, 2018.

[52] Ajay Gautam, Marcel Sadowski, Nils Prinz, Henrik Eickhoff, Nicolò Minafra, Michael Ghidiu, Sean P. Culver, Karsten Albe, Thomas F. Fässler, Mirijam Zobel, and Wolfgang G. Zeier. Rapid Crystallization and Kinetic Freezing of Site-Disorder in the Lithium Superionic Argyrodite Li6PS5Br. *Chemistry of Materials*, 31(24):10178–10185, December 2019. ISSN 15205002. doi: 10.1021/ACS.CHEMMATER.9B03852/ASSET/IMAGES/LARGE/CM9B03852_0008.JPEG. URL https://pubs.acs.org/doi/full/10.1021/acs.chemmater.9b03852. Publisher: American Chemical Society.

[53] R. D. Shannon. Revised effective ionic radii and systematic studies of interatomic distances in halides and chalcogenides. *Acta Crystallographica Section A: Crystal Physics, Diffraction, Theoretical and General Crystallography*, 32(5):751–767, September 1976. ISSN 0567-7394. doi: 10.1107/S0567739476001551. URL //scripts.iucr.org/cgi-bin/paper?a12967. Number: 5 Publisher: International Union of Crystallography.

[54] M. Evain, E. Gaudin, F. Boucher, V. Petricek, and F. Taulelle. Structures and Phase Transitions of the A7PSe6 (A = Ag, Cu) Argyrodite-Type Ionic Conductors. I. Ag7PSe6. *Acta Crystallographica Section B: Structural Science*, 54(4):376–383, August 1998. ISSN 0108-7681. doi: 10.1107/S0108768197019654. URL //scripts.iucr.

org/cgi-bin/paper?lc0002. Number: 4 Publisher: International Union of Crystallography.

[55] Heng Wang, Chuang Yu, Swapna Ganapathy, Ernst R. H. van Eck, Lambert van Eijck, and Marnix Wagemaker. A lithium argyrodite Li6PS5Cl0.5Br0.5 electrolyte with improved bulk and interfacial conductivity. *Journal of Power Sources*, 412: 29–36, February 2019. ISSN 0378-7753. doi: 10.1016/j.jpowsour.2018.11.029. URL http://www.sciencedirect.com/science/article/pii/S0378775318312643.

[56] Chuang Yu, Jart Hageman, Swapna Ganapathy, Lambert Van Eijck, Long Zhang, Keegan R. Adair, Xueliang Sun, and Marnix Wagemaker. Tailoring Li6PS5Br ionic conductivity and understanding of its role in cathode mixtures for high performance all-solid-state Li?S batteries. *Journal of Materials Chemistry A*, 7(17):10412–10421, April 2019. ISSN 2050-7496. doi: 10.1039/C9TA02126D. URL https://pubs.rsc.org/en/content/articlehtml/2019/ta/c9ta02126d. Publisher: The Royal Society of Chemistry.

[57] Ralf Widenhorn, Armin Rest, and Erik Bodegom. The Meyer Neldel rule for a property determined by two transport mechanisms. *Journal of Applied Physics*, 91 (10):6524–6528, May 2002. ISSN 0021-8979. doi: 10.1063/1.1469666. URL https://doi.org/10.1063/1.1469666.

[58] K. L Ngai. Meyer Neldel rule and anti Meyer?Neldel rule of ionic conductivity: Conclusions from the coupling model. *Solid State Ionics*, 105(1):231–235, January 1998. ISSN 0167-2738. doi: 10.1016/S0167-2738(97)00469-4. URL https://www.sciencedirect.com/science/article/pii/S0167273897004694.

[59] Sokseiha Muy, John C. Bachman, Hao-Hsun Chang, Livia Giordano, Filippo Maglia, Saskia Lupart, Peter Lamp, Wolfgang G. Zeier, and Yang Shao-Horn. Lithium Conductivity and Meyer-Neldel Rule in Li3PO4?Li3VO4?Li4GeO4 Lithium Superionic Conductors. *Chemistry of Materials*, 30(16):5573–5582, August 2018. ISSN 0897-4756. doi: 10.1021/acs.chemmater.8b01504. URL https://doi.org/10.1021/acs.chemmater.8b01504. Publisher: American Chemical Society.

[60] Yirong Gao, Nana Li, Yifan Wu, Wenge Yang, and Shou-Hang Bo. Rethinking the Design of Ionic Conductors Using Meyer?Neldel?Conductivity Plot. *Advanced Energy Materials*, 11(13):2100325, 2021. ISSN 1614-6840. doi: 10.1002/aenm.202100325. URL https://onlinelibrary.wiley.com/doi/abs/10.1002/aenm.202100325. _eprint: https://onlinelibrary.wiley.com/doi/pdf/10.1002/aenm.202100325.

4

Disentangling the Roles of Site Disorder and Chemical Composition in $Li_{6-x}PS_{5-x}Br_{1+x}$

"a map is not the territory"

Alfred Korzybski, A Non-Aristotelian System and Its Necessity for Rigour in Mathematics and Physics

This chapter has been published as:Al-Kutubi, Hanan, et al. "Decoding Structural Disorder, Synthesis Methods, and Short-and Long-Range Lithium-Ion Transport in Lithium Argyrodites (Li6–x PS5–x Br1+ x)." Chemistry of Materials 37.3 (2025): 869-883.

4.1 Introduction

The energy transition has resulted in a focus on electrical forms of energy and their storage. Lithium-ion batteries are one of the most advanced and prevalent forms of storage of electrical energy [1]. However, the combustible nature of the electrolyte has prompted the search for safer alternatives [2]. Solid-state electrolytes have garnered attention as a promising alternative due to their inherent safety [3]. Among the various classes of solid-state electrolytes, lithium argyrodites are among the most promising candidates due to their high conductivity (upward of 20 mS cm^{-1}), ease of synthesis, and malleability [4, 5]. Lithium argyrodites are a crystalline class of materials with cubic symmetry and space-group $F\bar{4}3m$, first mentioned by Deiseroth *et al.* [6]. Their general formula is Li_6PS_5X (X = Cl, Br, or I), and their structure is given in Figure 4.1. The backbone consists of PS_4 tetrahedra, with P sitting on the 4*b* sites and S on the 16*e* sites. The remaining sulfur and halogen occupy the 4*a* and 4*d* sites. The lithium ions can occupy six different types of tetrahedral sites termed T1–T5a [6–8]. Initially, lithium was thought to exclusively occupy 50% of the T5 sites (48*h*), forming a cage around the 4*d* site. Each cage vertex contains two T5 sites and hence one Li atom. The T5a (24*g*) site sits in between one pair of T5 sites and represents the smearing of the Li density between them. [6],[9],[10] Three jumps were identified based on this model, namely, doublet jumps within one T5-pair, intracage jumps between adjacent T5-pairs within one cage, and intercage jumps.[11] Later on, Deiseroth *et al.* postulated that intercage diffusion requires the T2 (48*h′*) and T4 (16*e*) sites as well.[10] This finding is supported by band-valence and molecular dynamics simulations as well as diffraction studies on argyrodite systems. [7, 12–17] Intercage jumps can occur via two pathways: T5–T2–T2–T5 or T5–T4–T5. The latter has been found to increase intercage diffusivity as it provides a lower energy pathway.[7, 12, 18, 19] While all three jumps are important for fast lithium diffusion, intercage jumps are seen as the limiting step due to their high energy barrier.[11] Facilitating intercage jumps is, therefore, considered an effective way to increase long-range ionic conductivity.

In an ordered structure, the 4*d* site is exclusively occupied by sulfur, leaving halogen on the 4*a* site. Site disorder occurs when this is no longer the case and has been shown both theoretically and experimentally to enhance the conductivity of argyrodites by facilitating intercage movement.[7, 17, 20–26] Occupancy of the 4*d* site by the halogen results in a reduction of the electrostatic interaction between the 4*d* site and the surrounding Li cage. The intercage distance decreases and lithium movement is facilitated.[7, 24, 27] Disorder is also correlated with increased occupancy of the T2 and T4 sites, indicating diffusion through the energetically lower T4 pathway.[25, 26, 28] Increase in site disorder is conventionally achieved through halogen substitution, with the excess halogen occupying the 4*d* site, resulting in an increase in conductivity. Gautam *et al.* have found that an increase in site disorder can also be achieved through altering the synthesis procedure, regardless of halogen content.[17, 24] The study has shown that materials with the same chemical composition or the same degree of 4*d* site disorder can display drastic differences in conductivity and structure.[29] This implies that site disorder and chemical composition should neither be seen nor treated as one descriptor and that site disorder is not a complete descriptor on its own.[29]

The configurational entropy (S_{conf}) is seen as a more complete descriptor, as it takes the site disorder of all positions into account. Increase in S_{conf} has been suggested to flatten

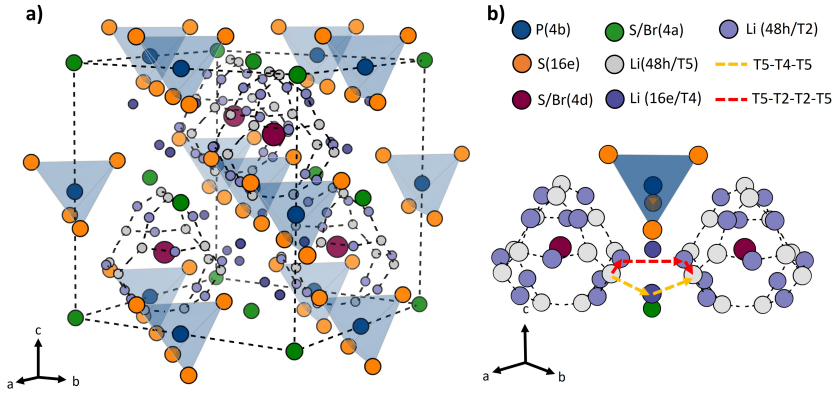

Figure 4.1: a) Illustrated crystal structure of Li_6PS_5Br showing the Li-cages (dotted lines) and sites and (b) Two lithium cages and the possible intercage jumps between them.

the energy landscape of lithium ionic conductors, resulting in an increase in conductivity, [30] although one recent computational study finds complex behavior.[31] In solid-state lithium-ion conductors, increase in S_{conf} is almost exclusively achieved through multi-ionic doping.[32] As with site disorder, this makes it difficult to differentiate between entropic effects and other consequences of altering the chemical composition, such as vacancy formation and change in lattice softness.

Furthermore, theoretical studies have found that, beyond structural parameters, concerted ion motion and coupling of lithium ions to the surrounding sublattice are pivotal for long-range ion movement that defines the conductivity measured with techniques such as electrochemical impedance spectroscopy (EIS) in a variety of lithium-ion conductors.[33–36] These effects could pose a potential blind spot when trying to relate results from EIS to structural descriptors that affect intercage movement. Conversely, EIS is also sensitive to pressure, particle morphology, and even the measurement setup, which could impede its ability to capture changes in local jump mechanics.[37–39]

In this study, we attempt to unravel the effects of chemical composition and site disorder on both long-range and short-range lithium dynamics, investigating the implicit assumption that an increase in short-range diffusion automatically results in increased long-range diffusion. We use solid-state NMR, a powerful technique to probe short-range lithium dynamics and examine the chemical environment of lithium and phosphorus within the $Li_{6-x}PS_{5-x}Br_{1+x}$ system (x = 0, 0.3, 0.5).[40, 41] We compare short-range lithium intercage and intracage dynamics with long-range conductivity probed with EIS as a function of site disorder, showing that a more complete descriptor is needed. To this end, we investigated the use of configurational entropy as a descriptor. Although our materials cannot be defined as "high entropy" ($S_{conf} < 1.5R$ for all materials), a correlation between configurational entropy and conductivity has been observed for materials of lower entropy such as ours.[42] We link the effect of increased configurational entropy to changes in the overall structure as well as distortion of the lithium substructure that are not apparent from diffraction alone. By increasing configurational entropy through chemical

substitution as well as quench-cooling, we can disentangle the effects of chemical composition and structural distortion on lithium dynamics. Our results provide a link between configurational entropy and short-range lithium movement that does not hold explicitly for long-range dynamics. This trend is also observed in the entropy of migration in the conductivity prefactor, which we are able to obtain from both EIS as well as NMR. Together our results afford us a more complete picture of the effect of structural parameters on both short-range intra- and intercage movement and long-range values obtained from EIS. We show that synthesis conditions have a profound effect on short-range lithium dynamics that are not immediately apparent from EIS. We find that enhanced short-range movement does not automatically translate into enhanced long-range conductivity. Although slow-cooled samples show a clear increase in long-range ionic conductivity with increased short-range intercage movement, quench-cooled samples displayed more complex behavior. The severance of this clear link by alteration of one step in the synthesis procedure is discussed.

4.2 Materials and Methods

The synthesis of the $Li_{6-x}PS_{5-x}Br_{1+x}$ system was carried out through mechanochemical milling using a Fritsch Pulverisette 7 premium line instrument. The initial precursors, lithium sulfide Li_2S (99.98%), phosphorus pentasulfide P_2S_5 (99%), and lithium bromide LiBr (99.99%) were purchased from Merck and Sigma-Aldrich and manually ground before ball milling. The milling process involved cycles of 10 min of milling followed by 10 min of rest over a 25 h period (10 mm ZrO_2 media and 510 rpm). The resulting powder was then pressed into a 1.2 cm diameter pellet and placed in a quartz ampule. The ampule was pretreated at 473 K for 12 h under a dynamic vacuum to remove moisture. Ampules were sealed under vacuum and placed in a furnace for annealing. The temperature was increased at a rate of 100 °C/h, until 550 °C for x = 0.0 and 430 °C for x = 0.3 and 0.5. Two cooling methods were used: rapid quenching in liquid nitrogen and slow cooling at a rate of 5 °C/h over a 4-day period. The obtained powder was stored in an argon-filled glovebox for further characterization. The samples are referred to according to their Br content (1, 3, and 5 for x = 0, 0.3, and 0.5, respectively) and cooling method (SC for slow cooling and QC for quenched).

Nuclear magnetic resonance measurements were performed on a Bruker Ascend 500 magnet with a NEO console for ^{6}Li and ^{31}P and a Bruker UltraShield 300 magnet with an Avance console for ^{7}Li. For the ^{6}Li, ^{31}P, and ^{7}Li measurements, a 4 mm rotor with a zirconia cap was employed together with a 4 mm triple resonance probe. Rotors were dried under dynamic vacuum overnight, filled, and closed in an argon-filled glovebox to avoid degradation. The ^{6}Li and ^{7}Li spectra were referenced vs LiCl in water and the ^{31}P spectra vs 85% H_3PO_4 in D_2O (Sigma). The Larmor frequencies were 73.6, 202.457, and 116.642 MHz for ^{6}Li, ^{31}P, and ^{7}Li, respectively. For the spectra given in the text, a one pulse/Bloch decay experiment was used for the ^{6}Li and ^{31}P MAS spectra and a solid-echo experiment was used for the ^{7}Li static spectra. Longitudinal relaxation in the laboratory frame (T_1) measurements were performed by using a saturation-recovery sequence.

For each sample, the 180° pulse length and spin–lattice relaxation time (T_1) were determined before acquiring the final spectra. The pulse length was the 180° pulse length divided by 2, and the delay between scans was $5T_1$ to ensure full relaxation. For the ^{6}Li

and ^{31}P spectra, a MAS rate of 5 kHz was employed to minimize dipolar interactions. For ^{6}Li, pulse lengths varied between 4.6 and 4.8 µs and delays were 40 or 50 s for 8 scans. For ^{31}P, pulse lengths were between 3.5 and 5.3 µs, delays were 50 s with at least 32 scans obtained. For ^{7}Li, pulse lengths varied between 2.95 and 3.75 µs. Analysis of the spin–lattice relaxation (SLR) data was done using Bruker TopSpin, sSnake [43], and a custom python script. Deconvolution of the ^{31}P and ^{7}Li peaks was performed using MestreNova.

Temperature-dependent electrochemical impedance spectroscopy (EIS) measurements were conducted using an Autolab PGSTAT and EC10 M impedance analyzer connected to a Fryka climate chamber. A frequency range of 10 MHz to 1 Hz and a perturbation amplitude of 0.01 V were used. The capacitance of the wires used was determined beforehand by replacing the sample cell with a 10 MΩ resistor.

Density functional theory (DFT) calculations based on the Perdew–Burke–Ernzerhof functional for solid-state systems (PBEsol) [44, 45] within the Vienna Ab initio Software Package (VASP) [46] were performed. Structure optimizations were conducted with an energy cutoff of 340 eV in 2 × 1 × 1 argyrodite supercells. The experimentally determined S- and Br- site occupancies for the six materials were used to create six corresponding structures.[29] A $Li_6PS_5Br_1$-structure with no site disorder was also analyzed. For each system, the lowest-energy configuration was identified from various random S/Br arrangements and subsequently studied with ab initio molecular dynamics (AIMD) in the NVT ensemble at 650 K to obtain decent statistics. The selected time step was 2 fs for a total computational time of 150 ps. The analysis was conducted according to the method of de Klerk *et al.*[47] Three positions were defined, namely, 48*h* (T5), 16*e* (T4), and 48*h*' (T2) in accordance with the lithium occupancy observed with neutron diffraction.[29] The simulation was divided into 5 parts to obtain the standard error.[11]

4.3 Results and Discussion

Previous work by Gautam *et al.* focused on diffraction and EIS to elucidate the relationship between site disorder and ionic conductivity in the $Li_{6-x}PS_{5-x}Br_{1+x}$ system.[29] The site disorder is defined as the percentage occupancy of Br^- on the 4*d* site and was varied by increasing the Br content (x = 0, 0.3, 0.5) as well as the cooling method used after synthesis. Samples were either slowly cooled over a span of several days or quenched immediately by submersion in liquid nitrogen. The results of the work of Gautam *et al.* are summarized in Figure 4.2, focusing on the effect of site disorder. For the X-ray and neutron diffraction patterns and a comparison between the effects of site disorder and x value, see Supporting Information (SI) section 1. No correlation between the peak width and the degree of disorder was observed (see Appendix section B.1). The cooling method and chemical composition have a clear effect on the EIS response given in Figure 4.2a. Figure 4.2b shows that increasing the Br content results in increased site disorder as additional Br displaces sulfur at the 4*d* site. Quenching increases site disorder further by "freezing in" the higher site disorder present at the synthesis temperature, resulting in higher room-temperature disorder at the same Br content.[17] The ionic conductivities and corresponding activation energies are expected to depend on both the Br content and the site disorder of the samples. The ionic conductivity was found to correlate more strongly with site disorder, as shown in Figure 4.2c. Samples with similar site disorders are found to have similar conductivities, regardless of Br content. This is less the case for the activation energies (Figure 4.2d),

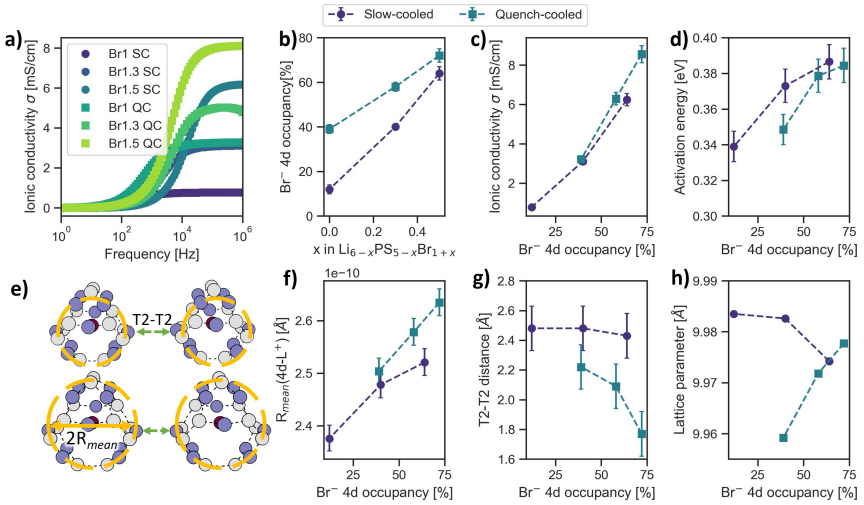

Figure 4.2: Results obtained by Gautam *et al.* [29] showing (a) the conductivity as a function of applied frequency from EIS measurements for each sample, (b) the 4*d* site disorder as a function of Br content, (c) the ionic conductivity from EIS as a function of site disorder, (d) the activation energy obtained from EIS as a function of Br content, (e) the effect of cage expansion on R_{mean} and the T2–T2 distance, (f) the R_{mean} values, and (g) the T2–T2 distance obtained from neutron diffraction. (h) Lattice parameters obtained from X-ray diffraction. Data is taken from ref [29].

showing a difference, especially at low bromine 4*d* occupancy. An increase of the activation energy with increasing conductivity is observed, congruent with the Meyer–Neldel rule. [48]

$$\sigma T = \sigma_0 e^{-E_a/k_B T} \tag{4.1}$$

The ionic conductivity can be defined using eq 4.1, with E_a being the activation energy and σ_0 being a prefactor that contains an entropic term (vide infra for a more detailed discussion). The Meyer–Neldel rule predicts an increase in the prefactor with increasing E_a resulting in an increase in conductivity. Some studies have seen the opposite behavior for other doped argyrodites, such as $Li_{6-x}PS_{5-x}Cl_{1+x}$ [20, 25] $Li_{6-x}PS_{4.5}Cl_xBr_{1.5-x}$ [42], and $Li_{6-x}PS_{5-x}Br_{1+x}$ [27] synthesized via a different procedure and different conditions. A systematic study of lithium-ion conductors by Gao *et al.* [48] predicts classical Neldel–Meyer behavior for materials with a Meyer–Neldel energy (MN energy) of less than 26 meV, which is the case for our materials (see Figure B.5 in the Appendix) and the opposite behavior for materials that show an MN energy above 26 meV, seen in the studies mentioned. Yelon *et al.*. define the Meyer–Neldel energy as the average energy of the excitations responsible for conduction, multiplied by a coupling constant. [49] Hence, it is possible that differences in chemical composition and synthesis method can affect the average excitation energy as well as the coupling constant, resulting in a different MN energy and hence different behavior.

Structural analysis using neutron- and X-ray diffraction revealed that an increase in site disorder results in an expansion of the lithium cage surrounding the 4*d* site as well

as increased occupancy of the T2 and T4 sites. This is shown in Figure 4.2f, where R_{mean} denotes the average radius of the Li cage and is found to correlate well with site disorder. The effect of the cooling method is also apparent for the lattice parameters given in Figure 4.2h, which show opposite trends for slow-cooled and quenched samples. These observations have been explored previously and are due to the occupancy of the 4*a* site and distribution of lithium and its vacancies.[29] The intercage distance, taken as the distance between two 4*d* sites minus twice the R_{mean} shows a clear decrease in both cases, yet also a clear difference between cooling methods. The results show that long-range ionic conductivity correlates well with site disorder, whereas its activation energy does not. Furthermore, the intercage distances display clear differences depending on cooling method. The long-range ionic conductivity seems to be inversely correlated to the intercage distance although a slight deviation is observed. Between the structure and long-range conductivity sits the realm of short-range conductivity, defined by the intercage and intracage jumps. To probe the interplay between structure and lithium dynamics further, solid-state NMR was used to probe short-range lithium movement as well as the local structure in more detail.

4.3.1 Ion Dynamics and Energetics

Spin–lattice relaxation nuclear magnetic resonance (SLR NMR) was used to probe the energetics of short-range lithium diffusion. NMR probes the nuclear spin states of materials through the application of radio frequency pulses. Under thermodynamic equilibrium, spins are distributed over the available energetic spin states of a material according to a Boltzmann distribution. The radio frequency pulse shifts the system away from thermodynamic equilibrium. Relaxation to equilibrium occurs via either spin–spin or spin–lattice relaxation, each with its own characteristic relaxation time (T_2 and T_1, respectively). Spin–lattice relaxation occurs via fluctuations in the local magnetic field at the characteristic Larmor frequency (ω_0) of the nuclei measured. These fluctuations depend on the surroundings and change as the nuclei diffuse. The speed of this change can be quantified by the decay of the autocorrelation function of these fluctuations. The decay will depend on the rate of diffusion and is characterized by the correlation time (τ_c). This time differs by an approximate order of magnitude from the residence time (τ) and is assumed to follow an Arrhenius-type behavior (Equation 4.2) where E_a is the activation energy and τ_0 is a prefactor.[50] In crystalline solids, the jump rate is defined as the inverse of the residence time.

$$\tau_c = \tau_0 e^{E_a/kT} \tag{4.2}$$

The modified Bloembergen–Purcell–Pound model (BPP model), given in Equation 4.3 defines the relationship between the average correlation time and the measurable T_1.[51] The classic BPP model for three-dimensional (3D), uncorrelated motion predicts that the T_1-rates will display a symmetric curve as a function of temperature, with a maximum at $1/\tau_c \approx \omega_0$. The constant C determines the height as well as the width of the curve and is proportional to the extent of dipolar and quadrupolar coupling. [1, 52] The two flanks on either side of the maximum are the high- and low-temperature flanks. For systems that show correlation effects or Coulombic interactions, the curve will display an asymmetry, with a smaller slope for the low-temperature flank compared to the high-temperature

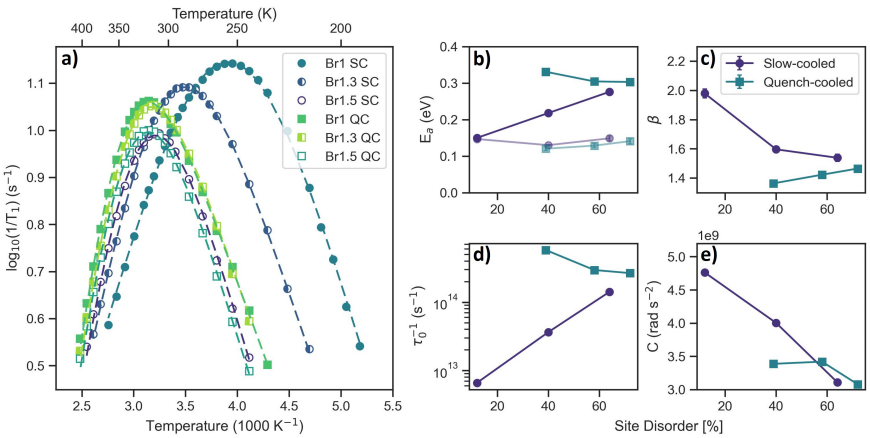

Figure 4.3: (a) Spin–lattice relaxation rates ($1/T_1$) measured using a saturation-recovery sequence and the fit (dashed lines) using the modified BPP model for the slow-cooled and quench-cooled samples as a function of temperature, (b) the activation energy (E_a) from the modified BPP fit (solid/solid line) and the low-temperature BPP E_a^{LT} (transparent/dashed line) obtained using Equation (4.4), (c) the asymmetry parameter, (d) prefactor, and (e) C values obtained from the modified BPP fit as a function of site disorder obtained from diffraction measurements.

flank.[53, 53] The β value quantifies this asymmetry by taking into account the possibility of multiple correlation times [53, 54] and is defined by eq 4.4. Here, E_a is the activation energy obtained from the BPP fit and E_a^{LT} corresponds to the activation energy associated with the low-temperature flank. For a symmetric curve, β is 2.

$$\frac{1}{T_1} = C\frac{\tau_c}{1+(\omega_0\tau_c)^{\beta}} \tag{4.3}$$

$$\beta = 1 + \frac{E_a^{LT}}{E_a} \tag{4.4}$$

In argyrodite systems, asymmetry is often encountered and is thought to be a manifestation of the different energy barriers for intercage and intracage jump processes.[21, 54–57] The low-temperature flank is associated with localized movement, namely, doublet and intracage jumps, whereas the high-temperature flank pertains to intercage jumps as well. Relaxometry T_1 measurements are sensitive to jumps that occur in the time scale of the Larmor frequency (ω_0 = 116 MHz in this case) and probe the jumps that occur within $1/\omega_0$. When very few intercage jumps occur within this time frame, both flanks represent local movement and a symmetric curve is obtained. The appearance of intercage movement at higher temperatures results in an asymmetric curve.

The T_1 relaxation times as a function of temperature as well as the values obtained from the modified BPP model fit are given in Figure 4.3.

For slow-cooled samples (SC), the T_1 curves, given in Figure 4.3a display a single peak that shifts to higher temperatures with increasing bromine content and site disorder, meaning that the temperature at which the jump rate approximates the Larmor frequency

($\omega_0 \approx 116.6$ MHz) increases. The Larmor frequency is mainly defined by the nucleus and differs only slightly for these materials, implying a lower jump rate at a given temperature, in contrast to the increased conductivity observed with EIS.

The activation energies obtained from fitting the relaxation curves are given in Figure 4.3b as a function of the site disorder and are similar to the literature. [21, 58–61] For the slow-cooled samples, an increase in the activation energy is observed. This is explained by a decrease in asymmetry parameter β (Figure 4.3c), which can be seen as a measure of the degree of intercage jumps. For Br1 SC, an almost symmetric curve hints toward a lack of intercage jumps. Increasing the Br content results in a decrease in β and hence more intercage movement. These jumps possess a larger activation barrier, resulting in an increase in E_a, a decrease in the overall jump rate, and a shift of the curve maxima to higher temperatures.

For quench-cooled samples, the opposite trend is observed. The Br1 QC sample shows the highest activation energy and asymmetry. This implies that intercage movement occurs readily in Br1 QC. An increase in the Br content and site disorder slightly lowers the activation energy and increases the asymmetry parameter. The asymmetry depends on the activation energy of the low-temperature flank (E_a^{LT}) and the high-temperature flank. A slight increase in E_a^{LT} is observed for both cooling methods, possibly correlated with the cage expansion observed with neutron diffraction, which reduces the rate of intracage and doublet jumps. This, combined with a slight decrease in the overall E_a, could result in a slightly higher β value.

Information about the Li environment involved in relaxation can be inferred from the C value (Figure 4.3e). Spin–lattice relaxation of lithium can occur either through dipolar- or quadrupolar interactions with the surrounding lattice. The extent of these interactions and the relative dominance of one over the other depends on the chemical environment. [62] Dipolar interactions depend on the gyromagnetic ratio of the surrounding nuclei and are inversely proportional to the distance between the nuclei. Quadrupolar interactions depend on the symmetry of the lithium environment, with a larger asymmetry resulting in a larger degree of coupling. Spin–lattice ^{7}Li relaxation of lithium argyrodites is known to be due to a mixture of these interactions. As can be seen in Figure 4.3e, an increase in disorder and Br content results in a decrease in the C value, implying a change in the lithium environment. Line shape analysis (vide infra) shows that quadrupolar coupling increases with site disorder. The decrease observed in Figure 4.3e could, therefore, be due to decreased dipolar interactions. In lithium argyrodites, this decrease has been correlated to an increased occupancy of the non-T5 sites. [26, 56] As these sites are further away from the 4d site and other lithium species, heteronuclear dipolar coupling between lithium and the 4d species and homonuclear coupling between lithium would decrease, resulting in a smaller C value. Calculation of the Li–Li distance using the C value gives results of a similar order of magnitude as expected (see Figure B.6 of the Appendix) but a different trend to Figure 4.2g. The Li–Li distances increase with increasing site disorder and are therefore not a reflection of the intercage distance but of the average Li–Li distance experienced by the lithium nuclei involved in relaxation. For slow-cooled samples, this trend indicates that the non-T5 sites associated with intercage movement play a more prominent role in relaxation with increased site disorder, corroborating the increase in intercage movement implied by the decrease in β and increase in E_a. For quench-cooled this explanation im-

plies that intercage movement occurs readily and increases slightly with increasing site disorder.

The SLR results indicate that both the cooling method and the Br content have an impact on the number of intercage jumps. The effect of the increased bromine content also differs per cooling method. For the slow-cooled samples, increased bromine content results in an increase in the number of intercage jumps and an increase in the activation energy. For quench-cooled samples, intercage movement occurs readily regardless of bromine content, though it decreases the activation barrier. A similar trend is seen in the MD simulations of these materials. The AIMD simulations were conducted at 650 K to obtain decent jump statistics as is common for lithium argyrodites, particularly when looking at the effects of site disorder. [11, 12, 22] Previous studies indicate good agreement between simulations and SLR data. [16, 63, 64]

Figure 4.4 shows results from MD simulations of a system with no site disorder ("Ord") and systems with 4*d* and 4*a* occupancies for bromine and sulfur equal to those obtained experimentally for the investigated samples. The lithium density plots given in Figure 4b,c,d show the effect of disorder on Li_6PS_5Br (for the lithium density map of all structures, see Figure B.8 in the Appendix). For a structure with no site disorder (Figure 4.4b), lithium sits in cages surrounding the 4*d* site and no intercage jumps occur during the simulation time. A similar situation is seen for the Br1 SC system (Figure 4.4c) albeit with a slight increase in intercage movement. The more homogeneous distribution of lithium density for the Br1 QC system (Figure 4.4d) indicates an increase in lithium diffusion between cages, as well as an increase in the occupancy of the non-T5 sites. This is also seen in the jump rates given in Figure 4.4a. For the slow-cooled samples, an increase in site disorder and Br content correlates with an increase in intercage jumps. Intercage jumps require more time as they span a longer distance and have a higher energy barrier, resulting in a decrease in the total jump rate within the simulation time. For the quench-cooled samples, the Br1.5 QC system displays the largest amount of intercage jumps and the lowest total jump rate. The increase in intercage jumps implies that the decrease in E_a and asymmetry seen for the quench-cooled samples in Figure 4.3 are not due to a decrease in the amount of intercage movement but due to a decrease in the overall energy barrier. Interestingly, the Br1 QC has a much higher intercage jump rate than Br1.3 SC, despite similar degrees of site disorder, mirroring the results from SLR NMR. Its intercage jump rate is also similar to Br1.3 QC, despite possessing a lower degree of site disorder.

The AIMD simulations agree well with the SLR results, indicating that for the slow-cooled samples, an increase in bromine content and site disorder result in an increase in intercage movement. For the quench-cooled samples, this trend is less prominent, as the Br1 QC sample displays a significant degree of intercage movement. Although these results follow a somewhat similar trend to the intercage distance in Figure 4.2g, neither this distance nor the bromine content or site disorder can fully explain the trends observed and why they differ from results obtained from EIS. A deeper look into the structure done in the next section might shed more light.

4.3.2 Structure–Property Relationship

A deeper investigation into the structural differences was performed using ^{6}Li and ^{31}P NMR. The ^{6}Li spectra given in Figure 4.5a are taken from previous work by Gautam *et al.*

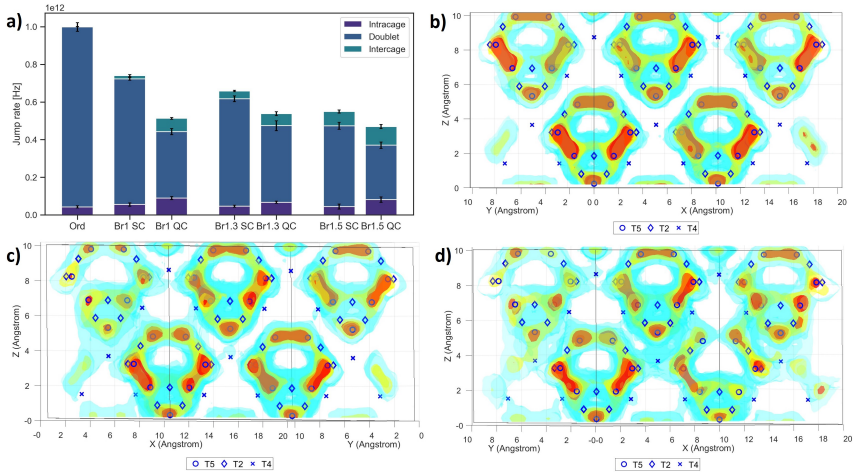

Figure 4.4: Results obtained from MD simulations at 650 K showing (a) the jump rates of the three jump types for a system with no site disorder ("Ord") and systems with equal site disorder to the experiment; (b) the lithium densities for Li_6PS_5Br with no site disorder; and structures representing (c) Br1 SC and (d) Br1 QC.

and show a shift with increasing disorder, which can be attributed to the expansion of the Li cage and occupancy of the non-T5 sites. [29] The ^{31}P NMR spectra, given in Figure 4.5b, show a distinct splitting, which is more pronounced for slow-cooled samples as well as prominent broadening of the peaks for the quench-cooled samples.

The splitting of the peaks is a result of the occupancy of the second coordination sphere. The phosphorus nuclei sit at the center of the PS_4-tetrahedra and are sensitive to the chemical identity of the atoms they are bonded to as well as those in the second coordination sphere, which consists of the four 4*d* sites surrounding the tetrahedra (see Figure 4.5f). Although substitution of the sulfur in the PS_4-tetrahedra result in shift differences of over 20 ppm, changes to the second coordination sphere result in differences of 2–8 ppm, giving rise to peak splitting. [9, 27, 65] The five distinct peaks that emerge have been attributed to the five possible ways in which the 4*d* sites in the second sphere can be occupied, with four S atoms and no Br represented by 4S–0B, the most electron-poor environment and four Br atoms represented by 0S–4B. The other four possibilities (three S, one Br, etc.) sit in between (see Figure 4.5c,e).

The peak integral is a direct representation of the number of nuclei in the corresponding environment. [66] Using the Br-occupancy at the 4*d* site obtained from XRD refinement, it is possible to calculate the theoretical random statistical probability distribution of the five environments using eq 4.5: [9, 27]

$$P(\mathrm{nS}(4-n)\mathrm{Br}) = \frac{4!}{n!(4-n)!} y^n (1-y)^{4-n} \tag{4.5}$$

Here, $P(\mathrm{nS}(4-n)\mathrm{Br})$ is the probability of obtaining the environment with n S atoms and $(4-n)$ Br atoms, with y being the fraction of 4*d* sites occupied by S. The obtained integrals and theoretical distributions are given in Figure 4.5d and 4.5e. For both cooling

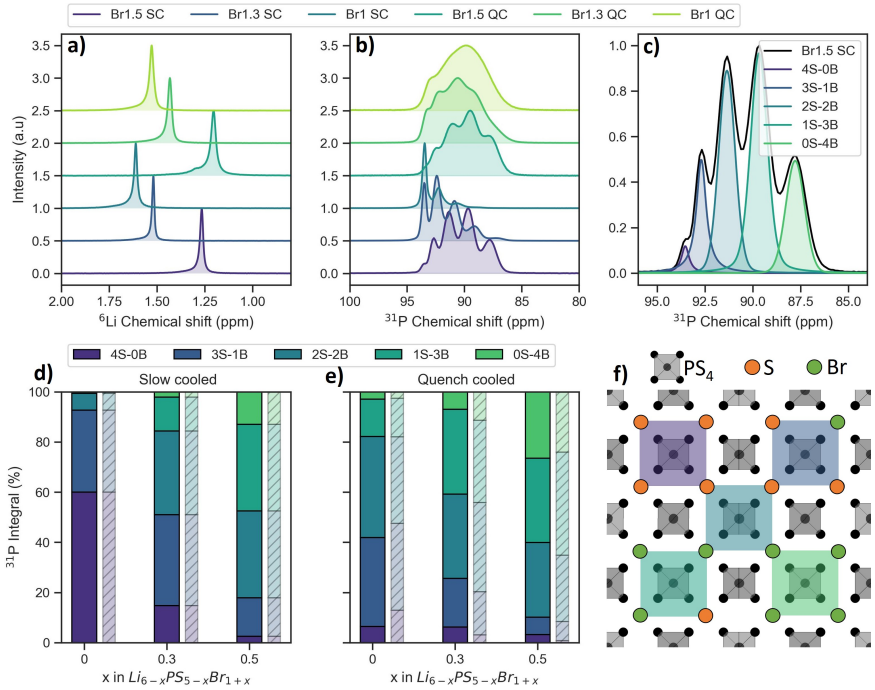

Figure 4.5: (a) ^{6}Li and (b) ^{31}P NMR spectra at MAS rate of 5 kHz for all samples measured at 293 K; (c) a deconvolution of the Br1.5 SC ^{31}P spectrum showing five environments, the integral fractions (solid) and the theoretical prediction (hashed) of the five environments for the slow-cooled (d) and quench-cooled (e) samples; and (f) illustration of the PS_4-tetrahedra surrounded by S/Br in the 2nd coordination shell leading to the five ^{31}P environments. Data for (a) are taken from ref [29].

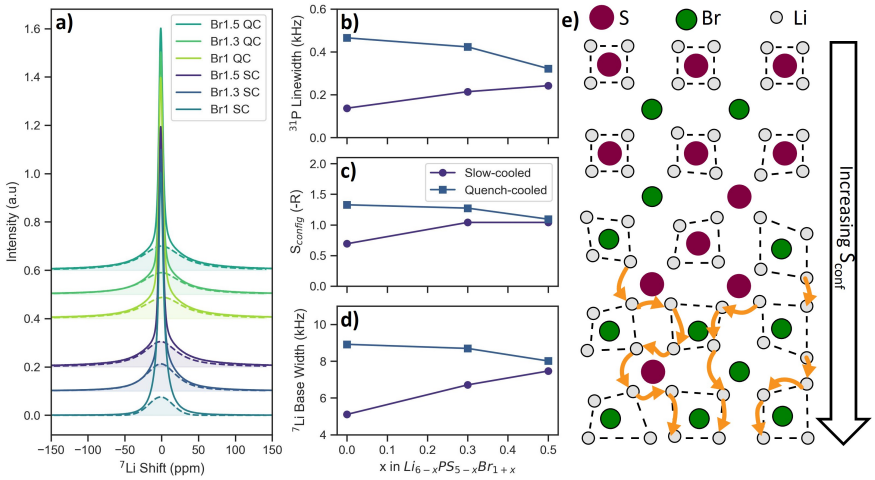

Figure 4.6: (a) Static ^{7}Li spectra taken at 203 K, the broad base highlighted, (b) the ^{31}P line width of the 2S–2B environment as a function of Br content at 293 K, (c) the calculated configurational entropy using eq 4.6, (d) the width of the base highlighted in (a), and (e) an illustration of the effect of increased configurational entropy, resulting in the distortion of lithium cages, the occupancy of non-T5 sites and increased percolation.

methods, the distributions are close to random, showing no preference and a statistical distribution of S and Br over the 4*a* and 4*d* sites.

Although the 4*d* site disorder is able to explain the peak integrals, it cannot account for the differences in peak width. For the quench-cooled samples, the convoluted ^{31}P peaks are significantly broader (see Figure 4.6b and Figure B.12 in the Appendix), indicating a higher degree of bond disorder, usually associated with Cl-based argyrodites. [6, 21] Besides the two coordination spheres mentioned, phosphorus is also sensitive to interactions with nuclei in the subsequent spheres, which include both the 4*d* and 4*a* sites. Although these interactions are not strong enough to induce peak splitting, a large degree of disorder within the entire anion sublattice can result in broadening of the peaks.

The configurational entropy can be used to quantify anion sublattice disorder through the ways in which Br and S can be placed on the 4*a* and 4*d* sites and is defined as [67]

$$S_{\text{conf}} = -R \sum_{i=1}^{n} x_i \ln x_i \tag{4.6}$$

Here, R is the gas constant and x_i represents the mole fraction of element x on sublattice i (see Appendix section B.6). The result, shown in Figure 4.6c, mirrors the trend in peak line width observed.

The configurational entropy depends on the occupancy of the 4*d* and 4*a* site and is a measure of the disorder in the entire anion sublattice. An increase in anion sublattice disorder is predicted to benefit long-range Li diffusion in lithium argyrodite systems through distortion of the lithium environment. [12, 30] Lithium occupies cages with 4*d* sites at the center and 4*a* sites close to the corners. When all 4*d* sites are occupied by sulfur and all 4*a* sites by bromine, these cages are symmetric and close to the 4*d* site. This is the most

energetically favorable position, minimizing interaction with neighboring lithium cations and making intercage movement unfavorable. Anion disorder, where both 4*a* and 4*d* sites are occupied by either element, results in distortion of these cages from this energetically favorable position as bromine is less electronegative than sulfur. Occupancy of non-T5 sites and intercage movement become more favorable, allowing for the formation of percolation pathways between cages (see Figure 4.6e). [12] More anion sublattice disorder would result in more percolation pathways and hence increased Li diffusion.

Experimentally, the distortion in the Li sublattice would result in the observed shift in the ^{6}Li spectra to lower ppm as the lithium cage expands and non-T5 sites are occupied (see Figure 4.5a) as well as a change in the quadrupolar coupling constant. Both isotopes of lithium (^{6}Li and ^{7}Li) are quadrupolar nuclei and hence sensitive to their environment's symmetry. In an ideal argyrodite structure, the Li-occupied cages are symmetric. Distortion of these cages due to disorder breaks this symmetry. [68] The sensitivity of a nucleus to this asymmetry is quantified by its quadrupolar moment. Although ^{6}Li possess a rather small moment of −0.0808 fm^2, ^{7}Li has a larger moment of −4.01 fm^2. In a ^{7}Li static spectrum, the asymmetric environment would manifest as a broad base in the line shape at lower temperatures. [62] The width of this base corresponds to the degree of asymmetry experienced by the lithium. Figure 4.6a shows the static solid-echo ^{7}Li spectra at 203 K of the investigated samples. A broad bump at the base can be seen, indicative of a quadrupolar interaction. The peaks were deconvoluted to obtain the base widths, shown in Figure 4.6d, which follow the same trend as the configurational entropy.

From this, we see that the quench-cooling method increases 4*d* site disorder and disorder of the entire anion sublattice, quantified by eq 4.6. This results in a distortion of the lithium cages, which has been linked with an increase in intercage movement. Comparison between S_{conf} and the β value in Figure 4.3c shows a correlation between the increased anion sublattice disorder and a larger degree of intercage movement for the slow-cooled samples. For the quench-cooled samples, intercage movement occurs readily. However, for Br1 QC, both SLR and MD simulations show a larger degree of intercage movement compared with Br1.3 SC, which has a similar degree of site disorder. This could be attributed to it possessing the largest degree of anion sublattice disorder/highest S_{conf} which facilitates intercage movement despite a lower degree of site disorder. Furthermore, Br1 QC and Br1.3 QC possess similar values for S_{conf} and appear to display similar intercage jump rates, implying that except for Br1.5 QC, the S_{conf} correlates well with the degree of intercage movement. Regarding the long-range movement measured with EIS, we observe an increase with increasing S_{conf} for the slow-cooled samples but not for the quench-cooled samples.

From the structural information obtained via MAS NMR, we see that the site disorder on the 4*d* site alone cannot fully describe the structural changes observed. The configurational entropy takes the disorder of the entire sublattice into account and is able to describe the system more fully. Previous studies on Li argyrodites have noted a correlation between ^{31}P peak width and increased S_{conf}. [69] Using the ^{7}Li quadrupolar interaction, we are able to further link this to Li cage distortion as well. In previous studies on Li argyrodites, S_{conf} was varied through cationic and anionic doping, combined with slow cooling of the samples, and long-range techniques such as EIS and PFG NMR were used to probe lithium movement. [42, 69, 70] By using two cooling methods, we are able to uncouple chemical

and structural effects on S_{conf} and investigate both long-range and short-range movement by using EIS and SLR NMR, respectively. For the slow-cooled samples, we see an increase in long-range lithium movement, congruent with previous studies [42, 69, 70] correlating with an increase in short-range movement. For the quench-cooled samples, there is a correlation between increasing short-range movement and increasing S_{conf}. However, this correlation is lost for long-range movement. The difference in behavior between EIS and SLR warrants a comparison of these techniques.

4.3.3 The Prefactor from EIS and NMR

The conductivity obtained from EIS follows eq 4.1, with E_a being the measurable activation energy barrier and σ_0 a prefactor. [16] Studies focusing on decreasing E_a often encounter the "prefactor dilemma" where a lower E_a also results in a lower prefactor and hence a lower conductivity. [71] It can be argued that in the present case an increase in the prefactor with increasing site disorder results in a higher conductivity, even though E_a is increasing as well. The correlation between the activation barrier and the prefactor is termed the Meyer–Neldel rule and has been observed in conductivity studies for a variety of materials including semiconductors [72] and ionic conductors. [48, 73] Various interpretations of the physical meaning of the Meyer–Neldel rule exist [74] and it appears to be applicable to many processes that display Arrhenius-type behavior, including lithium-ion movement within solids. [75] As both EIS and SLR NMR probe this movement, we will investigate and compare the results of both methods through the lens of Meyer–Neldel theory and attempt to correlate our observations with structural parameters.

The thermally activated jump rate (ν) of ions in a material can be described using an Arrhenius equation (eq 4.7) with ΔG_M being the migrational energy barrier, defined as the difference in free energy between the initial and saddle point. [76, 77]

$$\nu = \nu_0 e^{-\Delta G_M / k_B T} \tag{4.7}$$

ΔG_M is defined as eq 4.8, with ΔH_M and ΔS_M being the enthalpy and entropy of migration, respectively, [78] giving eq 4.9, for the jump rate. [79]

$$\Delta G_M = \Delta H_M - T\Delta S_M \tag{4.8}$$

$$\nu = \nu_0 e^{\Delta S_M / k_B} e^{-\Delta H_M / k_B T} \tag{4.9}$$

E_a from eq 4.1, can be further defined as consisting of the enthalpy of migration and the enthalpy of defect formation (ΔH_F). The enthalpy of defect formation is close to negligible for most ionic conductors. [71, 80] The ionic conductivity was used to obtain the hopping frequency (ω) and ΔH_M (see section B.7 of the Appendix for more details). Almond *et al.* argue that when ΔH_F is negligible, ω is the same as the hopping frequency in eq 4.7, and can be defined as eq 4.10. [81]

$$\omega = \omega_0 e^{\Delta S_M / k_B} e^{-\Delta H_M / k_B T} \tag{4.10}$$

The difference between E_a and ΔH_M, given in Figure 4.7a, is small, showing that ΔH_F is negligible (see Figure B.8). By using the hopping frequency, we do not need to estimate the effects of the other terms in the equation describing conductivity (Section B.7

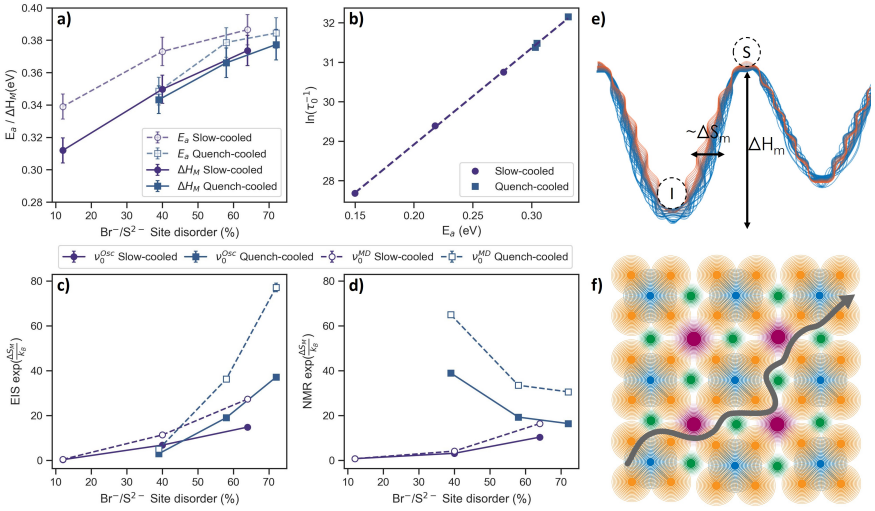

Figure 4.7: (a) Activation energy (E_a) and enthalpy of migration (ΔH_M) obtained from the EIS data; (b) the natural logarithm of the prefactor vs the activation energy obtained from the modified BPP fit, showing a linear correlation in line with the Meyer–Neldel rule; (c) entropy of migration (ΔS_M) from the obtained the EIS data; (d) entropy of migration (ΔS_M) from the obtained the BPP fit; (e) illustration showing the enthalpy of migration as the difference in energy between the initial (I) and saddle-points (S) and the entropy of migration as being proportional to the number of ways it can be surmounted; and (f) an illustration showing the crystal lattice as a collection of vibrating atoms allowing lithium movement through coupling to the phonon modes.

of the Appendix). The obtained prefactor contains only an attempt frequency (ω_0) and an entropic term

$$\left(e^{\Delta S_M/k_B}\right).$$

A similar analysis can be performed with the data obtained from SLR. The prefactor from T_1 SLR (τ_0^{-1}) is given in Figure 4.3d and is thought to be in the order of phonon frequencies of lithium ions in the material. [21, 82] It is expected to be between 10^{12} and 10^{14} Hz and has been shown to increase with decreasing lattice softness.[28, 83] Lattice softness refers to the polarizability of the lattice and hence the atoms within it. Larger, more polarizable atoms such as Br will form a softer lattice compared to smaller, harder atoms such as Cl. [28, 83] As more sulfur is substituted by bromine, lattice softness is expected to decrease, explaining the increase in τ_0^{-1} for the slow-cooled samples in Figure 4.3d. Unexpectedly, for the quench-cooled samples, a slight decrease in the τ_0^{-1} is observed. The difference in trend between the cooling methods hints at a stronger interplay with other structural parameters besides chemical composition. Plotting the natural logarithm of the NMR prefactors versus the activation energy reveals that they are linearly correlated (Figure 4.7b). This implies that the NMR jump process given by Equation (4.2) follows the Meyer–Neldel rule and can be described by using eq 4.9 as well. The inverse of the correlation time (τ_c) from eq 4.2 can be substituted for ν, giving:

$$\tau_c^{-1} = \tau_0^{-1} e^{-E_a/kT} = \nu_0 e^{\Delta S_M/k_B} e^{-\Delta H_M/k_B T} \tag{4.11}$$

$$\tau_c^{-1} = \nu_0 e^{\Delta S_M/k_B} e^{-E_a/kT} \tag{4.12}$$

The experimentally obtained NMR prefactor can then be expressed as

$$\tau_0^{-1} = \nu_0 e^{\Delta S_M/k_B},$$

consisting of an approximate attempt frequency term (ν_0) and a term for the entropy of migration. [21, 84, 85] To obtain the entropic term for EIS and SLR NMR, the experimentally obtained prefactors should be divided by an attempt frequency (ν_0). Two methods for obtaining ν_0 values were used and compared, namely, from MD simulations (ν_0^{MD}) or calculated by assuming a classical hopping mechanism based on Equation 4.13 (ν_0^{Osc}) [86] (see Section B.8 of the Appendix for more details). The results for EIS and NMR are given in Figure 4.7c and d, respectively, and show a clear difference in trends for the two techniques. It must be noted that for NMR, the prefactor describes both intercage and intracage jumps, and hence, the value for a_0 used in Equation 4.13 could be overestimated, resulting in a smaller value for ν_0 and hence an underestimation of ΔS_M. However, both ν_0^{MD} and ν_0^{Osc} give the same trends.

$$\nu_0^{Osc} = \frac{1}{a_0^2}\sqrt{\frac{E_a}{M_{Li}}} \tag{4.13}$$

The entropy of migration has been interpreted in various ways, with the two most prominent interpretations being the multiexcitation entropy model (MEE) and the phonon vibrational model. [87–89]

Yelon *et al.* argue that when the energy barrier for a jump (ΔH_M) is larger than $\hbar\omega$ (the energy of available excitations) and $k_B T$, multiple excitations must work together to surmount it. [49, 79] The higher this barrier, the more excitations are needed and hence the more ways there are of combining them. The entropic term (ΔS_M) can therefore be defined as the number of ways to assemble the necessary amount of excitations needed ($n = \Delta H_M/\hbar\omega$) to pass the barrier from the total number possible (N) in the interaction volume, resulting in Equation 4.14, which can be simplified when assuming that $n \ll N$ (see Figure 4.7e).

$$\Delta S_M = k_B \ln\left[\frac{N!}{n!(N-n)!}\right] \sim k_B \frac{\Delta H_M}{\hbar\omega} \ln N \tag{4.14}$$

The ΔS_M values obtained from NMR and EIS are shown in Figure 4.7c,d, respectively, exhibiting a clear difference in trends yet somewhat similar values. Both follow the trends observed for the ΔH_M values obtained from the respective techniques (for NMR, these are the E_a values given in Figure 4.3b), which are congruent with Equation 4.14.

For NMR, there is a difference in ΔS_M values between the cooling methods used, mirroring the trend seen for S_{conf} (Figure 4.6c). S_{conf} is a measure of the distortion of the lithium cage. A more distorted cage results in more lithium ions occupying less energetically favorable positions, destabilizing the initial state. This could result in more states being available to assemble the necessary excitations and, hence, a larger N value in Equation 4.14.

For EIS, the ΔS_M values do not correlate with S_{conf}, correlating with the 4*d* site disorder/Br content instead. Discrepancies between NMR and EIS have been observed before

for activation energies and are ascribed to correlation effects and the difference in the length scale probed (see section B.11 of the Appendix for a rough calculation). [90–92] NMR is sensitive to movement occurring within the time frame of the Larmor frequency (116 MHz) and is hence more local, whereas EIS is sensitive to long-range movement. [93] This difference in length scale also affects the prefactors obtained and hence the entropy of migration. [94]

The second interpretation, from which Equation 4.15 is derived, is related to the phonon vibrations of the materials and is often used to relate the ΔS_M values obtained from EIS to material structure and chemical composition. [28, 95–97] Here, ΔS_M is the ratio of the product of the normal frequencies of the lattice where lithium is at the initial site (ν_i^I) and the lattice where lithium is at the saddle point (ν_i^S). The attempt frequency ν_0 is seen as the frequency of the vibrational mode that carries lithium across the saddle point. This equation relates the entropy of migration to the lattice vibrations experienced by the lithium ion during diffusion. [98]

$$\Delta S_M = k_B \ln\left(\frac{\prod_{i=1}^{3N} \nu_i^I}{\prod_{i=1}^{3N-1} \nu_i^S}\right) \tag{4.15}$$

Although determination of the components of Equation 4.15 is challenging, various relationships have been found between the vibrational characteristics of the lattice and the prefactor obtained from EIS and AIMD. [98] Elemental substitution is the most common method to alter lattice softness, as quantified by the Debye frequency. Various studies have found that the addition of "softer", larger, more polarizable elements such as I in Li_6PS_5X (X = Cl, Br, I) results in a decrease in the Debye frequency along with a decrease in the EIS prefactor and activation energy. [28, 95–97] Although this explains the general trend in ΔS_M observed in Figure 4.7d, the difference between the two cooling methods implies that chemical composition alone does not describe the lattice vibrations experienced by lithium fully. Gelin *et al.* performed a computational study on the diffusion of ions in crystalline silicon and germanium, showing that movement of many atoms along the diffusion path results in the alteration of the phonon mode spectrum of the material, with lower vibrational modes becoming more enhanced. Enhancement of these soft modes results in a higher ΔS_M. [89] Xu *et al.*. have shown that for sulfide-based lithium-ion conductors, coupling between lithium ions and low-medium frequency modes, specifically those associated with the sulfur and bromine surrounding the intercage bottleneck is seen and results in an enhancement of the soft phonon modes as well. [34] They argue that coupling of lithium ions with these modes benefits long-range movement, as it allows lithium to oscillate with larger amplitude in the direction of bottlenecks. This was later also observed computationally for Li_6PS_5Cl. [99] Furthermore, previous NMR studies on argyrodite systems have found a correlation between the coupling of lithium- and PS_4-tetrahedral motion around the bottleneck between lithium cages and increased ion conductivity obtained from EIS for Li_6PS_5X (X = Cl, Br, I) with the degree of coupling depending on the lattice parameter and the degree of site disorder. [56, 61, 100] Hence it is possible that the difference in ΔS_M values obtained from EIS stems from the degree of coupling between lithium and the PS_4 tetrahedra. Spin relaxation T_1 NMR is sensitive to local movement and hence the ratio of intracage and intercage jumps. As EIS is sensitive to only long-range movement, the coupling between ions and the lattice vibrations

associated with low-frequency modes becomes more pronounced.

4.4 Conclusion

In this study, the effects of increasing Br content ($x = 0, 0.3, 0.5$) and using two synthesis cooling methods (slow-cooling and quench-cooling) were explored using EIS, ^{7}Li T_1 SLR NMR, and ^{6}Li, ^{7}Li, and ^{31}P NMR, allowing us to disentangle chemical composition and site disorder.

Using ^{7}Li T_1 SLR NMR, we are able to probe the short-range lithium dynamics of the $Li_{6-x}PS_{5-x}Br_{1+x}$-series. For slow-cooled samples, an increase in Br content/site disorder results in an increase in intercage movement. For the quench-cooled samples, intercage movement occurs readily for all samples and an increase in Br content/4*d* site disorder lowers the energy barrier for intercage movement. The same is observed in MD simulations of the systems.

The chemical environment was probed with ^{6}Li, ^{7}Li, and ^{31}P NMR. The ^{31}P MAS NMR line width reflects the degree of site disorder across the entire anion sublattice and was found to be described well by the configurational entropy (S_{conf}) of this sublattice. The distortion of the Li cage can be quantified with the ^{7}Li static NMR base width, being a measure of the quadrupolar interaction. This distortion correlates with the ^{31}P line width and S_{conf}, showing that increase in anion sublattice disorder/S_{conf} results in increased Li cage distortion. In addition, increase in S_{conf} correlates with increase in intercage movement seen via ^{7}Li T_1, congruent with theoretical predictions. (12) Additionally for the slow-cooled samples, an increase in S_{conf} results in increase EIS conductivity in agreement with previous studies.[42, 69, 70] For quench-cooled samples, this is not the case. Hence, we conclude that an increase in S_{conf} through chemical doping results in increased EIS conductivity, whereas an increase in S_{conf} through quenching does not, indicating that the correlation between configurational entropy and conductivity is intricate.

The prefactor obtained from ^{7}Li T_1 NMR obeys the Meyer–Neldel law, allowing extraction of the migration entropy ΔS_M and comparison to values obtained from EIS. We find that the ΔS_M obtained from NMR correlates well with S_{conf} and hence the degree of cage distortion for both cooling methods. On the other hand, the ΔS_M obtained from EIS shows a correlation with S_{conf} for the slow-cooled samples only. There is a correlation between ΔS_M and the 4*d* site disorder and chemical composition. This implies that the chemical composition and soft phonon modes resulting from the interaction between lithium and the 4*d* site are more important for long-range diffusion.

Our results highlight the importance of the synthesis method on the chemical structure and analysis of the materials. By changing the cooling method from slow cooling to quenching, the relationship between structural descriptors (site disorder or S_{conf}) and short-range and long-range diffusion is changed completely. The implicit assumption that improved short-range diffusion automatically results in improved long-range conductivity is challenged, and the importance of chemical composition and ion–phonon interactions are highlighted. We observe that an increase in site disorder results in an increase in EIS conductivity and corresponding activation energy, regardless of the cooling method used. However, we observe that the cooling method has a profound effect on short-range lithium movement probed by T_1 SLR NMR, that goes beyond 4*d* occupancy.

Bibliography

[1] A. Kalair, N. Abas, M. S. Saleem, A. R. Kalair, and N. Khan. Role of energy storage systems in energy transition from fossil fuels to renewables. *Energy Storage*, 3(1): e135, 2021. ISSN 2578-4862. doi: 10.1002/est2.135.

[2] Qingsong Wang, Binbin Mao, Stanislav I. Stoliarov, and Jinhua Sun. A review of lithium ion battery failure mechanisms and fire prevention strategies. *Progress in Energy and Combustion Science*, 73:95–131, 2019. ISSN 0360-1285. doi: 10.1016/j.pecs.2019.03.002.

[3] Zhonghui Gao, Huabin Sun, Lin Fu, Fangliang Ye, Yi Zhang, Wei Luo, and Yunhui Huang. Promises, challenges, and recent progress of inorganic solid-state electrolytes for all-solid-state lithium batteries. *Advanced materials*, 30(17):1705702, 2018.

[4] Xiangtao Bai, Yi Duan, Weidong Zhuang, Rong Yang, and Jiantao Wang. Research progress in li-argyrodite-based solid-state electrolytes. *Journal of Materials Chemistry A*, 8(48):25663–25686, 2020.

[5] Chuang Yu, Feipeng Zhao, Jing Luo, Long Zhang, and Xueliang Sun. Recent development of lithium argyrodite solid-state electrolytes for solid-state batteries: Synthesis, structure, stability and dynamics. *Nano Energy*, 83:105858, 2021.

[6] Hans-Jörg Deiseroth, Shiao-Tong Kong, Hellmut Eckert, Julia Vannahme, Christof Reiner, Torsten Zaiß, and Marc Schlosser. Li6ps5x: a class of crystalline li-rich solids with an unusually high li+ mobility. *Angewandte Chemie*, 120(4):767–770, 2008.

[7] Nicolo Minafra, Marvin A Kraft, Tim Bernges, Cheng Li, Roman Schlem, Benjamin J Morgan, and Wolfgang G Zeier. Local charge inhomogeneity and lithium distribution in the superionic argyrodites li6ps5x (x= cl, br, i). *Inorganic Chemistry*, 59(15): 11009–11019, 2020.

[8] Laidong Zhou, Nicolo Minafra, Wolfgang G Zeier, and Linda F Nazar. Innovative approaches to li-argyrodite solid electrolytes for all-solid-state lithium batteries. *Accounts of chemical research*, 54(12):2717–2728, 2021.

[9] Shiao Tong Kong, Özgül Gün, Barbara Koch, Hans Joerg Deiseroth, Hellmut Eckert, and Christof Reiner. Structural characterisation of the li argyrodites li7ps6 and li7pse6 and their solid solutions: Quantification of site preferences by mas-nmr spectroscopy. *Chemistry–A European Journal*, 16(17):5138–5147, 2010.

[10] Hans-Jörg Deiseroth, Joachim Maier, Katja Weichert, Vera Nickel, Shiao-Tong Kong, and Christof Reiner. Li7ps6 and li6ps5x (x: Cl, br, i): possible three-dimensional diffusion pathways for lithium ions and temperature dependence of the ionic conductivity by impedance measurements. *Zeitschrift für anorganische und allgemeine Chemie*, 637(10):1287–1294, 2011. ISSN 0044-2313.

[11] Niek J. J. de Klerk, Irek Rosłoń, and Marnix Wagemaker. Diffusion mechanism of li argyrodite solid electrolytes for li-ion batteries and prediction of optimized halogen doping: The effect of li vacancies, halogens, and halogen disorder. *Chemistry of Materials*, 28(21):7955–7963, 2016. ISSN 0897-4756.

[12] Benjamin J. Morgan. Mechanistic origin of superionic lithium diffusion in anion-disordered li6ps5x argyrodites. *Chemistry of Materials*, 33(6):2004–2018, 2021. ISSN 0897-4756.

[13] Ruth Schlenker, Anna-Lena Hansen, Anatoliy Senyshyn, Tatiana Zinkevich, Michael Knapp, Thomas Hupfer, Helmut Ehrenberg, and Sylvio Indris. Structure and diffusion pathways in lli6ps5cl argyrodite from neutron diffraction, pair-distribution function analysis, and nmr. *Chemistry of Materials*, 32(19):8420–8430, 2020. ISSN 0897-4756.

[14] R. P. Rao and S. Adams. Studies of lithium argyrodite solid electrolytes for all-solid-state batteries. *physica status solidi (a)*, 208(8):1804–1807, 2011. ISSN 1862-6300.

[15] Prasada Rao Rayavarapu, Neeraj Sharma, Vanessa K. Peterson, and Stefan Adams. Variation in structure and li+-ion migration in argyrodite-type li6ps5x (x = cl, br, i) solid electrolytes. *Journal of Solid State Electrochemistry*, 16(5):1807–1813, 2012. ISSN 1432-8488.

[16] Oliver Pecher, Shiao-Tong Kong, Thorsten Goebel, Vera Nickel, Katja Weichert, Christof Reiner, Hans-Jörg Deiseroth, Joachim Maier, Frank Haarmann, and Dirk Zahn. Atomistic characterisation of li+ mobility and conductivity in li7−xps6−xix argyrodites from molecular dynamics simulations, solid-state nmr, and impedance spectroscopy. *Chemistry – A European Journal*, 16(28):8347–8354, 2010. ISSN 0947-6539. doi: 10.1002/chem.201000501.

[17] Ajay Gautam, Marcel Sadowski, Nils Prinz, Henrik Eickhoff, Nicolò Minafra, Michael Ghidiu, Sean P. Culver, Karsten Albe, Thomas F. Fässler, Mirijam Zobel, and Wolfgang G. Zeier. Rapid crystallization and kinetic freezing of site-disorder in the lithium superionic argyrodite li6ps5br. *Chemistry of Materials*, 31(24):10178–10185, 2019. ISSN 0897-4756. doi: 10.1021/acs.chemmater.9b03852.

[18] Wenze Huang, Lindong Cheng, Satoshi Hori, Kota Suzuki, Masao Yonemura, Masaaki Hirayama, and Ryoji Kanno. Ionic conduction mechanism of a lithium superionic argyrodite in the li–al–si–s–o system. *Materials Advances*, 1(3):334–340, 2020. ISSN 2633-5409. doi: 10.1039/d0ma00115e.

[19] Wenze Huang, Kazuhiro Yoshino, Satoshi Hori, Kota Suzuki, Masao Yonemura, Masaaki Hirayama, and Ryoji Kanno. Superionic lithium conductor with a cubic argyrodite-type structure in the li–al–si–s system. *Journal of Solid State Chemistry*, 270:487–492, 2019. ISSN 0022-4596. doi: 10.1016/j.jssc.2018.12.015.

[20] Parvin Adeli, J. David Bazak, Kern Ho Park, Ivan Kochetkov, Ashfia Huq, Gillian R. Goward, and Linda F. Nazar. Boosting solid-state diffusivity and conductivity in

lithium superionic argyrodites by halide substitution. *Angewandte Chemie International Edition*, 58(26):8681–8686, 2019. ISSN 1433-7851. doi: 10.1002/anie.201814222.

[21] I. Hanghofer, M. Brinek, S. L. Eisbacher, B. Bitschnau, M. Volck, V. Hennige, I. Hanzu, D. Rettenwander, and H. M. R. Wilkening. Substitutional disorder: structure and ion dynamics of the argyrodites li6ps5cl, li6ps5br and li6ps5i. *Physical Chemistry Chemical Physics*, 21(16):8489–8507, 2019. ISSN 1463-9076. doi: 10.1039/c9cp00664h.

[22] Andreas R. Stamminger, Benedikt Ziebarth, Matous Mrovec, Thomas Hammerschmidt, and Ralf Drautz. Ionic conductivity and its dependence on structural disorder in halogenated argyrodites li6ps5x (x = br, cl, i). *Chemistry of Materials*, 31 (21):8673–8678, 2019. ISSN 0897-4756. doi: 10.1021/acs.chemmater.9b02047.

[23] Ajay Gautam, Michael Ghidiu, Emmanuelle Suard, Marvin A. Kraft, and Wolfgang G. Zeier. On the lithium distribution in halide superionic argyrodites by halide incorporation in li7–xps6–xclx. *ACS Applied Energy Materials*, 4(7):7309–7315, 2021. ISSN 2574-0962. doi: 10.1021/acsaem.1c01417.

[24] Ajay Gautam, Marcel Sadowski, Michael Ghidiu, Nicolò Minafra, Anatoliy Senyshyn, Karsten Albe, and Wolfgang G. Zeier. Engineering the site-disorder and lithium distribution in the lithium superionic argyrodite li6ps5br. *Advanced Energy Materials*, 11(5), 2021. ISSN 1614-6832. doi: 10.1002/aenm.202003369.

[25] Xuyong Feng, Po-Hsiu Chien, Yan Wang, Sawankumar Patel, Pengbo Wang, Haoyu Liu, Marcello Immediato-Scuotto, and Yan-Yan Hu. Enhanced ion conduction by enforcing structural disorder in li-deficient argyrodites li6–xps5–xcl1+x. *Energy Storage Materials*, 30:67–73, 2020. ISSN 2405-8297. doi: 10.1016/j.ensm.2020.04.042.

[26] Katharina Hogrefe, Nicolò Minafra, Isabel Hanghofer, Ananya Banik, Wolfgang G. Zeier, and H. Martin R. Wilkening. Opening diffusion pathways through site disorder: The interplay of local structure and ion dynamics in the solid electrolyte li6+xp1-xgexs5i as probed by neutron diffraction and nmr. *Journal of the American Chemical Society*, 144(4):1795–1812, 2022. ISSN 0002-7863. doi: 10.1021/jacs.1c11571.

[27] Pengbo Wang, Haoyu Liu, Sawankumar Patel, Xuyong Feng, Po-Hsiu Chien, Yan Wang, and Yan-Yan Hu. Fast ion conduction and its origin in li6-xps5-xbr1+x. *Chemistry of Materials*, 32(9):3833–3840, 2020. ISSN 0897-4756. doi: 10.1021/acs.chemmater.9b05331.

[28] Marvin A. Kraft, Sean P. Culver, Mario Calderon, Felix Böcher, Thorben Krauskopf, Anatoliy Senyshyn, Christian Dietrich, Alexandra Zevalkink, Jürgen Janek, and Wolfgang G. Zeier. Influence of lattice polarizability on the ionic conductivity in the lithium superionic argyrodites li6ps5x (x = cl, br, i). *Journal of the American Chemical Society*, 139(31):10909–10918, 2017. ISSN 0002-7863. doi: 10.1021/jacs.7b06327.

[29] Ajay Gautam, Hanan Al-Kutubi, Theodosios Famprikis, Swapna Ganapathy, and Marnix Wagemaker. Exploring the relationship between halide substitution, structural disorder, and lithium distribution in lithium argyrodites (li6-xps5-xbr1+x).

Chemistry of Materials, 35(19):8081–8091, 2023. ISSN 0897-4756. doi: 10.1021/acs.chemmater.3c01525.

[30] Yan Zeng, Bin Ouyang, Jue Liu, Young-Woon Byeon, Zijian Cai, Lincoln J. Miara, Yan Wang, and Gerbrand Ceder. High-entropy mechanism to boost ionic conductivity. *Science*, 378(6626):1320–1324, 2022. ISSN 0036-8075. doi: 10.1126/science.abq1346.

[31] Anastasia K. Lavrinenko, Theodosios Famprikis, James A. Quirk, Victor Landgraf, Pedro B. Groszewicz, Jouke R. Heringa, Stef Smeets, Victor Azizi, Simone Ciarella, James A. Dawson, Marnix Wagemaker, and Alexandros Vasileiadis. Optimizing ionic transport in argyrodites: a unified view on the role of sulfur/halide distribution and local environments. *Journal of Materials Chemistry A*, 12(39):26596–26611, 2024. ISSN 2050-7488. doi: 10.1039/d4ta04628e.

[32] Simon Schweidler, Miriam Botros, Florian Strauss, Qingsong Wang, Yanjiao Ma, Leonardo Velasco, Gabriel Cadilha Marques, Abhishek Sarkar, Christian Kübel, Horst Hahn, Jasmin Aghassi-Hagmann, Torsten Brezesinski, and Ben Breitung. High-entropy materials for energy and electronic applications. *Nature Reviews Materials*, 9(4):266–281, 2024. ISSN 2058-8437. doi: 10.1038/s41578-024-00654-5.

[33] Xingfeng He, Yizhou Zhu, and Yifei Mo. Origin of fast ion diffusion in super-ionic conductors. *Nature Communications*, 8(1), 2017. ISSN 2041-1723. doi: 10.1038/ncomms15893.

[34] Zhenming Xu, Xi Chen, Hong Zhu, and Xin Li. Anharmonic cation–anion coupling dynamics assisted lithium-ion diffusion in sulfide solid electrolytes. *Advanced Materials*, 34(49), 2022. ISSN 0935-9648. doi: 10.1002/adma.202207411.

[35] Ballal Ahammed and Elif Ertekin. Configurational disorder, strong anharmonicity, and coupled host dynamics lead to superionic transport in li3ycl6 (lyc). *Advanced Materials*, 36(16), 2024. ISSN 0935-9648. doi: 10.1002/adma.202310537.

[36] Gabriel Krenzer, Chang-Eun Kim, Kasper Tolborg, Benjamin J. Morgan, and Aron Walsh. Anharmonic lattice dynamics of superionic lithium nitride. *Journal of Materials Chemistry A*, 10(5):2295–2304, 2022. ISSN 2050-7488. doi: 10.1039/d1ta07631k.

[37] Md-Jamal Uddin and Sung-Jin Cho. Reassessing the bulk ionic conductivity of solid-state electrolytes. *Sustainable Energy & Fuels*, 2(7):1458–1462, 2018. ISSN 2398-4902. doi: 10.1039/c8se00139a.

[38] Irina V. Krasnikova, Mariam A. Pogosova, Alexey O. Sanin, and Keith J. Stevenson. Toward standardization of electrochemical impedance spectroscopy studies of li-ion conductive ceramics. *Chemistry of Materials*, 32(6):2232–2241, 2020. ISSN 0897-4756. doi: 10.1021/acs.chemmater.9b04899.

[39] Marius Müller, Henry Auer, Alexander Bauer, Sven Uhlenbruck, Martin Finsterbusch, Katja Wätzig, Kristian Nikolowski, Sebastian Dierickx, Dina Fattakhova-Rohlfing, Olivier Guillon, and André Weber. Guidelines to correctly measure the

lithium ion conductivity of oxide ceramic electrolytes based on a harmonized testing procedure. *Journal of Power Sources*, 531:231323, 2022. ISSN 0378-7753. doi: 10.1016/j.jpowsour.2022.231323.

[40] Oliver Pecher, Javier Carretero-González, Kent J. Griffith, and Clare P. Grey. Materials' methods: Nmr in battery research. *Chemistry of Materials*, 29(1):213–242, 2017. ISSN 0897-4756. doi: 10.1021/acs.chemmater.6b03183.

[41] A. Kuhn, M. Kunze, P. Sreeraj, H.-D. Wiemhöfer, V. Thangadurai, M. Wilkening, and P. Heitjans. Nmr relaxometry as a versatile tool to study li ion dynamics in potential battery materials. *Solid State Nuclear Magnetic Resonance*, 42:2–8, 2012. ISSN 0926-2040. doi: 10.1016/j.ssnmr.2012.02.001.

[42] Shenghao Li, Jing Lin, Mareen Schaller, Sylvio Indris, Xin Zhang, Torsten Brezesinski, Ce-Wen Nan, Shuo Wang, and Florian Strauss. High-entropy lithium argyrodite solid electrolytes enabling stable all-solid-state batteries. *Angewandte Chemie International Edition*, 62(50), 2023. ISSN 1433-7851. doi: 10.1002/anie.202314155.

[43] S. G. J. van Meerten, W. M. J. Franssen, and A. P. M. Kentgens. ssnake: A cross-platform open-source nmr data processing and fitting application. *Journal of Magnetic Resonance*, 301:56–66, 2019. ISSN 1090-7807. doi: 10.1016/j.jmr.2019.02.006.

[44] John P. Perdew, Kieron Burke, and Matthias Ernzerhof. Generalized gradient approximation made simple. *Physical Review Letters*, 77(18):3865–3868, 1996. ISSN 0031-9007. doi: 10.1103/physrevlett.77.3865.

[45] John P. Perdew, Adrienn Ruzsinszky, Gábor I. Csonka, Oleg A. Vydrov, Gustavo E. Scuseria, Lucian A. Constantin, Xiaolan Zhou, and Kieron Burke. Restoring the density-gradient expansion for exchange in solids and surfaces. *Physical Review Letters*, 100(13), 2008. ISSN 0031-9007. doi: 10.1103/physrevlett.100.136406.

[46] G. Kresse and J. Furthmüller. Efficiency of ab-initio total energy calculations for metals and semiconductors using a plane-wave basis set. *Computational Materials Science*, 6(1):15–50, 1996. ISSN 0927-0256. doi: 10.1016/0927-0256(96)00008-0.

[47] Niek J. J. de Klerk, Eveline van der Maas, and Marnix Wagemaker. Analysis of diffusion in solid-state electrolytes through md simulations, improvement of the li-ion conductivity in β-li3ps4 as an example. *ACS Applied Energy Materials*, 1(7): 3230–3242, 2018. ISSN 2574-0962. doi: 10.1021/acsaem.8b00457.

[48] Yirong Gao, Nana Li, Yifan Wu, Wenge Yang, and Shou-Hang Bo. Rethinking the design of ionic conductors using meyer–neldel–conductivity plot. *Advanced Energy Materials*, 11(13), 2021. ISSN 1614-6832. doi: 10.1002/aenm.202100325.

[49] A. Yelon, B. Movaghar, and R. S. Crandall. Multi-excitation entropy: its role in thermodynamics and kinetics. *Reports on Progress in Physics*, 69(4):1145–1194, 2006. ISSN 0034-4885. doi: 10.1088/0034-4885/69/4/r04.

[50] Paul Heitjans, Sylvio Indris, and Martin Wilkening. Solid-state diffusion and nmr. *Diffusion Fundamentals*, 2(45):1–20, 2005. ISSN 1862-4138. doi: 10.62721/diffusion-fundamentals.2.231.

[51] N. Bloembergen, E. M. Purcell, and R. V. Pound. Relaxation effects in nuclear magnetic resonance absorption. *Physical Review*, 73(7):679–712, 1948. ISSN 0031-899X. doi: 10.1103/physrev.73.679.

[52] Lawrence G Werbelow. Relaxation theory for quadrupolar nuclei. *EMagRes*, 2011, 2007.

[53] Martin Meyer, Philipp Maass, and Armin Bunde. Spin-lattice relaxation: Non-bloembergen-purcell-pound behavior by structural disorder and coulomb interactions. *Physical Review Letters*, 71(4):573–576, 1993. ISSN 0031-9007. doi: 10.1103/physrevlett.71.573.

[54] K. L. Ngai and O. Kanert. Comparisons between the coupling model predictions, monte carlo simulations and some recent experimental data of conductivity relaxations in glassy ionics. *Solid State Ionics*, 53-56:936–946, 1992. ISSN 0167-2738. doi: 10.1016/0167-2738(92)90275-t.

[55] Martin Wilkening and Paul Heitjans. From micro to macro: Access to long-range li+ diffusion parameters in solids via microscopic 6,7li spin-alignment echo nmr spectroscopy. *ChemPhysChem*, 13(1):53–65, 2012. ISSN 1439-4235. doi: 10.1002/cphc.201100580.

[56] M. Brinek, C. Hiebl, K. Hogrefe, I. Hanghofer, and H. M. R. Wilkening. Structural disorder in li6ps5ipeeds 7li nuclear spin recovery and slows down 31p relaxation–implications for translational and rotational jumps as seen by nuclear magnetic resonance. *The Journal of Physical Chemistry C*, 124(42):22934–22940, 2020. ISSN 1932-7447. doi: 10.1021/acs.jpcc.0c06090.

[57] Chuang Yu, Lambert van Eijck, Swapna Ganapathy, and Marnix Wagemaker. Synthesis, structure and electrochemical performance of the argyrodite li 6 ps 5 cl solid electrolyte for li-ion solid state batteries. *Electrochimica Acta*, 215:93–99, 2016. ISSN 0013-4686. doi: 10.1016/j.electacta.2016.08.081.

[58] Heng Wang, Chuang Yu, Swapna Ganapathy, Ernst R. H. van Eck, Lambert van Eijck, and Marnix Wagemaker. A lithium argyrodite li6ps5cl0.5br0.5 electrolyte with improved bulk and interfacial conductivity. *Journal of Power Sources*, 412:29–36, 2019. ISSN 0378-7753. doi: 10.1016/j.jpowsour.2018.11.029.

[59] Viktor Epp, Özgül Gün, Hans-Jörg Deiseroth, and Martin Wilkening. Highly mobile ions: Low-temperature nmr directly probes extremely fast li+ hopping in argyrodite-type li6ps5br. *The Journal of Physical Chemistry Letters*, 4(13):2118–2123, 2013. ISSN 1948-7185. doi: 10.1021/jz401003a.

[60] Chuang Yu, Swapna Ganapathy, Ernst R. H. van Eck, Lambert van Eijck, Shibabrata Basak, Yanyan Liu, Long Zhang, Henny W. Zandbergen, and Marnix Wagemaker.

Revealing the relation between the structure, li-ion conductivity and solid-state battery performance of the argyrodite li6ps5br solid electrolyte. *J. Mater. Chem. A*, 5 (40):21178–21188. ISSN 2050-7488. doi: 10.1039/c7ta05031c.

[61] Isabel Hanghofer, Bernhard Gadermaier, and H. Martin R. Wilkening. Fast rotational dynamics in argyrodite-type li6ps5x (x: Cl, br, i) as seen by 31p nuclear magnetic relaxation—on cation–anion coupled transport in thiophosphates. *Chemistry of Materials*, 31(12):4591–4597, 2019. ISSN 0897-4756. doi: 10.1021/acs.chemmater.9b01435.

[62] R. Bertermann and W. Müller-Warmuth. Universality of nmr results in lisicon systems and other solid lithium conductors. *Zeitschrift für Naturforschung A*, 53(10-11): 863–873, 1998. ISSN 1865-7109. doi: 10.1515/zna-1998-10-1110.

[63] Chuang Yu, Yong Li, Mathew Willans, Yang Zhao, Keegan R. Adair, Feipeng Zhao, Weihan Li, Sixu Deng, Jianwen Liang, Mohammad Norouzi Banis, Ruying Li, Huan Huang, Li Zhang, Rong Yang, Shigang Lu, Yining Huang, and Xueliang Sun. Superionic conductivity in lithium argyrodite solid-state electrolyte by controlled cl-doping. *Nano Energy*, 69:104396, 2020. ISSN 2211-2855. doi: 10.1016/j.nanoen.2019.104396.

[64] Chuang Yu, Swapna Ganapathy, Niek J. J. de Klerk, Irek Roslon, Ernst R. H. van Eck, Arno P. M. Kentgens, and Marnix Wagemaker. Unravelling li-ion transport from picoseconds to seconds: Bulk versus interfaces in an argyrodite li6ps5cl-li2s all-solid-state li-ion battery. *Journal of the American Chemical Society*, 138(35):11192–11201, 2016. ISSN 0002-7863. doi: 10.1021/jacs.6b05066.

[65] Barbara Koch, Shaio Tong Kong, Özgül Gün, Hans-Jörg Deiseroth, and Hellmut Eckert. Site preferences and ion dynamics in lithium chalcohalide solid solutions with argyrodite structure: I. a multinuclear solid state nmr study of the system li6ps5-xsexcl and li6ps5-xsexbr. *Zeitschrift für Physikalische Chemie*, 236(6-8):853–874, 2022. ISSN 0942-9352. doi: 10.1515/zpch-2021-3135.

[66] Malcolm H Levitt. *Spin dynamics: basics of nuclear magnetic resonance*. John Wiley & Sons, 2008.

[67] Z. Mollaei, F. Kermani, M. Kahani, F. Moosavi, S. Mollazadeh, and J. Vahdati Khaki. Configurational entropy as a simple input data for glass science and engineering. *Materials Today Communications*, 32:104153, 2022. ISSN 2352-4928. doi: 10.1016/j.mtcomm.2022.104153.

[68] Sharon E. Ashbrook. Recent advances in solid-state nmr spectroscopy of quadrupolar nuclei. *Physical Chemistry Chemical Physics*, 11(32):6892, 2009. ISSN 1463-9076. doi: 10.1039/b907183k.

[69] Jing Lin, Mareen Schaller, Sylvio Indris, Volodymyr Baran, Ajay Gautam, Jürgen Janek, Aleksandr Kondrakov, Torsten Brezesinski, and Florian Strauss. Tuning ion mobility in lithium argyrodite solid electrolytes via entropy engineering.

Angewandte Chemie International Edition, 63(30), 2024. ISSN 1433-7851. doi: 10.1002/anie.202404874.

[70] Jing Lin, Gennady Cherkashinin, Mareen Schäfer, Georgian Melinte, Sylvio Indris, Aleksandr Kondrakov, Jürgen Janek, Torsten Brezesinski, and Florian Strauss. A high-entropy multicationic substituted lithium argyrodite superionic solid electrolyte. *ACS Materials Letters*, 4(11):2187–2194, 2022. ISSN 2639-4979. doi: 10.1021/acsmaterialslett.2c00667.

[71] Sean P. Culver, Raimund Koerver, Thorben Krauskopf, and Wolfgang G. Zeier. Designing ionic conductors: The interplay between structural phenomena and interfaces in thiophosphate-based solid-state batteries. *Chemistry of Materials*, 30(13): 4179–4192, 2018. ISSN 0897-4756. doi: 10.1021/acs.chemmater.8b01293.

[72] R. Metselaar and G. Oversluizen. The meyer-neldel rule in semiconductors. *Journal of Solid State Chemistry*, 55(3):320–326, 1984. ISSN 0022-4596. doi: 10.1016/0022-4596(84)90284-6.

[73] Anshuman Dalvi, N. Parvathala Reddy, and S. C. Agarwal. The meyer–neldel rule and hopping conduction. *Solid State Communications*, 152(7):612–615, 2012. ISSN 0038-1098. doi: 10.1016/j.ssc.2012.01.018.

[74] Reginald Paul and Venkataraman Thangadurai. Understanding transport properties of conducting solids: Meyer-neldel rule revisited. *Ionics*, 27(11):4917–4925, 2021. ISSN 0947-7047. doi: 10.1007/s11581-021-04212-9.

[75] Alan G. Jones. Reconciling different equations for proton conduction using the meyer-neldel compensation rule. *Geochemistry, Geophysics, Geosystems*, 15(2):337–349, 2014. ISSN 1525-2027. doi: 10.1002/2013gc004911.

[76] Malcolm M. Haring. The theory of rate processes (glasstone, samuel; laidler, keith j.; eyring, henry). *Journal of Chemical Education*, 19(5):249, 1942. ISSN 0021-9584. doi: 10.1021/ed019p249.1.

[77] John B Goodenough. Review lecture-fast ionic conduction in solid. *Proceedings of the Royal Society of London. A. Mathematical and Physical Sciences*, 393(1805):215–234, 1984.

[78] W von Meyer and H Neldel. Relation between the energy constant and the quantity constant in the conductivity–temperature formula of oxide semiconductors. *Z. tech. Phys*, 18(12):588–593, 1937.

[79] A. Yelon, B. Movaghar, and H. M. Branz. Origin and consequences of the compensation (meyer-neldel) law. *Physical Review B*, 46(19):12244–12250, 1992. ISSN 0163-1829. doi: 10.1103/physrevb.46.12244.

[80] J. B. Boyce and B. A. Huberman. Superionic conductors: Transitions, structures, dynamics. *Physics Reports*, 51(4):189–265, 1979. ISSN 0370-1573. doi: 10.1016/0370-1573(79)90067-x.

[81] D. P. Almond, C. C. Hunter, and A. R. West. The extraction of ionic conductivities and hopping rates from a.c. conductivity data. *Journal of Materials Science*, 19(10): 3236–3248, 1984. ISSN 0022-2461. doi: 10.1007/bf00549810.

[82] Kai Volgmann, Viktor Epp, Julia Langer, Bernhard Stanje, Jessica Heine, Suliman Nakhal, Martin Lerch, Martin Wilkening, and Paul Heitjans. Solid-state nmr to study translational li ion dynamics in solids with low-dimensional diffusion pathways. *Zeitschrift für Physikalische Chemie*, 231(7-8):1215–1241, 2017. ISSN 2196-7156. doi: 10.1515/zpch-2017-0952.

[83] Marco Villa and John L. Bjorkstam. Prefactor anomalies. *Solid State Ionics*, 9-10: 1421–1426, 1983. ISSN 0167-2738. doi: 10.1016/0167-2738(83)90188-1.

[84] Stefan Breuer and Martin Wilkening. Mismatch in cation size causes rapid anion dynamics in solid electrolytes: the role of the arrhenius pre-factor. *Dalton Transactions*, 47(12):4105–4117, 2018. ISSN 1477-9226. doi: 10.1039/c7dt04487a.

[85] Davide Di Stefano, Anna Miglio, Koen Robeyns, Yaroslav Filinchuk, Marine Lechartier, Anatoliy Senyshyn, Hiroyuki Ishida, Stefan Spannenberger, Denise Prutsch, Sarah Lunghammer, Daniel Rettenwander, Martin Wilkening, Bernhard Roling, Yuki Kato, and Geoffroy Hautier. Superionic diffusion through frustrated energy landscape. *Chem*, 5(9):2450–2460, 2019. ISSN 2451-9294. doi: 10.1016/j.chempr.2019.07.001.

[86] M. J. Rice and W. L. Roth. Ionic transport in super ionic conductors: a theoretical model. *Journal of Solid State Chemistry*, 4(2):294–310, 1972. ISSN 0022-4596. doi: 10.1016/0022-4596(72)90121-1.

[87] D.P. Almond and A.R. West. The activation entropy for transport in ionic conductors. *Solid State Ionics*, 23(1-2):27–35, 1987. ISSN 0167-2738. doi: 10.1016/0167-2738(87)90078-6.

[88] A. S. Nowick, W.-K. Lee, and H. Jain. Survey and interpretation of pre-exponentials of conductivity. *Solid State Ionics*, 28-30:89–94, 1988. ISSN 0167-2738. doi: 10.1016/s0167-2738(88)80013-4.

[89] Simon Gelin, Alexandre Champagne-Ruel, and Normand Mousseau. Enthalpy-entropy compensation of atomic diffusion originates from softening of low frequency phonons. *Nature Communications*, 11(1), 2020. ISSN 2041-1723. doi: 10.1038/s41467-020-17812-2.

[90] O. Bohnke. The fast lithium-ion conducting oxides li3xla2/3–xtio3 from fundamentals to application. *Solid State Ionics*, 179(1-6):9–15, 2008. ISSN 0167-2738. doi: 10.1016/j.ssi.2007.12.022.

[91] O. Bohnke. Anomalies in li+ ion dynamics observed by impedance spectroscopy and 7li nmr in the perovskite fast ion conductor (li3xla2/3-x□1/3-2x)tio3. *Solid State Ionics*, 158(1-2):119–132, 2003. ISSN 0167-2738. doi: 10.1016/s0167-2738(02)00720-8.

[92] K. L. Ngai and C. León. Relating macroscopic electrical relaxation to microscopic movements of the ions in ionically conducting materials by theory and experiment. *Physical Review B*, 60(13):9396–9405, 1999. ISSN 0163-1829. doi: 10.1103/physrevb.60.9396.

[93] Martin Wilkening, Roger Amade, Wojciech Iwaniak, and Paul Heitjans. Ultraslow li diffusion in spinel-type structured li4ti5o12—a comparison of results from solid state nmr and impedance spectroscopy. *Phys. Chem. Chem. Phys.*, 9(10):1239–1246, 2007. ISSN 1463-9076. doi: 10.1039/b616269j.

[94] Anna Jodlbauer, Jonas Spychala, Katharina Hogrefe, Bernhard Gadermaier, and H. Martin R. Wilkening. Fast li ion dynamics in defect-rich nanocrystalline li4ps4i□the effect of disorder on activation energies and attempt frequencies. *Chemistry of Materials*, 36(3):1648–1664, 2024. ISSN 0897-4756. doi: 10.1021/acs.chemmater.3c02988.

[95] Ronghan Chen, Zhenming Xu, Yuechuan Lin, Buyao Lv, Shou-Hang Bo, and Hong Zhu. Influence of structural distortion and lattice dynamics on li-ion diffusion in li3ocl1−xbrx superionic conductors. *ACS Applied Energy Materials*, 4(3):2107–2114, 2021. ISSN 2574-0962. doi: 10.1021/acsaem.0c02519.

[96] Thorben Krauskopf, Sokseiha Muy, Sean P. Culver, Saneyuki Ohno, Olivier Delaire, Yang Shao-Horn, and Wolfgang G. Zeier. Comparing the descriptors for investigating the influence of lattice dynamics on ionic transport using the superionic conductor na3p4-xsex. *Journal of the American Chemical Society*, 140(43):14464–14473, 2018. ISSN 0002-7863. doi: 10.1021/jacs.8b09340.

[97] Tim Bernges, Sean P. Culver, Nicolò Minafra, Raimund Koerver, and Wolfgang G. Zeier. Competing structural influences in the li superionic conducting argyrodites li6ps5-xsexbr ($0 \le x \le 1$) upon se substitution. *Inorganic Chemistry*, 57(21):13920–13928, 2018. ISSN 0020-1669. doi: 10.1021/acs.inorgchem.8b02443.

[98] Sokseiha Muy, Roman Schlem, Yang Shao-Horn, and Wolfgang G. Zeier. Phonon–ion interactions: Designing ion mobility based on lattice dynamics. *Advanced Energy Materials*, 11(15), 2021. ISSN 1614-6832. doi: 10.1002/aenm.202002787.

[99] Jingxuan Ding. *Phonon anharmonicity and ionic diffusion in emergent energy materials*. PhD thesis, Duke University, 2022.

[100] Katharina Hogrefe, Isabel Hanghofer, and H. Martin R. Wilkening. With a little help from 31p nmr: The complete picture on localized and long-range li+ diffusion in li6ps5i. *The Journal of Physical Chemistry C*, 125(41):22457–22463, 2021. ISSN 1932-7447. doi: 10.1021/acs.jpcc.1c06242.

5

Probing Lithium Diffusion in $Li_{6-x}PS_{5-x}Br_{1+x}$ through ^{31}P and ^{7}Li Relaxometry

"I don't even know what a matrix is."

Erwin Schrödinger

5.1 Introduction

Argyrodite is a crystalline material with the $F\bar{4}3m$ space group (see Figure 5.1a). The backbone consist of PS_4^{3-}–tetrahedra with phosphorous on the $4b$- and sulphur on the $16e$ site (Figure 5.1b). The remaining S and the halogen are distributed over the $4a$ and $4d$–sites (Figure 5.1c). Early studies postulated that lithium occupies 50% of the T5–sites, forming a cage around the $4d$–site. Each cage vertex contains a pair of T5-sites, of which one is occupied on average. Three different types of jumps were defined based on this model (Figure 5.1e), namely doublet jumps between neighbouring T5-sites, intracage jumps between neighbouring cage vertexes and intercage jumps between T5-sites of neighbouring cages. Intercage jumps were shown to have the highest activation energy and therefore seen as the limiting step in long-range lithium diffusion.[1] Subsequent computational studies argue that non-T5 sites play a role in intercage movement as well. Neutron diffraction studies have found lithium at the T2- and T4-sites and have correlated increased occupancy of these sites with increased conductivity. [2]

In an ordered structure, sulphur occupies the $4d$–site and halogen sits at the $4a$–site. Site disorder occurs when this is no longer the case and is defined as the halogen $4d$–site occupancy. Studies have shown that increasing the $4d$–site disorder, either through changing the chemical composition or through altering of the synthesis procedure, can greatly improve conductivity for halogen argyrodites, including Br-argyrodites.[2, 3] The previous chapter investigated the energetics of lithium ion diffusion in the series $Li_{6-x}PS_{5-x}Br_{1+x}$ (x=0; 0.3; 0.5). Site-disorder was induced through increasing of the Br-content as well as changing the synthesis cooling method, allowing us to disentangle the effects of chemical composition and site-disorder. The energetics of lithium movement were studied using electrochemical impedance spectroscopy (EIS) and ^{7}Li spin-lattice relaxometry NMR (SLR NMR), allowing us to probe two different diffusion length-scales. Comparing the results showed that short-range and long-range movement seem to be correlated to different factors. Whereas long-range movement, probed with EIS, seems to rely on the chemical composition and $4d$–site disorder, short-range movement relies heavily on disorder within the entire anion sublattice (quantified by the configurational entropy) and the distortion of the lithium cage. Our study postulates that short-range movement depends on structural factors such as cage distortion. On the other hand, long-range movement is influenced by interactions between lithium ions and the soft phonon modes of the lattice, depending on both the anion sublattice as well as the chemical composition of the material.

Due to the presence of both dipolar and quadrupolar interactions, ^{7}Li relaxometry has focussed almost exclusively on the activation energy and asymmetry of system, neglecting a thorough investigation of the BPP pre-factor and the structural information it holds. Furthermore, ^{7}Li relaxometry in argyrodites is sensitive to both intra– and intercage movement and cannot distinguish between them (see Chapter 3). On the other hand, ^{31}P is a dipolar nucleus making it insensitive to quadrupolar interactions. It occupies the centre of the PS_4^{3-}–tetrahedra inside the argyrodite structure. These tetrahedra sit between Li-cages, making ^{31}P a potential probe for intercage movement (see Figure 5.1e). Previous work on ^{31}P spin-lattice relaxometry in argyrodites have explored this possibility by looking at ^{31}P T_1 and $T_{1\rho}$ relaxation times.[4–6] Activation energies from ^{31}P T_1 correlated with those obtained from ^{7}Li T_1, specifically for intercage movement, showing ^{31}P to be sensitive to this type of Li-movement.[4] Furthermore, activation energies obtained from

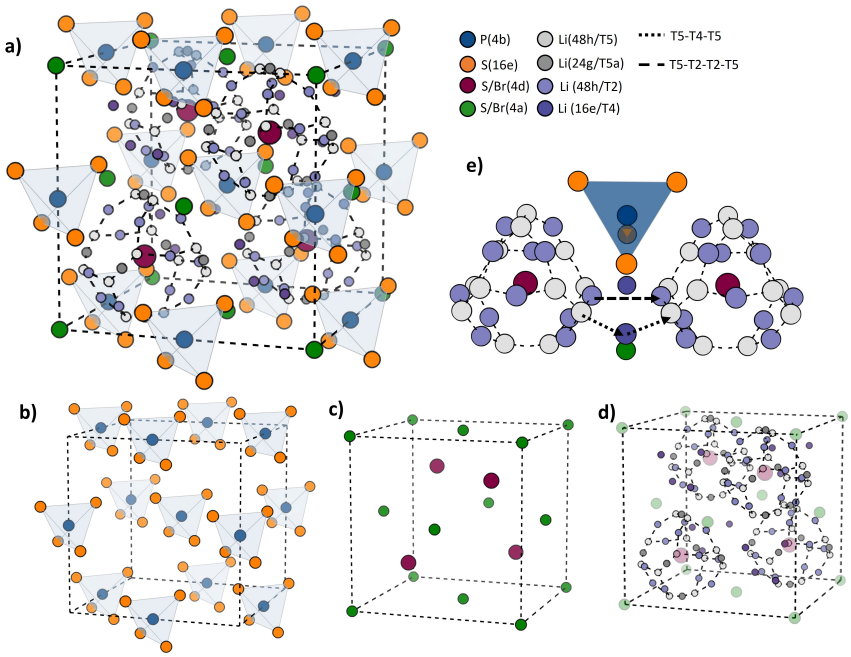

Figure 5.1: a) The structure of argyrodite, b) the position of the PS_4^{3-}–tetrahedra, c) the 4*a*– and 4*d*–sites and d) the Li-cages relative to the 4*a*– and 4*d*–sites.

^{31}P $T_{1\rho}$ were similar to that obtained for long-range Li-movement from EIS. However, this relationship was lost when the particle size was reduced.[7] Whereas these studies suggest that the source of ^{31}P relaxation is correlated with ^{7}Li movement, a homonuclear version of the BPP-model, which only takes ^{31}P–^{31}P interaction into account, was used to fit the data. Here we explore the use of a more suitable model to fit ^{31}P T_1 and $T_{1\rho}$ in the series $Li_{6-x}PS_{5-x}Br_{1+x}$, taking into account the source of relaxation, which affects both the formulas used as well as the results obtained. We look at the effect of altering the chemical composition as well as the cooling method. We explore the use of ^{31}P as a probe for movement of ^{7}Li in the system and fit the data using different models pertaining to different relaxation sources. By selecting the correct model, we are able to identify the source of relaxation and fit the activation energies more accurately. We can identify which sites play a large role in the diffusion of lithium and how their involvement and energetics changes with $4d$–site disorder and chemical composition. Furthermore, by measuring at the spin-lock frequency, we are able to identify the bottlenecks for lithium diffusion as well probe interactions beyond the limit of computational methods.

5

5.2 Materials and Methods

Synthesis of $Li_{6-x}PS_{5-x}Br_{1+x}$ system was carried out through mechanochemical milling using a Fritsch Pulverisette 7 premium line instrument. The initial precursors, lithium sulphide Li_2S (99.98%), phosphorus pentasulfide P_2S_5 (99%) and lithium bromide LiBr (99.99%) were purchased from Merck and Sigma Aldrich and manually ground before ball milling. The milling process involved cycles of 10 minutes of running followed by 10 minutes of rest over a 25 hour period (10 mm ZrO_2 media and 510 rpm). The resulting powder was then pressed into a 1.2 cm diameter pellet and placed in a quartz ampoule. The ampoule was pre-treated at 80 ˚ C for 12 hours under a dynamic vacuum to remove moisture. Ampoules were sealed under vacuum and placed in a furnace for annealing. The temperature was increased at a rate of 100 ˚C/h, until 550 ˚C for x = 0.0 and 430 ˚C for x = 0.3 and 0.5. Two cooling method were used: rapid quenching in liquid nitrogen and slow cooling at a rate of 5 ˚C/h over a 4-day period. The obtained powder was stored in an argon-filled glove box for further characterization. The samples are referred to according to their Br-content (1, 1.3 and 1.5 for x=0, 0.3 and 0.5 respectively in $Li_{6-x}PS_{5-x}Br_{1+x}$) and cooling method (SC for slow-cooling and QC for quenched). Nuclear magnetic resonance measurements were performed on a Bruker UltraShield 300 with an Avance console. Variable temperature experiments were conducted using a 5 mm two channel high temperature gonio probe from NMR Service GmbH. Custom 5mm outer diameter PEEK tubes were dried under dynamic vacuum overnight and filled and closed in an argon-filled glovebox to avoid degradation. The Larmor frequencies were 121.495 MHz and 116.642 MHz for ^{31}P and ^{7}Li, respectively. Longitudinal relaxation in the laboratory frame (T_1) measurements were performed using a saturation-recovery sequence. Spin-lock $T_{1\rho}$ measurements were performed at 10 kHz for ^{31}P and 10 kHz and 20 kHz for ^{7}Li. A recycle delay of 5* T_1 was used in all cases. Analysis of the spin-lattice relaxation (SLR) data was done using Bruker TopSpin, sSnake [8] and custom python scripts.

5.3 Results and discussion

5.3.1 An Overview

Three compositions were investigated in the $Li_{6-x}PS_{5-x}Br_{1+x}$ system, namely x=0, 0.3 and 0.5. For each composition, two cooling methods (slow-cooling and quench-cooling) were explored, resulting in six samples. For each sample, the abbreviation Brx CM is used with x being the Br-content and CM being the cooling method, either slow-cooling (SC) or quench-cooling (QC). Both increase in bromine content and the use of quench-cooling increase $4d$–site disorder and facilitate the intercage movement of lithium. Chapters 2 and 3 explore the effects of increased $4d$–site disorder on the overall structure and the lithium diffusion mechanism using diffraction, ^{7}Li T_1 NMR and EIS. In short, we find that increase in $4d$–site disorder results in an expansion and distortion of the lithium cage, reducing the intercage distance and flattening the energy landscape and facilitating lithium movement. Solid state NMR spin lattice relaxation is used to probe ^{31}P and ^{7}Li dynamics by measuring longitudinal relaxation in the laboratory frame (T_1) and the rotating frame ($T_{1\rho}$). An overview of the obtained results is given in Figure 5.2, showing the T_1's and $T_{1\rho}$'s at a spin-lock frequency of 10 kHz for both ^{7}Li and ^{31}P. For ^{7}Li, T_1's show one peak with a shifting maximum position, discussed thoroughly in the previous chapter. The ^{7}Li $T_{1\rho}$ data was fit using three components at low temperatures and two components at high temperatures (see Section C.1 of the Appendix for more details). For the Br1 SC-sample, only two components were present at low temperature, whereas the Br1.5 QC sample could be fit with three components throughout the temperature range. The ^{7}Li $T_{1\rho}$ data show one side of a low-temperature peak, followed by a plateau for all components. The ^{31}P T_1 data show two distinct peaks that merge with increasing Br-content and $4d$–site occupancy for the slow-cooled samples . For the quench-cooled samples, the peaks are all partially merged. The ^{31}P $T_{1\rho}$ data also display two peaks. However, these peaks do not merge. Instead, the high-temperature peak increases in height with increasing Br-content. The degree to which this occurs differs per cooling method. Interestingly, at low temperature the third component of the ^{7}Li $T_{1\rho}$ data coincides significantly with the ^{31}P $T_{1\rho}$ data. At high temperatures, the plateau in the ^{7}Li $T_{1\rho}$ seems to coincide with the ^{31}P $T_{1\rho}$ data as well, although this is less straightforward. Similar to the previous chapter, the interpretation of these results will be based on the BPP-model, named after Bloembergen, Purcell and Pound .[9]

5.3.2 The BPP-model

All nuclei in a material experience a magnetic field whose magnitude depends on the nature of the nucleus and the surrounding environment. Movement of the nucleus or its surrounding results in fluctuations in this field. The BPP–model involves the autocorrelation of the fluctuations in the magnetic field experienced by the nuclei under study ($G(t)$). Diffusion causes the autocorrelation function to decay. In the BPP-model, $G(t)$ is assumed to exhibit an exponential decay with a characteristic correlation time τ_c.

$$G(t) = G(0)e^{-\frac{|t|}{\tau_c}} \tag{5.1}$$

The original model dealt with fluctuations in the homonuclear dipolar interactions

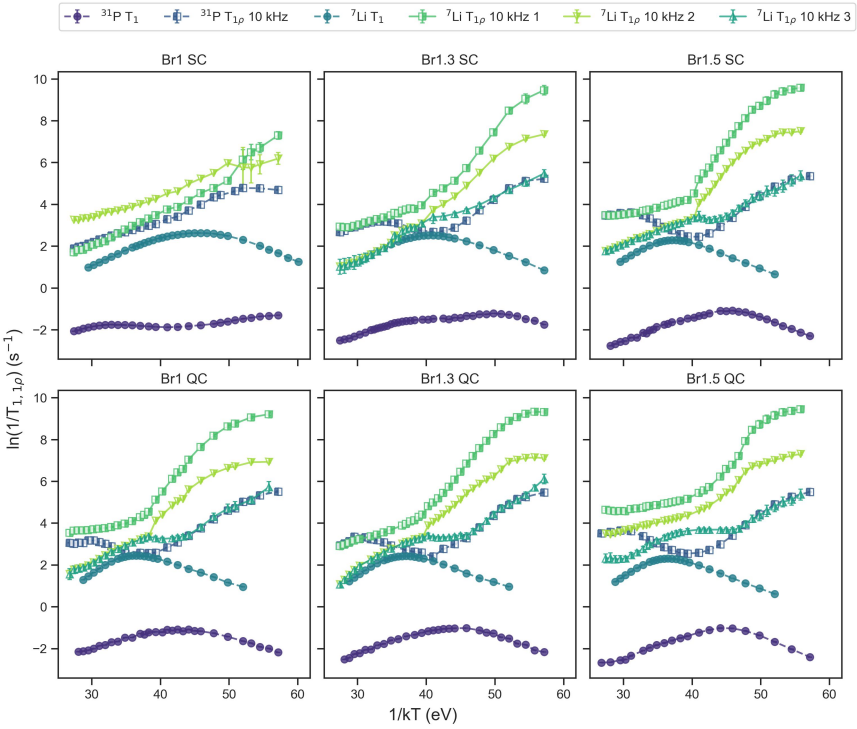

Figure 5.2: An overview of the ^{7}Li and ^{31}P longitudinal (T_1) and 10 kHz spin-lock ($T_{1\rho}$) relaxation times as a function of temperature for the six samples mentioned in the text.

due to isotropic, 3-dimensional molecular tumbling. The correlation time is a measure of the molecular motion and is assumed to follow an Arrhenius equation, with E_a being the activation energy of movement.

$$\tau_c = \tau_0 e^{\frac{E_a}{kT}} \tag{5.2}$$

Since then, the BPP-model has been adapted to describe hopping motion in a variety of solids, including lithium ion conductors.[10–12] Here, τ_c approximates the residence time of an ion i.e. the inverse of the hopping frequency.

Fluctuations of the surrounding magnetic field at the Larmor frequency result in relaxation, the extent of which relies on the spectral density function. The BPP-formula for homonuclear dipolar interactions is the same for both tumbling and ionic hopping [13]:

$$\frac{1}{T_1^{II}} = \frac{2}{5}\left(\frac{\mu_0}{4\pi}\right)^2 \frac{\hbar^2 \gamma_I^4}{r_{II}^6} I(I+1)[J(\omega_I) + 4J(2\omega_I)] \tag{5.3}$$

Here, γ_I is the gyromagnetic ratio of the nucleus, I is its spin number, ω_I its Larmor frequency in rad/s and r_{II} is the distance between nuclei. The spectral density function at frequency ω, $J(\omega)$ is defined as [9]:

$$J(\omega) = \frac{\tau_c}{1 + (\omega\tau_c)^\beta} \tag{5.4}$$

The BPP-model therefore gives a relationship between the energetics of ion movement and the relaxation rate.

For the isotropic tumbling described in the original BPP-model, the curve resulting from 5.3 is symmetrical as a function of temperature. However, for Li-ion conductors an asymmetry is often observed, with a steeper high-temperature flank.[14] This is taken into account with the β-factor **??** with $\beta = 2$ resulting in a symmetric curve and $\beta < 2$ giving a steeper high-temperature flank. The resulting model is termed the modified BPP-model and is ubiquitous in the analysis of ^{7}Li NMR relaxation data in lithium-ion conductors.[14]

Mathematically, the β-factor is a manifestation of 5.1 being a stretched exponential decay instead of simple exponential.

$$G(t) = G(0)e^{\left(\frac{-|t|}{\tau_c}\right)^\beta} \tag{5.5}$$

Physically, this is ascribed to a distribution of correlation times (τ_c) or activation energies [15, 16] and has been attributed to the presence of a vacancy diffusion mechanism, Coulombic interactions or structural disorder.[11] In lithium argyrodites, it is thought to be due to the different jump barriers for intra-cage and intercage jumps, which dominate different temperature regimes.[15, 17] For isotropic diffusion with only one activation energy, β is equal to 2. For argyrodites, when both intra- and intercage jumps are present, a β-value between 1.5 and 2 is often observed.

Homonuclear dipolar interactions are not the only source of magnetic field fluctuations. Since the seminal work by Bloembergen, Purcell and Pound, relationships between the T_1 and $T_{1\rho}$ relaxation times and the power spectral density have been developed for other sources of relaxation.

5.3.3 Sources of Relaxation

Relaxation occurs through fluctuations at the Larmor frequency in the magnetic field experienced by nuclei (for more details, see Chapter 2). Possible sources of fluctuations are (Figure 5.3):

- Homonuclear dipolar coupling
- Quadrupolar coupling
- Heteronuclear dipolar coupling
- Chemical shift anisotropy
- Cross-correlation
- Spin-rotation relaxation

Spin-rotation relaxation was found to be an unlikely source (see section C.2 of the Appendix) and is therefore not discussed further.

Homonuclear Dipolar Coupling

Homonuclear dipolar coupling occurs due to fluctuations in the relative spatial arrangement of like-spins (Figure 5.3a). The formula for T_1 relaxation is given by 5.3.

The $T_{1\rho}$ formula for homonuclear dipolar interactions is given in 5.6. Here ω_1 is the spin-lock frequency and the other variables are the same as 5.3. [18]

$$\frac{1}{T_{1\rho}^{II}} = \frac{2}{10}\left(\frac{\mu_0}{4\pi}\right)^2 \frac{\gamma_I^4 \hbar^2}{r_{II}^6} I(I+1)[3J(2\omega_1) + 5J(\omega_I) + 2J(2\omega_I)] \tag{5.6}$$

Quadrupolar interactions

The ^{7}Li-nuclei is both abundant and quadrupolar, meaning that its T_1 and $T_{1\rho}$ relaxation will be dominated by homonuclear dipolar interactions and quadrupolar interactions. The formulas for pure quadrupolar-induced relaxation are [19]:

$$\frac{1}{T_1} = \frac{3\pi^2}{100}\left(\frac{2I+3}{I^2(2I-1)}\right) C_Q^2 (1 + \frac{\eta^2}{3})(4J(2\omega_I) + J(\omega_I)) \tag{5.7}$$

$$\frac{1}{T_{1\rho}} = \frac{3\pi^2}{200}\left(\frac{2I+3}{I^2(2I-1)}\right) C_Q^2 (1 + \frac{\eta^2}{3})(2J(2\omega_I) + 5J(\omega_I) + 3J(2\omega_1)) \tag{5.8}$$

Here I is the spin number, C_Q is the quadrupolar coupling constant, η the asymmetry constant and ω_I and ω_1 the Larmor frequency and spin-lock frequency respectively.

Both Equation 5.3 and Equation 5.7 show the same dependence on the power spectral density and can be simplified to Equation 5.9 with the pre-factor C depending on the relative strength of the dipolar and quadrupolar interaction. [20] The same is true for $T_{1\rho}$ (Equations 5.6 and 5.8), giving Equation 5.10. The Equation 5.9 is used extensively to fit ^{7}Li SLR data and was used to fit the ^{7}Li T_1 data discussed in the previous chapter.

$$\frac{1}{T_1} = C[J(\omega_I) + 4J(2\omega_I)] \tag{5.9}$$

$$\frac{1}{T_{1\rho}} = Q\left[2J(2\omega_I) + 5J(\omega_I) + 3J(2\omega_1)\right] \tag{5.10}$$

The pre-factors in Equations 5.3, 5.6, 5.7 and 5.8 contain structural information. However, due to ^{7}Li being sensitive to both dipolar and quadrupolar interactions, extracting this information is difficult. The use of a purely dipolar nuclei would alleviate this problem.

The NMR active isotope of phosphorus, ^{31}P, is a 1/2-spin nuclei, making it insensitive to quadrupolar interactions. Furthermore, in the lithium argyrodite structure (Figure 5.1) it is relatively immobile and distant from other phosphorous nuclei, resulting in weak homonuclear interactions. Other sources of relaxation can dominate ^{31}P relaxation, making it a useful probe.

Heteronuclear Dipolar Coupling

Heteronuclear dipolar relaxation is caused by fluctuations in the spatial arrangement with respect to unlike spins (Figure 5.3b).

The general formula for the T_1 relaxation time of spin I due to heteronuclear dipolar interactions is [13]:

$$\frac{1}{T_1^{IS}} = \frac{2}{15}\left(\frac{\mu_0}{4\pi}\right)^2 \frac{\hbar^2\gamma_I^2\gamma_S^2}{r_{IS}^6} S(S+1)\left[J(\omega_I - \omega_S) + 3J(\omega_I) + 6J(\omega_I + \omega_S)\right] \tag{5.11}$$

Likewise, for $T_{1\rho}$ one obtains [18]:

$$\frac{1}{T_{1\rho}^{IS}} = \frac{1}{15}\left(\frac{\mu_0}{4\pi}\right)^2 \frac{\hbar^2\gamma_I^2\gamma_S^2}{r_{IS}^6} S(S+1)\left[J(\omega_I - \omega_S) + 3J(\omega_I) + 6J(2\omega_I + \omega_S) + 6J(\omega_S) + 2J(\omega_1)\right] \tag{5.12}$$

Here, I and S are the spin numbers of the observed and non-observed nuclei, ω_I and ω_S are the Larmor frequencies, ω_1 is the spin-lock frequency, and r_{IS} the distance between spins I and S. J is the spectral density function, which is taken to be the same as the one used for homonuclear interaction (Equation 5.4).[18] All frequencies are in angular units.

The possible heteronuclear interactions in this system are ^{31}P–^{7}Li, ^{31}P–^{33}S, ^{31}P–^{79}Br and ^{31}P–^{81}Br for ^{31}P relaxometry. Lithium is abundant and mobile within the structure, making ^{31}P–^{7}Li interactions the most likely source of ^{31}P-relaxation and ^{7}Li–^{7}Li homonuclear interactions the most likely source of ^{7}Li–relaxation. Further on, we shall see that ^{7}Li–^{31}P interactions are also possible.

The use of a stretched exponential and the resulting β-factor are commonplace in the analysis of homonuclear interactions, especially for ^{7}Li.[11] In power spectral densities describing heteronuclear interactions, they have, to our knowledge, never been used before. In the classical heteronuclear model, just as in the homonuclear model, an exponential decay of the autocorrelation function is assumed. The stretched exponential at the root of the β-factor takes into account a distribution of correlation times or activation energies.[15, 16] For ^{31}P–^{7}Li interactions, it is possible that the distribution of correlation times is also "felt" by ^{31}P, justifying the use of a stretched exponential in heteronuclear ^{31}P–^{7}Li interactions. Furthermore, using $\beta = 2$ results in a bad fit for ^{31}P–^{7}Li (see Section C.3 of the Appendix). Therefore, a β-factor is used when fitting ^{31}P–^{7}Li heteronuclear interactions.

The NMR active isotope of sulphur, ^{33}S, has a natural abundance of 0.75% and a relatively low gyromagnetic ratio of 2.055×10^7 rad/sT, making it an unlikely source of ^{31}P relaxation. Whereas the formulas presented here for T_1 do not take natural isotope abundance into account, the Bloch equations, which describe relaxation as a function of time, do.[21] The contribution of the heteronuclear dipolar relaxation mechanism will be proportional to the concentration of the unlike spin, which depends on the natural abundance. Hence, compared to other sources of relaxation, the contribution of ^{33}S is expected to be insignificant.

Bromine sits at the $4d$–sites within the lithium T5–cage and at the $4a$—sites between cages. Whereas bromine is not known to diffuse within the timescales explored, it could be influenced by nearby lithium movement. Bromine has two NMR active isotopes, namely ^{79}Br and ^{81}Br, with natural abundances of 50.6% and 49.4% and gyromagnetic ratios of 6.72×10^7 and 7.22×10^7 rad/sT, respectively. This would mean that each isotope should be fit independently, resulting in two sets of equations and complicating the fitting procedure. In section C.4 of the Appendix, we see that taking a weighted average of the two gyromagnetic ratios produces a similar result as fitting the two isotopes independently. This approach is therefore used.

Chemical Shift Anisotropy

Besides dipolar interactions, fluctuations in the chemical shift anisotropy can also result in relaxation (Fig. 3c). The chemical shift anisotropy (CSA) arises from an asymmetry in the electron density surrounding the nucleus (see 2). In our system, distortion of the PS_4^{3-}–tetrahedra could result in CSA. Movement of these tetrahedra, such as full or partial rotation, could result in fluctuations in the CSA and hence relaxation.

The formula for T_1 relaxation due to CSA interactions is [21]:

$$\frac{1}{T_1^{\mathrm{CSA}}} = \frac{2}{15}\,\omega_I^2\,\Delta\sigma^2\,J(\omega_I) \tag{5.13}$$

Here, the chemical shift anisotropy $\Delta\sigma$ is defined as

$$\Delta\sigma = \sigma_{zz} - \frac{1}{3}\left(\sigma_{xx} + \sigma_{yy} + \sigma_{zz}\right), \tag{5.14}$$

with σ_{zz}, σ_{xx}, and σ_{yy} being the principal components of the chemical shift tensor according to the Haeberlen–Mehring–Spiess convention [22–24]. The quantity ω_I is the Larmor frequency in angular units.

For $T_{1\rho}$, the corresponding expression is

$$\frac{1}{T_{1\rho}^{\mathrm{CSA}}} = \frac{1}{45}\,\omega_I^2\,\Delta\sigma^2\left[3J(\omega_I) + 4J(\omega_1)\right]. \tag{5.15}$$

Cross-correlation

Nuclei can experience fluctuations from several mechanisms simultaneously. Cross-correlation occurs when these mechanisms share a common source, causing a temporal correlation between the resulting fluctuations. In molecules, two nuclei can experience this cross-correlation differently depending on their relative positions (see Figure 5.3e) [21]. Cross-correlation effects result from heterogeneity in the relative spatial arrangement of the

vectors describing the interfering relaxation mechanisms. Simply put, cross-correlation arises when the correlating mechanisms affect nuclei of the same spin in different ways.

Studies of cross-correlation and its theoretical framework focus almost exclusively on (rigid) molecular systems, which display well-defined heterogeneity [25]. Our system is polycrystalline, with phosphorus occupying only a single crystallographic site in a cubic lattice. The most likely source of cross-correlation would be ^{7}Li motion causing fluctuations in the position of Br, or (partial) rotation of the PS_4^{3-}–group [26]. Due to the cubic arrangement of the lattice, ^{7}Li motion is isotropic relative to phosphorus, i.e. it is identical in all three spatial dimensions (see Fig. 3f).

We therefore expect no cross-correlation effects of the type described in the existing literature. The development of a new theoretical framework lies beyond the scope of this work. Owing to the isotropic nature of the system, we assume a simple additive contribution of relaxation mechanisms in the presence of any cross-correlation.

5.3.4 Approach

Four sources of ^{31}P relaxation are investigated in this study (see Fig. 3), namely:

- Chemical shift anisotropy (CSA),
- ^{31}P–^{31}P homonuclear dipolar interactions,
- ^{31}P–^{7}Li heteronuclear dipolar interactions,
- ^{31}P–Br heteronuclear dipolar interactions.

For ^{7}Li, the following sources of relaxation are explored:

- ^{7}Li–^{7}Li homonuclear dipolar/quadrupolar interactions,
- ^{7}Li–^{31}P heteronuclear dipolar interactions.

For ^{31}P, the expected temperature dependence of T_1 and $T_{1\rho}$ for each relaxation mechanism is shown in Fig. 3d and e. For homonuclear interactions, a single relaxation peak is obtained, with the degree of asymmetry depending on the β factor. The same behavior is observed for CSA-based relaxation. In contrast, heteronuclear interactions exhibit a more complex temperature dependence. This is due the three spectral density contributions at different frequencies, namely ω_I, ω_S, and $2\omega_I + \omega_S$, resulting in a superposition of the corresponding relaxation curves.

This effect is more prominent for ^{31}P–^{7}Li interactions due to the larger Larmor frequency of ^{7}Li (~ 116 MHz) compared to that of $^{79/81}$Br (~ 75–81 MHz), causing a clearer split between the first two contributions and the third. Each interaction has a different dependence on the power spectral densities as well as a different pre-factor. Pre-factors can be obtained experimentally or calculated from additional information. By comparing the magnitude of the pre-factor obtained from fitting the relaxation data to those calculated, we can assess the likelihood of an interaction being the source of relaxation. The pre-factors are defined in Table 5.1. For more details on the calculation of the homonuclear and heteronuclear dipolar interaction pre-factors, see Section C.5 of the Appendix.

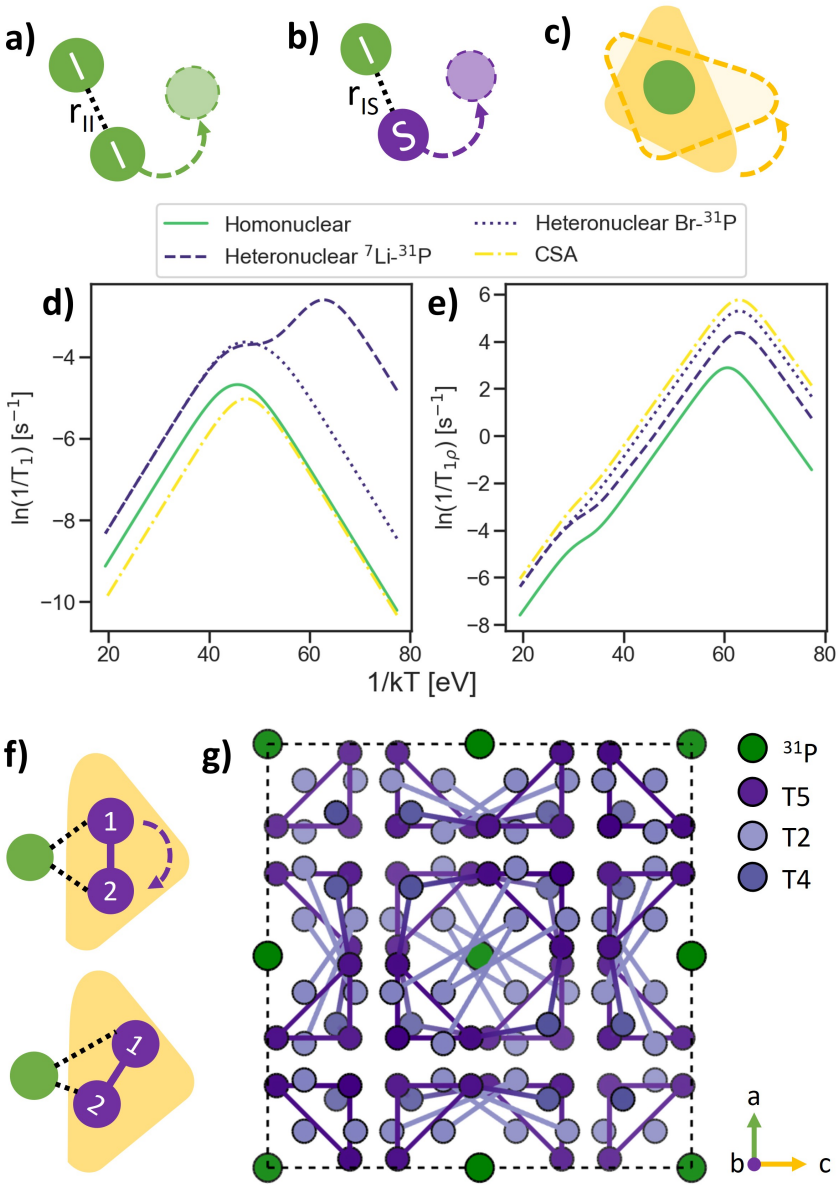

Figure 5.3: Illustrating a) homonuclear dipolar interaction between two like spins, which depends on r_{II}, the distance between spins, b) heteronuclear dipolar interaction between two unlike spins which depends on r_{IS}, the distance between spins, c) chemical shift anisotropy (CSA) fluctuations and the resulting d) T_1 and e) $T_{1\rho}$ curves for the various interactions, f)The concept of cross-correlation or a rigid atom in purple between heteronuclear dipolar interaction with the green atom and chemical shift anisotropy in yellow. As the molecule rotates, both interactions will fluctuate, hence they are cross-correlated. The interaction will be different for atoms 1 and 2 and g) the lithium movement within the cubic argyrodite structure is symmetric with regards to the ^{31}P atom.

Table 5.1: Overview of the relaxation interactions explored in this work and their corresponding pre-factors.

Interaction	T_1 pre-factor	$T_{1\rho}$ pre-factor
Homonuclear dipolar	$\frac{2}{5}\left(\frac{\mu_0}{4\pi}\right)^2 \frac{\hbar^2\gamma_I^4}{r_{II}^6} I(I+1)$	$\frac{2}{10}\left(\frac{\mu_0}{4\pi}\right)^2 \frac{\hbar^2\gamma_I^4}{r_{II}^6} I(I+1)$
Heteronuclear dipolar	$\frac{2}{15}\left(\frac{\mu_0}{4\pi}\right)^2 \frac{\hbar^2\gamma_I^2\gamma_S^2}{r_{IS}^6} S(S+1)$	$\frac{1}{15}\left(\frac{\mu_0}{4\pi}\right)^2 \frac{\hbar^2\gamma_I^2\gamma_S^2}{r_{IS}^6} S(S+1)$
Chemical shift anisotropy	$\frac{2}{15}\omega_I^2\Delta\sigma^2$	$\frac{1}{45}\omega_I^2\Delta\sigma^2$

For ^{7}Li, similar shapes are obtained, however, its quadrupolar nature makes comparison of calculated and obtained pre-factors challenging.

The equations presented given contain multiple variables, each of which introduces uncertainty into the fitting procedure. To mitigate this, parameters obtained from fitting one dataset are used as input for subsequent fits. Accordingly, the fitting procedure begins with the ^{7}Li $T_{1\rho}$ data, followed by the ^{31}P $T_{1\rho}$ data, and finally the ^{31}P T_1 data. The rationale for this sequential approach will become apparent in the following sections.

5.3.5 Fitting ^{7}Li $T_{1\rho}$

Spin-lattice relaxation in the rotating frame allows us to investigate movement in a fashion similar to T_1. However, whereas T_1 measurements are sensitive to fluctuations in the range of the Larmor frequency, $T_{1\rho}$ measurements allow us to investigate fluctuations in the vicinity of a much lower, predetermined spin-lock frequency. This allows us to examine low-frequency jumps, associated with long-range diffusion. The ^{7}Li $T_{1\rho}$ data, acquired at spin lock frequencies of 10 kHz are given in Figure 5.4 together with the final fits.

To obtain $T_{1\rho}$'s at each temperature, data required fitting with three exponential decay components (Exp 1, Exp 2 and Exp 3) at low temperatures, except for Br1 SC which did not have a third component. At higher temperatures, the component with the longest relaxation time is beyond the measurement range and cannot be accurately determined without compromising probe integrity. The data was therefore fit with two components in this temperature range, except for Br1.5 QC, which displayed three distinct components throughout. (See section C.1 of the Appendix for more details on the ^{7}Li $T_{1\rho}$ fitting procedure). Taking Br1.5 QC as an example, three components can be distinguished at low temperatures (see Figure 5.5a), with the third component stretching beyond the measurement range with increasing temperature. Overall signal intensity also decreases with increasing temperature. NMR is sensitive towards transitions between nuclear spin states, with the intensity of the signal depending on the state population difference. This population difference follows a Boltzmann distribution and decreases with increasing temperature.

Being a spin-3/2 nucleus, ^{7}Li is sensitive to both dipolar and quadrupolar interactions, , making it hard to obtain structural information from the BPP pre-factor. Similar to ^{7}Li T_1, the high abundance of lithium in the system, combined with its mobility, makes homonuclear dipolar and quadrupolar interactions the most likely sources of relaxation. Relaxation driven by quadrupolar interactions is bi-exponential in time, $F_{1p}(t)$, with a 1 : 4 ratio

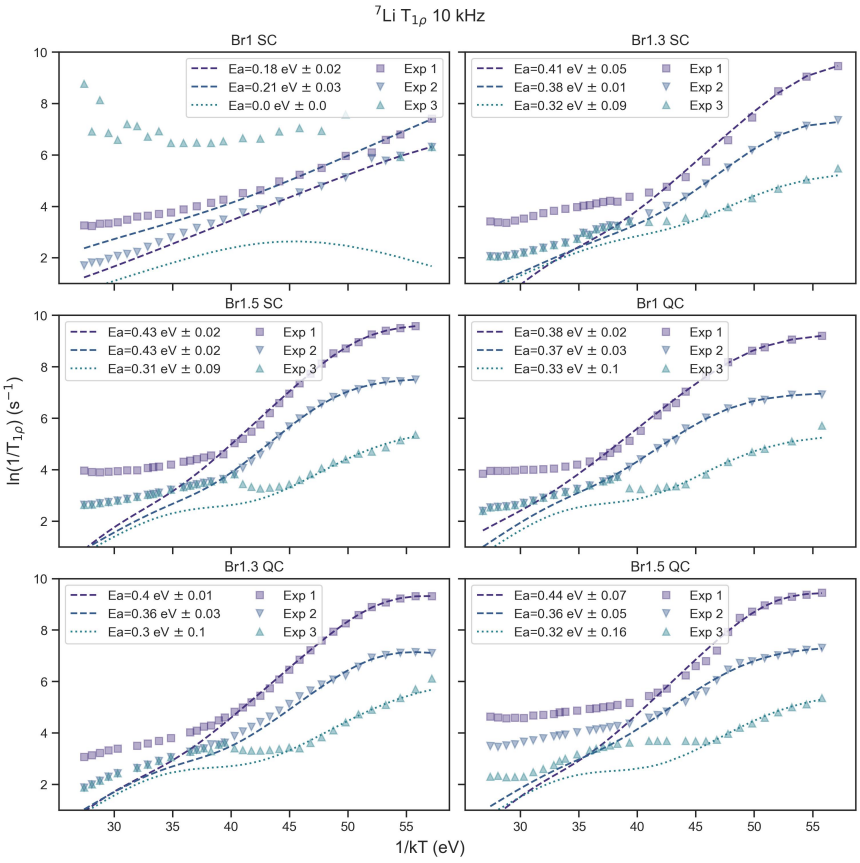

Figure 5.4: The ^{7}Li spin-lock relaxation times as a function of temperature for all six samples at a spin-lock frequency of 10 kHz. At low temperatures, data was fit using three exponential components. At higher temperatures, two components were used for all samples except Br1SC, where a third component was absent throughout.

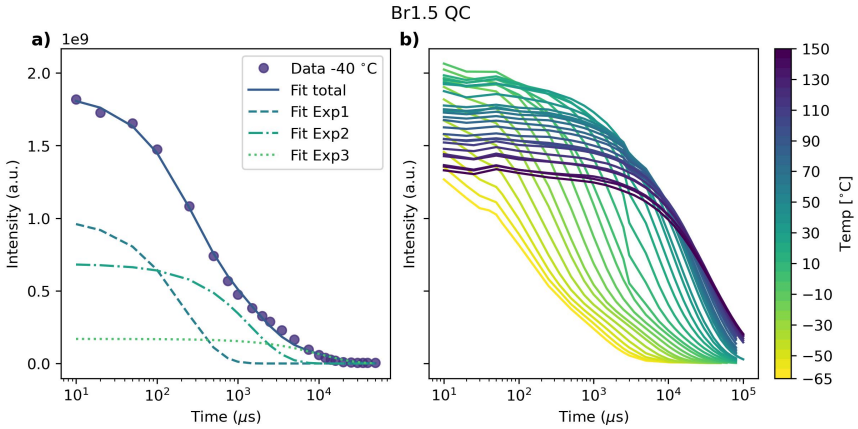

Figure 5.5: The ^{31}P $T_{1\rho}$ for Br1.3 QC as a function of delay time a) at -40 °C showing the three exponential decay components and b) for all temperatures measured.

between the two components for both T_1 and $T_{1\rho}$ [27].

For $T_{1\rho}$, the signal intensity following application of a spin-lock pulse in a single isotropic environment is given by:

$$F_{1p}(t) = \frac{4}{5}e^{-r_{3p}t} + \frac{1}{5}e^{-r_{4p}t}, \tag{5.16}$$

with

$$r_{3p} = \sigma^2\left[\frac{3}{4}J(2\omega_1) + J(\omega_I) + \frac{1}{4}J(2\omega_I)\right], \tag{5.17}$$

and

$$r_{4p} = \sigma^2\left[J(\omega_I) + J(2\omega_I)\right]. \tag{5.18}$$

Here, σ^2 is the mean square of the angular quadrupolar frequency.

These expressions are valid provided that the spin-lock frequency exceeds the linewidth, which is always the case for the systems studied here (see Section C.6 of the Appendix for the ^{7}Li linewidths). However, the ratio obtained by fitting the curves at low temperatures deviates from 1 : 4 value for all components (see Section C.1 of the Appendix). Furthermore, the smaller component is expected to be independent of the applied spin-lock frequency. However, comparison of measurements performed at 10 kHz and 20 kHz shows that this condition is also not fulfilled (see Section C.1 of the Appendix)).

These deviations could arise from anisotropic motion or the presence of multiple chemical environments. Another possibility is that different relaxation processes are being probed, which is considered more likely given the distinct activation energies obtained for the individual components.

As discussed above, asymmetry in the relaxation curves can be accounted for by introducing the β factor. Accurate determination of this parameter requires both sides of the relaxation peak to fall within the measured temperature range. As shown in Fig. 4, only the high-temperature slope lies within the range and plateaus near the low-temperature

limit. The $T_{1\rho}$ measurement is limited by T_1, which increases at low temperatures. Experimental constraints make low-temperature measurements for extended periods of time difficult, resulting in a limited temperature range and most likely causing the observed plateau.

Although the β factor was fitted to account for this behavior, it does not carry physical meaning in this context. While this introduces an additional source of uncertainty, it was not possible to obtain satisfactory fits with $\beta = 2$.

The first two components (Exp 1 and Exp 2) were fit using Equation 5.10 , which describes relaxation due to homonuclear dipolar- and quadrupolar interactions. The pre-factors obtained likely contain dipolar and quadrupolar contributions and cannot be used to extract structural information without additional information. The activation energies differ between the components and are similar to those obtained from EIS, for all samples except Br1 SC, implying that the data represents long-range movement and might belong to different pathways (see Figure 5.13). From ^{7}Li T_1 studies, we know that intercage movement is limited for Br1SC and the activation energy obtained is similar to that belonging to intracage movement obtained from ^{7}Li T_1.

We observe that the third component overlaps significantly with the low-temperature ^{31}P $T_{1\rho}$ curve, implying a shared source for all samples except Br 1 SC (see Figure 5.2). As ^{31}P is a spin 1/2–nuclei and is only sensitive to dipolar interactions, ^{31}P–^{7}Li dipolar interactions are a likely source for the 3rd component. Component three ('Exp 3' in Figure 5.3) was fit using Equation 5.11 for heteronuclear dipolar interactions. The activation energies agree with those obtained for the low-temperature peak observed for ^{31}P $T_{1\rho}$ (vide infra). The pre-factor obtained also agrees with that of a ^{31}P–^{7}Li interaction, most likely T2–^{31}P. However, this cannot be said with certainty (see Section C.7 of the Appendix). To summarize long-range lithium movement is probed using ^{7}Li $T_{1\rho}$ at 10 kHz. The data obtained could be fit using three components. The appearance of three components is not due to splitting associated with quadrupolar nuclei, implying that components represent different pathways. All components have different activation energies, further supporting this conclusion. The Ea's of the 1st and 2nd component are similar to EIS suggesting long-range motion. The third component overlaps with ^{31}P $T_{1\rho}$, suggesting a mutual source. The activation energies are similar, supporting this conclusion. The high temperature plateau of component 3 also overlaps with the ^{31}P $T_{1\rho}$ data. However, due to technical limitation, this cannot be said with certainty.

5.3.6 Fitting ^{31}P $T_{1\rho}$

The ^{31}P $T_{1\rho}$'s at a spin-lock frequency of 10 kHz for each material are given in Figure 5.6 and show a low-temperature peak which remains relatively stationary as a function of temperature for each sample, with varying slope and high-temperature peak. For the slow-cooled samples, the high-temperature peak appears and shifts to higher temperatures with increasing Br-content, whereas for the quench-cooled samples it is always present and relatively stationary.

In contrast to ^{7}Li, ^{31}P is a spin-1/2 nucleus and therefore does not experience quadrupolar interactions. Consequently, the relevant pre-factors arise solely from dipolar and CSA interactions and can be used to extract structural information. By comparing the pre-factors obtained from fitting the experimental data with those calculated theoretically, we

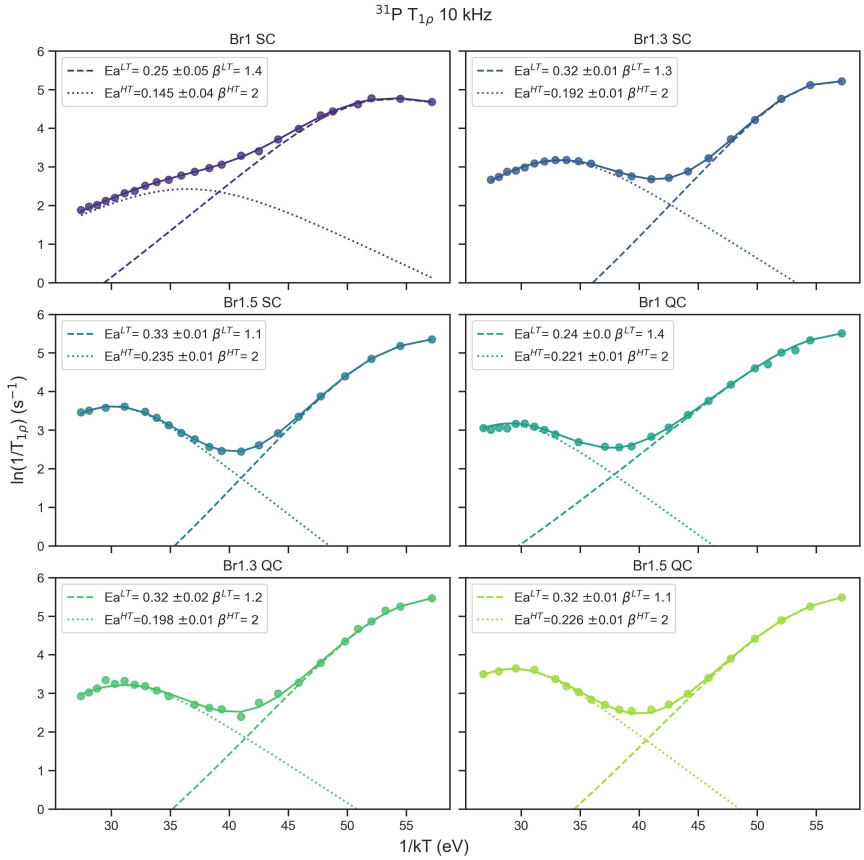

Figure 5.6: The ^{31}P $T_{1\rho}$-values obtained as a function of temperature at a spin-lock frequency of 10 kHz for each sample. The data was fit using two ^{31}P–^{7}Li interaction models as explained in the text.

can comment on the likelihood of each interaction as being the source of relaxation.

The relaxation mechanisms explored for ^{31}P are:

- ^{31}P–^{31}P homonuclear dipolar interactions,
- ^{31}P–^{7}Li heteronuclear dipolar interactions,
- ^{31}P–$^{79/81}Br$ heteronuclear dipolar interactions,
- Chemical shift anisotropy (CSA).

The question arises whether the model chosen for the high-temperature peak would affect the results obtained for the low-temperature peak and vice versa. Figure 5.3e shows the $T_{1\rho}$–curves for the respective equations when the same parameters for the pre-factor, activation energy, τ_0 and β are used. We see that for the model describing ^{31}P–^{7}Li dipolar interactions, a small secondary bump is observed on the high-temperature slope. The low-temperature slope is the same straight line for all models. This means that to fit the low-temperature peak, the choice for the high-temperature model does not have a large effect. Similar to ^{7}Li $T_{1\rho}$, only one side of the low-temperature peak lies within the measured temperature range, plateauing at the limit. The β-factor is used to account for this plateau and has no physical meaning. For the high-temperature peak, only Br1 SC and Br1.3 SC have both slopes within the measured temperature range. A β-value of 2 was found for both (see Figure 5.6). Therefore, for other samples, a β-value of 2 was used. Fitting the high-temperature β resulted in similar values but larger uncertainties for all relaxation models (see Section C.3 of the Appendix).

The Low–Temperature ^{31}P $T_{1\rho}$ Peak

We can comment on the likelihood of a relaxation source from the magnitude of the obtained pre-factor. Taking the high temperature peak as a ^{31}P–^{7}Li interaction, the pre-factors for the low-temperature peak are given in Figure 5.7. From Figures 5.7c and d, we can eliminate the ^{31}P–^{31}P homonuclear and ^{31}P–$^{79/81}Br$ heteronuclear dipolar interactions as the source of relaxation.

The CSA-values are compared to those obtained from fitting ^{31}P magic angle spinning (MAS) spectra in Figure 5.7a (see Section C.8 of the Appendix for the fits). Whereas this method of obtaining the CSA is not fully accurate, it does provide a rough estimate for the size of the CSA.[28, 29] The difference between the CSA-values obtained from fitting the left and right side-bands is attributed to asymmetry in the electronic response of the probe as we observe it for every sample, regardless of nucleus.[30] For this reason, the sidebands were fit separately on either side of the peak. The ^{31}P spectra contain 5 peaks, representing the different ways in which sulphur and bromine can be arranged around phosphorus. Hence the sidebands contain 5 peaks as well. The average CSA-value of the three central peaks was taken as these have the highest intensity. The values from the ^{31}P $T_{1\rho}$ fits are in the same order of magnitude as the ones from the MAS spectra, making CSA-induced relaxation a possible source for both peaks. The pre-factor obtained for the ^{31}P–^{7}Li interaction corresponds closely to the pre-factor calculated from the P-T2 distances obtained from diffraction (see Figure 5.7b). The T2-site sits between the T5-cage surrounding the $4d$–site and is associated with intercage lithium movement (see Figure 5.1).[3, 31] This

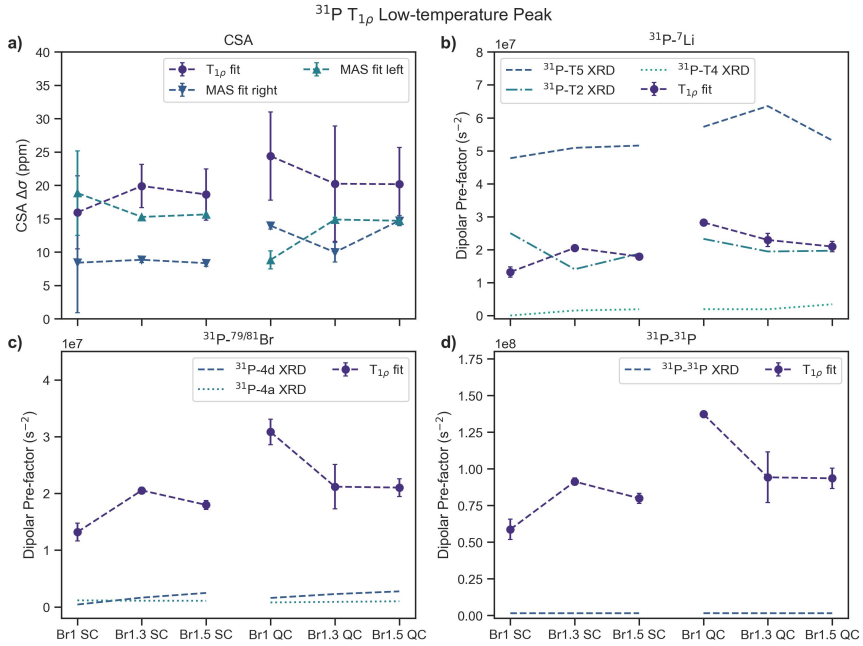

Figure 5.7: The pre-factors obtained from fitting the low-temperature peak using a) CSA interaction- (Equation 5.13), b) ^{31}P–^{7}Li interactions-, c) ^{31}P–Br interaction(Equation 5.11) and d) ^{31}P–^{31}P homonuclear interaction model (Equation 5.6). The high-temperature peak was fit simultaneously using a ^{31}P–^{7}Li interaction model.

would imply that the low temperature peak represents the intercage movement of lithium. An almost identical curve is seen in the ^{7}Li $T_{1\rho}$ data (vide ultra), hinting at a shared source of relaxation. The pre-factors obtained from ^{31}P and ^{7}Li $T_{1\rho}$ both correspond with a ^{31}P–T2 interaction (see Section C.7 of the Appendix). The additional evidence from ^{7}Li $T_{1\rho}$ makes ^{31}P–^{7}Li the most likely source of relaxation for the LT peak.

The High–Temperature ^{31}P $T_{1\rho}$ Peak

Having identified the LT peak as ^{31}P–^{7}Li, we can now fit the HT peak. Here, β was taken as 2, as this results in a smaller uncertainty (see Section C.3 of the Appendix). The pre-factors obtained are given in Figure 5.8. The values and their uncertainties fall beyond the uncertainty of the measured CSA-values, making it an unlikely source (see Figure 5.8a). Similarly, Figure 5.8d shows that homonuclear ^{31}P–^{31}P interactions are unlikely. However, both ^{31}P–^{7}Li and ^{31}P–$^{79/81}Br$ dipolar interactions are possible. Like the T2-site, the T4-site sits between two cages and is increasingly thought to play an important role in intercage movement. The calculated activation energy of the T5-T4-T5 pathway is lower than that of the T2-pathway (see the previous chapter) and neutron diffraction studies by Gautam *et al.* have observed increasing lithium occupancy of the T4-site wi th increasing site-disorder.[2, 3] However, the occupancy is low compared to that of the T2-site, implying that despite a lower activation energy, the T4-pathway is less populated (see previous chapter).[2] The calculated pre-factor follows the same trend as the fitted one, albeit possessing a lower magnitude (see Figure 5.8b), meaning there could be more to these observations. According to Figure 5.8c, ^{31}P–$^{79/81}Br$ interactions are also a likely relaxation source. Bromine can occupy two sites, the 4*d*–site which sits at the centre of the lithium T5-cage and the 4*a*–site which sits between cages. As lithium is the most mobile species in the system, fluctuations in the Br–^{31}P interaction are likely due to lithium movement in the vicinity. Adding the calculated ^{31}P–^{7}Li T4 pre-factor to those calculated for ^{31}P–$^{79/81}Br$ for the 4*a*–site (T4 + 4*a*) and ^{31}P–$^{79/81}Br$ for the 4*d*–site results in a surprising strong overlap in both magnitude and trend (see Figure 5.8c). This seems especially true for the^{31}P–^{31}P-$^{79/81}Br$ 4*a*+^{31}P–^{7}Li T4-curve. The implication follows that the high-temperature peak represents long-range lithium movement through the T4-site together in conjunction with fluctuations in the 4*a*–^{31}P distance. The appearance of this peak at higher temperatures implies that this movement is less common than movement through the T2-site, associated with the low-temperature peak, in agreement with the low lithium occupancy of the T4-site from neutron diffraction data. Theoretical studies have shown that intercage movement in sulphur-based lithium-ion conductors involves movement of bromine and sulphur as lithium passes and argue that these movements work together to improve lithium-diffusion.[32] It is cautiously speculated that this cation-coupled movement is rare in argyrodites as it requires constructive coupling of bromine 4*a*–movement and lithium T4-movement, hence possessing a larger entropic barrier. This would explain the low occurrence of this type of lithium pathway despite its lower activation energy. It must be noted that the low frequency of this cation-coupled interaction, in the realm of kHz, makes it challenging to observe with current MD-simulations, which probe movement occurring at the MHz-regime.[33]

The final fits are given in Figure 5.6 with two ^{31}P–^{7}Li dipolar interaction models and β_{HT}=2. For the high-temperature peak, we ascribe relaxation to both ^{31}P–^{7}Li and ^{31}P–

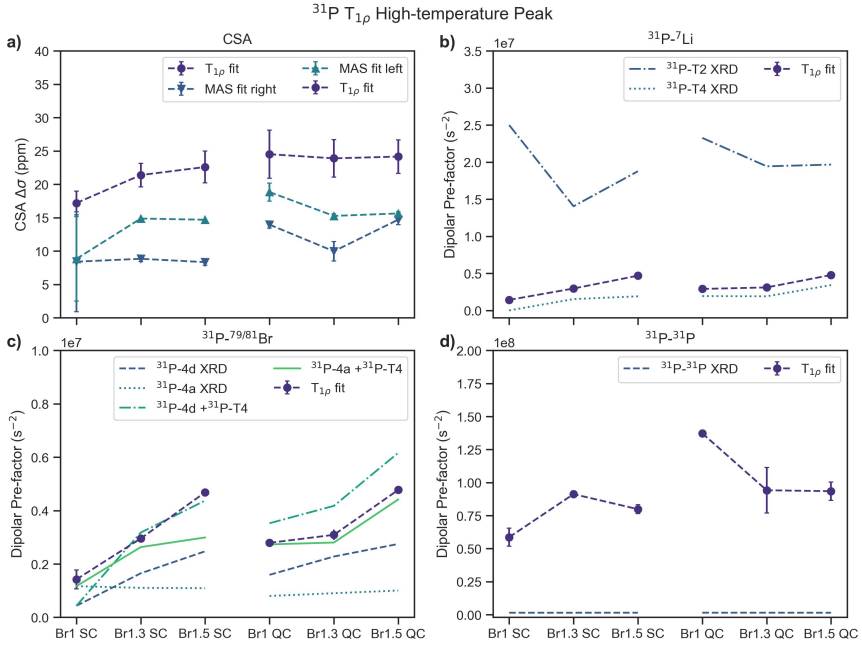

Figure 5.8: The pre-factors obtained from fitting the high-temperature peak using a) CSA interaction- (Equation 5.13), b) ^{31}P–^{7}Li interaction-, c) ^{31}P–Br interaction(Equation 5.11) and d) ^{31}P–^{31}P homonuclear interaction model (Equation 5.6). The low-temperature peak was fit simultaneously using a ^{31}P–^{7}Li interaction model and a β-value of 2 was used for all high-temperature fits.

$^{79/81}Br$ interactions. The equation describing heteronuclear interaction (Equation 5.13) uses the Larmor frequency of the measured nuclei (ω_I) and one interacting nuclei (ω_S). In this case, there would be three types of interacting nuclei, namely ^{7}Li, 79Br and 81Br. We find that fitting the data using the Larmor frequency of ^{7}Li as ω_S give almost identical values for pre-factor, activation energy and β_{LT} as using the Larmor frequency of ^{79}Br or ^{81}Br (see Section C.3 of the Appendix), hence we show the ^{31}P–^{7}Li fit as a representative in Figure 5.6.

The above analysis of the pre-factors shows that both peaks in Figure 5.6 represent intercage movement. The low-temperature peak corresponds to movement through the T2-site with activation energies around 0.3 eV for all samples except Br1 QC, close to the value obtained from EIS. The anomalous behaviour of Br1 QC could be due to its high configurational entropy, which results in much more efficient intercage movement. Interestingly, ^{7}Li T_1 data gives an activation energy close to EIS for Br1 QC, implying that the bottleneck in this material is not T2-mediated intercage movement but perhaps intracage movement or intercage movement through the T4–site.

The high-temperature peak appears to represent intercage movement through the T4–site, in tandem with interaction between lithium and bromine on the 4*a*–site. This type of behaviour has been predicted computationally for sulphur-based lithium conductors [32] and has been alluded to in the previous chapter as playing a role in long-range lithium ion conductivity. The activation energy obtained is much lower, around 0.2 eV, yet higher temperature at which the peak maximum appears, implies that this movement is significantly less common. Interestingly, the peak maximum shifts to higher temperatures with increasing 4*d*–site disorder and T4-site occupancy. It could be that at low 4*d*–site disorder, the T4–site only experiences back-and-forth T4-T5 jumps, whereas increasing site-disorder results in T5-T4-T5 jumps, connecting lithium cages. Hence, the peak maximum shift to higher temperatures indicates an increase in long-range intercage movement. Another explanation might involve the 4*a*–site occupancy. Bromine site occupancy increases for both 4*d*– and 4*a*–sites in a similar fashion. It is possible that the increasing 4*a*–site occupancy of the harder, less electronegative bromine as opposed to the softer, more electronegative sulphur affects movement through the T4-site.

5.3.7 Fitting ^{31}P T_1

The longitudinal relaxation rates (T_1) for ^{31}P are given in Figure 5.9. Like the $T_{1\rho}$ data, two peaks can be observed, one at low temperature (LT) and one at high temperature (HT). For the slow-cooled samples, an increase in site-disorder/Br-content results in both peaks moving towards intermediate temperatures and finally merging. For the quench-cooled samples, the peaks have already merged for Br1 QC but appear to become less broad and more defined with increasing site-disorder/Br-content. Previous studies into ^{31}P T_1 NMR in argyrodites Li_6PS_5X show two peaks that move closer together for as X goes from I to Br and Cl, correlating with increased 4*d*–site disorder.[4] The low-temperature peak was assigned to PS_4^{3-} rotational dynamics and the high temperature peak was ascribed to ^{31}P–^{7}Li interactions. It is postulated that as X moves from I to Br and to Cl, lattice parameters decrease, slowing down PS_4^{3-}–rotation and moving the PS_4^{3-}–rotational peak to higher temperatures. Conversely, lithium movement is facilitated and the ^{31}P–^{7}Li peak moves to lower temperature, resulting in the peaks moving closer together and finally

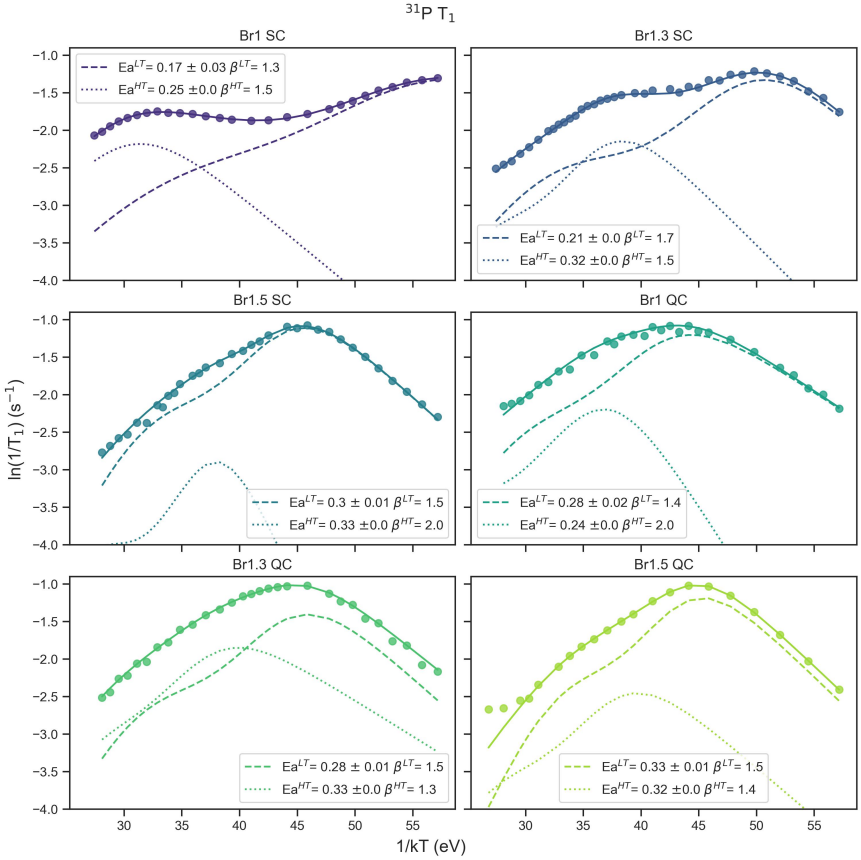

Figure 5.9: The ^{31}P T_1 relaxation times as a function of temperature for each sample with the final fit (solid line) discussed in the text composed of a low-temperature (LT, dashed line) and high-temperature (HT, dotted line) component. The data was fit using two ^{31}P–^{7}Li dipolar interactions corresponding to fit 11 in Table 5.2 with detailed discussion in the main text.

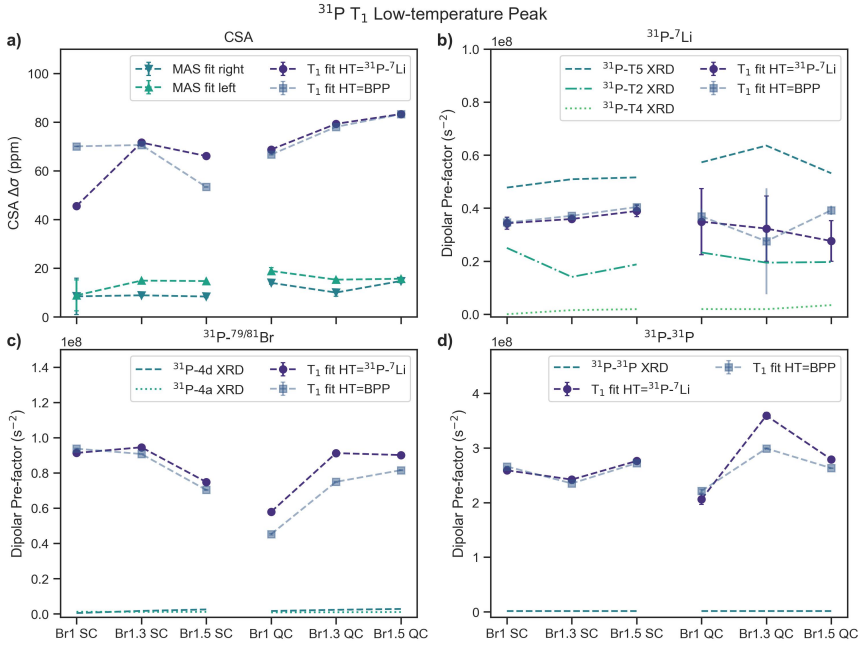

Figure 5.10: The pre-factors obtained from fitting the low-temperature peak using a) CSA interactions (Equation 5.12) compared to the pre-factors calculated using the CSA values obtained from MAS (triangular ticks) b) the ^{31}P–^{7}Li interactions, c) ^{31}P–$^{79/81}Br$ interactions (Equation 5.10) and d) ^{31}P–^{31}P homonuclear interactions (Equation 5.3), compared the calculated values from the inter-atomic distances from neutron diffraction (lines). The high-temperature peak (HT) was fit simultaneously as a ^{31}P–^{7}Li interaction (HT= ^{31}P–^{7}Li) or a modified homonuclear BPP-model (HT =BPP).

merging. A similar trend is seen in Figure 5.9 for the ^{31}P T_1–spectra obtained as a function of Br-doping, where two peaks are observed that move closer together with increasing site-disorder. The high temperature peak coincides somewhat with the ^{7}Li T_1 peak. Here, we use the formulas mentioned above to explore the source of relaxation in a more rigorous fashion.

The Low–Temperature ^{31}P T_1 Peak

Previous studies ascribe the low-temperature peak to relaxation due to PS_4^{3-}–rotation. Relaxation through PS_4^{3-}–rotation can be caused by ^{31}P–^{33}S heteronuclear interactions, spin-rotation relaxation or fluctuation in the chemical shift anisotropy (CSA). Both ^{31}P–^{33}S heteronuclear interactions and spin-rotation relaxation are unlikely in this system, as explained above. CSA interactions and ^{31}P–^{7}Li heteronuclear dipolar coupling were investigated as possible sources of relaxation, along with ^{31}P–^{31}P homonuclear interactions. The high temperature peak was fit using a modified homonuclear ^{31}P–^{31}P interaction, similar to Hangofer *et al.*[4] or a ^{31}P–^{7}Li interaction. The pre-factors obtained are given in Figure 5.10.

For the CSA-model (Figure 5.10a), the pre-factors were compared to CSA values obtained from fitting the ^{31}P MAS NMR spectra. The 4-fold difference between the measured

CSA-values and those obtained from T_1–fitting indicate that the CSA is not responsible for the low-temperature peak. Homonuclear interactions (Figure 5.10d), can be excluded due to the pre-factor as well. Using the P-P distance obtained from neutron diffraction, the obtained pre-factor from Equation 5.3 is two orders of magnitude too small (see Section C.3 of the Appendix). Similarly ^{31}P–$^{79/81}$Br interactions can be excluded as well (Figure 5.10c). The source remaining is ^{31}P–^{7}Li heteronuclear dipolar interaction. Figure 5.10b shows that the obtained and calculated pre-factors for ^{31}P–T2 and ^{31}P–T5 are of a similar order of magnitude. Furthermore, using the results obtained from the ^{7}Li T_1 fits from the previous chapter in Equation 5.10 results in a remarkably close fit of the low-temperature peak for Br1 SC and Br1.3 SC and the high-temperature-peak for all other samples (see Section C.9 of the Appendix). These results strongly imply that both the low temperature peaks represent heteronuclear ^{31}P–^{7}Li dipolar coupling and not PS_4^{3-}–rotation, as was previously suggested.

The High–Temperature ^{31}P T_1 Peak

Previous studies ascribed the high temperature peak to ^{31}P–^{7}Li interactions due to the close proximity of its peak maximum to that of ^{7}Li T_1. However, in this study this is not always the case, most notably for samples Br1 SC and Br1.3 SC (see Figure 5.2). Using the approach outlined above, we can rigorously explore the source of relaxation. The low-temperature peak is fit using a ^{31}P-^{7}Li heteronuclear model and Figure 5.11 shows the pre-factors obtained.

Similar to the low-temperature peak, ^{31}P–^{7}Li dipolar interactions seem to be the most probable source of relaxation, noting good agreement with the pre-factor calculated based on ^{31}P–T2 distances.

The errors obtained in Figure 5.11b are quite significant compared to Figure 5.11a, c and d. It must be noted that the ^{31}P–^{7}Li interactions are the only instance in which a modified BPP-model was used and hence β was not 2 (see above). However, using a β of 2 results in a worse fit (see Section C.10 of the Appendix). The large errors are attributed to the shape of the ^{31}P–^{7}Li interaction, showing two clear peaks and adding complexity to the fit (see Figure 5.3d).

Fitting ^{31}P T_1

By eliminating all other options, we can assume that both peaks in the ^{31}P T_1 spectra are due to ^{31}P–^{7}Li dipolar interactions. Furthermore, we observe that using the values obtained from ^{7}Li T_1 measurements results in a remarkably close fit for the high-temperature peak (see Section C.9 of the Appendix). We also observe a relatively large error in the fit, prompting an investigation into how the fit can be improved. The result is a system with two equations, one for each peak, containing 4 variables each. A small summary of the fitting approaches taken is given in Table 5.2.

Encouraged by the overlap observed when using the values of E_a, τ_0, and β obtained from the ^{7}Li T_1 fits (see Section C.9 of the Appendix), we attempt to fix these parameters when fitting the low-temperature peak of the ^{31}P T_1 data. The extent to which these parameters were constrained varies between fitting approaches (see fits 1–7). However, inspection of the resulting fits shows that this approach does not adequately describe the experimental data (see Section C.11 of the Appendix). Other options were also explored,

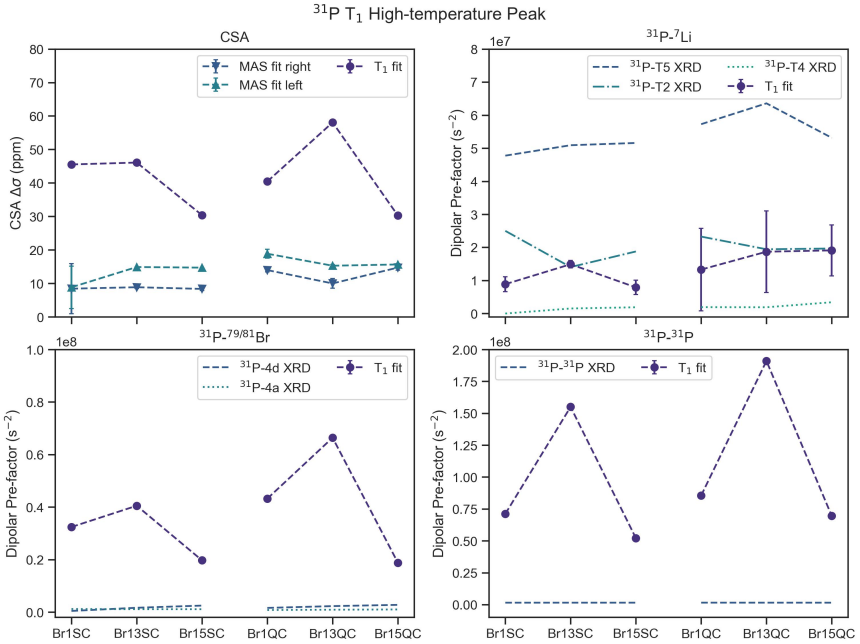

Figure 5.11: The pre-factors obtained from fitting the high-temperature peak using a) CSA interactions (Equation 5.12) compared to the pre-factors calculated using the CSA values obtained from MAS (triangular ticks), b) the ^{31}P–^{7}Li interactions, c) ^{31}P–$^{79/81}Br$ interactions (Equation 5.10) and d) ^{31}P–^{31}P homonuclear interactions (Equation 5.3), compared the calculated values from the inter-atomic distances from neutron diffraction (lines). The low-temperature peak was fit simultaneously as a ^{31}P–^{7}Li interaction model.

Table 5.2: Overview of the different fitting approaches used for the ^{31}P T_1 data. Variables were either fitted using a least-squares procedure (*Fit*), with *beta* fixed at 2, using results from the ^{7}Li T_1 fit discussed in the previous chapter(^{7}Li T_1), using results from the ^{31}P $T_{1\rho}$ fits or by assuming that the activation energies are equal.

Fit #	$Q^{(1)}$	$\tau_0^{(1)}$	$E_a^{(1)}$	$\beta^{(1)}$	$Q^{(2)}$	$\tau_0^{(2)}$	$E_a^{(2)}$	$\beta^{(2)}$
1	Fit	Fit	^{7}Li T_1	^{7}Li T_1	Fit	Fit	Fit	2
2	Fit	Fit	^{7}Li T_1	^{7}Li T_1	Fit	Fit	Fit	^{7}Li T_1
3	Fit	Fit	^{7}Li T_1	^{7}Li T_1	Fit	Fit	Fit	Fit
4	Fit	Fit	^{7}Li T_1	Fit	Fit	Fit	Fit	2
5	Fit	Fit	Fit	^{7}Li T_1	Fit	Fit	Fit	Fit
6	Fit	Fit	^{7}Li T_1	Fit	Fit	Fit	Fit	Fit
7	Fit	Fit	^{7}Li T_1	Fit	Fit	Fit	^{7}Li T_1	Fit
8	Fit	Fit	Fit	Fit	Fit	Fit	Fit	2
9	Fit	Fit	Fit	2	Fit	Fit	Fit	2
10	Fit	Fit	E_a^{HT}	Fit	Fit	Fit	E_a^{LT}	Fit
11	Fit	Fit	Fit	Fit	Fit	Fit	^{31}P $T_{1\rho}$	Fit
12	Fit	Fit	Fit	Fit	Fit	Fit	Fit	Fit

such as assuming symmetry or β=2 (fits 1, 4, 8 and 9) or assuming equal activation energies (fit 10). The results obtained for all fitting approaches are summarized for each parameter in Section C.12 of the Appendix. The extracted values of τ_0 and E_a show significant variation depending on the fitting strategy employed. In contrast, the pre-factors ($Q^{(1)}$ and $Q^{(2)}$) remain relatively consistent across the different approaches. This robustness suggests that the relaxation process probes lithium motion occurring at two distinct sites.

The pre-factors obtained for the high temperature peak sit between the calculated pre-factors for the T2-site and the T4-site, whereas the low-temperature peak seems to sit between the T5- and T2-sites. The high-temperature contribution seems to be the intercage movement through the T2- and T4-site, whereas the low-temperature peak seems to be the intercage and intracage movement through the T2-sites and T5-sites, respectively. Upon increasing of the Br-content/site disorder, intercage movement is facilitated, resulting in a shift of the high-temperature peak maximum to lower temperatures. Conversely, the T5-site, will experience an increasing amount of intercage movement. As this movement is less frequent due to its higher energy barrier and longer jump distance, the low-temperature peak maximum will shift to higher temperatures until the two peaks overlap.

The T2-site intercage movement also appears in the ^{31}P $T_{1\rho}$ results. Assuming that the high temperature ^{31}P T_1 peak and the low temperature ^{31}P $T_{1\rho}$ peak represent the same movement, we can use the activation energy obtained from ^{31}P $T_{1\rho}$ as a constant in fitting the ^{31}P T_1's (fit 11) to reduce the uncertainty of the fit. The values obtained from fitting all parameters (fit 12) are compared to the ones obtained using a high-temperature Ea (Ea1) from ^{31}P $T_{1\rho}$ (fit 11) are given in Section C.13 of the Appendix, resulting in a reduction of fit uncertainty.

By comparing the obtained pre-factors to calculated values, we find that both ^{31}P T_1 peaks are due to ^{31}P–^{7}Li dipolar interactions. Contributions to ^{31}P T_1 from PS_4^{3-}–rotation, previously suggested in literature, were ruled out. The high-temperature peak is ascribed to intercage movement through the T2-site whereas the low-temperature peak seems to belong to a mixture of intra- and intercage movement between the T5- and T2-site. Increase in site-disorder/Br-content results in facilitation of intercage movement and the shift of the high temperature peak to lower temperature. Conversely, the low-temperature peak will become more intercage in nature, shifting to higher temperatures and resulting in an overlap of the two peaks.

5.3.8 Tying Everything Together

A comparison of the activation energies obtained from the fits discussed is given in Figure 5.12. Figure 5.12a shows the activation energies for the ^{7}Li $T_{1\rho}$ components. The first two components have energies close to those obtained from EIS, implying that they belong to long-range lithium movement. Interestingly, they are all somewhat larger than the EIS-values. This could be due to inaccuracy of the fit, represented by the error bars, which overlaps with the EIS-values in some cases. Another possibility is the that the model used is too simplistic. Unlike short-range movement, long-range movement requires extended percolation pathways that traverse multiple chemical environments and possible grain boundaries. However, at the time of writing, the authors are not aware of a more involved model with a closed form that can be used to fit the data obtained. The third

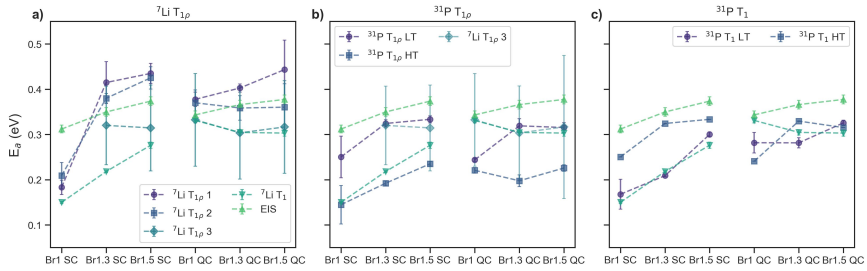

Figure 5.12: The activation energies obtained from a) the $^{7}Li\ T_{1\rho}$, b) the $^{31}P\ T_{1\rho}$ and c) the $^{31}P\ T_1$ fits compared to those obtained from $^{7}Li\ T_1$ and EIS.

component in $^{7}Li\ T_{1\rho}$ shows a remarkable overlap with the low-temperature contribution of the $^{31}P\ T_{1\rho}$ data (see Figure 5.2). From Figure 5.12b, we see a remarkable similarity in activation energies for all samples except Br1 QC, further implying that they share a common source. The large uncertainty of fit can be attributed to the plateau observed at intermediate temperatures, where the 3rd and 2nd component merge (see Figure 5.2 and Figure 5.4). This plateau is not taken into account in the equation used to fit the data (Equation 5.13).

The activation energies obtained from $^{31}P\ T_{1\rho}$ (Figure 5.12b) show a much smaller uncertainty for all samples except the high-temperature component of Br1 SC. This is due to the obscurement of the high-temperature peak within the low-temperature slope. For the low-temperature peaks, attributed to long-range lithium movement through the T2-site, we see a small increase in activation energy with increased Br-content for all samples except Br1 QC. This is unexpected as the decrease in intercage distance and increased distortion of the lithium cage should result in a decrease in the energy barrier for intercage movement. The activation energies from EIS mirrored this trend, albeit possessing a large magnitude. In the previous chapter, this was explained using the Neldel-Meyer rule, where an increase in conductivity is accompanied by both an increase in EIS pre-factor and activation energy. Previously, we observed that the attempt frequency and activation energy obtained from $^{7}Li\ T_1$ also obey they Neldel-Meyer rule. However, due to the peak maxima lying outside of the measured temperature range, the uncertainty in τ_0 obtained here is much larger, making a similar trend difficult to ascertain for $^{31}P\ T_{1\rho}$ (see Section C.14 of the Appendix). For the high-temperature peak, associated with movement through the T4–site, the slow-cooled and quench-cooled samples show a difference in trend. The slow-cooled samples mirror the trend observed for the $^{7}Li\ T_1$, with an increase in activation energy with $4d$–site disorder/Br-content. This could indicate an extension of the pathway observed i.e. a progression from more localized back-and-forth motion towards movement that connects cages. For the quench-cooled samples, an increase in activation energy is observed when going from Br1.3 QC to Br1.5 QC, possibly also due to an increase in long-range movement. For Br1 QC, both the high-temperature and low-temperature activation energies deviate from the trends observed for the other samples and lie close to each other in value. In the previous chapter, Br1 QC was shown to have the highest degree of configurational entropy, which is associated with a flattening of the energy landscape. This

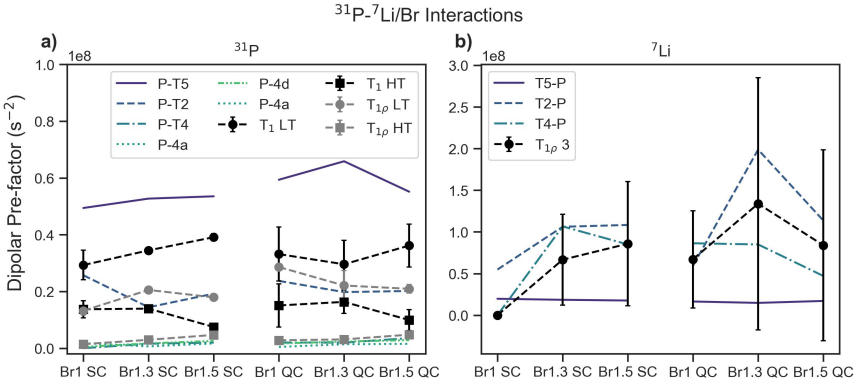

Figure 5.13: Comparison of the calculated dipolar pre-factors of the a) ^{31}P interactions compared to the experimentally obtained low-temperature peak (LT) and high-temperature peak (HT) values and b) ^{7}Li interactions compared to the experimentally obtained pre-factor for component 3 of ^{7}Li $T_{1\rho}$.

5

interpretation would also explain why the low-temperature and high-temperature activation energies are very similar for this sample, as a flattening of the energy landscape would result in both pathways becoming closer in energy.

Figure 5.12c shows the activation energies obtained from ^{31}P T_1, with the high-temperature Ea-value set to the ^{31}P $T_{1\rho}$ low-temperature Ea-value. The low-temperature E_a-value closely follows the values obtained from ^{7}Li T_1, except for Br1QC, implying that this is most likely the mix intercage and intra-cage movement associated with the T5- and T2-sites. In the case of Br1 QC, the activation energy sits between that of ^{7}Li T_1 and the high-temperature ^{31}P T_1 E_a-value. It is possible that the significant overlap in the ^{31}P T_1 peaks results in a larger uncertainty and hence an underestimation of the value.

A comparison of the fitted and calculated dipolar pre-factors are given in Figure 5.13. For ^{31}P, we see that that the $T_{1\rho}$–values show a better overlap with calculated ones. It must be noted that the calculation method used (see Section C.5 of the Appendix) relies on the use of crystallographic occupancies. These are known to change with temperature for argyrodites, with increasing temperature resulting in a decrease of T5-occupancy and an increase in T2-occupancy.[31] A comparison between the occupancies obtained from Rietveld refinement and those needed to obtain a perfect overlap are given in Section C.5 of the Appendix. Whereas this could partially explain the deviations observed for the T2- and T4-site, the change in T5-occupancy is too large. For ^{7}Li, there is a significant overlap between the various calculated pre-factors. The high mobility of ^{7}Li and its fractional occupancy over various sites makes calculations of a dipolar pre-factor challenging. Hence the values should only be taken as an approximation of the order of magnitude. The overlap between the experimental data and the calculated T2-based pre-factor was used as an additional point in verifying that the T2-site is responsible for both the ^{31}P $T_{1\rho}$ LT-peak and the third ^{7}Li $T_{1\rho}$ contribution.

Another possible reason for deviation between experimental and calculated pre-factor values could be the timescale probed. For T_1, SLR is sensitive to movement occurring in the timescale of the Larmor frequency (116 MHz), which encompasses intra-cage and in-

tercage jumps, resulting in the pre-factor representing an average of multiple jumps and jump distances. On the other hand, $T_{1\rho}$ measurements sense movement near the spin-lock frequency, which encompasses almost exclusively long-range intercage movement. The relative infrequency of these jumps and their homogenously defined start- and end-sites, means that the dipolar pre-factor is less a convolution of multiple pre-factors belonging to multiple sites. Finally, the model used has an effect. The formulas given in Equations 5.11 and 5.12 are derived for molecular systems. Models have also been derived for diffusion in solid state. However, these do not possess a closed form and have so far, to our knowledge, only been developed for T_1 relaxation due to homonuclear interactions.[34–36] Furthermore, their open form makes it significantly more complex to fit experimental data, which has, to our knowledge, not been attempted so far. As derivation of a new model and development of a new fitting algorithm are beyond the scope of the current work, a modified BPP-model was used. This approach is ubiquitous in the area of ^{7}Li SLR solid state research to obtain the activation energy.[11] A comparison of the closed-form BPP-model and two solid-state models have shown relatively small deviations and values within the same order of magnitude.[13] Given the computational advances seen in recent years, we hope that future research can remedy this. Our study represents an introduction into the possibilities of using heteronuclear interactions as probes for lithium transport. We explore the use of different models beyond the homonuclear modified BPP and show that selection of the appropriate model allows us to understand our system better. By shedding light on the pre-factor, we can gain valuable insights that lie beyond ^{7}Li SLR and even MD-simulations. The development of more detailed models and more involved computational approaches to understand the results could extend our insight even further.

5.4 Conclusion

In this work, Li-ion dynamics are investigated using ^{7}Li and ^{31}P spin–lattice relaxation (SLR) NMR. Phosphorus occupies a position between lithium cages and has been used to probe lithium intercage motion. By exploiting the Bloembergen–Purcell–Pound (BPP) pre-factor, the dominant sources of relaxation can be identified and structural information can be extracted. Long-range lithium motion is probed using ^{7}Li $T_{1\rho}$ measurements at a spin-lock frequency of 10 kHz. The resulting relaxation data can be described using three components. The activation energies of the first and second components are comparable to those obtained from electrochemical impedance spectroscopy (EIS), indicating that they are associated with long-range lithium diffusion. The third component overlaps with the ^{31}P $T_{1\rho}$ data, and the similarity in activation energies suggests a common underlying relaxation mechanism. For ^{31}P, long-range lithium motion probed via $T_{1\rho}$ at 10 kHz reveals two distinct relaxation peaks. The low-temperature peak is attributed to intercage motion mediated by the T2–site, consistent with the ^{7}Li $T_{1\rho}$ data. The high-temperature peak is assigned to ^{31}P–^{7}Li dipolar interactions involving the T4–site, in conjunction with fluctuations in the ^{31}P–Br interaction. The relatively high temperature at which this peak occurs suggests that the $T5$–$T4$–$T5$ pathway is less frequently utilized than the $T5$–$T2$–$T2$–$T5$ pathway. This interpretation is consistent with the lower occupancy of the T4–site obtained from Rietveld refinement. It is cautiously speculated that this cation-coupled lithium motion is rare in argyrodites, as it requires constructive cou-

pling between bromine motion on the 4*a* site and lithium motion on the T4–site, resulting in a higher entropic barrier. This provides a possible explanation for the low occurrence of this pathway despite its comparatively low activation energy and the low occupancy of the T4–site. The ^{31}P T_1 data exhibit two relaxation peaks that converge with increasing disorder on the 4*d*–site. Analysis of the corresponding BPP pre-factors indicates that both peaks arise from ^{31}P–^{7}Li heteronuclear dipolar interactions. Fitting the ^{31}P T_1 data using two such interactions can be performed in multiple ways, leading to different extracted values for E_a, τ_0, and β. However, the dipolar pre-factors remain relatively constant, regardless of fitting approach. The high-temperature ^{31}P T_1 peak is assigned to intercage motion via the T2–site, whereas the low-temperature peak is attributed to a combination of intra- and intercage motion involving the T5– and T2–site. Increasing site–disorder and bromine–content facilitate intercage motion, shifting the high-temperature peak to lower temperatures. Conversely, the low-temperature peak becomes increasingly intercage-like, shifting to higher temperatures and eventually merging with the high-temperature peak. The T4–site does not appear to play a significant role in lithium jumps on the T_1 timescale, which is expected given its low occupancy relative to the T2–site. The results obtained here are in good agreement with, and complementary to, those presented in Chapters 3 and 4. The increase in intercage motion with increasing site–disorder and–bromine content is mirrored in the ^{31}P T_1 data. Unlike ^{7}Li T_1 NMR and EIS, which either cannot distinguish between intra- and intercage motion or probe only intercage motion, the present approach resolves two site-specific contributions that gradually merge. From this we are also able to see that the $T2$–site is the main site for inter-cage movement and the main bottleneck for long-range diffusion. The T4–site, which seems to slightly participate in intercage movement has a secondary effect. From the ^{31}P $T_{1\rho}$ we see that, together with bromine, the T4–site can add an additional, low-energy pathway for long-range lithium movement through constructive anion-cation coupling. The use of dipolar-coupled ^{31}P nuclei as probes of ^{7}Li motion allows the utilization of different versions of the BPP-model and identification of the specific lithium sites engaged in lithium diffusion. The calculated dipolar pre-factors are within the same order of magnitude as those obtained from experimental fitting. Further studies into the dipolar pre-factor in solids and in the presence of fractional occupancy could help improve the overlap between calculation and experiment and make heteronuclear dipolar interactions a viable method for the investigation of diffusion in solids.

Bibliography

[1] Niek J. J. de Klerk, Irek Rosłoń, and Marnix Wagemaker. Diffusion mechanism of li argyrodite solid electrolytes for li-ion batteries and prediction of optimized halogen doping: The effect of li vacancies, halogens, and halogen disorder. *Chemistry of Materials*, 28(21):7955–7963, 2016. ISSN 0897-4756. doi: 10.1021/acs.chemmater.6b03630.

[2] Ajay Gautam, Hanan Al-Kutubi, Theodosios Famprikis, Swapna Ganapathy, and Marnix Wagemaker. Exploring the relationship between halide substitution, structural disorder, and lithium distribution in lithium argyrodites (li6-xps5-xbr1+x). *Chemistry of Materials*, 35(19):8081–8091, 2023. ISSN 0897-4756. doi: 10.1021/acs.chemmater.3c01525.

[3] Ajay Gautam, Marcel Sadowski, Michael Ghidiu, Nicolò Minafra, Anatoliy Senyshyn, Karsten Albe, and Wolfgang G. Zeier. Engineering the site-disorder and lithium distribution in the lithium superionic argyrodite li6ps5br. *Advanced Energy Materials*, 11(5), 2021. ISSN 1614-6832. doi: 10.1002/aenm.202003369.

[4] Isabel Hanghofer, Bernhard Gadermaier, and H. Martin R. Wilkening. Fast rotational dynamics in argyrodite-type li6ps5x (x: Cl, br, i) as seen by 31p nuclear magnetic relaxation—on cation–anion coupled transport in thiophosphates. *Chemistry of Materials*, 31(12):4591–4597, 2019. ISSN 0897-4756. doi: 10.1021/acs.chemmater.9b01435.

[5] Katharina Hogrefe, Isabel Hanghofer, and H. Martin R. Wilkening. With a little help from 31p nmr: The complete picture on localized and long-range li+ diffusion in li6ps5i. *The Journal of Physical Chemistry C*, 125(41):22457–22463, 2021. ISSN 1932-7447. doi: 10.1021/acs.jpcc.1c06242.

[6] M. Brinek, C. Hiebl, K. Hogrefe, I. Hanghofer, and H. M. R. Wilkening. Structural disorder in li6ps5ipeeds 7li nuclear spin recovery and slows down 31p relaxation–implications for translational and rotational jumps as seen by nuclear magnetic resonance. *The Journal of Physical Chemistry C*, 124(42):22934–22940, 2020. ISSN 1932-7447. doi: 10.1021/acs.jpcc.0c06090.

[7] Marina Brinek, Caroline Hiebl, and H. Martin R. Wilkening. Understanding the origin of enhanced li-ion transport in nanocrystalline argyrodite-type li6ps5i. *Chemistry of Materials*, 32(11):4754–4766, 2020. ISSN 0897-4756. doi: 10.1021/acs.chemmater.0c01367.

[8] S. G. J. van Meerten, W. M. J. Franssen, and A. P. M. Kentgens. ssnake: A cross-platform open-source nmr data processing and fitting application. *Journal of Magnetic Resonance*, 301:56–66, 2019. ISSN 1090-7807. doi: 10.1016/j.jmr.2019.02.006.

[9] N. Bloembergen, E. M. Purcell, and R. V. Pound. Relaxation effects in nuclear magnetic resonance absorption. *Physical Review*, 73(7):679–712, 1948. ISSN 0031-899X. doi: 10.1103/physrev.73.679.

[10] Paul Heitjans, Sylvio Indris, and Martin Wilkening. Solid-state diffusion and nmr. *Diffusion Fundamentals*, 2(45):1–20, 2005. ISSN 1862-4138. doi: 10.62721/diffusion-fundamentals.2.231.

[11] A. Kuhn, M. Kunze, P. Sreeraj, H.-D. Wiemhöfer, V. Thangadurai, M. Wilkening, and P. Heitjans. Nmr relaxometry as a versatile tool to study li ion dynamics in potential battery materials. *Solid State Nuclear Magnetic Resonance*, 42:2–8, 2012. ISSN 0926-2040. doi: 10.1016/j.ssnmr.2012.02.001.

[12] Carla C. Fraenza, Steve G. Greenbaum, and Sophia N. Suarez. Nuclear magnetic resonance relaxation pathways in electrolytes for energy storage. *International Journal of Molecular Sciences*, 24(12):10373, 2023. ISSN 1422-0067. doi: 10.3390/ijms241210373.

[13] A. Abragam. *The Principles of Nuclear Magnetism*. Clarendon Press, 1961. ISBN 978-0-19-852014-6.

[14] Kai Volgmann, Viktor Epp, Julia Langer, Bernhard Stanje, Jessica Heine, Suliman Nakhal, Martin Lerch, Martin Wilkening, and Paul Heitjans. Solid-state nmr to study translational li ion dynamics in solids with low-dimensional diffusion pathways. *Zeitschrift für Physikalische Chemie*, 231(7-8):1215–1241, 2017. ISSN 2196-7156. doi: 10.1515/zpch-2017-0952.

[15] K. L. Ngai and O. Kanert. Comparisons between the coupling model predictions, monte carlo simulations and some recent experimental data of conductivity relaxations in glassy ionics. *Solid State Ionics*, 53-56:936–946, 1992. ISSN 0167-2738. doi: 10.1016/0167-2738(92)90275-t.

[16] Elke Göbel, W. Müller-Warmuth, H. Olyschläger, and H. Dutz. 7li nmr spectra, nuclear relaxation, and lithium ion motion in alkali silicate, borate, and phosphate glasses. *Journal of Magnetic Resonance*, 36(3):371–387, 1969. ISSN 0022-2364. doi: 10.1016/0022-2364(79)90114-8.

[17] K. L. Ngai and C. León. Relating macroscopic electrical relaxation to microscopic movements of the ions in ionically conducting materials by theory and experiment. *Physical Review B*, 60(13):9396–9405, 1999. ISSN 0163-1829. doi: 10.1103/physrevb.60.9396.

[18] Rauf Kurbanov, Tatjana Zinkevich, and Alexey Krushelnitsky. The nuclear magnetic resonance relaxation data analysis in solids: General r1/r1rho equations and the model-free approach. *The Journal of Chemical Physics*, 135(18), 2011. ISSN 0021-9606. doi: 10.1063/1.3658383.

[19] Stephen Wimperis, George E. Rudman, and Karen E. Johnston. Biexponential i = 3/2 spin–lattice relaxation in the solid state: Multiple-quantum 7li nmr as a probe of fast ion dynamics. *The Journal of Physical Chemistry C*, 128(13):5453–5460, 2024. ISSN 1932-7447. doi: 10.1021/acs.jpcc.4c00262.

[20] R. Bertermann and W. Müller-Warmuth. Universality of nmr results in lisicon systems and other solid lithium conductors. *Zeitschrift für Naturforschung A*, 53(10-11):863–873, 1998. ISSN 1865-7109. doi: 10.1515/zna-1998-10-1110.

[21] Malcolm H Levitt. *Spin dynamics: basics of nuclear magnetic resonance*. John Wiley & Sons, 2008.

[22] Ulrich Haeberlen. Advances in magnetic resonance. *Suppl*, 1:149–168, 1976.

[23] Michael Mehring. *Principles of high resolution NMR in solids*. Springer Science & Business Media, 2012.

[24] Ralf Born and Hans Wolfgang Spiess. Ab initio calculations of conformational effects on 13c nmr spectra of amorphous polymers. In *Ab Initio Calculations of Conformational Effects on 13C NMR Spectra of Amorphous Polymers*, pages 1–121. Springer, 1997.

[25] A. Kumar. Cross-correlations in nmr. *Progress in Nuclear Magnetic Resonance Spectroscopy*, 37(3):191–319, 2000. ISSN 0079-6565. doi: 10.1016/s0079-6565(00)00023-6.

[26] Simon Gelin, Alexandre Champagne-Ruel, and Normand Mousseau. Enthalpy-entropy compensation of atomic diffusion originates from softening of low frequency phonons. *Nature Communications*, 11(1), 2020. ISSN 2041-1723. doi: 10.1038/s41467-020-17812-2.

[27] Donald E. Woessner. Nmr relaxation of spin-3/2 nuclei: Effects of structure, order, and dynamics in aqueous heterogeneous systems. *Concepts in Magnetic Resonance*, 13(5):294–325, 2001. ISSN 1043-7347. doi: 10.1002/cmr.1015.

[28] Hazime Saitô, Isao Ando, and Ayyalusamy Ramamoorthy. Chemical shift tensor – the heart of nmr: Insights into biological aspects of proteins. *Progress in Nuclear Magnetic Resonance Spectroscopy*, 57(2):181–228, 2010. ISSN 0079-6565. doi: 10.1016/j.pnmrs.2010.04.005.

[29] Alexey Krushelnitsky, Rauf Kurbanov, Detlef Reichert, Guenter Hempel, Horst Schneider, and Vladimir Fedotov. Expanding the frequency range of the solid-state t1 ρ experiment for heteronuclear dipolar relaxation. *Solid State Nuclear Magnetic Resonance*, 22(4):423–438, 2002. ISSN 0926-2040. doi: 10.1006/snmr.2002.0071.

[30] Pedro B. Groszewicz, Hergen Breitzke, and Gerd Buntkowsky. Compensating the asymmetric probe response in broad mas nmr spectra of quadrupolar nuclei. *Solid State Nuclear Magnetic Resonance*, 84:227–233, 2017. ISSN 0926-2040. doi: 10.1016/j.ssnmr.2017.06.006.

[31] Nicolo Minafra, Marvin A Kraft, Tim Bernges, Cheng Li, Roman Schlem, Benjamin J Morgan, and Wolfgang G Zeier. Local charge inhomogeneity and lithium distribution in the superionic argyrodites li6ps5x (x= cl, br, i). *Inorganic Chemistry*, 59(15):11009–11019, 2020.

[32] Zhenming Xu, Xi Chen, Hong Zhu, and Xin Li. Anharmonic cation–anion coupling dynamics assisted lithium-ion diffusion in sulfide solid electrolytes. *Advanced Materials*, 34(49), 2022. ISSN 0935-9648. doi: 10.1002/adma.202207411.

[33] Zhuoyuan Zheng, Jie Zhou, and Yusong Zhu. Computational approach inspired advancements of solid-state electrolytes for lithium secondary batteries: from first-principles to machine learning. *Chemical Society Reviews*, 53(6):3134–3166, 2024. ISSN 0306-0012. doi: 10.1039/d3cs00572k.

[34] C. A. Sholl. Nuclear spin relaxation by translational diffusion in solids. *Journal of Physics C: Solid State Physics*, 7(18):3378–3386, 1974. ISSN 0022-3719. doi: 10.1088/0022-3719/7/18/021.

[35] H. C. Torrey. Nuclear spin relaxation by translational diffusion. *Physical Review*, 92 (4):962–969, 1953. ISSN 0031-899X. doi: 10.1103/physrev.92.962.

[36] D. A. Faux, D. K. Ross, and C. A. Sholl. Nuclear spin relaxation by translational diffusion in solids: X. monte carlo calculation for the simple hopping model. *Journal of Physics C: Solid State Physics*, 19(21):4115–4133, 1986. ISSN 0022-3719. doi: 10.1088/0022-3719/19/21/015.

6

Probing Space–Charge Layer Formation in Solid Electrolyte – Ionic Liquid Systems

"God made the bulk; surfaces were invented by the devil"

Wolfgang Pauli

6.1 Introduction

The global energy transition has intensified the focus on electrochemical energy storage technologies, with batteries playing a central role. However, conventional lithium-ion batteries face several drawbacks, including limited energy density and safety concerns arising from the use of flammable liquid electrolytes. Solid-state electrolytes (SSEs) have emerged as a promising alternative due to their enhanced thermal and electrochemical safety. Nevertheless, their widespread adoption is hindered by issues such as limited electrochemical stability and high interfacial resistance.[1] To overcome interfacial resistances, solid electrolytes can be combined with liquid or polymer electrolytes to form hybrid systems. [2]

Among potential liquid-phase additives, ionic liquids (ILs)–salts that are liquid at or near room temperature—have attracted attention due to their low volatility, non-flammability, and relatively low toxicity compared to conventional organic solvents.[3, 4] Despite these advantages, ILs alone are typically unsuitable as electrolytes in lithium batteries due to their low ionic conductivity and low lithium-ion transference numbers. However, when used in conjunction with SSEs, ILs have been shown to reduce grain boundary resistance and enhance ionic conductivity without compromising safety.[2]

To ensure ionic conduction in the ionic liquids within these so-called hybrid systems, a lithium-based salt is added. However, increasing the salt concentration results in increased viscosity and a decrease in ionic conductivity. Recently hybrid systems consisting of either LLZO or LAGP and an ionic liquid without a lithium salt were shown to possess good ionic conductivity, a transference number close to 1 and reduced lithium dendrite growth.[5–7] However, the mechanism of ion conduction is still not fully understood. Paolella *et al.* found the presence of LiTFSI and argued that cation exchange had taken place between a proton from the ionic liquid and lithium from the solid electrolyte, a phenomena seen before LLZO and LAGP.[7]

In this work, we propose an alternative explanation based on the formation of a space charge layer at the interface between the solid and liquid components. Traditionally, the term refers to the layer that forms at the interface of two different semiconductors upon contact, due to differences in electron potential.[8] In the context of solid-state batteries, similar interfacial space charge layers are hypothesized to arise due to mismatches in lithium chemical potential and the poor electronic conductivity of solid electrolytes. When two materials with different lithium chemical potentials are placed in contact, the system will attempt to establish thermodynamic equilibrium at the interface through the movement of lithium ions. To maintain charge neutrality, electron transfer is also required. However, solid state electrolytes are electronic insulators and unable to allow for the movement of electrons. The result is a thin interfacial layer with lithium ions on one side and electrons on the other. Lithium is unable to move to return due to thermodynamic effects and unable to diffuse further due to electrostatics. This layer is thought to be responsible for extra resistivity in solid-state batteries.[9, 10]

Despite its theoretical significance, experimental evidence for space charge layers in solid-state systems remains limited as they are theorized to be less than 1 nm in width.[11] The effects observed can be attributed to surface reactions, chemical inhomogeneities or experimental inaccuracies. Recently, it was shown that solid state NMR can be used to probe effects of space charge layers.[12] However, this is still an indirect assessment of space charges. Here, we use solid state NMR to investigate the existence of space charges

at solid state electrolyte interfaces. This is done by mixing a nanosized solid state electrolyte with an ionic liquid. By using an ionic liquid with no lithium salt added, we are able to detect the presence of any lithium moieties, should they form. Through nanosizing the electrolyte, we are able to maximize the surface contact area between the two materials and hence maximize the NMR signal intensity. Through this method we are able to confirm and study the formation of a space charge layer forming at the interface between Li_6PS_5Cl and EMIN TFSI. Furthermore, we are able to show the practical use if this phenomenon by cycling symmetric cells with $Li_{1.5}Al_{0.5}Ge_{1.5}P_3O_{12}$ and PYR14 TFSI with minimal stack pressure.

6.2 Materials and Methods

Argyrodite (Li_6PS_5Cl /LSPC) was synthesised in-house as well as commercially acquired. Synthesized argyrodite was made using the method of Yu *et al.*[13] Briefly, Li_2S (Sigma-Aldrich), P_2S_5 (Merck) and LiCl (Sigma-Aldrich) were mixed in stoichiometric amounts using a planetary ball-mill for 1 hour at 110 rpm. The powder was then pressed into pellets and sealed in a carbon-coated quartz ampule under argon and heated to 550 ˚C at a rate of 100 ˚C/h. The sample was held at 550 ˚C for 10 hours and allowed to cool slowly to room temperature afterwards. To obtain nano-sized argyrodite, the pellet was crushed with a mortar and pestle and the powder was then ball-milled at 500 rpm for 6 hours under argon atmosphere. Commercial Ampecera Argyrodite (pass 325 mesh, D50< 10 μm, fine powder) was purchased from MSE Supplies and used without further purification before storage. 1-Ethyl-methylimidazolium bis(trifluoromethylsulfonyl)imide (EMIN TFSI) was purchased from Sigma and used without purification before storage. $Li_{1.5}Al_{0.5}Ge_{1.5}P_3O_{12}$ (LAGP) (Ampcera, 500 nm) was purchased from MSE Supplies and 1-Butyl-1-methylpyrrolidinium bis(trifluoromethylsulfonyl)imide (PYR14) was purchased from Solvionic and were used without further purification. Lithium cobalt oxide was purchased from Nanoshell and dried at 80 ˚C in vacuum overnight before storage. To avoid contamination or degradation all materials were stored in an Argon-filled glovebox with H_2O < 5.0 ppm and O_2 < 0.1 ppm.

X–ray diffraction was performed using a PANalytical X'Pert Pro X-ray diffractometer with Cu Kα X-rays at wavelengths of λ_1 = 1.540598 Å and λ_2 = 1.544426 Å. To prevent degradation, custom-designed air-tight holders were used. These were filled and sealed in an argon-filled glovebox before measurement. Rietveld refinement was carried out using GSAS-II software. Confocal Raman spectroscopy was performed on a Renishaw inVia confocal Raman microscope using a wavelength of 785 nm. To prevent exposure to air, samples were sealed in glass capillaries under an argon atmosphere beforehand.

Solid-state NMR experiments were performed on a Bruker Ascend 500 MHz magnet with a NEO console and a Bruker 4.0 mm triple-resonance probe, unless otherwise specified. Corresponding Larmor frequencies were 202.457, 73.6, and 194.37 MHz for ^{31}P, ^{6}Li, and ^{7}Li, respectively. Samples were referenced versus LiCl in water at 0 ppm or 85% H_3PO_4 in D2O (Sigma) at 0 ppm. A recycle delay of $5 \times T_1$ was chosen for all measurements, except the saturation recovery experiments, to ensure full relaxation.

Two-dimensional ^{6}Li exchange experiments between lithium cobalt oxide and Li_6PS_5Cl were performed using a three-pulse sequence developed by Jeener *et al.*[14] at a Larmor frequency of 73.6 MHz. A MAS rate of 6 kHz was used with a 3.2 mm MAS probe. The nutation frequency and longitudinal relaxation rate were determined beforehand. Spectra

were obtained using a recycle delay of 30 s, 16 scans, and 440 slices collected in the indirect dimension. Mixing times of 1 μs and 1 s were used.

Spin–lattice relaxation rates of ^{7}Li were probed on a Bruker UltraShield 300 with an Avance console, corresponding to a Larmor frequency of 116.642 MHz, and an NMR Service static HT-X 500 WB probe over a temperature range from 227 to 337 K. The spin–lattice relaxation rate in the laboratory frame (T_1) was measured using either a saturation recovery pulse sequence for the home-made Li_6PS_5Cl or an inversion recovery sequence for the commercial Li_6PS_5Cl.[15] Spin–lattice relaxation in the rotating frame ($T_{1\rho}$) was measured using a spin-lock technique with locking frequencies of 10, 20, and 30 kHz. Transverse relaxation rates (T_2) were determined using a Carr–Purcell–Meiboom–Gill echo sequence.[15] The obtained transients were analysed using a custom Python script and sSnake.[16] MestreNova was used for peak deconvolution and integration. Pulsed–field gradient NMR was performed using a Bruker Avance NEO 600 MHz narrow-bore spectrometer equipped with a diffusion probe and a stimulated echo sequence. Diffusion coefficients were obtained by fitting the resulting decay curves with the Stejskal–Tanner equation.[17]

Electrochemical impedance spectroscopy (EIS) was performed using an Autolab PGSTAT302N potentiostat with an ECI10M module. A potential perturbation of 10 mV was applied over a frequency range from 10 MHz to 10 mHz. Approximately 200 mg of material was cold-pressed between stainless-steel plungers inside an argon-filled glovebox and fastened by hand using large screws. Pure Li_6PS_5Cl was either pressed and fastened gently by hand or pressed at 2 MPa using a hydraulic press. Samples containing ionic liquid were pressed and fastened gently by hand to prevent separation of liquid and solid and leakage of the slurry into the edges of the cell. Measurements were conducted over a temperature range from 20 °C to −50 °C using a Fryka Cold Box B35-50/LOGG freezer. Custom wires were used for all measurements below 0 °C. The capacitance of the wires was measured beforehand using a 10 MΩ resistor.[18]

Symmetric cells were prepared using the same custom solid-state cells. Lithium discs with a diameter of 6 mm and 9.25 mm indium discs were pressed onto the stainless-steel plungers. The discs were approximately equal in thickness, resulting in a Li:In atomic ratio of approximately 2:1. Samples were sandwiched between the metal discs and the cell was fastened with minimal pressure by hand to prevent short-circuiting. For the 2 MPa Li_6PS_5Cl sample, the pellet was pressed between the plungers using a hydraulic press before adding lithium and indium. For LAGP, the cells were pressed at 1 MPa for the pristine cell and hand-pressed for cells containing ionic liquid. The cells were cycled between −1 V and 1 V at a current density of 0.05 mA cm^{-2}.

6.3 Results and Discussion

6.3.1 The Chemical Environment

X–ray Diffraction

Li_6PS_5Cl crystallizes in a face-centered cubic structure with space group $F\bar{4}3m$.[19] The structure, given in Figure 6.1, consists of phosphorous occupying the 4b sites and forming PS_4^{3-}–tetrahedra with the sulphur atoms at the 16e sites. The remaining sulphur and chlorine atoms occupy the 4a/4d sites. Lithium ions primarily reside at the 48h (T5) sites,

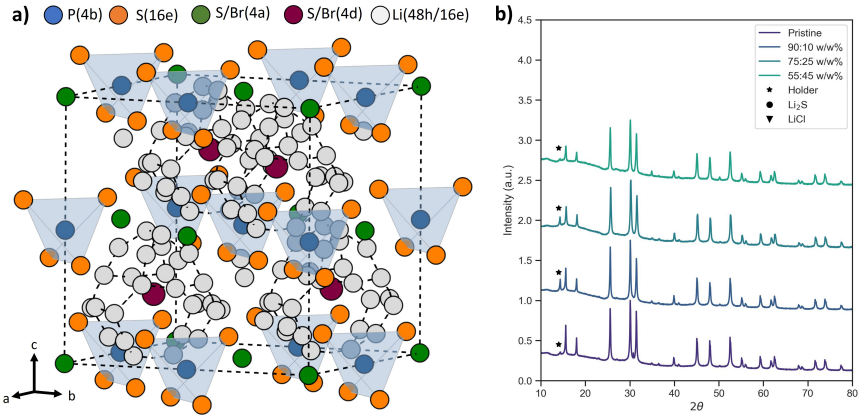

Figure 6.1: The crystal structure of Li_6PS_5Cl (a) and the X-ray diffraction patterns obtained for the pristine commercially obtained Li_6PS_5Cl and with addition of EMIN TFSI at various weight ratios (b).

which form cage-like environments surrounding the 4*d* sites. Additionally, lithium occupies the T2– and T4–sites. On an atomic level, lithium-ion diffusion occurs through several distinct pathways: direct hopping between neighbouring 48*h* sites (termed doublet jumps), movement within a single cage (intra-cage jumps), and transitions between cages (inter-cage jumps).[20] On a macroscopic level, lithium diffusion also involves transport across grain boundaries between crystallites.[21]

The XRD patterns of commercial Li_6PS_5Cl mixed with EMIM TFSI in varying ratios are shown in Figure 6.1, while the pattern for the lab-synthesized Li_6PS_5Cl is provided in the Appendix Section D.1. The pristine material exhibits minor impurity peaks corresponding to Li_2S and LiCl. These impurities remain when EMIN TFSI is added, implying minimal dissolution. Furthermore, no obvious degradation of the Li_6PS_5Cl is observed when EMIN TFSI is added. Rietveld refinement yields a particle size of approximately 70 nm using the Scherrer equation (see Section D.1 of the Appendix).

Static and MAS NMR

Unlike X-ray diffraction, nuclear magnetic resonance is sensitive to both crystalline and amorphous chemical species and was used to probe the samples further. The static ^7Li spectra for the commercial mixtures are given in Figure 6.2.

The static NMR linewidth serves as an indicator of ion mobility and depends on the homonuclear dipole-dipole interactions experienced by the nuclei.[22] At low temperatures, in the so-called rigid lattice regime, the linewidth is dominated by homonuclear dipole–dipole interactions between neighbouring nuclei. These interactions are not averaged and thus produce a broad spectral line reflecting the range of local magnetic environments. As temperature increases, jumps between sites become more frequent, nuclei are able to experience different environments, and the dipolar interactions are averaged. The faster the nuclei move, the more similar this averaged interaction will be, resulting in a decrease in linewidth with temperature, termed motional narrowing. At sufficiently high temperatures, the line adopts a Lorentzian shape, with the linewidth primarily de-

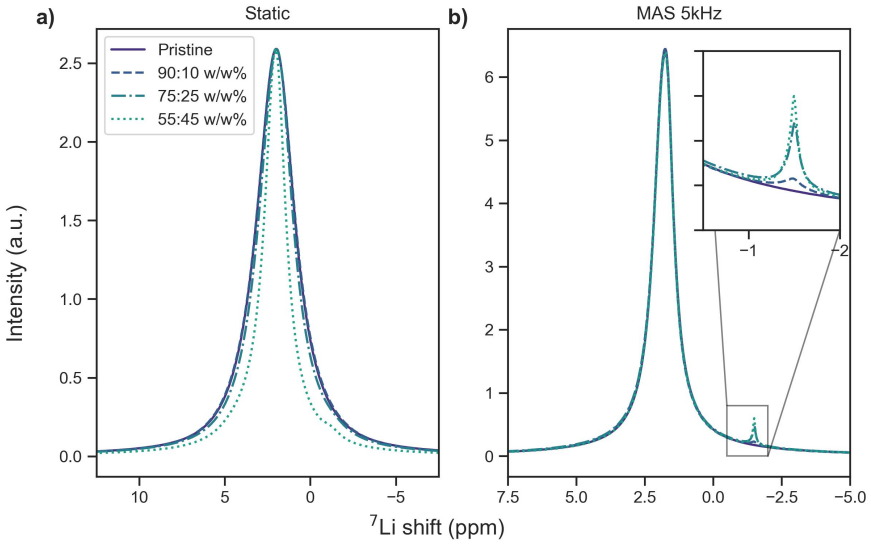

Figure 6.2: The static (a) and MAS (B) ^{7}Li one pulse NMR spectra for pristine commercially obtained Li_6PS_5Cl and with addition of EMIN TFSI in various weight ratios.

termined by external magnetic field inhomogeneities. At intermediate temperatures, the theoretical line shape can be deconvoluted into a fast-moving Lorentzian component and a slower Gaussian contribution. The influence of the addition of IL to the linewidth of Li_6PS_5Cl can be seen in Figure 6.2a. As IL is added, the linewidth first increases slightly (90:10 w/w%), followed by a clear decrease, indicating an increase in ionic mobility. Dipolar, and to a small extent quadrupolar interactions result in a broadening of the ^{7}Li NMR spectrum. Magic angle spinning or MAS, averages out these interactions and allows for higher resolution. The MAS spectra, given in Figure 6.2b, reveal the presence of a second lithium environment, which increases in both intensity and peak area as more ionic liquid is added.

Figure 6.3a compares the ^{7}Li chemical shift of the second environment with those of Li_6PS_5Cl precursors and of LiTFSI. The new resonance does not coincide with any precursor signal but lies very close to the LiTFSI reference, strongly suggesting that lithium in this environment is coordinated to the $TFSI^-$ anion of the ionic liquid.

To rule out the effect of concentration on the chemical shifts of LiCl and Li_2S, saturated solutions of LiCl and Li_2S were diluted 100 times and the range in chemical shifts was compared (see Figures D.3 and D.4 in the Appendix). Furthermore, a small amount of Li_6PS_5Cl was mixed with an excess of EMIN TFSI and mixed. The liquid was then pipetted from the top so as to not extract any Li_6PS_5Cl. The ^{7}Li spectrum of the supernatant showed only the signals of Li_6PS_5Cl and Li_2S; no resonance appeared at the shift characteristic of the second environment (see Appendix Figure D.6). Finally, ^{31}P and ^{1}H NMR were also performed and showed no signs of the formation of new chemical species (see Figures D.5, D.6 and D.7 of the Appendix).

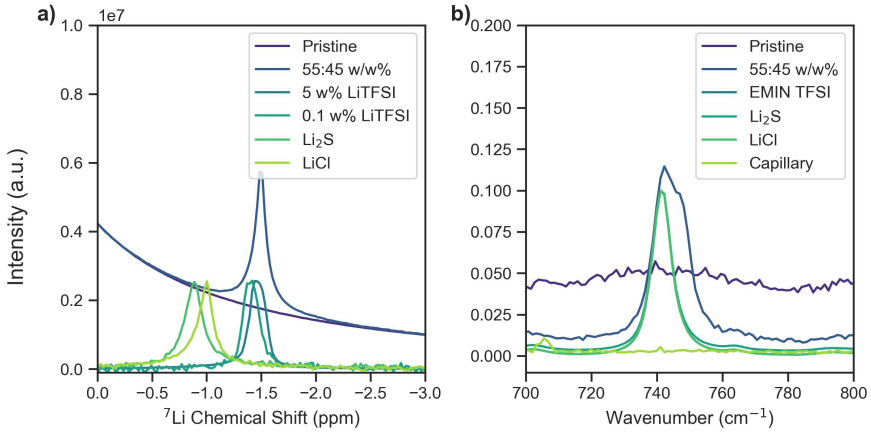

Figure 6.3: Comparison of the ^{7}Li chemical shift (a) and the Raman spectra (a) of the pristine Li_6PS_5Cl and after the addition of EMIN TFSI with those of LiCl, Li_2S and LiTFSI in EMIN TFSI.

Raman Spectroscopy

The Raman spectra (Figure 6.3b) reveal the appearance of a new vibrational environment, consistent with changes in the $TFSI^-$ vibrational modes upon coordination with lithium ions.[23] This spectral feature is not observed when LiCl or Li_2S is added to EMIM TFSI, indicating that simple dissolution of lithium salts does not produce the same effect. Furthermore, typical degradation products of Li_6PS_5Cl , such as P_2S_x species with vibrational modes at 378 and 705 cm^{-1}, often associated with electrochemical decomposition during battery operation, are absent (see Section D.3 of the Appendix).[24] These findings strongly suggest that the second environment observed in the MAS NMR spectra arises from the in situ formation of LiTFSI within the hybrid electrolyte system.

Variable Temperature NMR

To further rule out the presence of an impurity or degradation as the source of the second environment, its temperature dependence was investigated using MAS NMR. The resulting spectra are given in Figure 6.4. For pristine Li_6PS_5Cl, lowering the temperature results in a upfield shift to lower ppm, while increasing the temperature causes a downfield shift. The effect of temperature on the main Li_6PS_5Cl peak for 75:25 w/w%Li_6PS_5Cl :EMIN TFSI shows a similar trend in chemical shift as a function of temperature. The second environment in the hybrid also exhibits a similar temperature-dependent shift, but it disappears entirely below 223 K-coinciding with the known freezing point of EMIM TFSI.[25] This does not happen when LiTFSI is dissolved in EMIN TFSI (see Figure 6.4d). At elevated temperatures, the second environment broadens and decreases in intensity. Similar behaviour has been reported for LLZO in contact with a Li-glyme complex and has been attributed to chemical exchange between distinct lithium environments.[26] In the absence of chemical exchange, distinct chemical environments manifest as different peaks on the NMR spectra. When exchange between two distinct environments occurs at a rate larger than the difference in frequency between the two peaks representing them, the NMR spectrum is affected. The peaks will broaden and, if the rate is fast enough, eventually coalesce.[27]

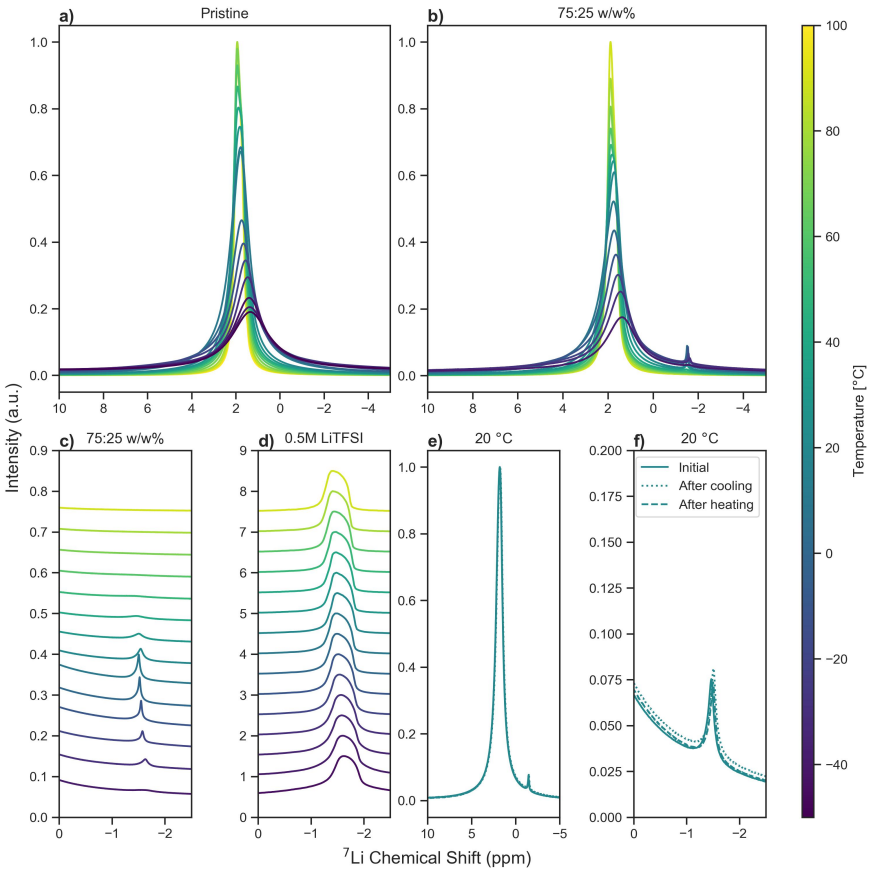

Figure 6.4: The effect of temperature on the MAS spectra of pristine Li_6PS_5Cl (a), 75:25 w/w% Li_6PS_5Cl and EMIN TFSI (b) with a zoom-in on the 2nd environment (c) and 0.5 M LiTFSI in EMIN TFSI (d) as well as the spectra at 20 ˚C of 75:25 w/w% LSPC and EMIN TFSI after cooling to -40 ˚C and heating to 90 ˚C (e and f). The temperature for figures (a)-(d) is given by the bar (right), the legend for figures (e) and (f) is given in (f).

In this case, because the integral of the second environment is much smaller than that of the main Li_6PS_5Cl peak, the signal merges into the dominant environment rather than forming a distinct coalesced peak. Importantly, this process is reversible upon returning to room temperature, further supporting the interpretation of dynamic exchange rather than irreversible chemical change (see Figures 6.4e and f).

From these results we see that the addition of EMIN TFSI to nano-sized Li_6PS_5Cl results in the appearance of an additional chemical environment in the ^{7}Li MAS NMR spectrum. The chemical shift in the NMR spectrum as well as peak position in the Raman one indicate that this environment belongs to LiTFSI, formed by lithium from the argyrodite combining with the TFSI-anion of the ionic liquid. Variable temperature NMR shows that the formation of LiTFSI is a dynamic process and not the result of degradation. Here it is proposed to be due to space charge layer formation, hence Li-ions originating from the Li_6PS_5Cl

surface enter the ionic liquid near the surface. Static ^{7}Li NMR measurements indicate that the space charge layer formation is accompanied by increased lithium diffusivity.

6.3.2 Lithium Mobility

2D Exchange NMR

MAS ^{7}Li NMR reveals increased lithium mobility upon addition of the ionic liquid, as evidenced by the decrease of the static linewidth of Li_6PS_5Cl (see Figure 6.2b). To investigate whether lithium ions in this second environment exchange with those in the main argyrodite phase and hence participate and support long range diffusion, two -dimensional exchange spectroscopy (2D-EXSY) NMR was performed.

Figure 6.5 presents the ^{7}Li 2D-EXSY spectra as a function of mixing time. A set of distinct cross-peaks is observed between the two environments, confirming that lithium exchange occurs between the main Li_6PS_5Cl phase and the secondary environment associated with the ionic liquid. This demonstrates dynamic interaction and supports the hypothesis that the two lithium populations are not isolated but are part of an interconnected transport process.

It is, in principle, possible to distinguish between one-dimensional (1D) and three-dimensional (3D) diffusion by deriving the fundamental relationships that describe the evolution of cross-peak intensities as a function of mixing time. However, this analysis requires the appearance of a plateau in the cross-peak intensity at longer mixing times, a characteristic feature that is not observed in the present data (see Section D.4 of the Appendix). As a result, a definitive determination of the dimensionality of lithium diffusion is not possible in this case.

Longitudinal relaxation measurements (T_1) can be used to probe the energetics of lithium-ion motion in both the pristine and hybrid systems (see 2 and 5). Comparing pristine Li_6PS_5Cl to 75:25 w/w%, a single peak is observed for both with a maximum located at a similar temperature (see Figure 6.6). However, a noticeable decrease in activation energy is observed in the hybrid system. The T_1 relaxation rate is sensitive to lithium-ion jump processes occurring at frequencies near the Larmor frequency. These are typically attributed to intracage and intercage lithium movements within the crystal lattice. The observed decrease in activation energy may therefore reflect enhanced mobility along these pathways, potentially due to subtle modifications in the crystal structure upon formation of the space charge layer. Alternatively, it is also possible that a portion of the T_1 signal arises from lithium-ion jumps across grain boundaries. Although these are likely fewer in number, a reduction in their activation energy could contribute to the overall observed decrease in relaxation-derived activation energy.

Pulsed Field Gradient NMR

Pulsed Field Gradient Nuclear Magnetic Resonance (PFG NMR) enables the investigation of lithium ion transport over longer length scales than those accessible via spin-lattice (T_1) relaxation NMR.[17, 28] Figure 6.7 presents the diffusion coefficients and activation energies for ^{7}Li, ^{1}H, and ^{19}F in three systems: 0.5 M LiTFSI in EMIN TFSI, pure Li_6PS_5Cl, and a 75:25 w/w% mixture of Li_6PS_5Cl and EMIN TFSI. For ^{7}Li, a notable decrease in the diffusion coefficient is observed between the liquid electrolyte (0.5 M LiTFSI in EMIN TFSI) to the solid-state electrolyte (pure Li_6PS_5Cl). Interestingly, the diffusion coefficient in-

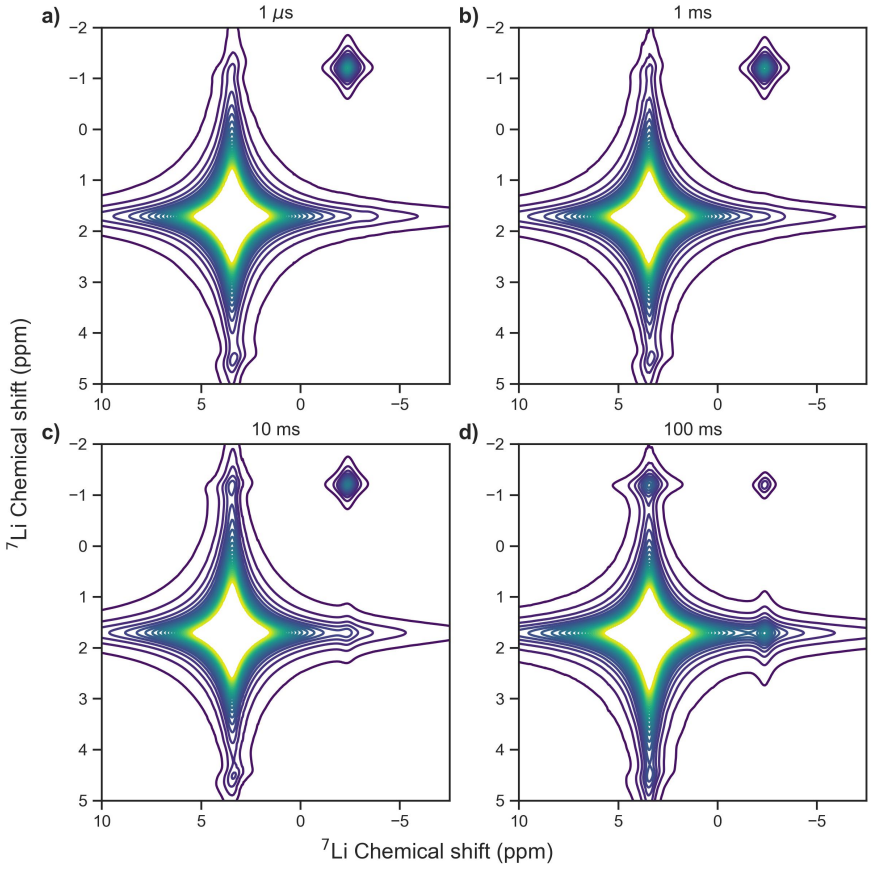

Figure 6.5: 2D Exchange NMR spectra of 75:25 w/w% Li_6PS_5Cl and EMIN TFSI at with a mixing time of 1 μs (a), 1 ms (b), 10 ms (c) and 100 ms (d).

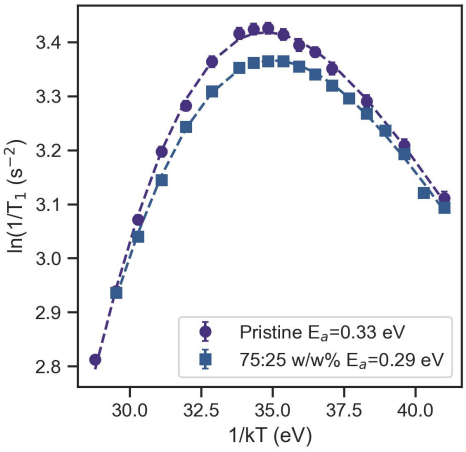

Figure 6.6: Spin–lattice relaxation rates ($1/T_1$) measured using a saturation-recovery sequence and the fit (dashed lines) using the modified BPP model for pristine Li_6PS_5Cl and the 75:25 w/w% Li_6PS_5Cl +EMIN TFSI system

creases slightly upon incorporation of EMIN TFSI. However, direct comparison between solid and liquid systems should be approached with caution, as diffusion in liquids is influenced by factors such as the identity of the counter-ion, ion concentration, and ion-solvent interactions.[29] The activation energies for lithium ion diffusion exhibit an inverse trend, decreasing from the liquid to the solid system and remaining relatively unchanged in the mixed system. The diffusivity of the TFSI-anion, represented by ^{19}F, shows a substantial change between the purely liquid electrolyte and the mixed system. In the liquid state, ^{19}F diffusion is significantly higher and its activation energy differs from that of ^{7}Li. Upon mixing with Li_6PS_5Cl, the diffusivity of ^{19}F decreases and its activation energy becomes more comparable to that of ^{7}Li, suggesting stronger correlation between Li^+ and $TFSI^-$ mobility in the hybrid environment. A similar trend is observed for ^{1}H, indicating a correlated motion between lithium and both the EMIN-cation and the TFSI-anion.

$$t_i = \frac{N_i D_i}{\sum_i N_i D_i} \tag{6.1}$$

These interactions also influence the cation transference number, defined by Equation X and reported in Table 1 for both the 0.5 M LiTFSI in EMIN TFSI and the 75:25 w/w% Li6PS6Cl:EMIN TFSI mixture. The transference number depends on the number density (N) and diffusivity (D_i) of ionic species. While conventional liquid electrolytes typically exhibit transference numbers between 0.5 and 0.65, ionic liquids such as EMIN TFSI tend to show significantly lower values (0.1), in agreement with our observations.[30] In the case of the mixed system, precise determination of the lithium concentration is challenging due to the undefined amount of lithium in the space charge layer. However, using the integral of the second NMR environment given in Figure 6.2b (corresponding to 0.7% of the total peak area) and a molecular weight of 268.397 g/mol for Li6PS6Cl, we estimate an average lithium ion concentration of 0.713 M in EMIN TFSI. The results, given in Table 6.1 show

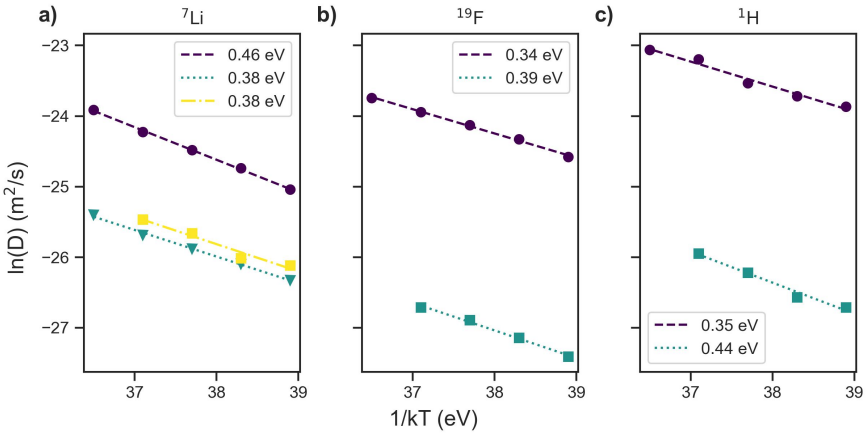

Figure 6.7: Diffusion coefficients obtained from PFG NMR as a function of temperature for ^{7}Li (a), ^{19}F (b), and ^{1}H (c). The dotted and dashed lines represent the fit using the Arhenius equation to obtain the activation energy

an increase in transference number, despite a lower concentration of lithium. Unlike the 0.5 M solution of LiTFSI in EMIN TFSI, the concentration of lithium in the hybrid system is likely not uniform, being larger around the argyrodite particles and falling off rapidly. Consequently, the local transference number in the vicinity of the argyrodite particles may be significantly higher than the bulk average calculated.

Table 6.1: Transference numbers for the 0.5 M LiTFSI in EMIN TFSI and a 75:25 w/w% misture of Li_6PS_5Cl and EMIN TFSI.

	0.5 M LiTFSI in EMIN TFSI	Li_6PS_5Cl + EMIN TFSI (75:25)
^{7}Li	0.025	0.152
^{19}F	0.347	0.282
^{1}H	0.619	0.566

The PFG NMR results indicate that LiTFSI in the hybrid system behaves differently from LiTFSI dissolved in EMIN, indicating correlated motion between lithium and TFSI in the hybrid system. This is reflected in both the change in activation energies as well as the transference number.

Electrochemical Impedance Spectroscopy -Blocking Electrodes

Like PFG NMR, electrochemical impedance spectroscopy allows for probing of long-range lithium movement and furthermore provides the total ionic conductivity of a system. The results for both the pristine argyrodite and the hybrid system, across different weight ratios of argyrodite to ionic liquid, are presented in Figure 6.8. These results demonstrate that the incorporation of ionic liquid leads to a notable increase in conductivity.

Figure 6.9 illustrates how temperature influences the EIS-response of pristine argyrodite and two hybrid argyrodite/ionic liquid composites prepared at different weight ra-

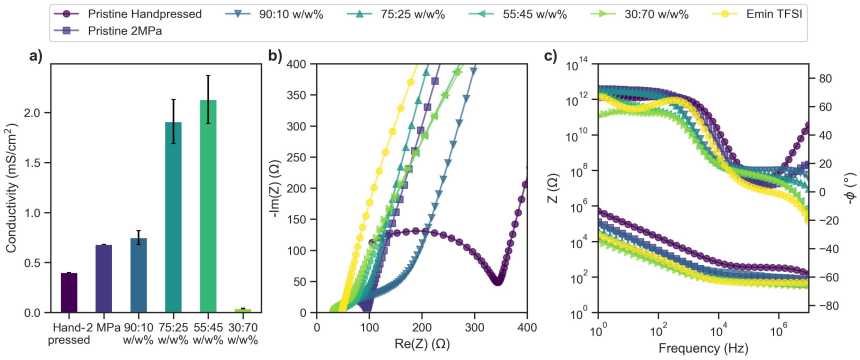

Figure 6.8: The conductivity obtained from EIS for pristine argyrodite and argyrodite with various amounts of EMIN TFSI (a) and the Nyquist (b) and Bode (c) plots. The solid lines represent the fit according to the models discussed.

tios. The equivalent-circuit models used to fit the impedance data are depicted in Figure 6.10.

For pristine argyrodite (Figure 6.10a) the spectrum is described by a constant-phase element (CPE) that accounts for the blocking behaviour of the electrodes (P_{elec}), a resistance corresponding to lithium-ion transport through the Li_6PS_5Cl lattice (R_{LSPC}), and a second CPE that compensates for wire capacitance (P_{wires}). The resulting Arrhenius plot (Figure 6.9d) yields an activation energy of ≈ 0.40 eV, in agreement with pulsed-field-gradient NMR measurements (Figure 6.8a). Introducing the ionic liquid alters the circuit (Figure 6.10b). In addition to the CPEs associated with the blocking electrodes and wires, two resistive elements are required in series; one parallel to a CPE and one not. These components represent two sequential lithium-transport processes, namely migration through the argyrodite particles and migration across the surrounding space-charge layer. Accordingly, the conductivity plots for the 90:10 and 75:25 composites (Figure 6.9e and 6.9f, respectively) display two distinct activation energies—one matching pristine argyrodite and the other approximating that obtained with PFG NMR for LiTFSI dissolved in EMIN-TFSI, albeit slightly higher (see Figure 6.7a).

Below the ionic liquid freezing point the circuit changes once more with two resistances acting in parallel (see Figure 6.10c). Conductivity data (Figure 6.9e and 6.9f) reveal that one resistance becomes temperature-independent, consistent with a frozen ionic liquid phase that behaves as a purely Ohmic resistor, incapable of lithium transport. The remaining resistance retains an activation energy comparable to pristine argyrodite and is therefore assigned to particle–particle pathways that remain in contact. The practical impact of freezing depends on composition. In the 90:10 sample (Figure 6.9e) only a modest conductivity drop is observed, implying that most argyrodite particles remain connected or are separated merely by a thin frozen film. In contrast, the 75:25 composite (Figure 6.9f) exhibits a pronounced conductivity decline, indicating more extensive contact loss as the ionic liquid solidifies.

It is important to note that fitting the impedance data is complicated by inductive effects and stray capacitance originating from the measurement setup, particularly the

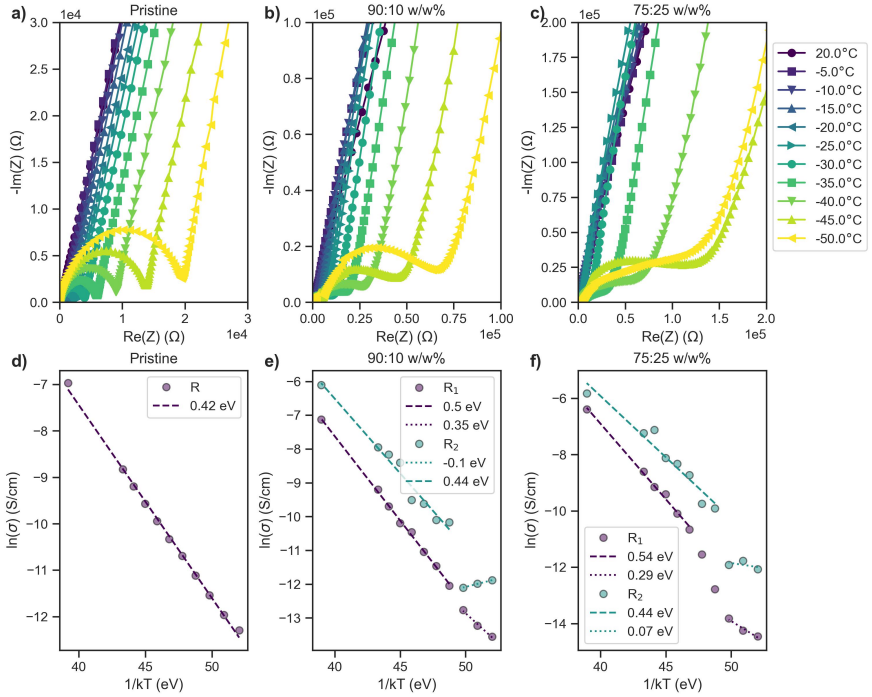

Figure 6.9: The temperature dependent Nyquist plots for pristine Li_6PS_5Cl pressed at 2 MPa (a) and 90:10 (b) and 75:25 w/w% Li_6PS_5Cl + EMIN TFSI (c) and the corresponding fit (solid lines), the resultant conductivities (c, d and f) and fits using the Arhenius equation (dashed lines).

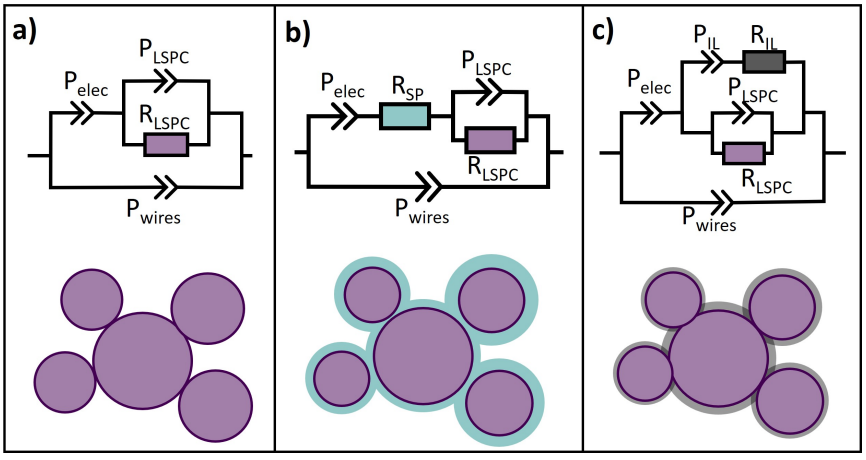

Figure 6.10: The model circuit and simplified illustration of the system for pristine Li_6PS_5Cl (a), Li_6PS_5Cl and EMIN TFSI (b) and Li_6PS_5Cl and EMIN TFSI below the freezing point of EMIN TFSI (c).

wiring. The stray capacitance introduced by the wires was independently measured and accounted for in the equivalent circuit using a constant phase element (P_{wires}). However, uncontrollable switching in the electrical gain of the measurement device introduce additional, unquantifiable capacitance. This variability manifests as abrupt discontinuities in the impedance spectra, particularly noticeable in the Bode plots for several materials (see Section D.6 of the Appendix) and in the Nyquist plots at higher frequencies.

6.3.3 Electrochemical Cycling

Whereas blocking electrodes are useful for investigating energetics, their large capacitance makes fitting the EIS data challenging. To examine the practical application of the space charge layer and circumvent the above-mentioned issue, symmetric cells using lithium-indium were constructed and cycled. The results are given in Figure 6.11 for the first 10 cycles only (top) and all 100 cycles (bottom) for the pristine argyrodite pressed at 2 MPa and hybrid systems with different weight ratios, pressed gently by hand. From the figure, it can be seen that the addition of ionic liquid results the appearance of a voltage plateau during the initial cycles. The EMIN TFSI used is known to be electrochemically unstable against lithium and theoretical results indicate that it would not be stable against a lithium-indium alloy. The plateau disappears in subsequent cycles, likely due to the formation of an SEI-layer.[31, 32] The initial plateau is far less pronounced for the 90:10 w/w%-system. This is likely due to the plateau depending on the amount of ionic liquid degradation occurring, which depends on the amount of ionic liquid present at the interface. The lower section of Figure 6.11 shows that the addition of EMIN TFSI results in a decrease of the overpotential during long term cycling when compared to pressed pristine Li_6PS_5Cl. However, the addition of 45 w/w% EMIN TFSI results in a high overpotential. This is likely due to the EMIN TFSI itself not being conductive and acting as a capacitor. However, it should be noted that the addition of ionic liquid results in a significant decrease in overpotential for the 90:10 w/w% and 75:25 w/w% -systems.

Impedance spectroscopy was performed on cells before cycling, after 10 cycles and after 100 cycles, with the results given in Figure 6.13. The models used to fit the spectra are given in Figure 6.12a for the pristine argyrodites and Figure 6.12b for the samples containing ionic liquid. For the pristine argyrodites (Figure 6.12a), the bulk conductivity is represented by one resistance (R_{LSPC}) and one constant phase element (P_{LSPC}) in parallel. Additionally, two constant phase elements, one representing the wires (P_{Wires}) and one representing the surface roughness between the electrolyte pellet and the metal (P_{Int}), are placed in parallel and in series, respectively. For the samples containing ionic liquid (Figure 6.12b), two resistances and constant phase elements are placed in parallel, representing the space charge layer (R_{SP} and P_{SP}) and the solid electrolyte (R_{LSPC} and P_{LSPC}). A constant phase element representing the wires is placed in parallel (P_{Wires}). Unlike the constant phase element used for the pristine argyrodite (P_{Int} in Figure 6.12a), a resistance is required in series (R_{Int}), likely representing the formation of the SEI–layer upon degradation of the ionic liquid.

The total resistance, given as $R_{total} = R_{LSPC} + R_{SP} + R_{Int}$, is given in FIG Figure 6.13f. For the hand–pressed sample, an increase in the resistance is observed, likely due to degradation of the argyrodite. A similar effect is seen for the argyrodite pressed under 2 MPa, however, here the increase stabilizes after 10 cycles. For the 90:10 and 75:25 w/w% -samples,

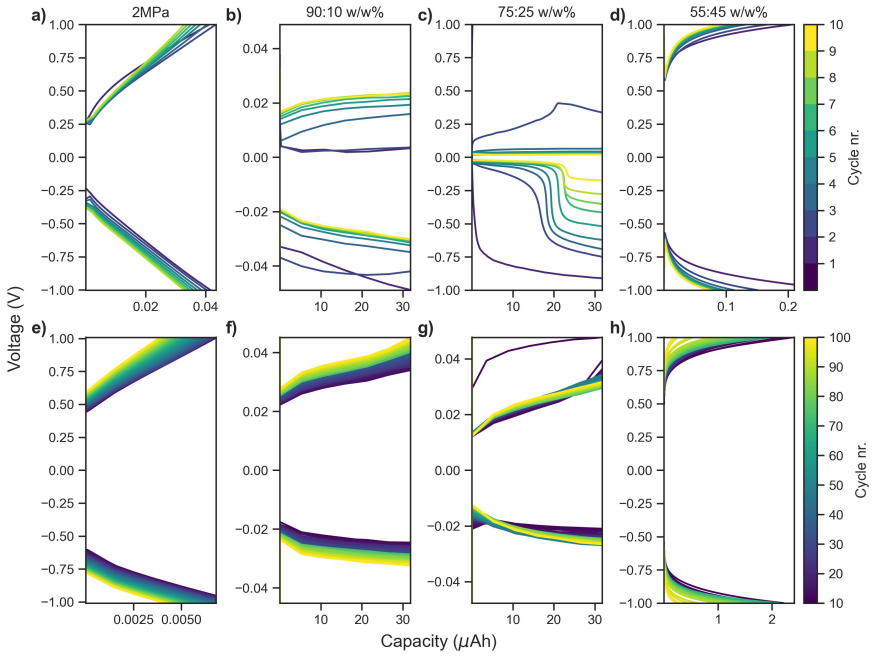

Figure 6.11: Electrochemical cycling Electrochemical performance of symmetric Li–In | Li_6PS_5Cl + EMIM TFSI | Li–In cells. Voltage profiles during galvanostatic cycling are shown for the first ten cycles (top) and for all 100 cycles (bottom) for pristine Li_6PS_5Cl pressed at 2 MPa and for hybrid systems containing varying weight fractions of EMIM TFSI, gently pressed by hand.

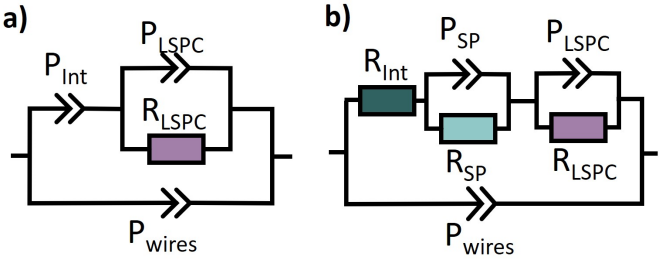

Figure 6.12: The model circuits used to fit the EIS results for the pristine Li_6PS_5Cl (a) and the Li_6PS_5Cl + EMIN TFSI systems (b).

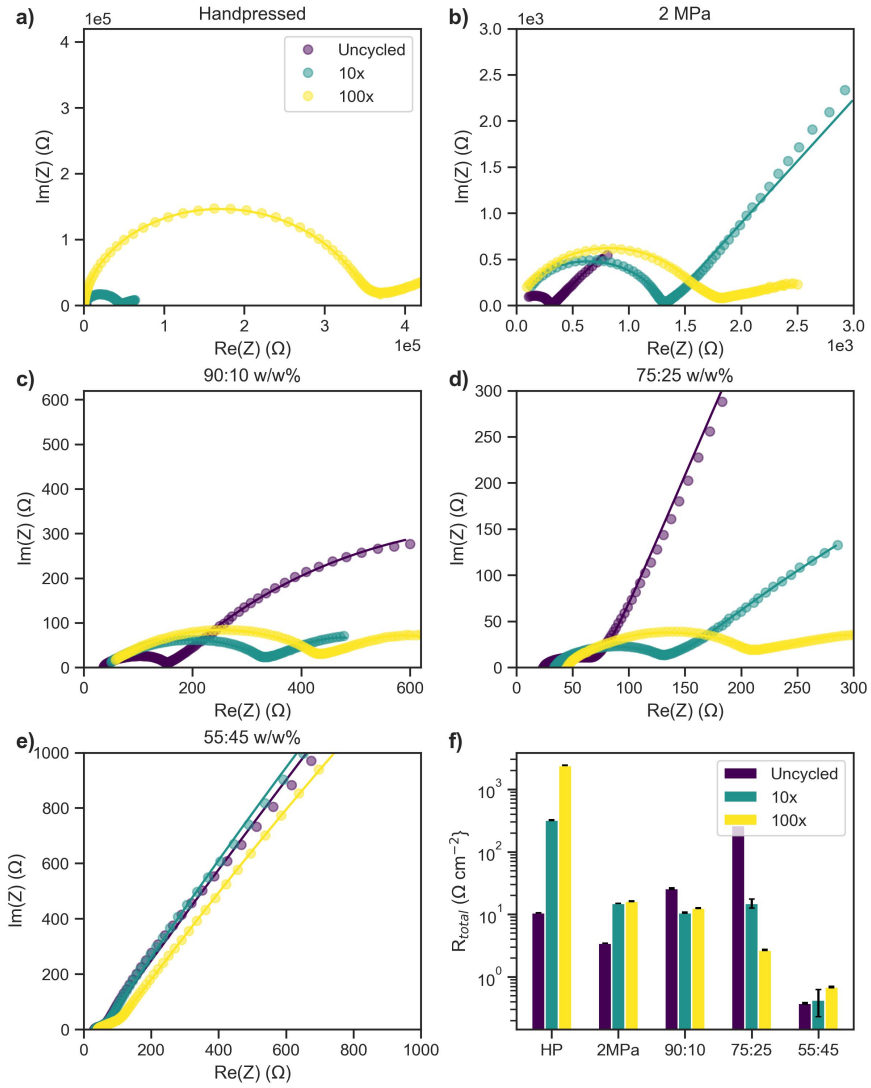

Figure 6.13: Nyquist plots for Li-In symmetric cells containing pristine Li_6PS_5Cl pressed by hand (a) and under 2 MPa (b), mixtures of EMIN TFSI and Li_6PS_5Cl with weight ratios of 90:10 (c), 75:25 (d) and 55:45 (e) and an overview of the total electrolyte resistance (f).

6

a decrease in interfacial resistance is observed, which is more pronounced for the latter sample. The reason for this is not clear and could be due to the formation of an SEI-layer. It is interesting to note that whereas the 90:10 w/w%-sample has a resistance similar to that the 2 MPa–sample after 100 cycles, the 75:25 w/w%-sample has a much lower resistance. For the 55:45 w/w%-sample, the resistance is constant, likely due to the large overpotential preventing the occurrence of any Faradaic reaction in the voltage window.

In conclusion, the addition of moderate amounts of EMIM TFSI (10 to 25 wt%) reduced long-term overpotentials significantly in Li-In symmetric cells when compared to pristine Li_6PS_5Cl. Impedance analysis showed lower interfacial resistance for these compositions as well.

Lithium Exchange within the Cathodic Mixture

The addition of ionic liquid results in improved conductivity within the electrolyte system and a reduction of overpotential during cycling. Here, lithium exchange within the cathodic mixture is explored.

Two-dimensional exchange NMR spectroscopy is a valuable technique for exploring the rate of lithium exchange between two distinct environments as a function of the mixing time. Here it is used to explore lithium exchange between the cathode material lithium cobalt oxide ($LiCoO_2$ or LCO) and argyrodite. Figure 6.14a and 6.14b show the spectra obtained for a mixture of pristine argyrodite and LCO for mixing times of 1 μs and 1 s, respectively. Chemical exchange between two environments manifests in the presence of so-called cross-peaks, which are absent in the case of pure argyrodite. The spectra for a 75:25 w/w% mixture of Li_6PS_5Cl and EMIN TFSI, are given in Figure 6.14c and 6.14d for mixing times of 1 μs and 1 s, respectively. Figure 6.14d shows the clear presence of cross peaks. These results indicate that the presence of a space charge layer does not only facilitate movement of lithium within the electrolyte but between the electrolyte and the cathode.

Electrochemical Impedance and Cycling Stability of LAGP with Ionic Liquid

Argyrodite-based solid electrolytes are known for their low grain boundary resistance, yet suffer from lower (electro)chemical stability in ambient air and while cycling. In contrast, materials such as lithium aluminium germanium phosphate ($Li_{1.5}Al_{0.5}Ge_{1.5}P_3O_{12}$ or LAGP) posses relatively high stability in air and a wider electrochemical window. However, LAGP suffers from significant grain boundary resistance, which can impede its performance in solid-state batteries.[33] The addition of ionic liquids could reduce the interfacial resistance.

The effect of the addition of EMIN TFSI on the EIS conductivity of LAGP in Li-In symmetric cells is given in Figure 6.15. The Nyquist plot for pristine LAGP, given in Figure 6.15a shows a large half semi-circle. The resistance could not be obtained as it goes beyond the limits of the equipment used. Figure 6.15b shows the effect of the addition of EMIN TFSI, which causes a clear reduction in resistance and the appearance of two semicircles.

Symmetric cells containing only pristine LAGP sandwiched between two Li-In electrodes could not be cycled, whereas the LAGP + EMIM TFSI-cell was able to cycle at a current density of 0.5 mA/cm^2. However, its capacity gradually decreased over time (Figure 6.16a), likely due to the chemical instability of EMIM TFSI when in contact with

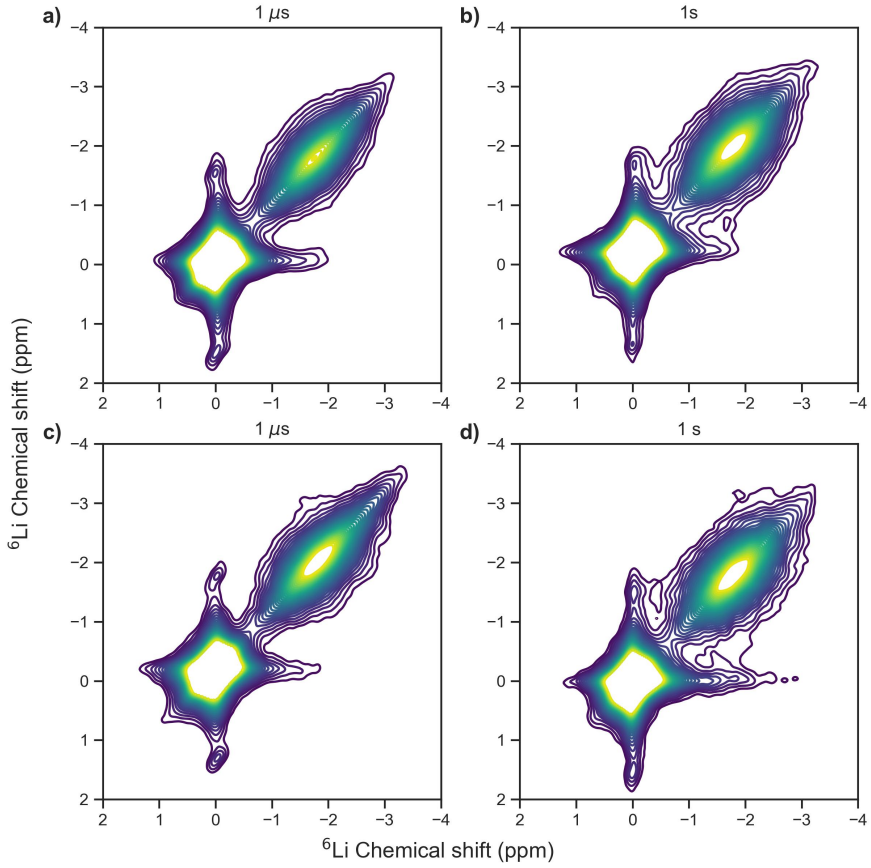

Figure 6.14: Two-dimensional exchange ^{7}Li NMR spectra demonstrating lithium exchange for a cathodic mixture comprising $LiCoO_2$ and either pristine Li_6PS_5Cl at mixing times of 1 μs (a) and 1 s (b), or a 75:25 w/w% mixture of Li_6PS_5Cl and EMIM TFSI at 1 μs (c) and 1 s (d).

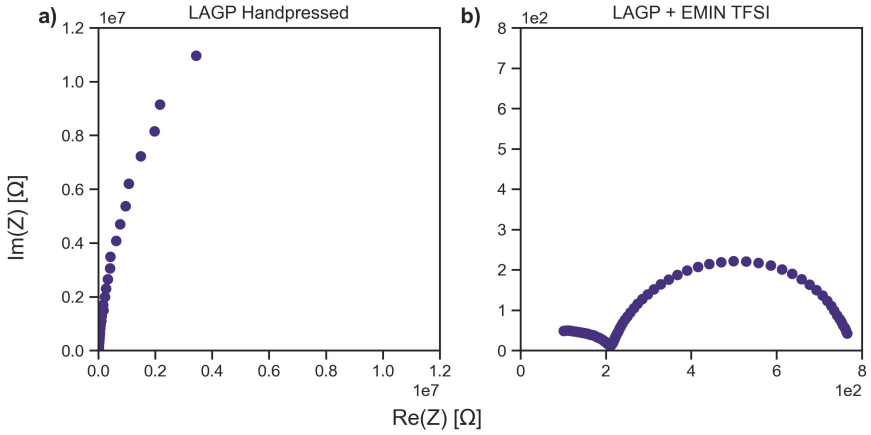

Figure 6.15: Nyquist plots of pristine LAGP (a) and after addition of EMIM TFSI (b).

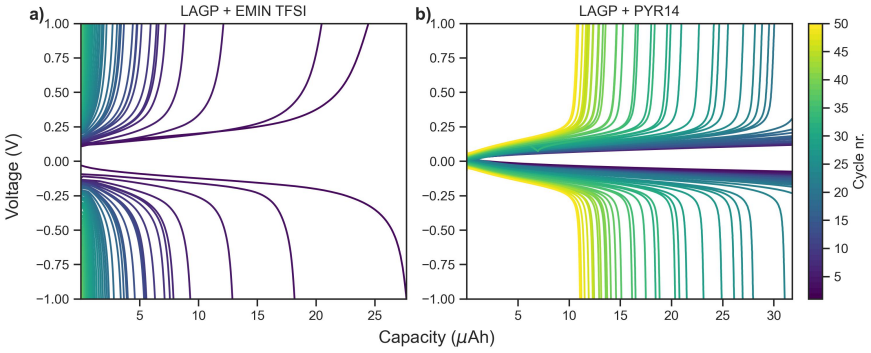

Figure 6.16: Cycling performance of Li–In | LAGP–ionic liquid | Li–In symmetric cells containing EMIN TFSI (a) or PYR14 (b) as ionic liquid.

lithium metal as well as degradation of LAGP. Substitution of EMIN TFSI with 1-butyl-1-methylpyrrolidinium bis(fluorosulfonyl)imide (PYR14) resulted in significantly enhanced cycling stability (Figure 6.16b), which can be ascribed to the superior chemical stability of PYR14 against lithium metal. Both electrolyte formulations were cycled under identical current densities. The cycling was both capacity- and voltage limited, with the LAGP and PYR14 system reaching the capacity limit during the initial cycles.

Electrochemical impedance spectra recorded before and after cycling are shown in Figure 6.18. Before cycling, both the EMIM TFSI- and PYR14 FSI-containing cells display two semicircles (see Figures 6.18a and 6.18c), which were fit using the equivalent circuit depicted in Figure 6.17a. Taking the larger semicircle as the bulk LAGP resistance results in a conductivity of around $7 times 10^{-5}$ S/cm2 for the cells before cycling, which is within the expected range for this material. The smaller semicircle is tentatively ascribed to the space charge layer.

Post-cycling, the impedance spectrum of the EMIN TFSI cell displays one clear semi-

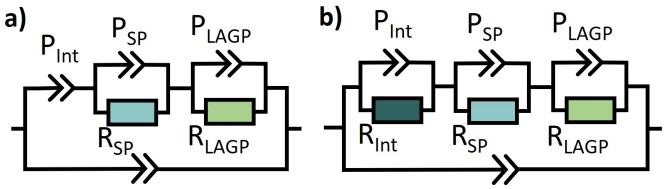

Figure 6.17: Model circuits used to fit the EIS data of the LAGP+ EMIN TFSI system before and after cycling and the LAGP+PYR14 after cycling (a) and the LAGP + PY14 system after cycling (b).

circle as well an additional, poorly defined feature, which appears at lower frequencies (see Figure 6.18b). This feature was fit as a semicircle, although its precise physical origin remains uncertain. It is hypothesized that the prominent semi-circle is related to the formation of a resistive solid electrolyte interphase (SEI) layer, originating from the decomposition of EMIM TFSI. The large resistance associated with this feature appears to become the dominant source of impedance in the cell, resulting in the other features being obscured in the spectrum.

For the PYR14-containing cell, the impedance spectrum after cycling reveals three distinct semicircles (see Figure 6.18d). These were fit using the equivalent model given in Figure 6.17b and are attributed to the space charge layer, the LAGP electrolyte and the formation of an SEI-layer. The formation of an SEI layer occurs to a lesser degree than the EMIN-TFSI containing cell.

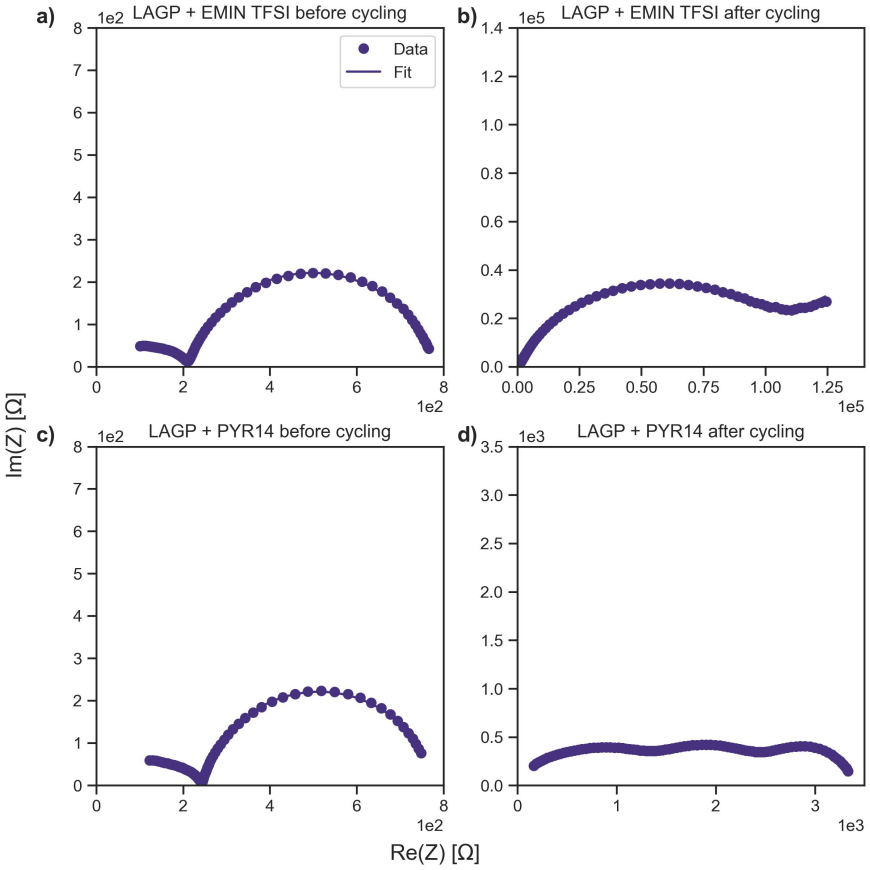

Figure 6.18: Nyquist plots of Li–In | LAGP–ionic liquid | Li–In symmetric cells containing EMIN TFSI or PYR14 as ionic liquid before and after cycling.

6.4 Conclusion

This chapter explores the formation and behaviour of a space charge layer by mixing an argyrodite-based solid ion conductor (Li_6PS_5Cl) with an ionic liquid (EMIN TFSI). Nanosizing the argyrodite creates a large interfacial area and using an ionic liquid with no added lithium salt allows the space charge layer to form a chemically distinct environment in the ionic liquid which can be studied with NMR.

Static ^{7}Li NMR demonstrates that the addition of EMIN TFSI significantly enhances the mobility of lithium ions in the solid electrolyte. MAS ^{7}Li NMR spectra reveal the existence of a distinct second chemical environment with a chemical shift similar to that of LiTFSI and unlike that of LiCl or Li_2S, two of the precursors of Li_6PS_5Cl. Raman spectroscopy further demonstrated the presence of LiTFSI and absence of the two precursors.

Temperature-dependent MAS NMR shows that the second environment reduces in intensity at elevated temperatures, indicating chemical exchange with the Li_6PS_5Cl-environment. Below the freezing point of EMIN TFSI, the second environment disappears as well, a phenomenon that is absent in a comparative sample containing only LITFSI in EMIN TFSI. Together, the low-temperature and high-temperature behaviour indicate a dynamic exchange between the two NMR environments, which ceases upon the freezing of EMIN TFSI and results, not in the disruption of exchange with an already-present environment in the EMIN TSFI but in the disappearance of said environment. The second environment is not inherently present in the EMIN TFSI but is created upon exchange with Li_6PS_5Cl, strongly implying that it is a space charge layer. Pulsed-field gradient NMR shows a stronger correlation between the movement of lithium and the EMIN and TFSI ions when EMIN TFSI is mixed with Li_6PS_5Cl. A rough estimate of the transference number of lithium shows an increase when mixing EMIN TFSI with Li_6PS_5Cl.

The improvement in lithium mobility seen with static NMR was explored further with electrochemical impedance spectroscopy. EIS shows an increase in ionic conductivity with the addition of EMIN TFSI to Li_6PS_5Cl along with two distinct contributions to the EIS spectra, one belonging to the Li_6PS_5Cl and one to the space charge layer. The contribution from the space charge layer shows a lower activation energy, resulting in improved interfacial ion movement and hence acting as a wetting agent. Upon freezing of EMIN TFSI, a drop in conductivity is observed, which becomes more pronounced as more EMIN TFSI is incorporated.

Furthermore, 2D-exchange NMR confirmed that the ionic liquid facilitates lithium-ion movement both within the electrolyte and across the $LiCoO_2$-electrolyte interface within the cathode material. This interaction between the electrolyte and cathode material is crucial for improving overall battery performance.

Cycling tests in Li-In symmetric cells demonstrated that the addition of EMIN TFSI improved initial conductivity and reduced overpotentials. When using LAGP as the electrolyte in Li–Li symmetric cells, the presence of EMIN TFSI results in a significant decrease in cell resistance and allows cells to be cycled under minimal pressure. However, the instability of EMIN TFSI in contact with lithium metal resulted in significant degradation after several cycles. In contrast, the use of a more stable ionic liquid, PYR14, significantly enhanced the cycling stability, leading to reduced SEI formation and better long-term performance. This was also confirmed with EIS analysis.

This chapter has shown that mixing Li_6PS_5Cl with EMIN TFSI results in the formation

of a space charge layer that is detectable with NMR. This space charge improves lithium mobility across the interface between of Li_6PS_5Cl particles and with cathode particles and results in a higher transference number within the EMINTFSI. Mixing with LAGP results in a profound decrease in interfacial resistance and allows for cycling of symmetric cells. Exchanging EMIN TFSI for a more stable PYR14 results in stable cycling and opens the possibility of practical applications.

Bibliography

[1] John Christopher Bachman, Sokseiha Muy, Alexis Grimaud, Hao-Hsun Chang, Nir Pour, Simon F. Lux, Odysseas Paschos, Filippo Maglia, Saskia Lupart, Peter Lamp, Livia Giordano, and Yang Shao-Horn. Inorganic solid-state electrolytes for lithium batteries: Mechanisms and properties governing ion conduction. *Chemical Reviews*, 116(1):140–162, 2016. ISSN 0009-2665. doi: 10.1021/acs.chemrev.5b00563.

[2] Chen-Zi Zhao, Bo-Chen Zhao, Chong Yan, Xue-Qiang Zhang, Jia-Qi Huang, Yifei Mo, Xiaoxiong Xu, Hong Li, and Qiang Zhang. Liquid phase therapy to solid electrolyte–electrode interface in solid-state li metal batteries: A review. *Energy Storage Materials*, 24:75–84, 2020. ISSN 2405-8297. doi: 10.1016/j.ensm.2019.07.026.

[3] Maciej Galiński, Andrzej Lewandowski, and Izabela Stępniak. Ionic liquids as electrolytes. *Electrochimica Acta*, 51(26):5567–5580, 2006. ISSN 0013-4686. doi: 10.1016/j.electacta.2006.03.016.

[4] Jiajia Li, Fangfang Li, Lan Zhang, Haitao Zhang, Ulla Lassi, and Xiaoyan Ji. Recent applications of ionic liquids in quasi-solid-state lithium metal batteries. *Green Chemical Engineering*, 2(3):253–265, 2021. ISSN 2666-9528. doi: 10.1016/j.gce.2021.03.001.

[5] Hanyu Huo, Ning Zhao, Jiyang Sun, Fuming Du, Yiqiu Li, and Xiangxin Guo. Composite electrolytes of polyethylene oxides/garnets interfacially wetted by ionic liquid for room-temperature solid-state lithium battery. *Journal of Power Sources*, 372:1–7, 2017. ISSN 0378-7753. doi: 10.1016/j.jpowsour.2017.10.059.

[6] Zhaoshuai Zhang, Long Zhang, Yanyan Liu, Hongqiang Wang, Chuang Yu, Hong Zeng, Li-min Wang, and Bo Xu. Interface-engineered li7la3zr2o12-based garnet solid electrolytes with suppressed li-dendrite formation and enhanced electrochemical performance. *ChemSusChem*, 11(21):3774–3782, 2018. ISSN 1864-5631. doi: 10.1002/cssc.201801756.

[7] Andrea Paolella, Giovanni Bertoni, Wen Zhu, Daniele Campanella, Andrea La Monaca, Gabriel Girard, Hendrix Demers, Alina Cristina Gheorghe Nita, Zimin Feng, Ashok Vijh, Abdelbast Guerfi, Michel Trudeau, Michel Armand, and Sergey A. Krachkovskiy. Unveiling the cation exchange reaction between the nasicon li1.5al0.5ge1.5(po4)3 solid electrolyte and the pyr13tfsi ionic liquid. *Journal of the American Chemical Society*, 144(8):3442–3448, 2022. ISSN 0002-7863. doi: 10.1021/jacs.1c11466.

[8] Chia-Chin Chen and Joachim Maier. Space charge storage in composites: thermodynamics. *Physical Chemistry Chemical Physics*, 19(9):6379–6396, 2017. ISSN 1463-9076. doi: 10.1039/c6cp08134g.

[9] Niek J. J. de Klerk and Marnix Wagemaker. Space-charge layers in all-solid-state batteries; important or negligible? *ACS Applied Energy Materials*, 2018. ISSN 2574-0962. doi: 10.1021/acsaem.8b01141.

[10] Jun Haruyama, Keitaro Sodeyama, Liyuan Han, Kazunori Takada, and Yoshitaka Tateyama. Space–charge layer effect at interface between oxide cathode and sulfide electrolyte in all-solid-state lithium-ion battery. *Chemistry of Materials*, 26(14): 4248–4255, 2014. ISSN 0897-4756. doi: 10.1021/cm5016959.

[11] Hideki Masuda, Nobuyuki Ishida, Yoichiro Ogata, Daigo Ito, and Daisuke Fujita. Internal potential mapping of charged solid-state-lithium ion batteries using in situ kelvin probe force microscopy. *Nanoscale*, 9(2):893–898, 2017. ISSN 2040-3364. doi: 10.1039/c6nr07971g.

[12] Zhu Cheng, Ming Liu, Swapna Ganapathy, Chao Li, Zhaolong Li, Xiaoyu Zhang, Ping He, Haoshen Zhou, and Marnix Wagemaker. Revealing the impact of space-charge layers on the li-ion transport in all-solid-state batteries. *Joule*, 4(6):1311–1323, 2020. ISSN 2542-4351. doi: 10.1016/j.joule.2020.04.002.

[13] Chuang Yu, Swapna Ganapathy, Jart Hageman, Lambert van Eijck, Ernst R. H. van Eck, Long Zhang, Tammo Schwietert, Shibabrata Basak, Erik M. Kelder, and Marnix Wagemaker. Facile synthesis toward the optimal structure-conductivity characteristics of the argyrodite li6ps5cl solid-state electrolyte. *ACS Applied Materials &Interfaces*, 10(39):33296–33306, 2018. ISSN 1944-8244. doi: 10.1021/acsami.8b07476.

[14] J. Jeener, B. H. Meier, P. Bachmann, and R. R. Ernst. Investigation of exchange processes by two-dimensional nmr spectroscopy. *The Journal of Chemical Physics*, 71 (11):4546–4553, 1979. ISSN 0021-9606. doi: 10.1063/1.438208.

[15] Eiichi Fukushima. *Experimental pulse NMR: a nuts and bolts approach*. CRC press, 2018.

[16] S. G. J. van Meerten, W. M. J. Franssen, and A. P. M. Kentgens. ssnake: A cross-platform open-source nmr data processing and fitting application. *Journal of Magnetic Resonance*, 301:56–66, 2019. ISSN 1090-7807. doi: 10.1016/j.jmr.2019.02.006.

[17] E. O. Stejskal and J. E. Tanner. Spin diffusion measurements: Spin echoes in the presence of a time-dependent field gradient. *The Journal of Chemical Physics*, 42(1): 288–292, 1965. ISSN 0021-9606. doi: 10.1063/1.1695690.

[18] Eis systems performance assessment gamry instruments. website. URL `https://www.gamry.com/application-notes/EIS/quick-check-of-eis-system-performance/`.

[19] Hans-Jörg Deiseroth, Shiao-Tong Kong, Hellmut Eckert, Julia Vannahme, Christof Reiner, Torsten Zaiß, and Marc Schlosser. Li6ps5x: a class of crystalline li-rich solids with an unusually high li+ mobility. *Angewandte Chemie*, 120(4):767–770, 2008.

[20] Niek J. J. de Klerk, Irek Rosłoń, and Marnix Wagemaker. Diffusion mechanism of li argyrodite solid electrolytes for li-ion batteries and prediction of optimized halogen doping: The effect of li vacancies, halogens, and halogen disorder. *Chemistry of Materials*, 28(21):7955–7963, 2016. ISSN 0897-4756.

[21] Chuang Yu, Swapna Ganapathy, Niek J. J. de Klerk, Irek Roslon, Ernst R. H. van Eck, Arno P. M. Kentgens, and Marnix Wagemaker. Unravelling li-ion transport from picoseconds to seconds: Bulk versus interfaces in an argyrodite li6ps5cl-li2s all-solid-state li-ion battery. *Journal of the American Chemical Society*, 138(35):11192–11201, 2016. ISSN 0002-7863. doi: 10.1021/jacs.6b05066.

[22] V. Epp, Ö. Gün, H.-J. Deiseroth, and M. Wilkening. Long-range li+ dynamics in the lithium argyrodite li7pse6 as probed by rotating-frame spin–lattice relaxation nmr. *Physical Chemistry Chemical Physics*, 15(19):7123, 2013. ISSN 1463-9076. doi: 10.1039/c3cp44379e.

[23] Jean-Claude Lassègues, Joseph Grondin, Christian Aupetit, and Patrik Johansson. Spectroscopic identification of the lithium ion transporting species in litfsi-doped ionic liquids. *The Journal of Physical Chemistry A*, 113(1):305–314, 2009. ISSN 1089-5639. doi: 10.1021/jp806124w.

[24] Yundong Zhou, Christopher Doerrer, Jitti Kasemchainan, Peter G. Bruce, Mauro Pasta, and Laurence J. Hardwick. Observation of interfacial degradation of li6ps5cl against lithium metal and licoo2 via in situ electrochemical raman microscopy. *Batteries & Supercaps*, 3(7):647–652, 2020. ISSN 2566-6223. doi: 10.1002/batt.201900218.

[25] Konrad Rotnicki, Angelina Sterczyńska, Zbigniew Fojud, Monika Jażdżewska, Anatolii Beskrovnyi, Janusz Waliszewski, and Małgorzata Śliwińska Bartkowiak. Phase transitions, molecular dynamics and structural properties of 1-ethyl-3-methylimidazolium bis(trifluoromethylsulfonyl)imide ionic liquid. *Journal of Molecular Liquids*, 313:113535, 2020. ISSN 0167-7322. doi: 10.1016/j.molliq.2020.113535.

[26] Gabrielle Foran, Adrien Mery, Marc Bertrand, Steeve Rousselot, David Lepage, David Aymé-Perrot, and Mickaël Dollé. Nmr study of lithium transport in liquid–ceramic hybrid solid composite electrolytes. *ACS Applied Materials &a Interfaces*, 14(38): 43226–43236, 2022. ISSN 1944-8244. doi: 10.1021/acsami.2c10666.

[27] A.D. Bain. *Chemical Exchange Effects in NMR*, pages 180–187. Elsevier, 2017. ISBN 9780128032244. doi: 10.1016/b978-0-12-409547-2.05074-5.

[28] Kee Sung Han, J. David Bazak, Ying Chen, Trent R. Graham, Nancy M. Washton, Jian Zhi Hu, Vijayakumar Murugesan, and Karl T. Mueller. Pulsed field gradient nuclear magnetic resonance and diffusion analysis in battery research. *Chemistry of Materials*, 33(22):8562–8590, 2021. ISSN 0897-4756. doi: 10.1021/acs.chemmater.1c02891.

[29] Yuria Saito, Hitoshi Yamamoto, Osamu Nakamura, Hiroyuki Kageyama, Hiroshi Ishikawa, Tatsuo Miyoshi, and Masao Matsuoka. Determination of ionic self-diffusion coefficients of lithium electrolytes using the pulsed field gradient nmr. *Journal of Power Sources*, 81-82:772–776, 1999. ISSN 0378-7753. doi: 10.1016/s0378-7753(99)00101-9.

[30] T. Frömling, M. Kunze, M. Schönhoff, J. Sundermeyer, and B. Roling. Enhanced lithium transference numbers in ionic liquid electrolytes. *The Journal of Physical Chemistry B*, 112(41):12985–12990, 2008. ISSN 1520-6106. doi: 10.1021/jp804097j.

[31] Paulo Schmitz, Rene Jakelski, Marcelina Pyschik, Kirsi Jalkanen, Sascha Nowak, Martin Winter, and Peter Bieker. Decomposition of imidazolium-based ionic liquids in contact with lithium metal. *ChemSusChem*, 10(5):876–883, 2017. ISSN 1864-5631. doi: 10.1002/cssc.201601496.

[32] Saeed Kazemiabnavi, Zhengcheng Zhang, Katsuyo Thornton, and Soumik Banerjee. Electrochemical stability window of imidazolium-based ionic liquids as electrolytes for lithium batteries. *The Journal of Physical Chemistry B*, 120(25):5691–5702, 2016. ISSN 1520-6106. doi: 10.1021/acs.jpcb.6b03433.

[33] Sorina Cretu, David G. Bradley, Li Patrick Wen Feng, Omer Ulas Kudu, Linh Lan Nguyen, Tuan Tu Nguyen, Arash Jamali, Jean-Noel Chotard, Vincent Seznec, John V. Hanna, Arnaud Demortière, and Martial Duchamp. The impact of intergrain phases on the ionic conductivity of the lagp solid electrolyte material prepared by spark plasma sintering. *ACS Applied Materials & Interfaces*, 15(33):39186–39197, 2023. ISSN 1944-8244. doi: 10.1021/acsami.3c03839.

Summary

The overarching objective of this thesis is to advance the understanding of lithium diffusion mechanisms in argyrodite-based solid electrolytes, spanning both bulk and interfacial regimes. The aim of the chapters has been to deepen the understanding of how synthesis methods affect composition, structure and the resulting lithium-ion dynamics, provide an exploratory study into the beneficial use of space-charge layers and refine the theoretical frameworks used to interpret NMR and EIS data.

The thesis is divided into two main parts. The first part, consisting of Chapters 3, 4, and 5, focuses on bromine-rich lithium argyrodites ($Li_{6-x}PS_{5-x}Br_{1+x}$) and investigates how synthesis conditions, chemical composition, and structural disorder affect lithium-ion dynamics across multiple length and time scales. The second part, consisting of Chapter 6, explores space-charge layer formation and interfacial lithium-ion transport enhancement in hybrid electrolyte systems consisting of nano-sized chlorine argyrodite (Li_6PS_5Cl) or lithium aluminium germanium phosphate ($Li_{1.5}Al_{0.5}Ge_{1.5}(PO_4)_3$, abbreviated as LAGP) and ionic liquids with no added lithium salt.

The first part of the thesis establishes a clear correlation between synthesis conditions, structural disorder and ionic conductivity through variation of the bromine content (x=0, 0.3 and 0.5) and the use of two different cooling methods (slow cooling versus quenching). Chapter 3 examines this correlation using X-ray and neutron diffraction and focusses on the use of bromine occupancy on the 4*a*- and 4*d* sites, also referred to as 4*a*/4*d*–site disorder, as descriptor. Within the argyrodite structure, the majority of lithium occupies the 5*a*–sites, which form a cage around the 4*d*–site. The results revealed that increase in bromine content and the use of quench cooling resulted in a lower bromine occupancy at the 4*a* site outside the lithium cage and a higher occupancy of the 4*d* site inside the cage. As a result, the lithium cage expands, resulting in decreased intercage distance and increase in lithium occupancy of the T4–site, associated with an alternative, lower energy intercage pathway. These changes are correlated with increased lithium-ion conductivity as seen through EIS.

Chapter 4 delves into the use of ^{31}P, ^{6}Li, and ^{7}Li NMR spectroscopy, as well as ^{7}Li spin–lattice relaxation (T_1, SLR) studies and electrochemical impedance spectroscopy (EIS), to disentangle chemical composition and 4*a*/4*d*–site disorder. The results reveal that increased bromine content leads to disorder across the entire anion sublattice, for which the configurational entropy (S_{conf}) is a more complete descriptor. An increase in S_{conf} was further found to correlate with lithium cage distortion, which is expected to result in enhanced lithium intercage movement. For slow-cooled samples, higher S_{conf} indeed correlates with both increased ionic conductivity measured by EIS and enhanced lithium mobility observed through ^{7}Li T_1 SLR. In contrast, for quenched samples this relationship breaks down, demonstrating that synthesis conditions critically influence structure–transport correlations.

Migration entropy (ΔS_m) derived from ^{7}Li T_1 SLR follows the Meyer–Neldel law and correlates with S_{conf} and lithium cage distortion, indicating that local disorder governs short-range dynamics. In contrast, ΔS_m extracted from EIS correlates with S_{conf} only for slow-cooled samples. For quench-cooled samples, ΔS_m correlates instead with $4d$–site disorder and bromine content, suggesting that long-range diffusion, as probed by EIS, depends more strongly on chemical composition and lithium–phonon interactions at the $4d$–site. These findings emphasize that the cooling method profoundly alters the interplay between disorder, diffusion, and conductivity. Increased site disorder enhances conductivity, but improved local lithium mobility does not necessarily translate into higher macroscopic transport, highlighting the complex link between structure, dynamics, and synthesis conditions.

Chapter 5 provides a more detailed mechanistic understanding of lithium-ion diffusion by employing ^{31}P and ^{7}Li spin–lattice (T_1) and spin–lock ($T_{1\rho}$) relaxation experiments to probe site-specific motion. The ^{31}P nucleus, positioned between lithium cages, was used as a heteronuclear dipolar probe to monitor lithium-ion dynamics, allowing differentiation between intra- and intercage lithium motion and their respective activation energies. The Bloembergen–Purcell–Pound (BPP) model was used to analyse the relaxation data. By choosing the appropriate model, the extracted BPP prefactors enabled identification of the dominant relaxation mechanisms and provided insight into the nature of Li–P dipolar coupling, as well as the specific lithium sites involved in relaxation.

Two distinct relaxation processes were identified: a low-temperature component associated with mixed inter- and intracage motion through T5–T2 sites, and a high-temperature component attributed to intercage motion via the T2 site. The analysis revealed that increased $4d$–site disorder facilitates intercage motion, causing convergence of the two relaxation processes, consistent with trends observed in Chapters 3 and 4. These results further established that the T2 site represents the main pathway and principal bottleneck for long-range lithium diffusion, whereas the T4 site, where lithium motion is coupled to Br–^{31}P interactions, contributes only marginally due to its low occupancy and higher entropic barrier.

Chapter 6 extends the investigation beyond bulk argyrodites to study interfacial space-charge layer formation by mixing nano-sized Li_6PS_5Cl with ionic liquids. Static and magic-angle spinning NMR (MAS NMR) reveal the emergence of a distinct lithium environment in Li_6PS_5Cl–EMIM TFSI composites, characterized by a chemical shift consistent with LiTFSI-like species rather than the precursor compounds. Raman spectroscopy corroborated this finding. Temperature-dependent MAS NMR demonstrated that this secondary environment decreases in intensity with increasing temperature, indicating dynamic chemical exchange with the Li_6PS_5Cl bulk. Below the freezing point of EMIM TFSI, the secondary environment disappeared entirely, confirming that it originates from dynamic interfacial exchange rather than pre-existing species in the ionic liquid.

Pulsed-field gradient NMR measurements showed correlated motion between lithium and the ionic-liquid cations and anions, while EIS measurements revealed two distinct conductive contributions attributable to the bulk electrolyte and the interfacial region. Together, these findings identified and characterized a space-charge layer that enhances overall ionic conductivity by facilitating Li^+ transport across particle interfaces. Electrochemical testing in symmetric cells demonstrated that the incorporation of EMIM TFSI

reduced interfacial resistance and overpotentials. However, chemical instability of EMIM TFSI against lithium metal led to degradation upon cycling. Replacing EMIM TFSI with the more stable ionic liquid PYR_{14} TFSI markedly improved long-term stability, reducing interfacial resistance and enabling cycling at minimal applied pressure. Finally, replacing Li_6PS_5Cl with lithium aluminium germanium phosphate ($Li_{1.5}Al_{0.5}Ge_{1.5}(PO_4)_3$, LAGP) demonstrated that this approach can alleviate grain-boundary resistance in solid-state electrolytes.

The results of this thesis provide a framework for understanding lithium-ion transport in argyrodite-based solid electrolytes across microscopic and macroscopic regimes, in both the bulk and at interfaces. Through a combination of solid-state NMR, electrochemical impedance spectroscopy, and diffraction methods, this work reveals how variations in bromine composition, synthesis conditions, and resulting structural disorder shape the lithium transport network and determine macroscopic conductivity. Furthermore, this work offers a novel approach to exploring space-charge phenomena in hybrid systems and demonstrates their utility for enhancing interfacial ionic conductivity.

From a methodological perspective, this thesis advances the application of multinuclear and relaxation-based NMR techniques for probing lithium dynamics in disordered solids. By correlating structural properties with experimentally derived entropy descriptors (S_{conf} and ΔS_m), and by exploring ^{31}P relaxation through the BPP model, this work strengthens the theoretical interpretation of NMR and EIS data in the field of solid electrolytes.

The findings of this thesis open several promising directions for future research. From a materials perspective, systematic exploration of mixed-halide argyrodites and controlled synthesis strategies could further optimize the balance between structural stability and ionic mobility. From a methodological standpoint, refinement of dipolar relaxation models that explicitly incorporate fractional site occupancy and dynamic disorder would enhance the precision of NMR-derived diffusion parameters. At the interfacial level, the demonstrated approach to space-charge layer characterization suggests that combining solid electrolytes with tailored ionic liquids provides a general strategy for mitigating interfacial resistance. Future operando NMR and *in situ* spectroscopic studies could yield deeper insight into the temporal evolution of such interfacial layers during battery cycling.

Overall, this work emphasizes that achieving high-performance solid-state electrolytes requires a comprehensive understanding of the effects of chemical composition and synthesis conditions, which cannot be captured by a single descriptor. Moreover, it highlights the beneficial role that space-charge layers can play in enhancing ion transport. The experimental and theoretical advances presented herein contribute to the rational design of next-generation solid electrolytes and hybrid interfaces, advancing the realization of safe, high-energy-density solid-state batteries.

Samenvatting

Samenvatting

Het overkoepelende doel van dit proefschrift is het uitbreiden van het begrip van lithiumdiffusiemechanismen in argyrodiet-gebaseerde vaste elektrolyten, zowel in het bulkregime als aan grensvlakken. De hoofdstukken zijn erop gericht inzicht te verkrijgen in hoe synthesemethoden de samenstelling, structuur en de daaruit voortvloeiende lithiumiondynamica beïnvloeden, een verkennende studie te bieden naar het gunstige gebruik van ruimte-ladingslagen (*space-charge layers*) en de theoretische kaders te verfijnen die worden gebruikt voor de interpretatie van NMR- en EIS-data.

Het proefschrift is opgedeeld in twee hoofdonderdelen. Het eerste deel, bestaande uit hoofdstukken 3, 4 en 5, richt zich op broomrijke lithiumargyrodieten ($Li_{6-x}PS_{5-x}Br_{1+x}$) en onderzoekt hoe synthesecondities, chemische samenstelling en structurele wanorde de lithium-iondynamica beïnvloeden over meerdere lengte- en tijdschalen. Het tweede deel, bestaande uit hoofdstuk 6, onderzoekt de vorming van zogenaamde "Space charge layers" en de verbetering van interfaciaal lithium-iontransport in hybride elektrolytsystemen die bestaan uit chloor-argyrodiet (Li_6PS_5Cl) met een deeltjesgrootte in de nanoregime, of lithiumaluminiumgermaniumfosfaat ($Li_{1.5}Al_{0.5}Ge_{1.5}(PO_4)_3$, LAGP) en ionische vloeistoffen zonder toegevoegd lithiumzout.

Het eerste deel van het proefschrift legt een duidelijke correlatie vast tussen synthesecondities, structurele wanorde en ionische geleidbaarheid door variatie van het broomgehalte (x = 0, 0,3 en 0,5) en door het gebruik van twee verschillende koelmethoden (langzaam afkoelen versus afschrikken). Hoofdstuk 3 onderzoekt deze correlatie met behulp van röntgen- en neutronendiffractie en richt zich op de broombezetting van de 4*a*- en 4d-posities, ook wel aangeduid als "4*a*/4*d*-site disorder", als descriptor. Binnen de argyrodietstructuur bevindt het merendeel van het lithium zich op de 5*a*-posities, die een kooi vormen rond de 4*d*-positie. De resultaten laten zien dat een toename van het broomgehalte en het toepassen van afschrikkoeling leiden tot een lagere broombezetting van de 4*a*-positie buiten de lithiumkooi en een hogere bezetting van de 4*d*-positie binnen de kooi. Hierdoor zet de lithiumkooi uit, wat resulteert in een kleinere afstand tussen de kooien en een hogere lithiumbezetting van de T4-positie, die geassocieerd is met een alternatieve intercage-transportroute met lagere energie. Deze veranderingen correleren met een verhoogde lithium-iongeleiding, zoals waargenomen met EIS.

Hoofdstuk 4 gaat dieper in op het gebruik van ^{31}P-, ^{6}Li- en ^{7}Li-NMR-spectroscopie, evenals ^{7}Li spin-roosterrelaxatie (T_1, SLR) en EIS, om de effecten van chemische samenstelling en 4*a*/4*d*-plaatswanorde te ontwarren. De resultaten tonen aan dat een hoger broomgehalte leidt tot wanorde over het gehele anionsublattice, waarvoor de configuratie-entropie (S_{conf}) een meer volledige descriptor vormt. Een toename van S_{conf} correleert bovendien met vervorming van de lithiumkooi, wat naar verwachting leidt tot een toename van intercage-lithiumbeweging.

Voor langzaam gekoelde monsters correleert een hogere S_{conf} met zowel een verhoogde ionische geleidbaarheid gemeten met EIS als met een hogere lithium-mobiliteit, waargenomen via ^{7}Li T_1 SLR. Voor afgeschrikte monsters valt deze relatie echter weg, wat aantoont dat synthesecondities een cruciale invloed hebben op structuur–transportcorrelaties. De migratie-entropie (ΔS_m), afgeleid uit ^{7}Li T_1 SLR, volgt de Meyer–Neldel-wet en correleert met S_{conf} en vervorming van de lithiumkooi, wat aangeeft dat lokale wanorde de kortafstandsdynamica bepaalt. Daarentegen correleert ΔS_m uit EIS alleen met S_{conf} voor langzaam gekoelde monsters. Voor afgeschrikte monsters correleert ΔS_m in plaats daarvan met 4d-plaatswanorde en broomgehalte, wat suggereert dat langeafstandsdiffusie, zoals onderzocht met EIS, sterker afhankelijk is van de chemische samenstelling en lithium–fononinteracties op de 4d-positie.

Hoofdstuk 5 biedt een meer gedetailleerd mechanistisch inzicht in lithium-iondiffusie door het gebruik van ^{31}P- en ^{7}Li spin-rooster- (T_1) en spin-lock- ($T_{1\rho}$) relaxatie-experimenten om plaats-specifieke beweging te onderzoeken. De ^{31}P-kern, gepositioneerd tussen lithiumkooien, werd gebruikt als heteronucleaire dipolaire probe om lithium-iondynamica te volgen. Het Bloembergen–Purcell–Pound (BPP)-model werd toegepast om de relaxatiegegevens te analyseren.

Hoofdstuk 6 breidt het onderzoek uit voorbij bulkargyrodieten door de vorming van interfaciale ruimte-ladingslagen te bestuderen via het mengen van nanogrootte Li_6PS_5Cl met ionische vloeistoffen. Statische en magic-angle spinning NMR (MAS NMR) onthullen het ontstaan van een distincte lithiumomgeving in Li_6PS_5Cl–EMIM TFSI-composieten. Temperatuurafhankelijke MAS NMR toont aan dat deze secundaire omgeving afneemt bij toenemende temperatuur, wat wijst op dynamische uitwisseling met de bulk. Onder het vriespunt van EMIM TFSI verdwijnt deze omgeving volledig, wat bevestigt dat zij voortkomt uit dynamische interfaciale uitwisseling.

Samenvattend benadrukt dit werk dat het bereiken van hoogwaardige vaste-stofelektrolyten een diepgaand begrip vereist van de invloed van chemische samenstelling en synthesecondities, die niet met één enkele descriptor kan worden vastgelegd. De combinatie van experimentele en theoretische vooruitgang die hier wordt gepresenteerd draagt bij aan het rationele ontwerp van volgende-generatie vaste elektrolyten en hybride interfaces, en bevordert daarmee de realisatie van veilige vaste-stofbatterijen met hoge energiedichtheid.

A

Appendix Chapter 3

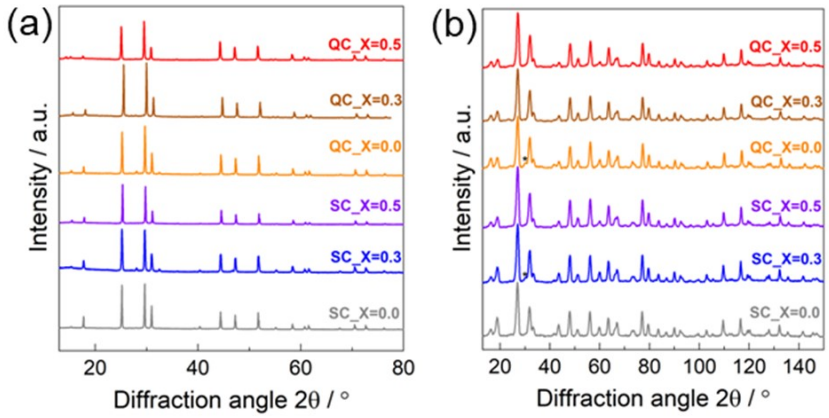

Figure A.1: (a) X-ray diffraction and (b) neutron diffraction patterns of $Li_{6-x}PS_{5-x}Br_{1+x}$ as a function of Br content for the slow-cooled "SC" and quench cooled "QC" methods.

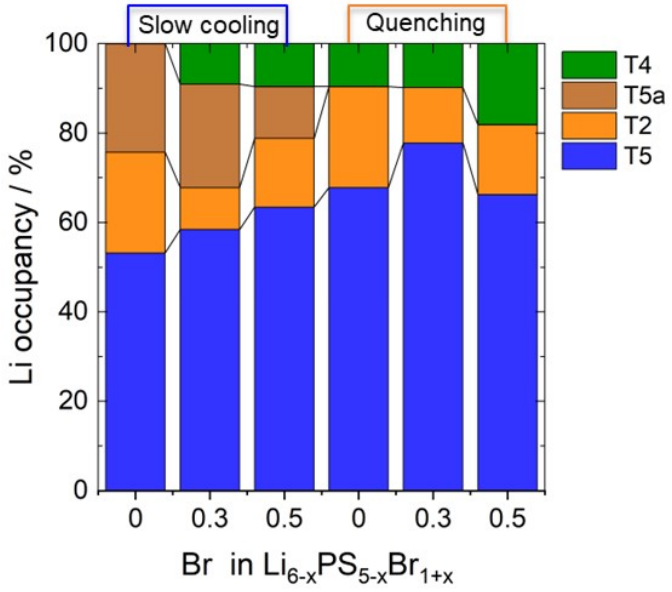

Figure A.2: Figure S2: The Li^+ distribution across the different sites of $Li_{6-x}PS_{5-x}Br_{1+x}$ as a function of Br content.

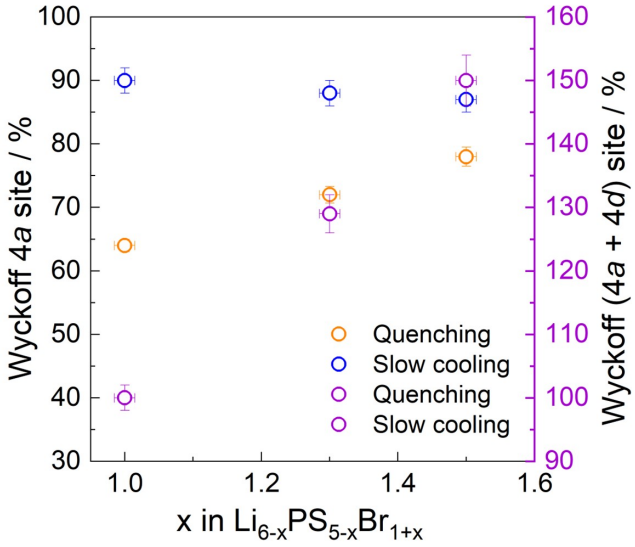

Figure A.3: Percentage of Br content distributed across Wyckoff 4a site, and total Br content in each composition ($Li_{6-x}PS_{5-x}Br_{1+x}$).

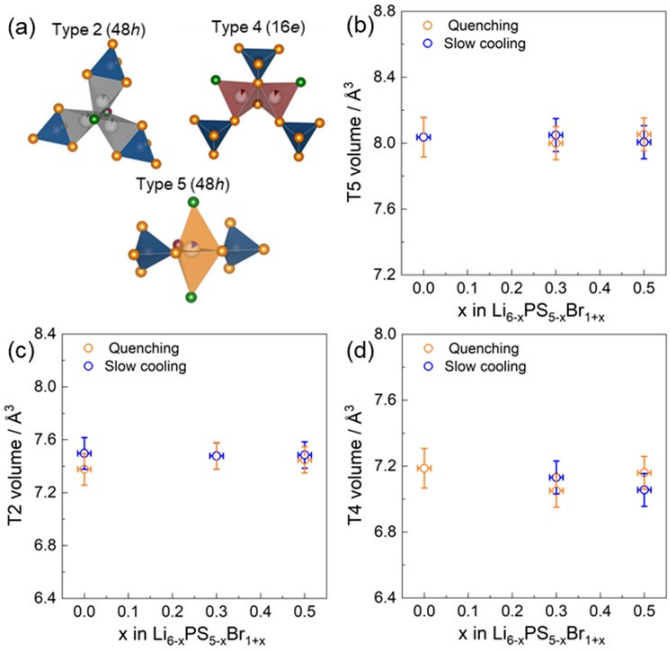

Figure A.4: (a) Lithium diffusion pathway showing the tetrahedral face-connection between the T2 and T4 site that connects the different Li^+ cages (proposed in [?]). (b) T5, (c) T2, and (d) T4 volume as a function of Br content.

A

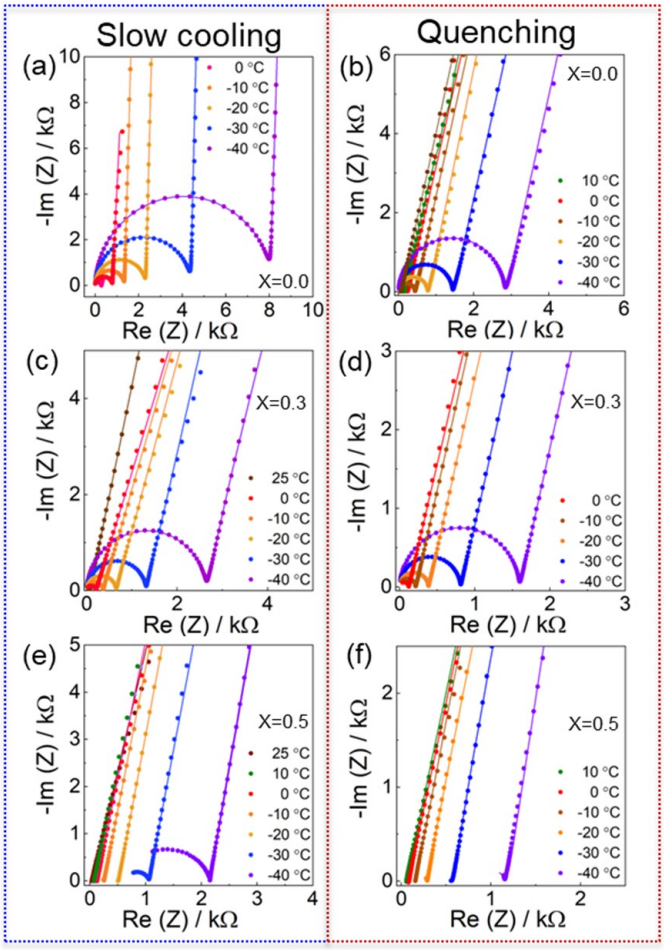

Figure A.5: (a) Nyquist plots of the impedance response of the $Li_{6-x}PS_{5-x}Br_{1+x}$ series at a temperature range of -0℃ to 10℃. The closed circles indicate the impedance data and line representing the obtained impedance, exhibited capacitances of around 1 to 8 x 10-10 F cm-2, and an α value of 0.89–0.9, corresponding to bulk transport.

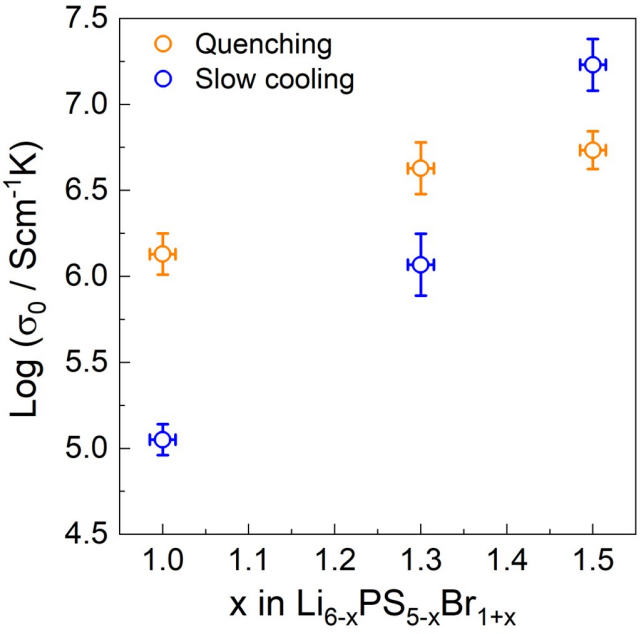

Figure A.6: Pre-factor (σ0) obtained from Arrhenius fits of the conductivity obtained from EIS using the ion (σ) = σ0 exp(-EA/kT)), for varying levels of Br content, slow cooling, and quenched compositions.

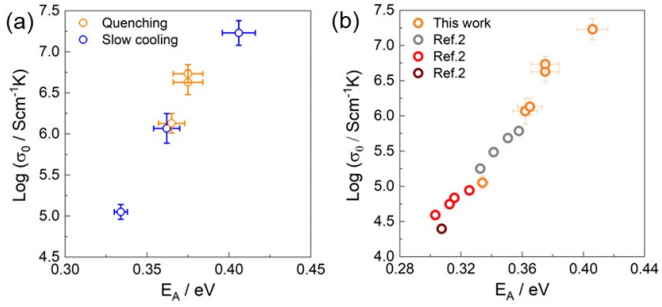

Figure A.7: Meyer-Neldel plot of log (σ0) vs. EA, showing the enthalpy-entropy compensation of the pre-factor with the activation barrier. The data for Li_6PS_5Br are taken from [**?**].

A

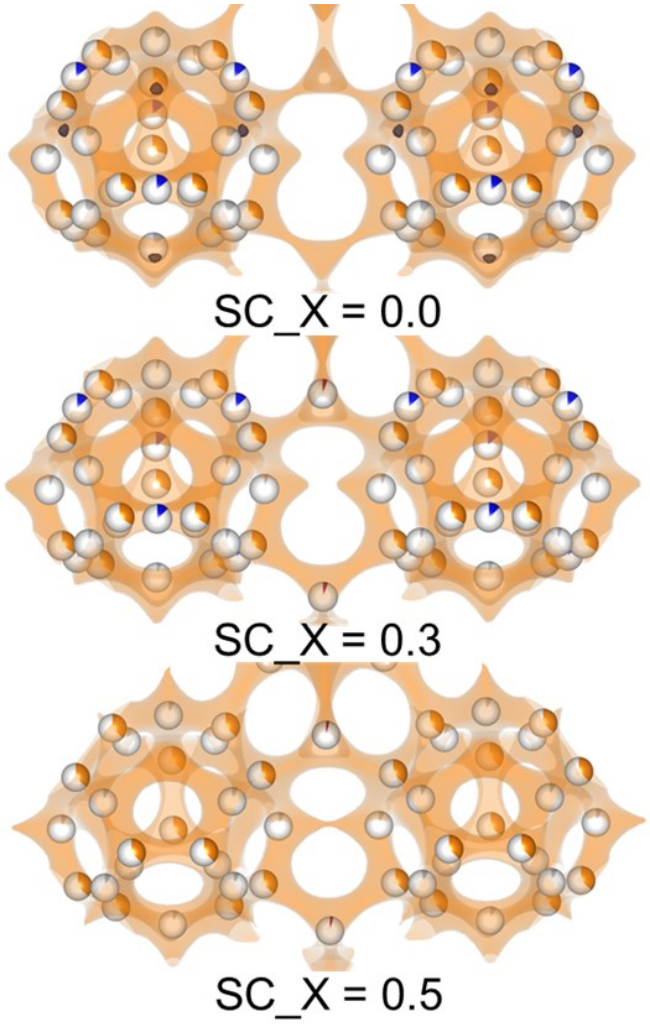

Figure A.8: BVSE lithium diffusion pathway of slow cooling compositions x=0.0, 0.3, and 0.5($Li_{6-x}PS_{5-x}Br_{1+x}$)

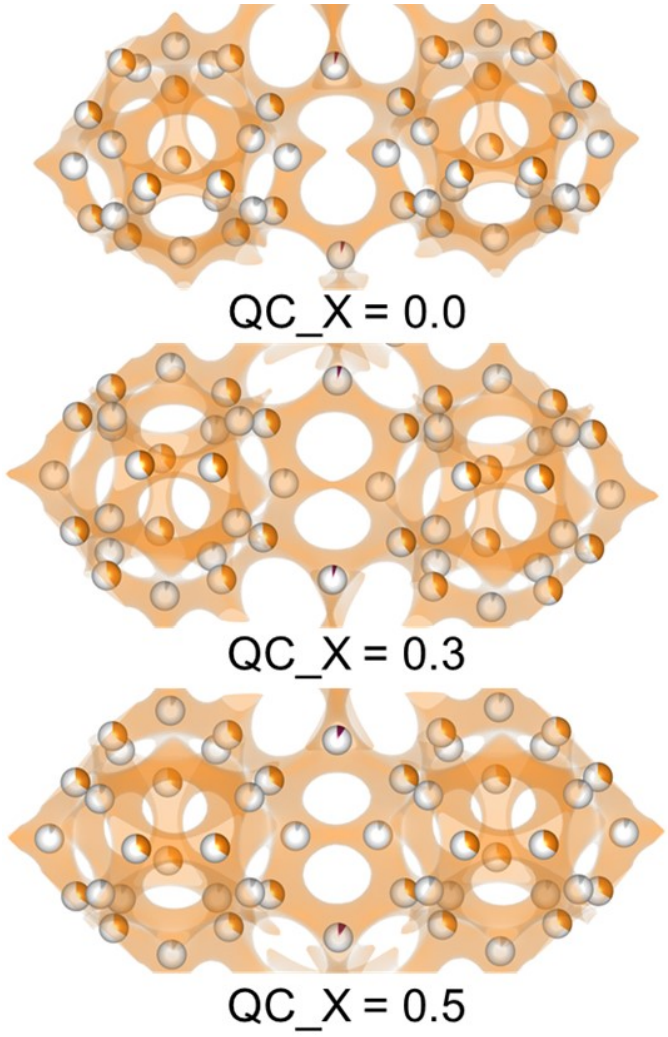

Figure A.9: BVSE lithium diffusion pathway of quenching compositions x=0.0, 0.3, and 0.5 ($Li_{6-x}PS_{5-x}Br_{1+x}$).

A

Table A.1: Constraints used to refine $Li_{6-x}PS_{5-x}Br_{1+x}$ neutron diffraction data.

Atom	Wyckoff site	x/a	y/b	z/c	Occ	Beq/ Å2
LiT5	48h	Pos1	Pos2	1-Pos1	Occ1	Var1
LiT2	48h	Pos3	Pos4	0.5+Pos4	((7-(1-Occ3+Occ4))*4-48*Occ1-24*Occ5-16*Occ6)/48	Var2
LiT5a	24g	0.25	Pos5	0.75	Occ5	Var1
LiT4	16e	Pos6	Pos6	Pos6	Occ6	Var3
Br1	4a	0	0	1	Occ3	Var4
Br2	4d	0.25	0.25	0.75	1-Occ4	Var5
P1	4b	0	0	0.5	1	Var6
S1	4d	0.25	0.25	0.75	Occ4	Var5
S2	16e	Pos7	-Pos7	0.5+Pos7	1	Var7
S3	4a	0	0	1	1-Occ3	Var4

Table A.2: Crystallographic data of slow-cooled Li_6PS_5Br sample. The lattice parameter, atomic positions, and occupancies are obtained from the Rietveld refinements against the neutron diffraction data. The uncertainty/error value is shown in brackets. a = 9.9835(2) Å; 0.52 wt Rwp = 6.0 %,; λ = 1.667 Å

Atom	Wyckoff site	x/a	y/b	z/c	Occ	Beq/ Å2
LiT5	48h	0.3036(1)	0.0231(2)	0.6964(1)	0.30(2)	2.2(3)
LiT2	48h	0.296(7)	0.087(6)	0.587(6)	0.13(2)	14(4)
LiT5a	24g	0.25	0.013(6)	0.75	0.135(6)	2.1(4)
LiT4	16e	–	–	–	–	–
Br1	4a	0	0	1	0.90(2)	2.92(2)
Br2	4d	0.25	0.25	0.75	0.12(2)	1.6(2)
P1	4b	0	0	0.5	1	2.92(2)
S1	4d	0.25	0.25	0.75	0.88(2)	1.44(4)
S2	16e	0.1185(4)	-0.1185(4)	0.6185(4)	1	2.02(7)
S3	4a	0	0	1.0	0.10(2)	1.6(2)

Table A.3: Crystallographic data of slow-cooled $Li_{5.7}PS_{4.7}Br_{1.3}$ sample. The lattice parameter, atomic positions, and occupancies are obtained from the Rietveld refinements against the neutron diffraction data. The uncertainty/error value is shown in brackets. a = 9.9826(2) Å; 0.4 wt Rwp = 6.4 % ; λ = 1.667 Å

Atom	Wyckoff site	x/a	y/b	z/c	Occ	Beq/ Å2
LiT5	48h	0.0306(9)	0.0207(1)	0.6937(1)	0.324(8)	3.5(2)
LiT2	48h	0.2927(9)	0.0862(7)	0.58	0.073(2)	10(2)
LiT5a	24g	0.25	0.011(7)	0.75	0.126(2)	2.9(3)
LiT4	16e	0.162(9)	0.162(9)	0.162(9)	0.044(7)	3.0(2)
Br1	4a	0	0	1	0.88(2)	2.68(9)
Br2	4d	0.25	0.25	0.75	0.40(1)	2.11(9)
P1	4b	0	0	0.5	1	1.46(5)
S1	4d	0.25	0.25	0.75	0.60(2)	2.11(9)
S2	16e	0.1181(3)	-0.1181(3)	0.6181(3)	1	2.38(6)
S3	4a	0	0	1.0	0.12(2)	2.68(9)

Table A.4: Crystallographic data of slow-cooled $Li_{5.5}PS_{4.5}Br_{1.5}$ sample. The lattice parameter, atomic positions, and occupancies are obtained from the Rietveld refinements against the neutron diffraction data. The uncertainty/error value is shown in brackets.a = 9.9742(2) Å; 0.6 wt % LiBr Rwp = 6.0 % ; λ = 1.667 Å

Atom	Wyckoff site	x/a	y/b	z/c	Occ	Beq/ Å2
LiT5	48h	0.309(1)	0.0147(2)	0.690(1)	0.326(9)	3.7(8)
LiT2	48h	0.283(3)	0.0855(7)	0.5854(7)	0.084(3)	14(3)
LiT5a	24g	0.25	0.015(2)	0.75	0.065(6)	3.8(4)
LiT4	16e	0.155(8)	0.155(8)	0.155(8)	0.05(1)	3.8(5)
Br1	4a	0	0	1	0.87(3)	2.32(9)
Br2	4d	0.25	0.25	0.75	0.64(3)	2.33(9)
P1	4b	0	0	0.5	1	2.11(1)
S1	4d	0.25	0.25	0.75	0.36(3)	2.33(9)
S2	16e	0.1186(3)	-0.1186(3)	0.6186(3)	1	3.2(1)
S3	4a	0	0	1.0	0.13(3)	2.32(9)

Table A.5: Crystallographic data of quenched Li_6PS_5Br sample. The lattice parameter, atomic positions, and occupancies are obtained from the Rietveld refinements against the neutron diffraction data. The uncertainty/error value is shown in brackets.a = 9.9592(2) Å; 0.81 wt % Li_3PO_4; 2.07 wt % LiBr Rwp = 3.59 % ; λ = 1.667 Å

Atom	Wyckoff site	x/a	y/b	z/c	Occ	Beq/ Å2
LiT5	48h	0.3088(9)	0.0181(1)	0.6912(9)	0.359	3.9(4)
LiT2	48h	0.300(7)	0.0789(5)	0.5789(5)	0.12(2)	13(4)
LiT5a	24g	–	–	–	–	–
LiT4	16e	0.158(7)	0.158(7)	0.158(7)	0.05(1)	3.89(4)
Br1	4a	0	0	1	0.64(2)	2.6(1)
Br2	4d	0.25	0.25	0.75	0.39(2)	2.1(1)
P1	4b	0	0	0.5	1	1.52(5)
S1	4d	0.25	0.25	0.75	0.61(2)	2.1(1)
S2	16e	0.1182(1)	-0.1182(1)	0.6182(1)	1	2.39(5)
S3	4a	0	0	1.0	0.36(2)	2.6(1)

A

Table A.6: Crystallographic data of quenched $Li_{5.7}PS_{4.7}Br_{1.3}$ sample. The lattice parameter, atomic positions, and occupancies are obtained from the Rietveld refinements against the neutron diffraction data. The uncertainty/error value is shown in brackets.a = 9.9718(2) Å; 0.27 wt % Li_3PO_4 Rwp = 5.10 % ; λ = 1.667 Å

Atom	Wyckoff site	x/a	y/b	z/c	Occ	Beq/ Å2
LiT5	48h	0.306(1)	0.178(2)	0.0694(1)	0.396(2)	4.9(5)
LiT2	48h	0.2699(9)	0.074(9)	0.574(7)	0.063(2)	9(3)
LiT5a	24g	–	–	–	–	–
LiT4	16e	0.154(2)	0.154(2)	0.154(2)	0.05(1)	4.8(4)
Br1	4a	0	0	1	0.72(2)	2.27(9)
Br2	4d	0.25	0.25	0.75	0.58(2)	2.13(9)
P1	4b	0	0	0.5	1	1.75(4)
S1	4d	0.25	0.25	0.75	0.42(2)	2.13(9)
S2	16e	0.1187(2)	-0.1187(2)	0.6940(8)	1	2.31(4)
S3	4a	0	0	1.0	0.28(2)	2.27(9)

Table A.7: Crystallographic data of quenched $Li_{5.5}PS_{4.5}Br_{1.5}$ sample. The lattice parameter, atomic positions, and occupancies are obtained from the Rietveld refinements against the neutron diffraction data. The uncertainty/error value is shown in brackets.

Atom	Wyckoff site	x/a	y/b	z/c	Occ	Beq/ Å2
LiT5	48h	0.3099(9)	0.0151(1)	0.6901(9)	0.34(1)	3.96(5)
LiT2	48h	0.288(3)	0.074(2)	0.574(2)	0.084(2)	13(2)
LiT5a	24g	–	–	–	–	–
LiT4	16e	0.152(4)	0.152(4)	0.152(4)	0.093(2)	3.90(5)
Br1	4a	0	0	1	0.78(2)	1.94(1)
Br2	4d	0.25	0.25	0.75	0.72(3)	2.35(1)
P1	4b	0	0	0.5	1.0	2.35(1)
S1	4d	0.25	0.25	0.75	0.28(3)	2.35(1)
S2	16e	0.11774(1)	-0.11774(1)	0.61774(1)	1.0	3.2(1)
S3	4a	0	0	1.0	0.22(2)	1.94(1)

B

Appendix Chapter 4

B.1 Results obtained by Gautam *et al.*

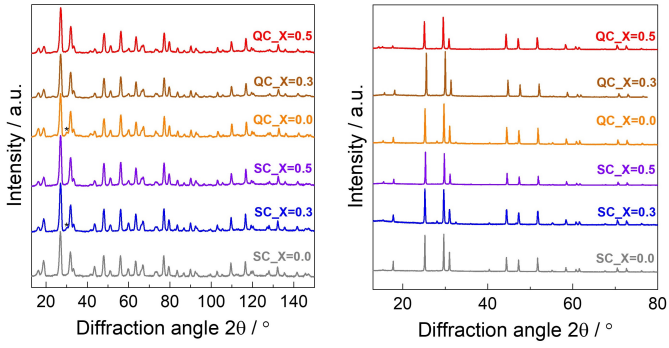

Figure B.1: The Neutron (left) and X-ray (right) diffraction patterns obtained for slow-cooled (SC) and quench-cooled (QC) samples. Reused with permission from A. Gautam *et al.* Chem. Mater. 2023, 35, 8081 [6] . Copyright 2023 American Chemical Society.

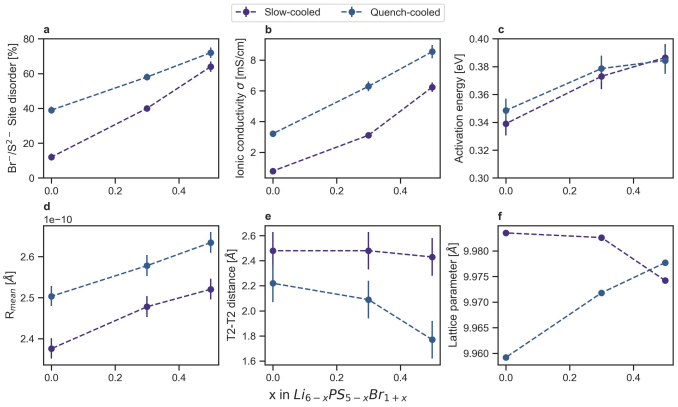

Figure B.2: Results obtained by Gautam *et al.* [6] showing as a function of Br-content (a) the 4*d* site disorder, (b) the ionic conductivity from EIS, (c) the activation energy obtained from EIS, and the structural parameters obtained from XRD and neutron diffraction including (d) the radius of the Li-cage, (e) the T2-T2-distance and the lattice parameter (f).

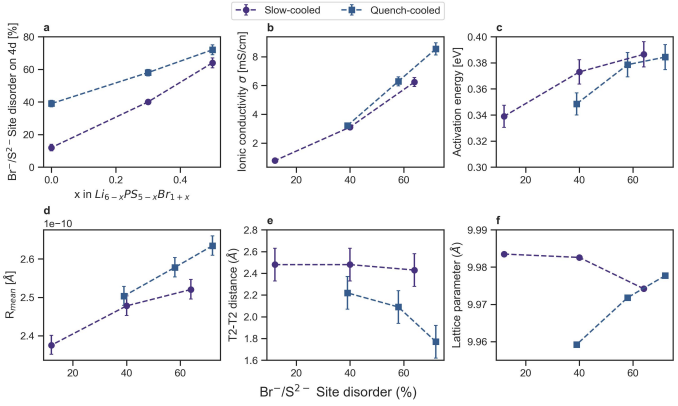

Figure B.3: Results obtained by Gautam *et al.* [6] showing as a function of site-disorder (a) the 4*d* site disorder, (b) the ionic conductivity from EIS, (c) the activation energy obtained from EIS, and the structural parameters obtained from XRD and neutron diffraction including (d) the radius of the Li-cage, (e) the T2-T2-distance and the lattice parameter (f).

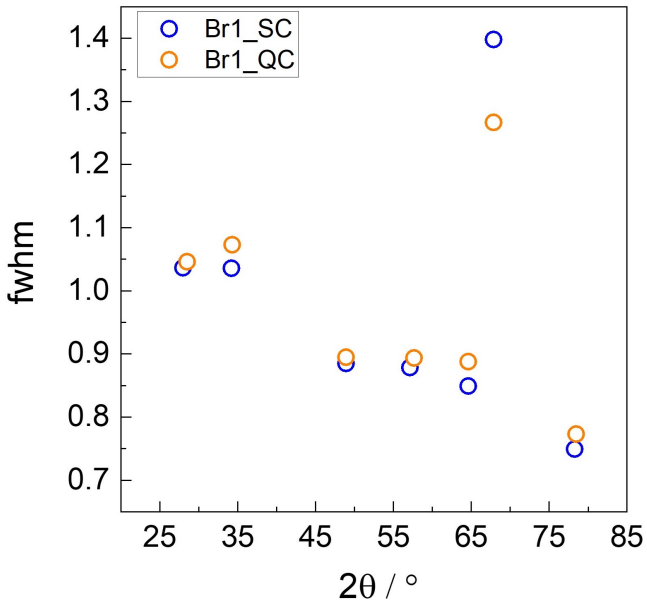

Figure B.4: The full-width half maximum obtained from X-ray diffraction for Br1 SC and Br1 QC as a function of diffraction angle. Reused with permission from A. Gautam *et al.* Chem. Mater. 2023, 35, 8081 [6]. Copyright 2023 American Chemical Society.

B.2 The Neldel-Meyer Energy

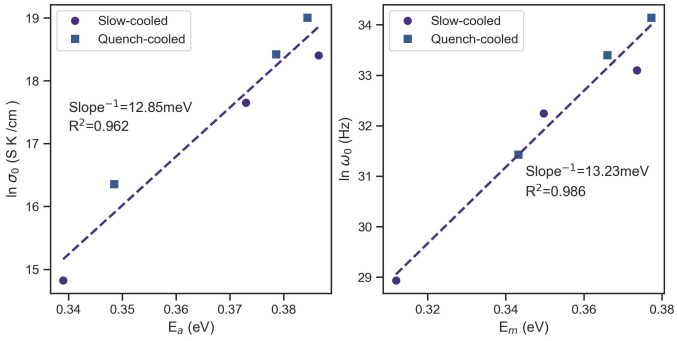

Figure B.5: The prefactor versus the activation energy from EIS (left) and hopping (right) and the inverse of the slope in meV corresponding to the Meyer–Neldel energy. Data for the right panel is taken from [6].

B.3 Distances calculated from Dipolar Coupling

The distances were calculated using the formula below, where γ_{Li} is the ^{7}Li gyromagnetic ratio, $\hbar$ the reduced Planck constant, μ_0 the vacuum permeability and C the constant ob-

tained from the modified BPP-model fit.

$$r = \sqrt[6]{\frac{3\gamma_{Li}^4 \hbar^2 \mu_0^2}{32\pi^2 C}}$$

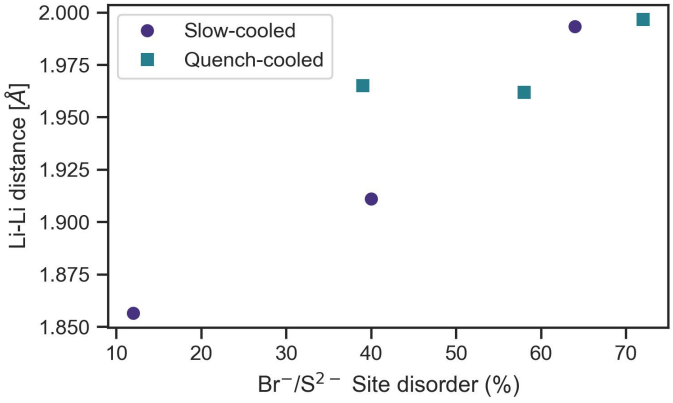

Figure B.6: The Li–Li distance calculated assuming exclusively homonuclear dipolar coupling as a function of site-disorder

B.4 The Br-occupancies on the 4*d*- and 4*a*-site

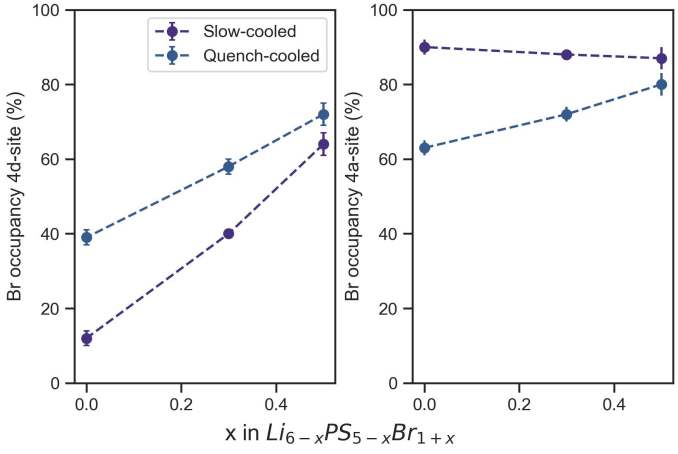

Figure B.7: Plots of the percentage of 4*d*–sites (left) and 4*a*–sites (right) occupied by bromine (Br) as a function of Br-content for the slow-cooled and quenched samples. The sulphur occupancy is defined as 100 %-Br occupancy. Data is taken from [6]

B.5 The Probability Density of Li^+ Obtained from MD-simulations

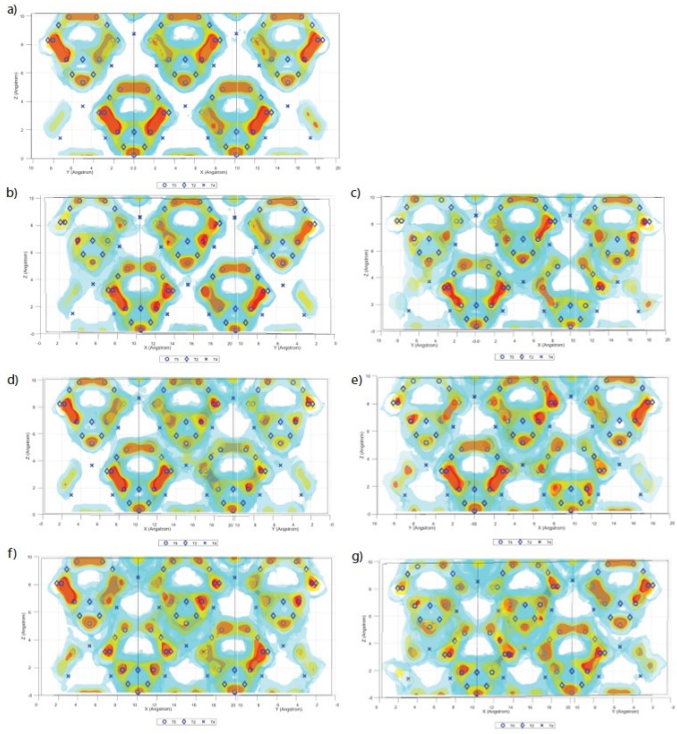

Figure B.8: The probability density of Li^+: a) Li_6PS_5Br with n site disorder; b) Li_6PS_5Br slow cooled; c) Li_6PS_5Br quench cooled; d) $Li_{5.7}PS_{4.7}Br_{1.3}$ slow cooled; e)$Li_{5.7}PS_{4.7}Br_{1.3}$ quench cooled; f)$Li_{5.5}PS_{4.5}Br_{1.5}$ slow cooled; g) $Li_{5.5}PS_{4.5}Br_{1.5}$ quench cooled.

B.6 Configurational Entropy

The configurational entropy was calculated using [12]:

$$S_{conf} = -R \sum_{i=1}^{n} x_i \ln x_i \tag{B.1}$$

Two sublattices were considered in this system, namely the $4a$- and $4d$- sublattices. For each sublattice, two elements were considered, namely sulfur and bromine. Using the occupancy of Br and Sulphur at the $4d$- and $4a$-sites as the x_i-values, the configurational entropy can be defined as:

$$S_{conf} = -R\left[Br_{4d}\ln(Br_{4d}) + S_{4d}\ln(S_{4d}) + Br_{4a}\ln(Br_{4a}) + S_{4a}\ln(S_{4a})\right]$$

B.7 EIS Data Processing

The obtained EIS data was processed to obtain the hopping frequency (ω) using the method of Almond *et al.* [2] and further developed by Li textitet al. [11] The angular-frequency-dependent conductivity (σ_ω) can be defined as:

$$\sigma_\omega = \sigma_0 + A\omega^n \tag{B.2}$$

with ω_0 being the conductivity in the d.c. limit. Almond *et al.* also derive that:

$$A = \frac{\sigma_0}{\omega_p^n} \tag{B.3}$$

with ω_p being the hopping rate. Combining these equations gives us:

$$\sigma_\omega = \sigma_0 \left[1 + \left(\frac{\omega}{\omega_p} \right)^n \right] \tag{B.4}$$

Li *et al.* show that ω_p can be obtained from the frequency-dependent conductivity spectra when:

$$\omega_p = 2\sigma_0 \tag{B.5}$$

In the Bode spectra obtained from EIS, this corresponds to the frequency at which the resistance is half of the d.c. limit resistance. By assuming that the system can be described as a resistance and a constant phase element in parallel, the obtained impedance can be expressed as [4]

$$Z(\omega) = \frac{R}{1 + (i\omega)^\alpha QR} \tag{B.6}$$

Here R is the resistance of the electrolyte, Q is the CPE-constant and α is the dimensionless constant that represents the deviation from ideal capacitor behaviour. By assuming that Z(ω_p)=0.5 R we get:

$$\omega_p = \left(\frac{1}{QR} \right)^\alpha \tag{B.7}$$

Obtaining the Q-, R- and α-values from the impedance fit allows us to obtain ω_p in rad/s for all samples at the temperatures given. These values were checked manually at 223 K using the Bode-plot obtained.

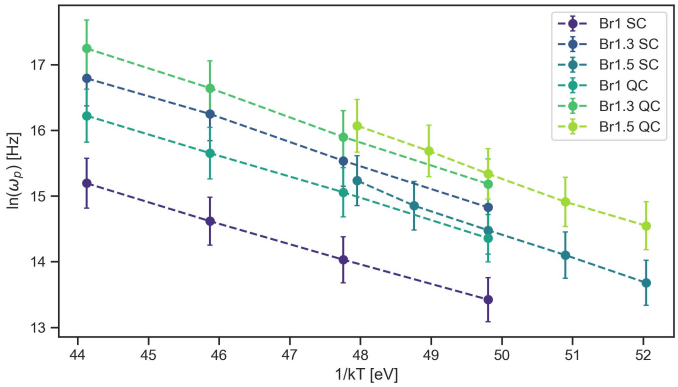

Figure B.9: The natural logarithm of the jump frequencies obtained from EIS-analysis vs. $1/k_BT$ for all six samples. The dashed lines are a guide for the eye.

Finally, using: $\omega = \omega_0 e^{\frac{\Delta S_M}{k_B}} e^{-\frac{\Delta H_M}{k_B T}}$ we can obtain ΔH_M and the entropic pre-factor. Note the conversion from rad/s to Hz.

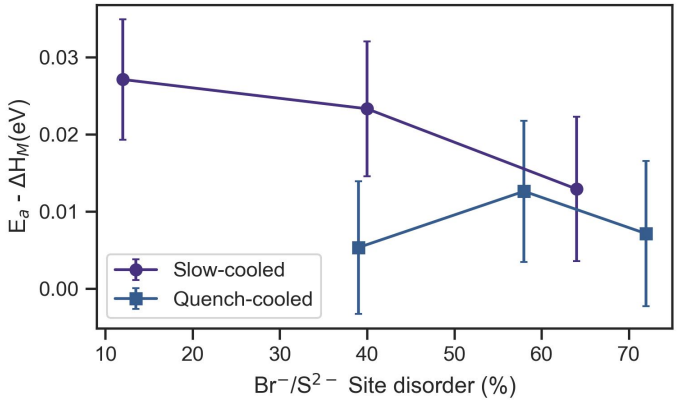

Figure B.10: The difference between the activation energy (E_a) and the enthalpy of migration (ΔH_m) obtained from EIS.

B.8 Calculation Distances 4*d*-sites

The formula for calculating ν^0_{Osc} is:

$$\nu^0_{Osc} = \frac{1}{a_0}\sqrt{\frac{2E_a}{M_{Li^+}}}$$

Here, M_{Li^+} is the mass of the lithium ion and E_a the activation energy obtained from the BPP-fit from SLR NMR or the ΔH_M-value from EIS.

The a_0 is defined as the distance between two $4d$–sites within the unit cell (see Figure ??a) minus the R_{mean}.

We know from symmetry that $b_1 + b_2 = a_0$.

B

The distance between two $4d$-sites at the centre of the Lithium cages (a) was calculated based on the cell constant (c) obtained using the formula:

$$a_0 = \sqrt{\frac{1}{2}c^2 + c^2} - 2R_{mean} = \frac{\sqrt{2}}{2}c - 2R_{mean}$$

The values for c and R_{mean} were obtained from Gautam et. al. [6].

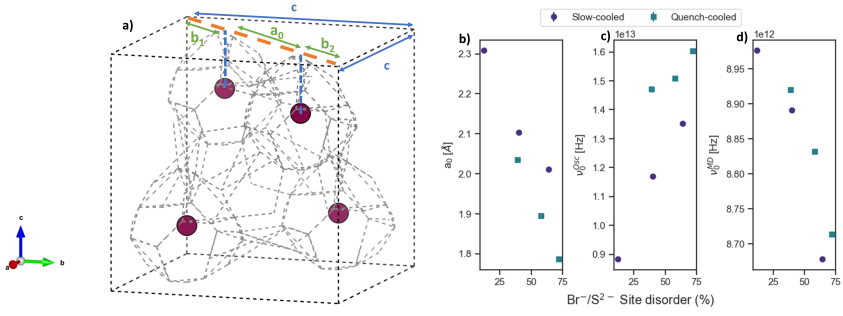

Figure B.11: Argyrodite lattice showing only the $4d$-site positions and Li-cage outlines and the definitions for c, a_0, b_1 and b_2, (b) the a_0 values obtained, (c) the ν_0^{osc}-values used in the main text and (d) the ν_0^{MD} -values obtained from MD-simulations and used in the main text.

B.9 The ^{31}P MAS NMR Linewidths

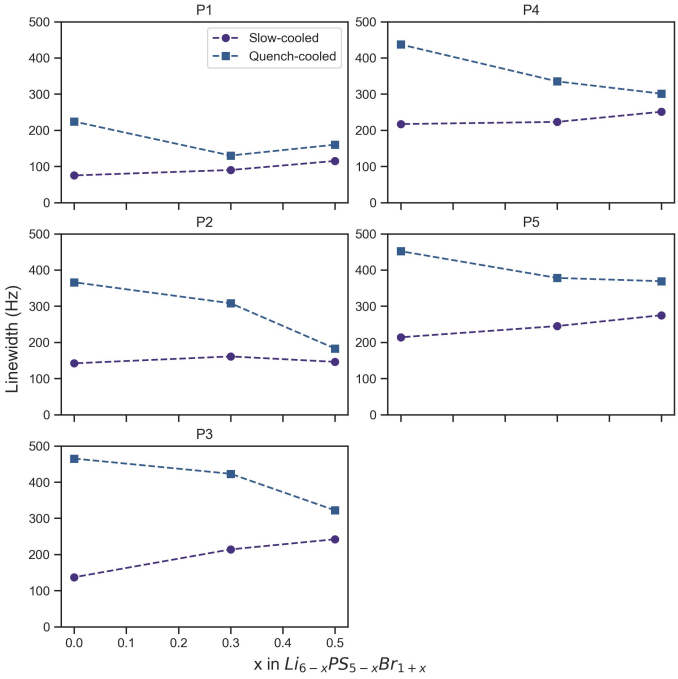

Figure B.12: The MAS linewidths of the ^{31}P environments mentioned in the main text at 293 K.

B.10 A Brief Explanation of Migrational Entropy

Classically, the entropy of a system can be described using the Boltzmann entropy equation (see below). This equation gives the relationship between the entropy of a system and W, the number of ways in which microscopically distinct states can give rise to the same macroscopic thermodynamic state.[17]

$$S = k_{\mathrm{B}} \ln(W) \tag{B.8}$$

The entropy of migration has been interpreted in various ways, with the two most prominent interpretations being the multi-excitation entropy model (MEE) and the phonon vibrational model.[1, 7, 14] To understand the relationship between this term and material structure, both interpretations will be discussed here.

The multi-excitation entropy model (MEE) provides a similar interpretation of ΔS_M to the classical one and assumes the existence of multiple excitations. Yelon *et al.* argue that when the energy barrier for a jump (ΔH_M) is larger than $\hbar\omega$ (the energy of available excitations) and $k_B T$, multiple excitations must work together to surmount it.[16, 17] The higher this barrier is, the more excitations are needed and hence the more ways there are of combining them. The entropic term (ΔS_M) can therefore be defined as the number of ways to assemble the necessary amount of excitations needed (n) to pass the barrier from

the total number possible (N) in the interaction volume, resulting in the equation below, which can be simplified when assuming that $n \ll N$.

$$\Delta S_M = k_B \ln \frac{N!}{n!(N-n)!} \approx k_B \frac{\Delta H_M \ln N}{\hbar\omega} \tag{B.9}$$

Assuming that for similar compounds the energy per excitation is similar, a higher ΔS_M-value can have two origins according to Equation (B.9). Either the energy barrier is larger (larger ΔH_M) or a larger number of excitations is available (larger N).The second interpretation is related to the phonon vibrations of the materials and is often used to relate the ΔS_M-values obtained from EIS to material structure and chemical composition.[3, 5, 9, 10]

Phonons describe the collective vibrations of atoms in a lattice and depend on the lattice parameters as well as the chemical composition. Phonon frequencies increase for harder, smaller, less polarizable atoms and more spatial constriction. The relationship between the entropy of migration and the phonon vibrations of the lattice is given by Equation (B.10).[8, 15] Here, ΔS_M is the ratio of the product of the normal frequencies of the lattice where lithium is at the initial site (ν_i^I) and the lattice where lithium is at the saddle point (ν_i^S). The attempt frequency ν_0 is seen as the frequency of the vibrational mode that carries lithium across the saddle point. Equation (B.10) relates the entropy of migration to the lattice vibrations experienced by the lithium ion during diffusion.[13]

$$\Delta S_M = k_B \ln \frac{\prod_{i=1}^{3N} \nu_i^I}{\prod_{i=1}^{3N-1} \nu_i^S} \tag{B.10}$$

B.11 Calculating the Diffusion Distances

The root mean square displacement of a particle, assuming three dimensional Brownian motion can be expressed as [18]20:

$$x = \sqrt{6Dt}$$

With D being the diffusion constant in [cm^2/s] and t being the time over which diffusion takes place in seconds.

For impedance spectroscopy, the relationship between conductivity and D is:

$$\sigma = \frac{D_{EIS} n e^2 z^2}{kT}$$

giving:

$$D_{EIS} = \frac{\sigma k T}{n e^2 z^2}$$

Here, σ is the conductivity in [S/cm], k is the Boltzmann constant, T is the temperature in [K], e is the elementary charge (1.602×10^{-19} C), z is the ionic charge (equal to 1 for Li^+) and n is the charge carrier density of lithium ions, which is defined as:

$$n = \frac{4(6-x)}{c^3}$$

Where the nominator is the amount of Li-ions per unit cell and c is the lattice constant in [cm]. For the time t, we take the inverse of maximum frequency of the EIS experiment ($1/10^6$ Hz).

For NMR, the diffusion constant is defined as:

$$D_{NMR} = \frac{a^2}{K\tau_c}$$

With a being the jump distance in [cm] taken as the distance between two $4d$-sites defined in section 8, K being a dimensionality constant equaling 6 for 3D diffusion and τ_c being the NMR correlation time in seconds defined as Equation (4.1) in the main text.

Using the above equations and the values derived from EIS and NMR, we obtain the following values for the D and MSD. Note that for the diffusion constant from EIS, k is in [J/K], whereas for NMR it is in [eV/K]. The equation for D_{NMR} is the same as that for x, with t being τ_c and x the intercage distance. Hence we also calculate the distance x by taking using D_{EIS}. The distances are approximations but show that the diffusion distance for EIS is about 10x as large as that of NMR.

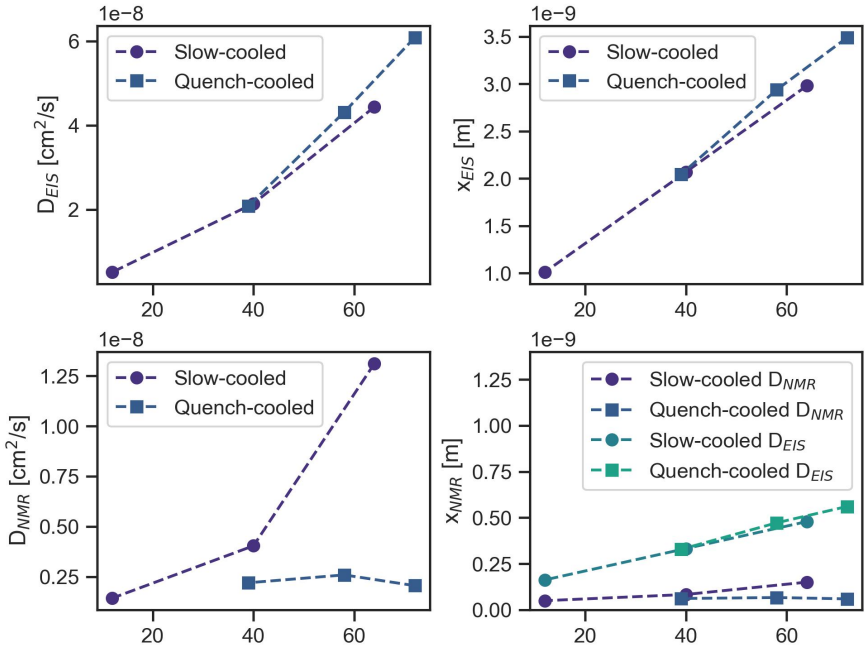

Figure B.13: The diffusivity (a) and diffusion distance (b) for EIS and the diffusivity calculated using T_1 (c) and diffusion distances from D and D_{EIS} (d). The time t is $1/10^6$ for EIS and $1/(1.6 \times 10^8)$ for NMR.

Bibliography

[1] D. Almond and A. West. The activation entropy for transport in ionic conductors. *Solid State Ionics*, 23(1-2):27–35, 1987.

[2] D. P. Almond, C. C. Hunter, and A. R. West. The extraction of ionic conductivities and hopping rates from a.c. conductivity data. *Journal of Materials Science*, 19(10):3236–3248, 1984.

[3] T. Bernges, S. P. Culver, N. Minafra, R. Koerver, and W. G. Zeier. Competing structural influences in the li superionic conducting argyrodites li6ps5-xsexbr ($0 \leq x \leq 1$) upon se substitution. *Inorganic Chemistry*, 57(21):13920–13928, 2018.

[4] B.-Y. Chang. Conversion of a constant phase element to an equivalent capacitor. *Journal of Electrochemical Science and Technology*, 11(3):318–321, 2020.

[5] R. Chen, Z. Xu, Y. Lin, B. Lv, S.-H. Bo, and H. Zhu. Influence of structural distortion and lattice dynamics on li-ion diffusion in li3ocl1−xbrx superionic conductors. *ACS Applied Energy Materials*, 4(3):2107–2114, 2021.

[6] A. Gautam, H. Al-Kutubi, T. Famprikis, S. Ganapathy, and M. Wagemaker. Exploring the relationship between halide substitution, structural disorder, and lithium distribution in lithium argyrodites (li6-xps5-xbr1+x). *Chemistry of Materials*, 35(19):8081–8091, 2023.

[7] S. Gelin, A. Champagne-Ruel, and N. Mousseau. Enthalpy-entropy compensation of atomic diffusion originates from softening of low frequency phonons. *Nature Communications*, 11(1), 2020.

[8] H. B. Huntington, G. A. Shirn, and E. S. Wajda. Calculation of the entropies of lattice defects. *Physical Review*, 99(4):1085–1091, 1955.

[9] M. A. Kraft, S. P. Culver, M. Calderon, F. Böcher, T. Krauskopf, A. Senyshyn, C. Dietrich, A. Zevalkink, J. Janek, and W. G. Zeier. Influence of lattice polarizability on the ionic conductivity in the lithium superionic argyrodites li6ps5x (x = cl, br, i). *Journal of the American Chemical Society*, 139(31):10909–10918, 2017.

[10] T. Krauskopf, S. Muy, S. P. Culver, S. Ohno, O. Delaire, Y. Shao-Horn, and W. G. Zeier. Comparing the descriptors for investigating the influence of lattice dynamics on ionic transport using the superionic conductor na3p4-xsex. *Journal of the American Chemical Society*, 140(43):14464–14473, 2018.

[11] X. Li, H. Liu, C. Zhao, J. T. Kim, J. Fu, X. Hao, W. Li, R. Li, N. Chen, D. Cao, Z. Wu, Y. Su, J. Liang, and X. Sun. Hopping rate and migration entropy as the origin of superionic conduction within solid-state electrolytes. *Journal of the American Chemical Society*, 2023.

[12] Z. Mollaei, F. Kermani, M. Kahani, F. Moosavi, S. Mollazadeh, and J. V. Khaki. Configurational entropy as a simple input data for glass science and engineering. *Materials Today Communications*, 32:104153, 2022.

[13] S. Muy, R. Schlem, Y. Shao-Horn, and W. G. Zeier. Phonon–ion interactions: Designing ion mobility based on lattice dynamics. *Advanced Energy Materials*, 11(15), 2021.

[14] A. S. Nowick, W.-K. Lee, and H. Jain. Survey and interpretation of pre-exponentials of conductivity. *Solid State Ionics*, 28-30:89–94, 1988.

[15] G. H. Vineyard. Frequency factors and isotope effects in solid state rate processes. *Journal of Physics and Chemistry of Solids*, 3(1-2):121–127, 1957.

[16] A. Yelon, B. Movaghar, and H. M. Branz. Origin and consequences of the compensation (meyer-neldel) law. *Physical Review B*, 46(19):12244–12250, 1992.

[17] A. Yelon, B. Movaghar, and R. S. Crandall. Multi-excitation entropy: its role in thermodynamics and kinetics. *Reports on Progress in Physics*, 69(4):1145–1194, 2006.

[18] C. Yu, S. Ganapathy, J. Hageman, L. van Eijck, E. R. H. van Eck, L. Zhang, T. Schwietert, S. Basak, E. M. Kelder, and M. Wagemaker. Facile synthesis toward the optimal structure-conductivity characteristics of the argyrodite li6ps5cl solid-state electrolyte. *ACS Applied Materials & Interfaces*, 10(39):33296–33306, 2018.

C

Appendix Chapter 5

C.1 Fitting Procedure ^{7}Li $T_{1\rho}$

As shown in Figure 5.5 in the main text, the ^{7}Li spin-lock relaxation exhibits three distinct contributions. Assuming that all three components decay exponentially, the relaxation data can be fitted using a tri-exponential decay model:

$$I(t) = I_0 \left(C_1 e^{-t/T_1} + C_2 e^{-t/T_2} + C_3 e^{-t/T_3} \right), \tag{C.1}$$

Here $I(t)$ and I_0 are the signal intensities at time t and at $t = 0$, respectively, t is the measurement time, and C_1, C_2, and C_3 are the proportionality constants of the three decay times ()T_1, T_2, and T_3).

It should be noted that in this context T_1 and T_2 do not refer to the conventional longitudinal and transversal NMR relaxation times, but are simply used to distinguish between the three contributions. We can deduce that $C3 = 1 - C1 - C2$, giving:

$$I(t) = I_0 \left[C_1 e^{-t/T_1} + C_2 e^{-t/T_2} + (1 - C_1 - C_2)\, e^{-t/T_3} \right] \tag{C.2}$$

The relaxation times obtained by fitting the experimental data using Equation. (C.2) at each temperature are shown in Figure C.1 for a spin-lock frequency of 10 kHz. The extracted parameters exhibit substantial uncertainties, particularly at elevated temperatures.

Quadrupolar nuclei, such as ^{7}Li, are expected to exhibit bi-exponential relaxation with an intensity ratio of $4:1$. If this mechanism is assumed to account for two of the observed relaxation components, the relaxation data can be described by:

$$I(t) = I_0 \left[0.8\, C_1 e^{-t/T_1} + 0.2\, C_1 e^{-t/T_2} + (1 - C_1) e^{-t/T_3} \right] \tag{C.3}$$

The corresponding fits are shown in Figure C.2.

Similar to before, the fit uncertainty becomes very large at elevated temperatures. At lower temperatures, uncertainty is significantly reduced. However, they are still observed for most samples, along with jumps in values between sequential datapoints. Figure 5.6

C

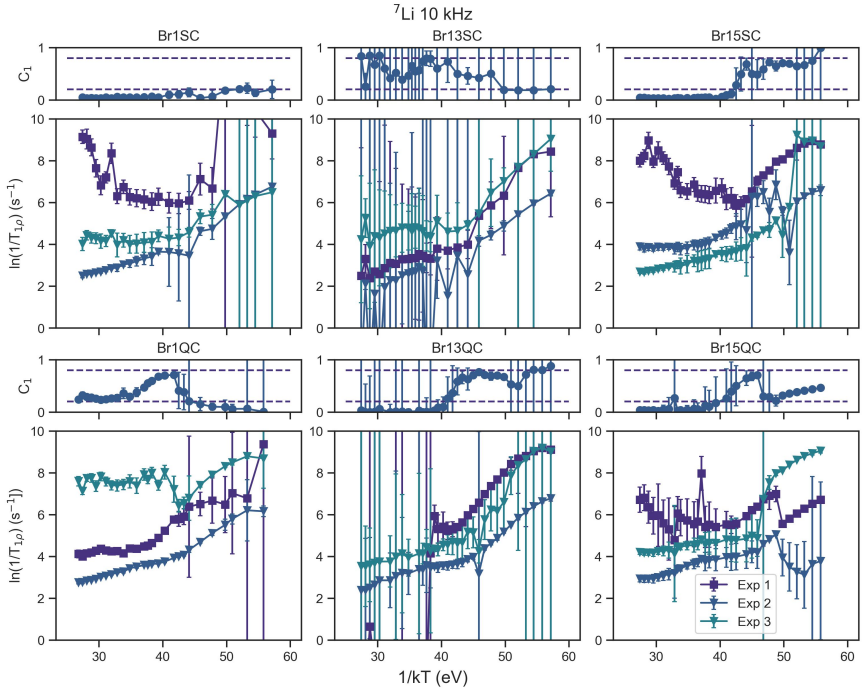

Figure C.1: The relaxation times and C_1-values obtained from fitting the ^{7}Li $T_{1\rho}$ data at a spin-lock frequency of 10 kHz using a tri-exponential fit according to Equation. (C.2) for each sample. The error bars represent the uncertainty in the fit.

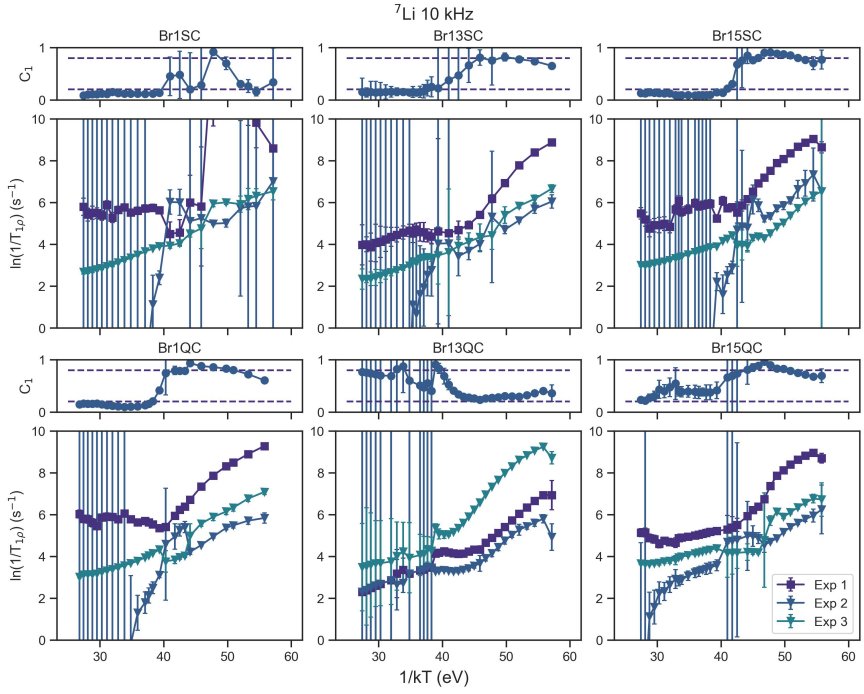

Figure C.2: The relaxation times and C_1-values obtained from fitting the ^{7}Li $T_{1\rho}$ data at a spin-lock frequency of 10 kHz using tri-exponential fit with the ratios of a bi-exponential quadrupolar relaxation mechanism, according to Equation (C.3). The error bars represent the uncertainty in the fit.

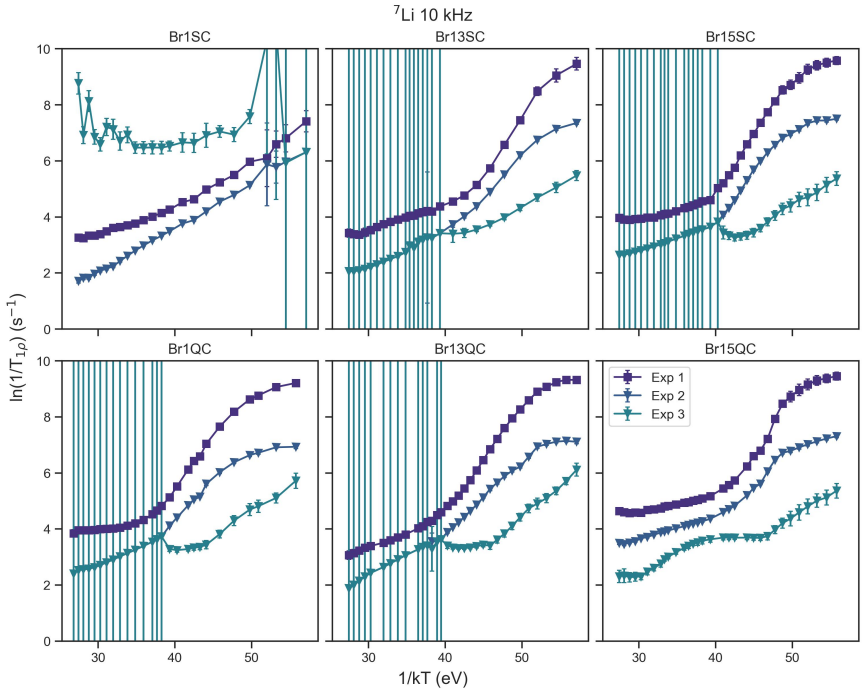

Figure C.3: The relaxation times and C_1 -values obtained from fitting the ^{7}Li $T_{1\rho}$ data at a spin-lock frequency of 10 kHz using tri-exponential fit according to Equation (C.2). The C_1 and C_2–values were determined manually from a measurement at –20 °C and treated as constant with temperature. The error bars represent the uncertainty in the fit.

in the main text shows three clear, defined contributions at lower temperatures. Assuming that the relative intensity of these contributions stays constant with temperature, it is possible to determine C1,C2 manually and use these values throughout the measured temperature range. The results using Equation (C.2) with C_1 and C_2 as constants, are given in Figure C.3. The data shows a significant reduction in fit uncertainty as well as a smooth progression between sequential points. The C_1 and C_2 values, also given Table C.1 and do not show a 4 : 1 ratio expected from bi-exponential quadrupolar relaxation.

A comparison between relaxation times at a spin-lock frequency of 10 kHz and 20 kHz is given in Figure C.4. The smaller component of a bi-exponential quadrupolar relaxation should not depend on spin-lock frequency. However, Figure C.4 shows this to be the case for almost all samples, making bi-exponential quadrupolar interaction an unlikely source of the multitude of components observed.

At elevated temperatures, the relaxation time associated with the smallest component (“Exp 3”) becomes too long to be reliably measured. When the uncertainty in this component exceeds 5% of the fitted value, the data are instead analyzed using a bi-exponential decay model, as given by Equation (C.4) (see Figure 5.5 in the main text). In this case, the parameters I_0, T_1, T_2, C_1, and C_2 are fitted independently at each temperature.

Table C.1: Values of C_1 and C_2 obtained from fitting the ^{7}Li $T_{1\rho}$ relaxation curves at −20 °C for each sample.

Material	C_1	C_2
Br1 SC	0.5838	0.3760
Br1.3 SC	0.5762	0.2938
Br1.5 SC	0.5398	0.3691
Br1 QC	0.5103	0.4032
Br1.3 QC	0.5604	0.3444
Br1.5 QC	0.5437	0.3668

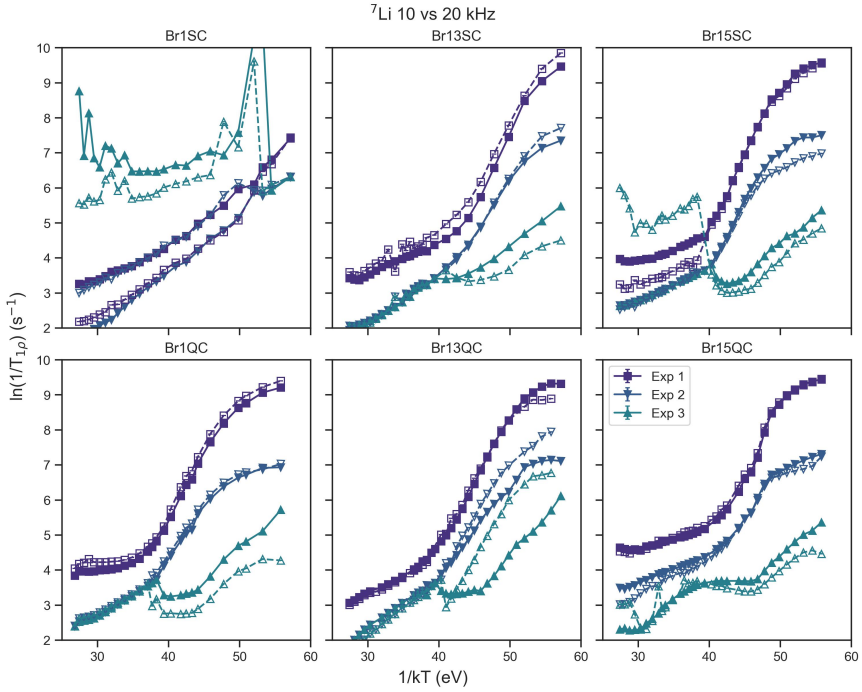

Figure C.4: Comparison of the ^{7}Li $T_{1\rho}$ relaxation curves at a spin-lock frequency of 10 kHz (solid) and 20 kHz (empty) for each sample. The relaxation curves were fit using pre-determined C_1– and C_2–values. The fit uncertainties omitted for sake of readability.

$$I(t) = I_0 \left(C_1 e^{-t/T_1} + C_2 e^{-t/T_2} \right) \tag{C.4}$$

C.2 Spin-rotation Relaxation

Rotational interactions can give rise to relaxation in rigid molecular systems, such as PO_4 and PF_6^-, for ^{17}O and ^{19}F nuclei, respectively [1, 19]. This mechanism is known as spin–rotational relaxation and originates from the magnetic field generated by the rotation of a molecular moiety. However, as ^{31}P is located at the center of the PS_4^{3-}–tetrahedra and therefore does not undergo rotational motion, spin–rotational relaxation is not expected to contribute significantly to ^{31}P relaxation.

The theoretical description of spin–rotational relaxation has only been derived for the high-temperature limit, where $\omega_0 \tau_c \gg 1$ (see Equation (C.5)), resulting in a linear temperature dependence that does not reproduce either the low- or high-temperature relaxation peaks observed experimentally [2]. The corresponding expression for the spin–lattice relaxation rate due to spin–rotational interactions is:

$$\frac{1}{T_1^{\mathrm{SR}}} = \frac{8\pi^2 kT}{3\hbar^2} \left(2I_\perp C_\perp^2 + I_\parallel C_\parallel^2 \right) \tau_{\mathrm{SR}} \tag{C.5}$$

Here $I_\perp$, $C_\perp$ and $I_\parallel$ and $C_\parallel$ are the perpendicular and parallel components of the inertia and spin rotation tensor.

The spin–rotation time τ_{SR} can be related to the rotational correlation time τ_c using Hubbard's formula:

$$\tau_{\mathrm{SR}} = \frac{\bar{I}}{6kT\tau_c} \tag{C.6}$$

where $\bar{I}$ is the mean moment of inertia.

In addition, computational studies have thus far found no evidence for PS_4^{3-} rotation occurring in argyrodites within the accessible simulation timescales [16, 20]. An example of a fit combining a ^{31}P–^{7}Li heteronuclear dipolar relaxation model with a spin–rotational contribution is shown in Figure C.5. The results demonstrate that the SR term produces an approximately linear contribution that cannot reproduce the experimental relaxation behavior. The numerical fit parameters, summarized in Table C.2, yield negative values for the SR-related variables. Constraining these parameters to be positive results in an SR contribution that is effectively zero, further confirming that spin–rotational relaxation does not play a significant role in the ^{31}P relaxation mechanism.

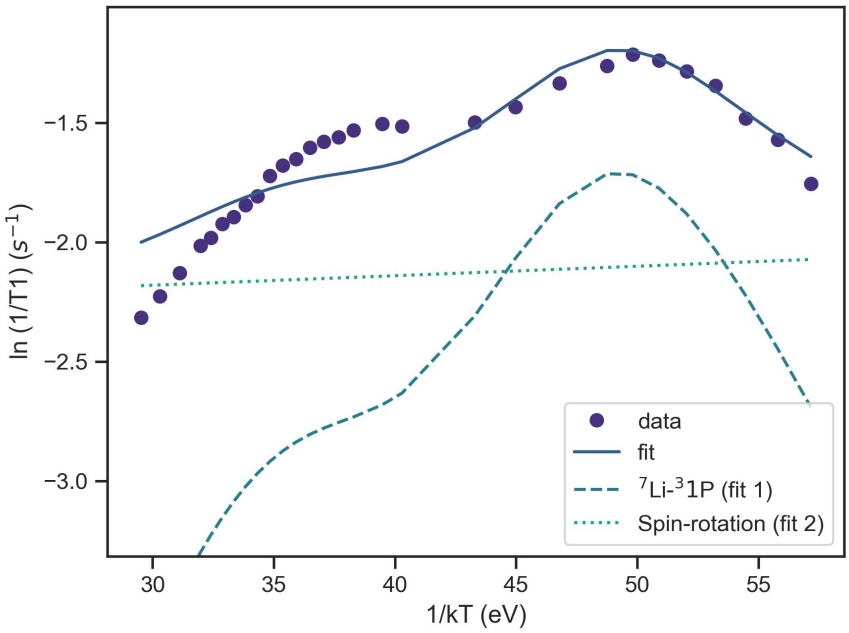

Figure C.5: An attempt to fit the Br1.3 SC ^{31}P T_1 data using a ^{7}Li–^{31}P and spin-rotation relaxation model as an example. The SR model results in a straight line which does not fit the curves observed.

Table C.2: Fit parameters corresponding to the model shown in Figure C.5, which combines ^{31}P–^{7}Li heteronuclear dipolar relaxation with a spin–rotational (SR) contribution. The SR-related parameters exhibit large uncertainties and non-physical negative values. Constraining all parameters to positive values yields an SR contribution that is effectively zero.

	C_1	$\tau_{0,1}$ (s)	$E_{a,1}$ (eV)	β_1	C_2	$\tau_{0,2}$ (s)	$E_{a,2}$ (eV)
Value	2.38×10^{7}	1.00×10^{-13}	0.258	1.743	-4.97×10^{-11}	-4.96×10^{-10}	-4.0×10^{-3}
Error	6.17×10^{6}	2.37×10^{-13}	0.052	0.619	4.45×10^{-11}	5.33×10^{-23}	0.029
Error (%)	25.9	237	20.0	35.5	−89.5	-1.08×10^{-11}	−718

C.3 The Effect of β on ^{3}1P T_1 and $T_{1\rho}$

For ^{3}1P T_1, see Figure C.6

For the ^{3}1P $T_{1\rho}$ high-temperature peak, a β-value of 2 was taken as a constant.Figure C.7 shows that fitting the β-value gives similar results, regardless of the model used.

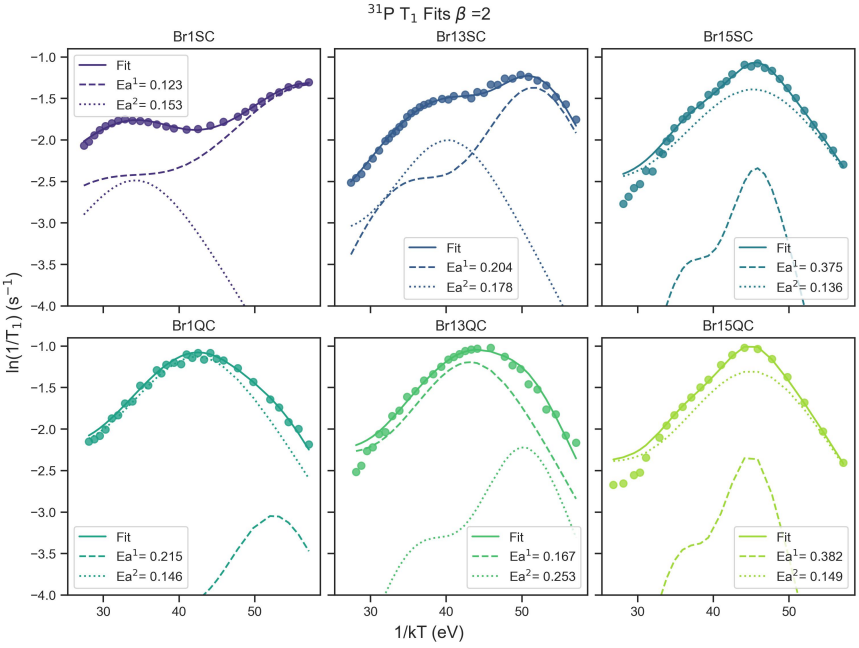

Figure C.6: The ^{31}P T_1 data and fit using two ^{7}Li–^{31}P heteronuclear BPP models with the asymmetry parameter β=2 for each sample.

C

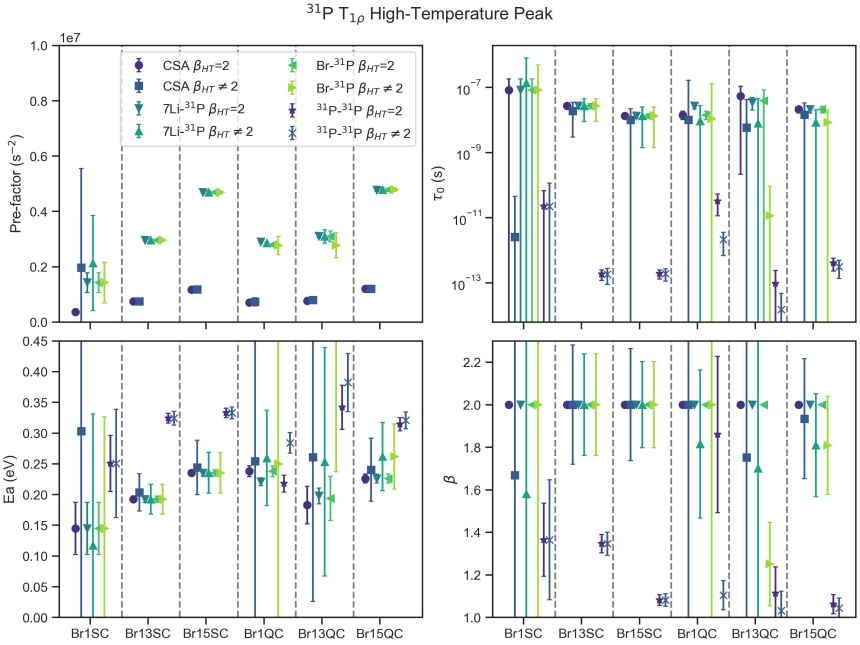

Figure C.7: The effect of beta on the fit results of the high-temperature ^{31}P $T_{1\rho}$ peak for a chemical shift anisotropy- (CSA), ^{31}P–^{7}Li heteronuclear dipolar- (^{7}Li–^{31}P), Br–^{31}P heteronuclear dipolar- (Br–^{31}P) or ^{31}P–^{31}P homonuclear model (^{31}P–^{31}P). A modified ^{7}Li–^{31}P heteronuclear dipolar BPP-model was used to fit the low-temperature peak.

C.4 Two Bromines versus One Avarage

Bromine has two NMR-active isotopes, ^{79}Br and ^{81}Br, with natural abundances of 50.69% and 49.31%, respectively. Their gyromagnetic ratios are $\gamma = 6.72$ and $7.22\ \mathrm{rad\,s^{-1}\,T^{-1}}$, corresponding to Larmor frequencies of 75.195 MHz and 81.055 MHz, respectively, at a magnetic field corresponding to a ^{1}H frequency of 300 MHz. The resulting ^{31}P–Br heteronuclear dipolar relaxation curves are shown in Figure C.8.

To account for the presence of both bromine isotopes, an effective bromine Larmor frequency is defined as the abundance-weighted root-mean-square average,

$$\omega_{\mathrm{Br}} = \sqrt{0.5069\,\omega^2_{^{79}\mathrm{Br}} + 0.4931\,\omega^2_{^{81}\mathrm{Br}}} \tag{C.7}$$

C

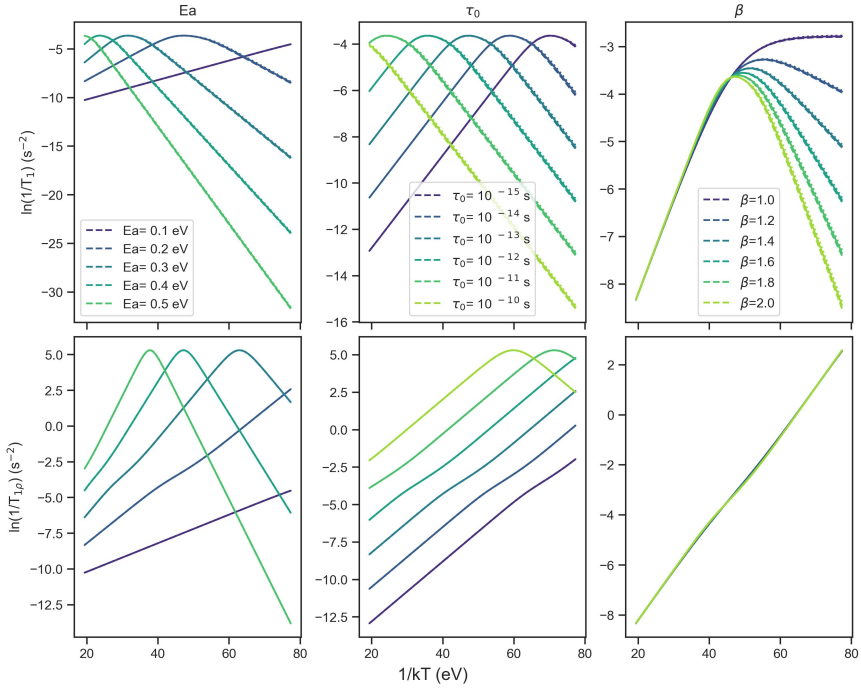

Figure C.8: The Br–^{31}P heteronuclear dipolar relaxation curves calculated using the Larmor frequency of ^{79}Br (dashed line), ^{81}Br (dotted line), and the abundance-weighted average bromine frequency (solid line). Results are shown for T_1 (upper panel) and $T_{1\rho}$ (lower panel) while varying the activation energy (E_a), attempt frequency (τ_0), and asymmetry factor (β).

C.5 Calculation of the Dipolar Pre–Factor

The heteronuclear dipolar pre-factor is defined as:

$$C = \left(\frac{\mu_0}{4\pi}\right)^2 \frac{\hbar^2 \gamma_I^2 \gamma_S^2}{r_{IS}^6} \tag{C.8}$$

In molecular systems, r_{IS} is readily defined as the distance between two distinct nuclei. However, in crystalline materials, this is not as straightforward. A crystal, by its very nature, is periodic, meaning that there is not simply one interatomic distance. Each nuclei will experience the nuclei in its nearest vicinity, the 'first shell' or first periodic arrangement as well as those in the following periodic arrangements, resulting in multiple distances between atoms of spin I and atoms of spin S. This is further complicated by the complexity of the crystal structure, which allows a nuclei to occupy a multitude of different sites, each with its own multiplicity and occupancy. In argyrodites, lithium is known to occupy the T5–, T5a–, T2– and T4–sites, with occupancies depending on the chemical composition and synthesis method. Sulphur and bromine can both occupy the 4*a*– and 4*d*–sites, with occupancies depending on similar parameters. So how does one calculate the pre-factor?

The original work by BPP defines the pre-factor as the magnitude of the local field strength due to dipolar interactions.[3] Previous work on the strength of dipolar interactions in crystalline inorganic materials is limited when compared to work dedicated to organic compounds.[15] Work that is done foccuses on more complex techniques such as REDOR, Double-quantum stuff to obtain the dipolar interaction strength and hence r_{IS}.[4, 5, 12] Studies regarding the dipolar interaction in crystalline solids are rare and often focus on theoretical derivations of one system [6, 7, 13] that require extensive knowledge of the system under study and involved mathematical derivation that does not have a closed form.[17] For more complex systems involving different heteroatoms which can occupy different sites, these approaches need to be developed and are beyond the scope of the current work. Is it possible to use a simple formula and derive an approximation?

Another formalism that describes the strength of dipolar interactions is the van Vleck second moment, which can be used to calculate the static dipolar linewidth for both homonuclear (Equation (C.9)) and heteronuclear (Equation (C.10)) cases [5]. Here, N_I denotes the number of observed nuclei. While N_I was not explicitly included in the original work by van Vleck [18], it has been introduced and widely used in subsequent studies. [8–10, 14]

For homonuclear dipolar interactions, the second moment is given by

$$M_2^{II} = \frac{3}{3} I(I+1)\left(\frac{\mu_0}{4\pi}\right)^2 \frac{\hbar^2 \gamma_I^4}{N_I \sum_{i \neq j} r_{ij}^6} \tag{C.9}$$

and for heteronuclear dipolar interactions by

$$M_2^{IS} = \frac{4}{15} S(S+1)\left(\frac{\mu_0}{4\pi}\right)^2 \frac{\hbar^2 \gamma_I^2 \gamma_S^2}{N_I \sum_I \sum_S r_{IS}^6} \tag{C.10}$$

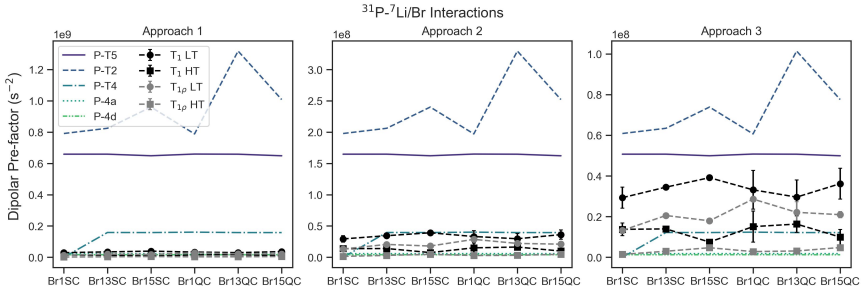

Figure C.9: The Br–^{31}P heteronuclear dipolar relaxation curves calculated using the Larmor frequency of ^{79}Br (dashed line), ^{81}Br (dotted line), and the abundance-weighted average bromine frequency (solid line). Results are shown for T_1 (upper panel) and $T_{1\rho}$ (lower panel) while varying the activation energy (E_a), attempt frequency (τ_0), and asymmetry factor (β).

The effect of fractional occupancy can also be incorporated into the second moment [11]. For the homonuclear case, this yield:

$$M_2^{II} = \frac{3}{3} I(I+1)\left(\frac{\mu_0}{4\pi}\right)^2 f_I \frac{\hbar^2 \gamma_I^4}{\sum_{i \neq j} r_{ij}^6}, \tag{C.11}$$

where f_I is the fractional occupancy of the I nucleus.

An important question is whether these expressions can be used to approximate the dipolar pre-factor in heteronuclear T_1 relaxation experiments. To investigate this, the experimentally obtained pre-factors for the ^{31}P T_1 and $T_{1\rho}$ data were compared with values calculated using different structural and statistical assumptions.

Using the general expression

$$C = \left(\frac{\mu_0}{4\pi}\right)^2 \hbar^2 \gamma_I^2 \gamma_S^2 Q, \tag{C.12}$$

a series of approaches were evaluated, which are summarized in Table C.3. These approaches examine the influence of the number of I nuclei in the unit cell (N_I), the number of S nuclei (N_S), the number of crystallographic sites they occupy ($N_{I,\mathrm{P}}$ and $N_{I,\mathrm{S}}$, respectively), their fractional occupancies (f_I and f_S), and the internuclear distance r_{IS}. The papers from which Equations (C.9) and (C.10) derive, contain a division by the number of atoms in resonance (N_I). The first issue when translating these approaches to the argyrodite system is the existence of corner and edge sites. The distance r_{IS} and the corresponding sum of distances $\sum_I \sum_S r_{IS}^{-6}$ are calculated from structural parameters obtained via Rietveld refinement using a custom Python script. This script generates a list of all crystallographic positions occupied by atom I and computes the distances between atoms I and S for each position of I in the lattice. Because some atoms occupy corner and/or edge sites, the number of atoms N_I can differ from the number of distinct crystallographic sites (or positions) N_I^P. This is the case for phosphorus, which has $N_I = 4$ atoms per unit cell but occupies $N_I^P = 13$ crystallographic sites. As a result, the total number of calculated distances is $N_I^P N_S^P$ rather than $N_I N_S$.

Table C.3: Overview of the different approaches used to calculate the dipolar factor Q.

Approach #	C
1	$\frac{1}{\sum_I \sum_S r_{IS}^{-6}}$
2	$\frac{1}{N_I \sum_I \sum_S r_{IS}^{-6}}$
3	$\frac{1}{N_I f_I \sum_I \sum_S r_{IS}^{-6}}$
4	$\frac{N_I N_S}{N_I f_I N_S f_S \sum_I \sum_S r_{IS}^{-6}}$
5	$\frac{1}{\sum_S r_{IS}^{-6}}$
6	$\frac{1}{\sum_I \sum_S \alpha r_{IS}^{-6}}$
7	$\frac{f_I f_S}{N_I \sum_I \sum_S \alpha r_{IS}^{-6}}$
8	$\frac{f_S}{f_I N_I \sum_I \sum_S \alpha r_{IS}^{-6}}$
9	$\frac{f_S}{N_I \sum_I \sum_S \alpha r_{IS}^{-6}}$
10	$\frac{f_I f_S}{\sum_I N_I \sum_S \alpha r_{IS}^{-6}}$

Here, α accounts for geometrical weighting factors with $\alpha = 0.5$ for plane, 0.25 for edge, 0.125 for corner, and 1 otherwise.

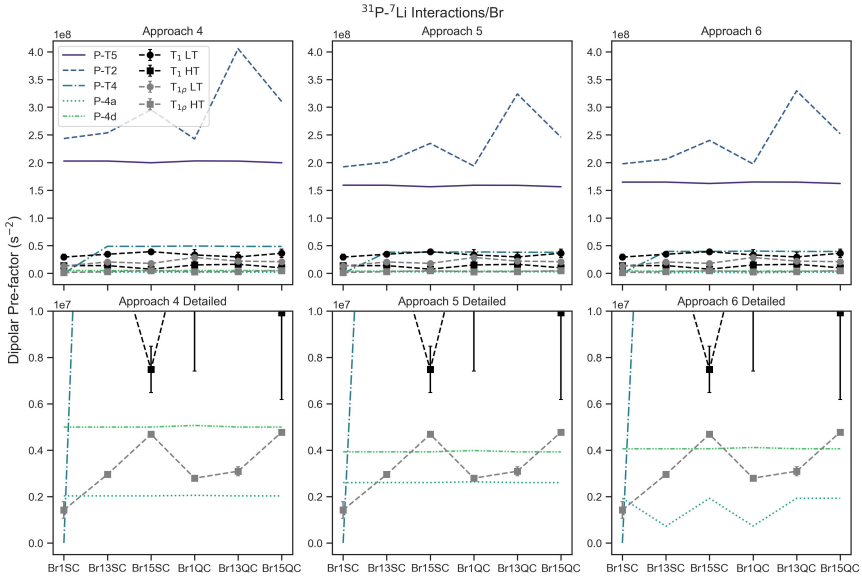

Figure C.10: The effect of approaches 4-6 to deal with site-symmetry on the calculated ^{31}P–^{7}Li dipolar pre-factor and comparison to the experimentally obtained dipolar pre-factor values from fitting the high-temperature (HT) and low-temperature (LT) peaks of the ^{31}P T_1 and $T_{1\rho}$ data. The upper panel shows all results and the lower panel a detailed view of the lower values.

The effect of dividing by nothing (Approach 1), by N_I (Approach 2) and by N_I^P are given in Figure C.9. We see that the calculated pre-factor without any modification is significantly larger than the experimentally obtained value. However, whereas Approach 3 seems somewhat close, it implies that the lithium $T4$–site is involved in most movement sensed by ^{31}P. Considering its low occupancy, this seems unlikely. Approaches 4-6 investigate different methods to deal with site-symmetry. For phosphorus, one site sits at the centre of the unit cell, whereas the other sites sit at the edges. Approach 5 takes only the distances to this centre site, eliminating the need to divide by the total number of sites/atoms. This approach is compared to Approach 4 and Approach 6, which use a pre-factor, either consisting of a ratio of the number of atoms and sites or depending on the nature of the S–atom. The results, given in Figure C.10, show that Approach 5 and 6 give almost identical results. However, the effect on the 4a–site, shows a difference for Approach 6. The 4a–site sits on corners and planes of the unit cell and Approach 6 seems able to take this into account.

Approach 5 is able to deal with site-symmetry, yet the values it yields are significantly larger than experimental results. These approaches assume that each site is fully occupied, which is not the case. Approaches 7-10 investigate different ways of taking the fractional occupancy into account. These are not expected to yield different results for ^{31}P–^{7}Li/Br interactions (see Figure C.11).

However, they affect ^{7}Li–^{31}P interactions. Figure C.11 shows the values calculated, compared to experimentally obtained ^{7}Li $T_{1\rho}$ values. From this, we see that only ap-

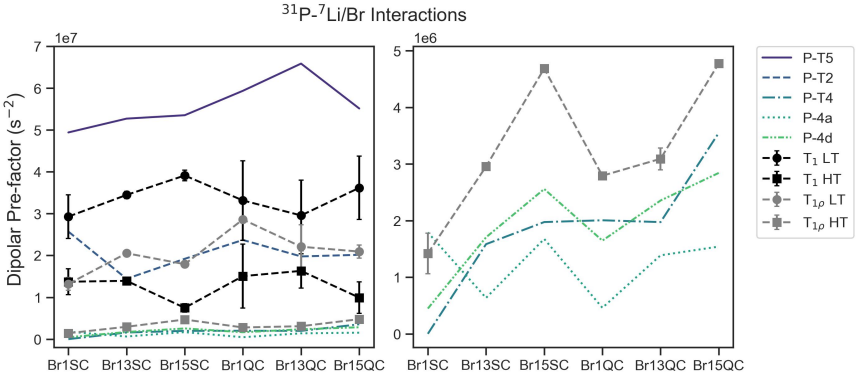

Figure C.11: A representation of approaches 7-10 , dealing with fractional site occupancy, on the calculated ^{31}P–^{7}Li and ^{31}P–Br dipolar pre-factor and comparison to the experimentally obtained dipolar pre-factor values from fitting the high-temperature (HT) and low-temperature (LT) peaks of the ^{31}P T_1 and $T_{1\rho}$ data (left) and a detailed view at lower pre-factor values (right). Approaches 7-10 yielded identical results.

proaches 8 and 10 give values within the experimental order of magnitude. Approach 10 approximates the experimental values better and implies that the low-temperature contribution in ^{7}Li $T_{1\rho}$ is associated with movement of the T4-site. The significant overlap with ^{31}P $T_{1\rho}$ data implies a common source, however. Figure C.11 shows that for ^{31}P $T_{1\rho}$, this would be lithium movement associated with the T2-site. Hence, Approach 8 is taken as the best method to calculate the dipolar interactions. It must be noted that the experimental ^{7}Li $T_{1\rho}$ values shows significant uncertainty in the fit and should mainly be used to compare orders of magnitude between calculated and experimental values. However, for ^{31}P, both Approaches 8 and 10 yield identical results.

C

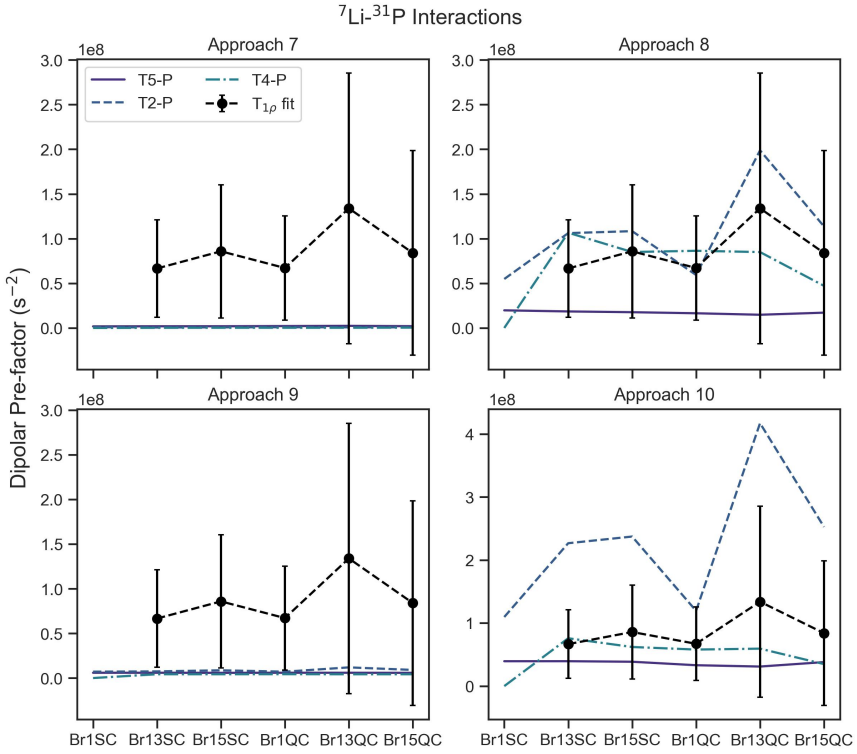

Figure C.12: A representation of the effect of approaches 7-10 , dealing with fractional site occupancy, on the calculated ^{7}Li–^{31}P dipolar pre-factor and comparison to the experimentally obtained dipolar pre-factor values from fitting ^{7}Li $T_{1\rho}$ data.

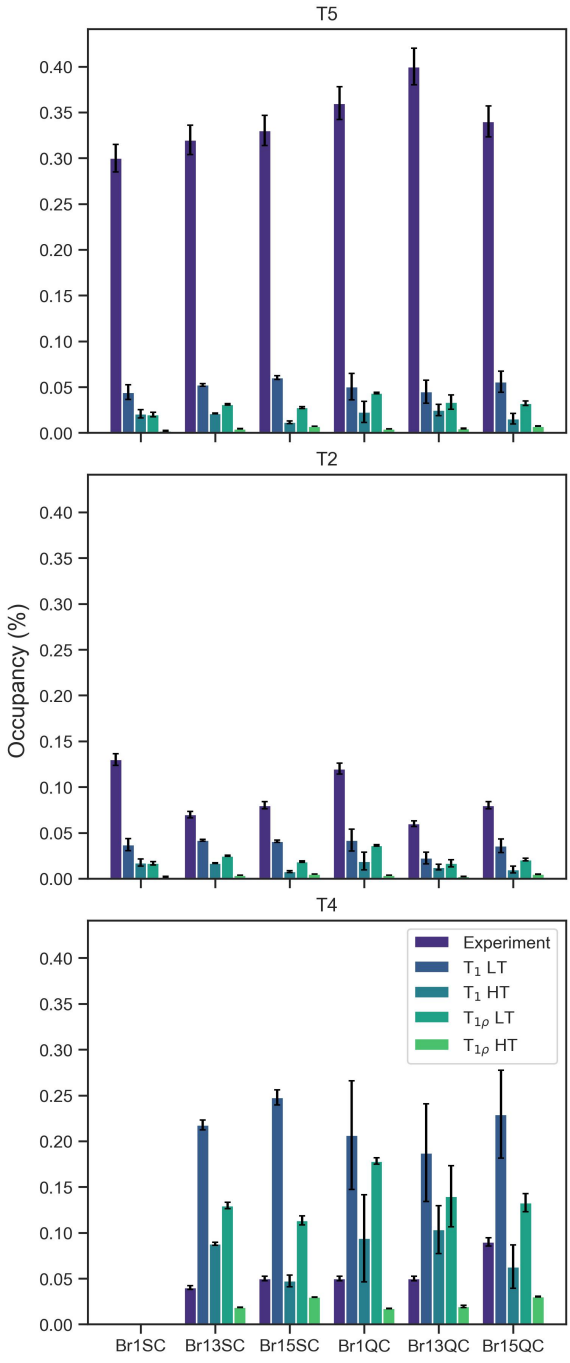

Figure C.13: The experimentally obtained ('Experiment') and calculated occupancies based on the dipolar pre-factors obtained from the low-temperature (LT) and high-temperature (HT) ^{31}P T_1 and $T_{1\rho}$ peaks for each lithium site. Approach 8 was used to define the relationship between the pre-factor and the occupancies.

C.6 The ^{7}Li Linewidths

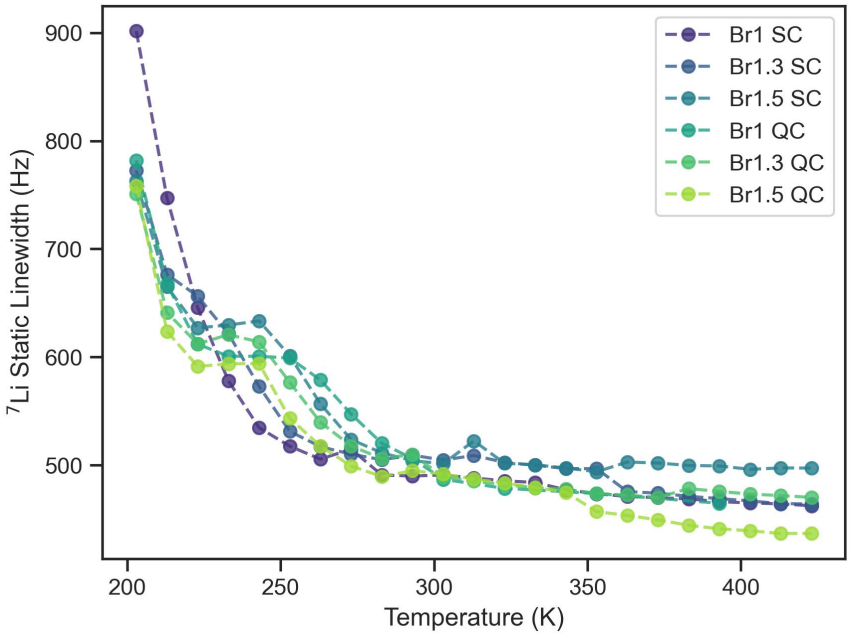

Figure C.14: The ^{7}Li static linewidth at a Larmor frequency of 72.88 MHz as a function of temperature. A small plateau is observed, attributed to quadrupolar interactions.

C.7 The ^{7}Li $T_{1\rho}$ Fit of the 3rd Exponential

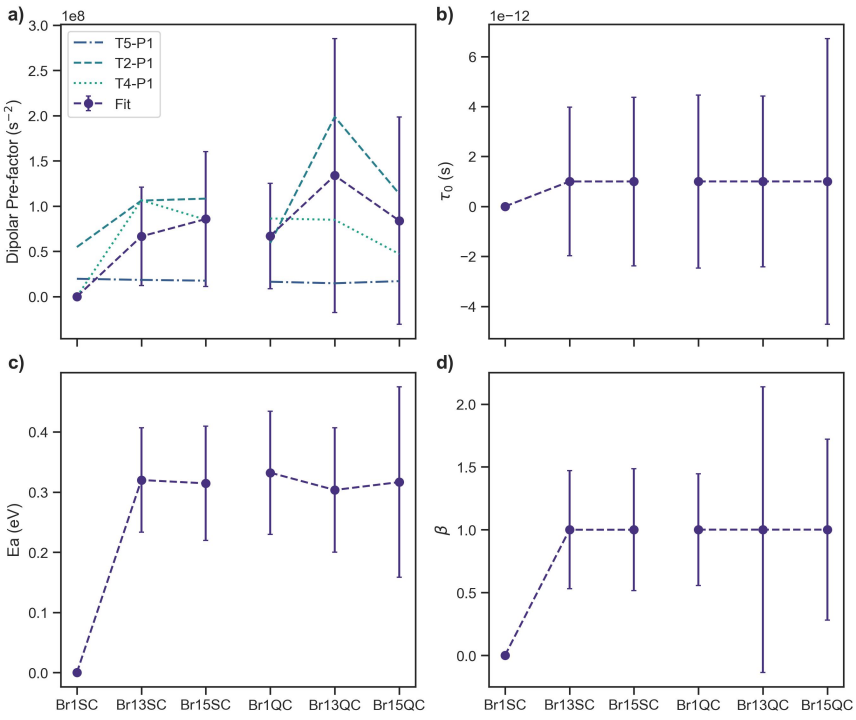

Figure C.15: The dipolar pre-factor, attempt frequency, activation energy and asymmetry parameter obtained from fitting the 3rd exponential contribution of the ^{7}Li $T_{1\rho}$ data at a spin lock frequency of 10 kHz. Br1SC lacked a third contribution and hence its result are all zero.

C.8 Chemical Shift Anisotropy Fit Example

Asymmetry in the probe response resulted asymmetry in sideband intensity. The spectrum was therefore fit twice, each time focussing on the sidebands on one side of the main peak. An example is given in Figure C.16, showing the main peak, deconvoluted into five contributions and the sideband fits on either side.

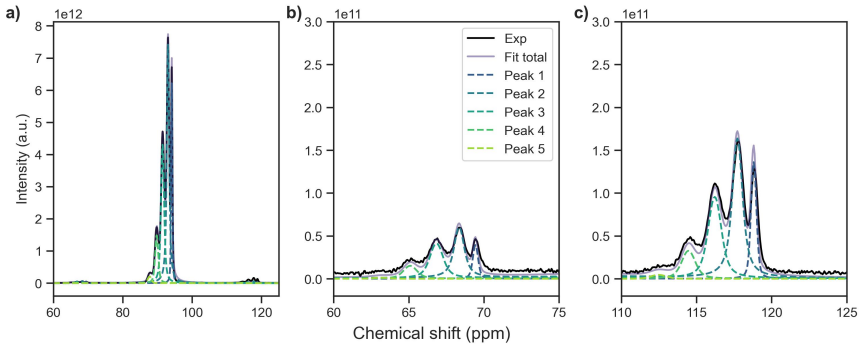

Figure C.16: An example of spectral fitting of an ^{31}P MAS spectrum of Br13SC showing an a) overall fit and b) the fit of the left and c) right sidebands. MAS rate was 5 kHz.

C.9 Inserting ^{7}Li T_1 Results into ^{3}1P T_1 Fit

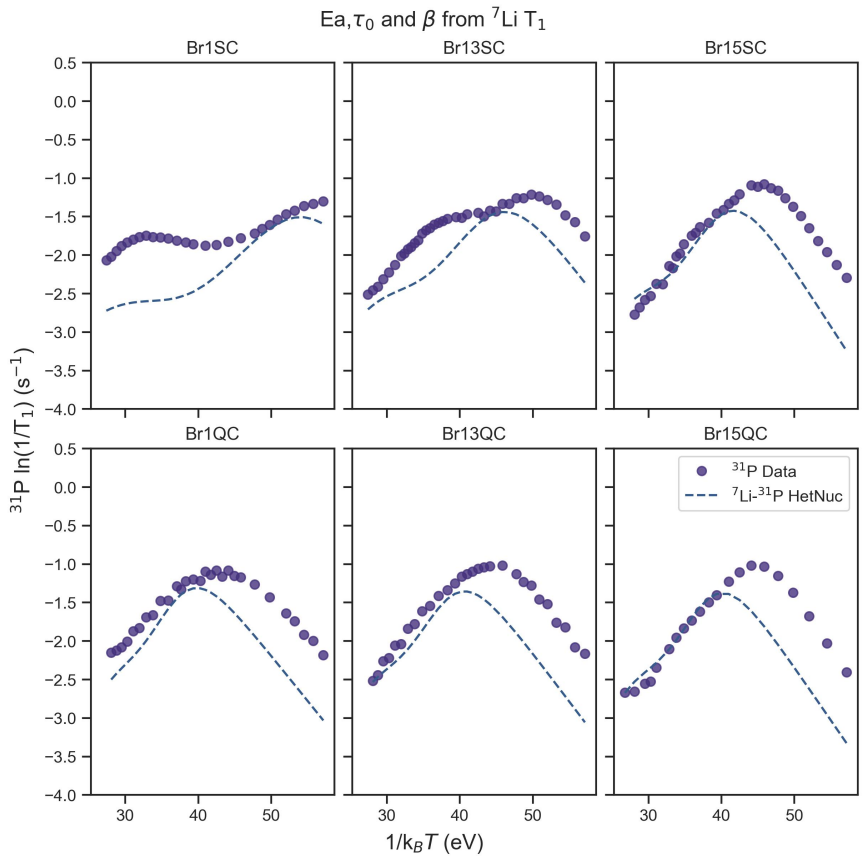

Figure C.17: The ^{31}P T_1 relaxation times for each sample as a function of temperature in comparison to a curve (dashed line) resulting from a heteronuclear dipolar ^{31}P–^{7}Li model with values for E_a, τ_0 and β from ^{7}Li T_1 fits mentioned in the previous chapter. A dipolar pre-factor value of 3× 107 s^{-2} was used to obtain a comparable height.

C

C.10 Fitting $^{3}1$P T_1 with β=2

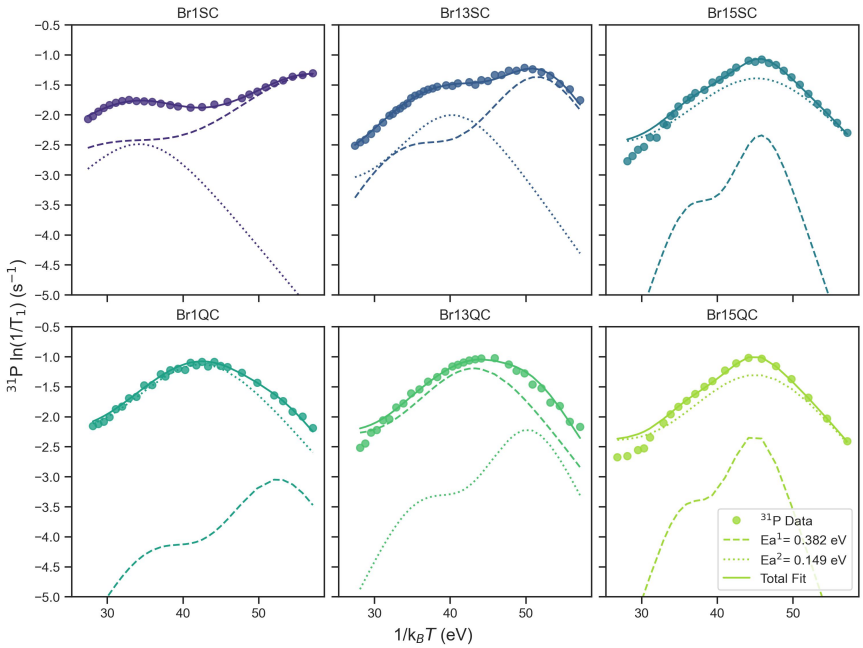

Figure C.18: Fits of the ^{31}P T_1 data using two ^{7}Li–^{31}P heteronuclear dipolar curves with both asymmetry factors (beta) equal to 2 for all six samples. The model results in a lower fit quality, especially at elevated temperatures.

C.11 Fitting $^{3}1$P T_1 with Values from ^{7}Li T_1

As can be seen in Figure C.19, the use of the ^{7}Li T_1 results in the ^{31}P T_1 fit, gives different fits depending on the approach taken, especially for Br1QC. The fits of Br1.5SC, Br1QC and Br1.5QC are not as good at high temperatures.

Table C.4: Section of the Table 5.2 in the main text summarizing the various fitting approaches used for the ^{31}P T_1data. Variables are either fitted using a least-squares method (*Fit*), assigned a constant value (2 for β), or fixed using results from the ^{7}Li T_1fit discussed in the previous chapter ("^{7}Li T_1").

Fit #	Q^1	τ_0^1	E_a^1	β^1	Q^2	τ_0^2	E_a^2	β^2
1	Fit	Fit	^{7}Li T_1	^{7}Li T_1	Fit	Fit	Fit	2
2	Fit	Fit	^{7}Li T_1	^{7}Li T_1	Fit	Fit	Fit	^{7}Li T_1
3	Fit	Fit	^{7}Li T_1	^{7}Li T_1	Fit	Fit	Fit	Fit
4	Fit	Fit	^{7}Li T_1	Fit	Fit	Fit	Fit	2
5	Fit	Fit	Fit	^{7}Li T_1	Fit	Fit	Fit	Fit
6	Fit	Fit	^{7}Li T_1	Fit	Fit	Fit	Fit	Fit
7	Fit	Fit	^{7}Li T_1	Fit	Fit	Fit	^{7}Li T_1	Fit

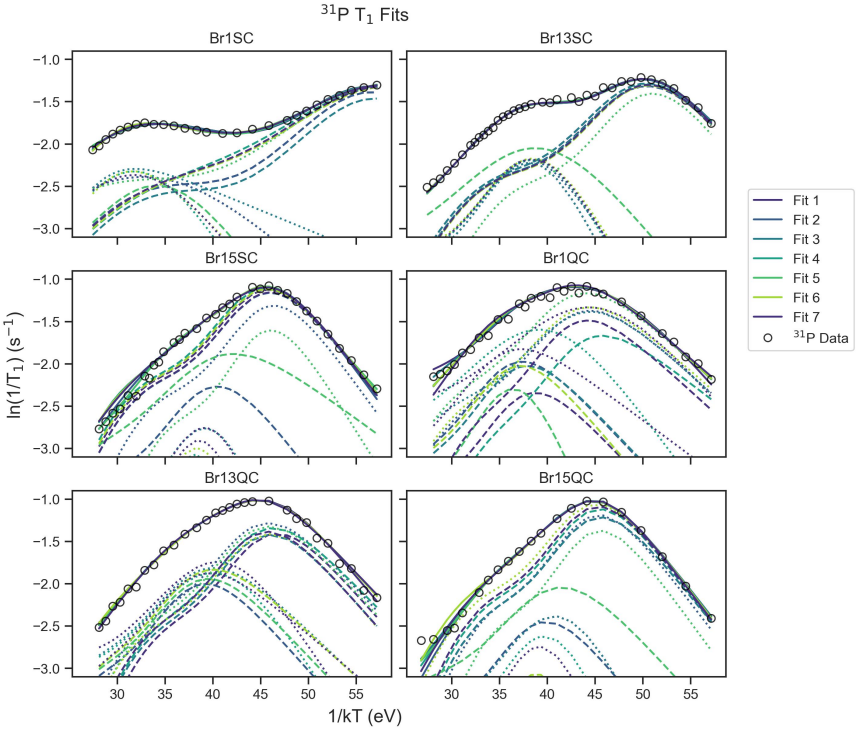

Figure C.19: The ^{31}P T_1 data fits using two ^{7}Li–^{31}P heteronuclear dipolar models (dashed and dotted line) and the total fit (solid line) for each sample. The fit numbers are given in Table C.4.

C

C.12 All $^{3}1$P T_1 Fit Results

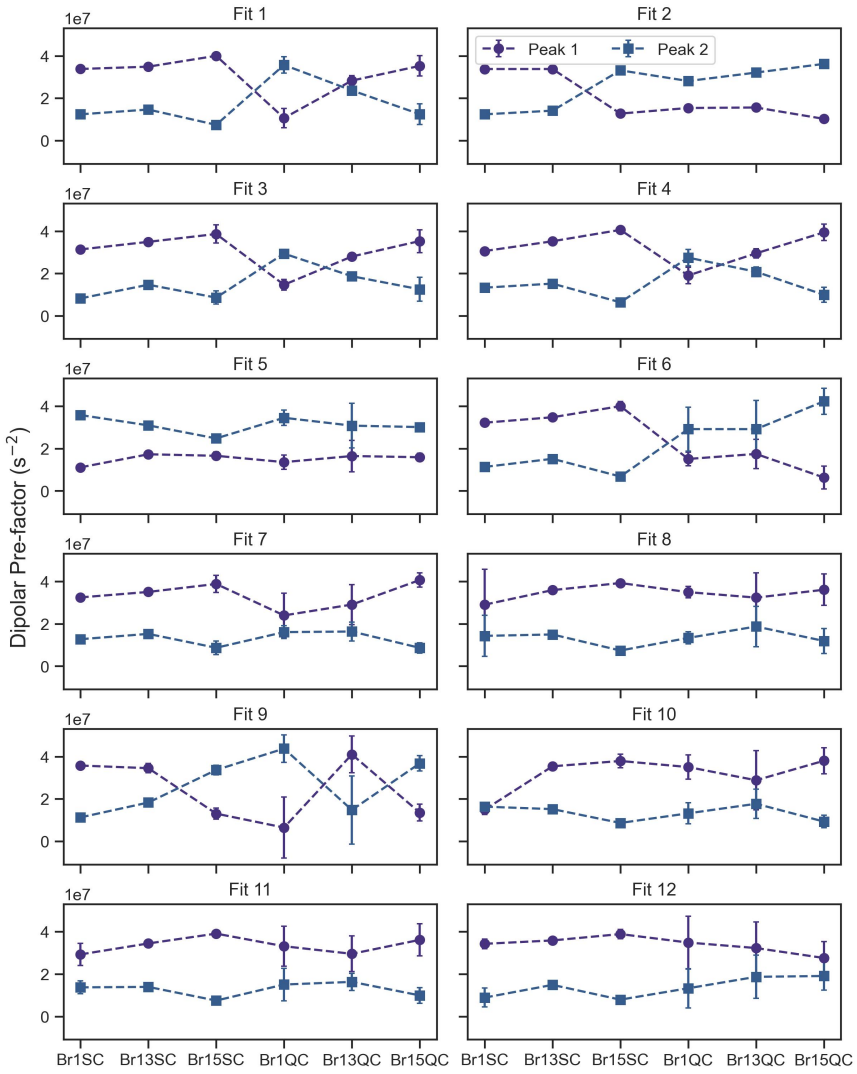

Figure C.20: All the dipolar pre-factors obtained for the two ^{7}Li–^{31}P models used (peak 1 and peak 2) for each fit mentioned in Table 5.2 in the main text.

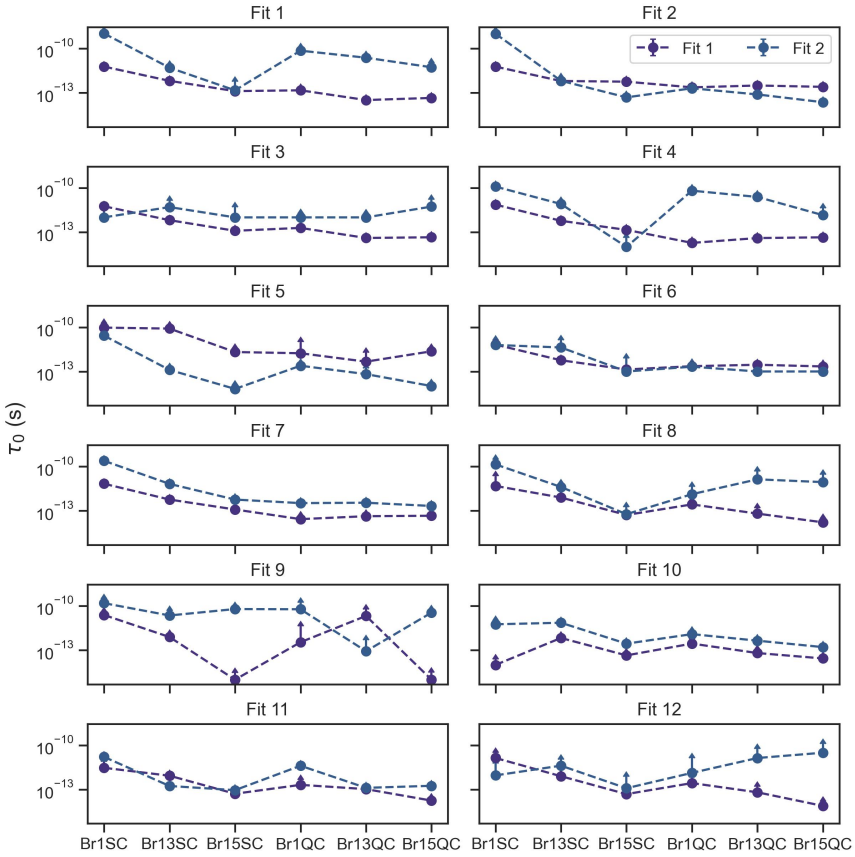

Figure C.21: All the inverse attempt frequencies obtained for the two ^{7}Li–^{31}P models used (peak 1 and peak 2) for each fit mentioned in Table 5.2 in the main text. The lower limit errorbar is omitted due to the logarithmic scale.

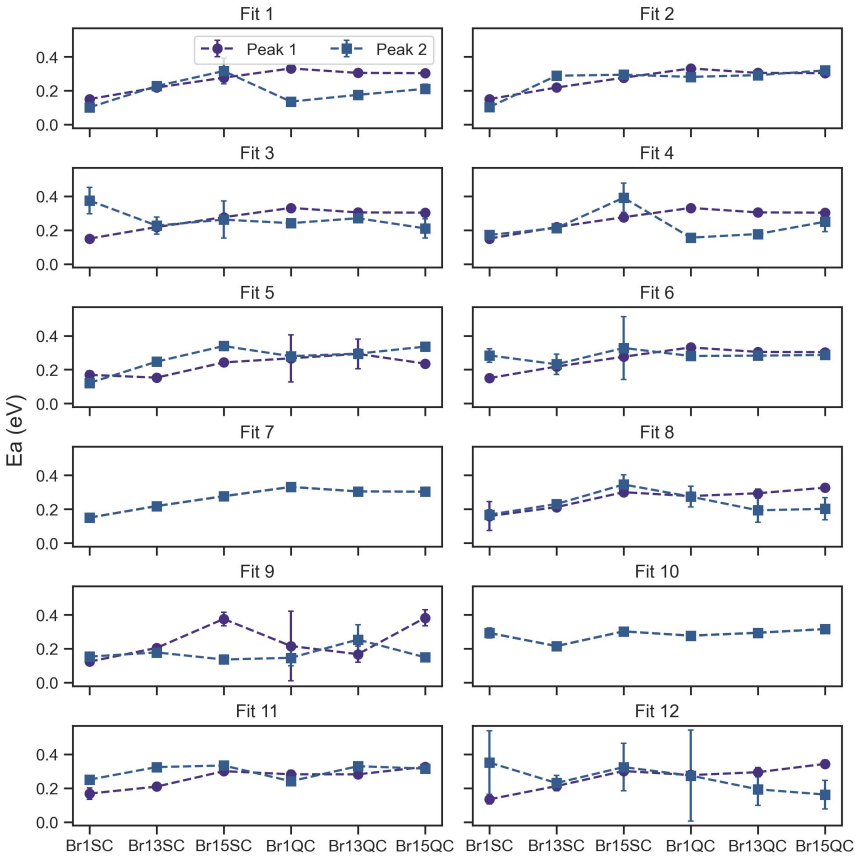

Figure C.22: All the activation energies obtained for the two ^{7}Li-^{31}P models used (peak 1 and peak 2) for each fit mentioned in Table 5.2 in the main text

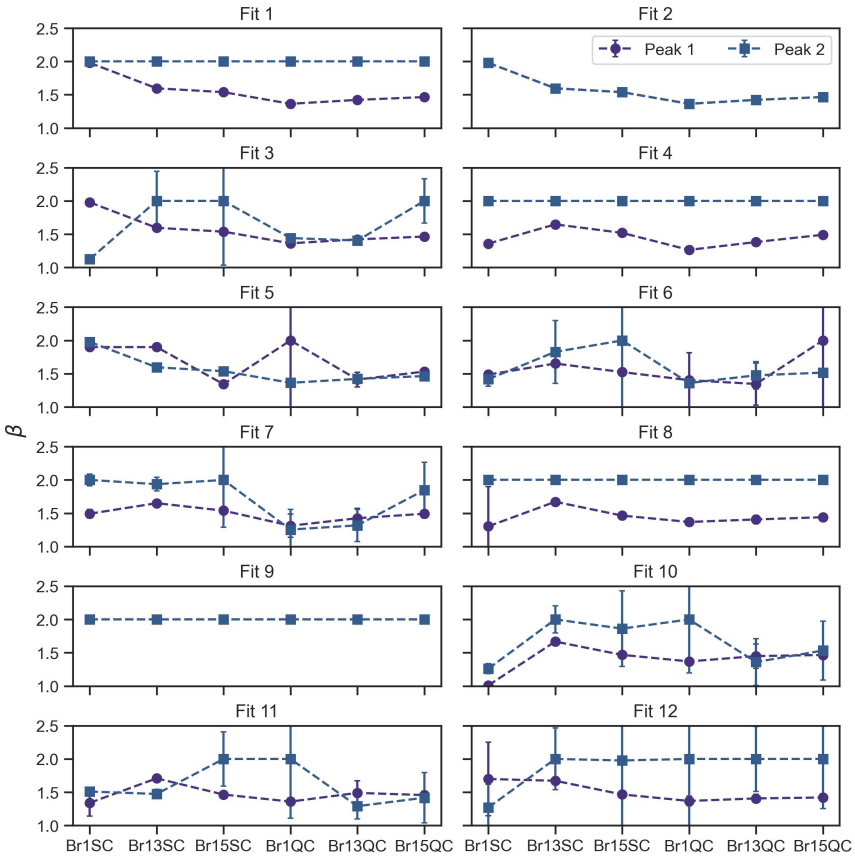

Figure C.23: All the assymestry parameters (β) obtained for the two ^{7}Li-^{31}P models used (peak 1 and peak 2) for each fit mentioned in Table 5.2 in the main text

C.13 Comparison Fit 5 and Fit 11 for $^{3}1$P T_1

We can from Figure C.24 see that the pre-factor remains almost the same, albeit with a reduction in fit uncertainty for all samples except Br15 QC. The asymmetry parameter β displays a large error in both fits due to the overlap of the peaks, making it difficult to define the asymmetry with certainty. The attempt frequency τ_0 suffers from a similar problem but less so, as it relies more on the activation energy and the peak maximum position. The activation energies show a different trend as well as a significant reduction in uncertainty, which will be discussed below.

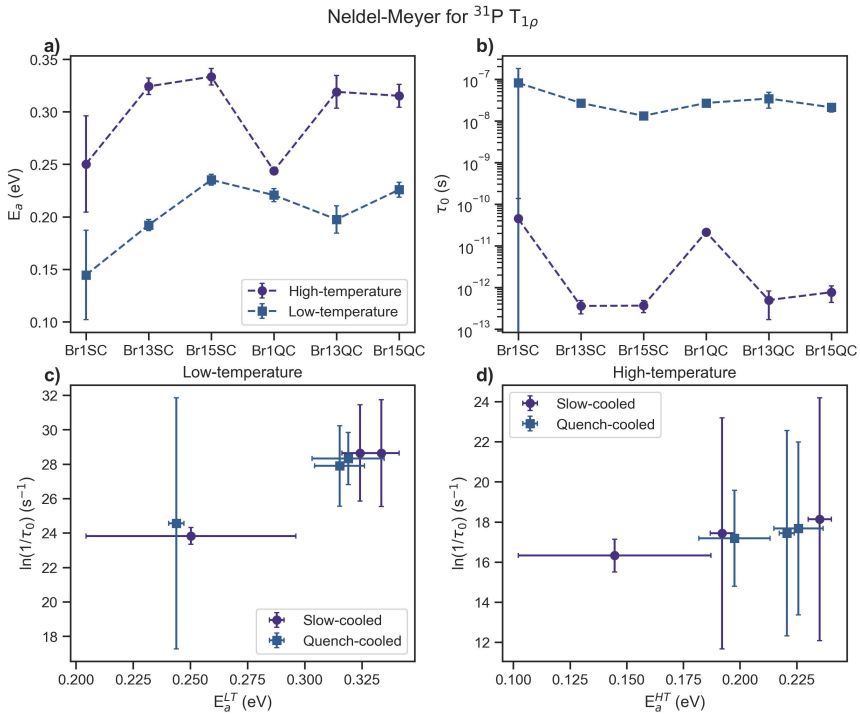

Figure C.24: The dipolar pre-factor, activation energy (E_a), attempt frequency (τ_0) and asymmetry factor (β) obtained for the high-temperature (circle) and low-temperature (square) from fitting all variables ('Fit all'/ Fit 5 in Table 5.2 in the main text) and from using the low-temperature activation energy from ^{31}P $T_{1\rho}$ as a constant for the E_a^{HT}. The error bars represent the uncertainty of the fit. For τ_0 only the upper limit of the uncertainty was given to improve readability.

C.14 Neldel–Meyer for ^{31}P T_1 Data

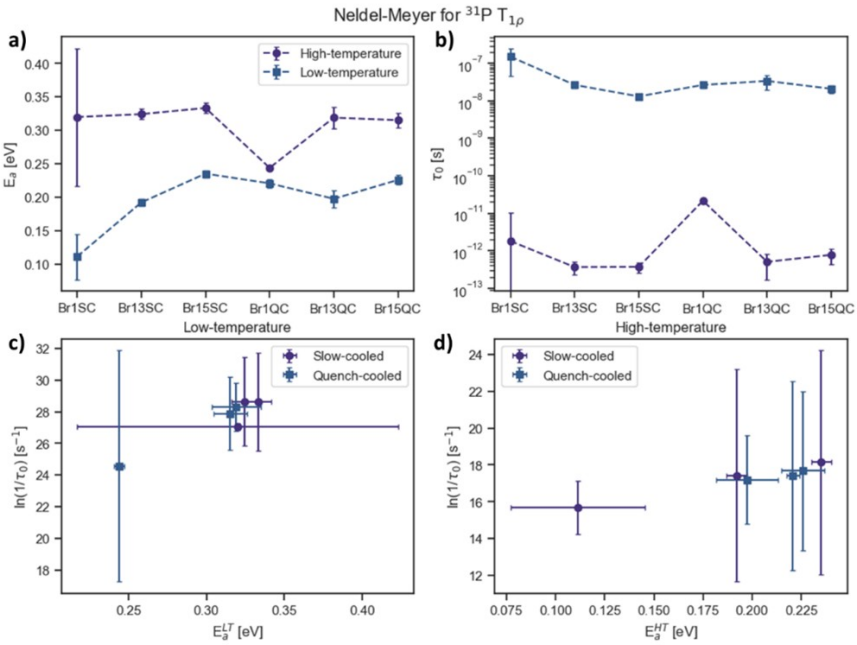

Figure C.25: The activation energy (a) and attempt frequency (b) for the low-temperature (LT) and high-temperature (HT) ^{31}P T_1 peaks for each sample as well as the logarithm of the inverse of the attempt frequency versus the activation energy for the LT (c) and HT (d) peaks.

Bibliography

[1] S. Albert and H. S. Gutowsky. Nuclear relaxation and spin exchange in ammonium hexafluorophosphate (nh4pf6). *The Journal of Chemical Physics*, 59(7):3585–3594, 1973.

[2] R. Blinc and G. Lahajnar. Nuclear-magnetic-resonance relaxation by spin-rotational interactions in the solid. *Physical Review Letters*, 19(12):685–687, 1967.

[3] N. Bloembergen, E. M. Purcell, and R. V. Pound. Relaxation effects in nuclear magnetic resonance absorption. *Physical Review*, 73(7):679–712, 1948.

[4] D. H. Brouwer, R. J. Darton, R. E. Morris, and M. H. Levitt. A solid-state nmr method for solution of zeolite crystal structures. *Journal of the American Chemical Society*, 127(29):10365–10370, 2005.

[5] H. Eckert, S. Elbers, J. D. Epping, M. Janssen, M. Kalwei, W. Strojek, and U. Voigt. *Dipolar Solid State NMR Approaches Towards Medium-Range Structure in Oxide Glasses*, pages 195–233. Springer Berlin Heidelberg, Oct. 2004.

[6] M. Eisenstadt and A. G. Redfield. Nuclear spin relaxation by translational diffusion in solids. *Physical Review*, 132(2):635–643, 1963.

[7] G. Garcia, J. Abriata, and J. Sofo. Hydrogen movement in cubic mg 2 nih 4. *Physical Review B*, 65(6):064306, 2002.

[8] R. Goc. Calculation of the nmr second moment for solid benzene with rotation and diffusion of molecules - numerical approach. *Zeitschrift für Naturforschung A*, 52(6-7):477–484, 1997.

[9] R. Goc. Computer calculation of the van vleck second moment for materials with internal rotation of spin groups. *Computer Physics Communications*, 162(2):102–112, 2004.

[10] H. S. Gutowsky and G. E. Pake. Structural investigations by means of nuclear magnetism. ii. hindered rotation in solids. *The Journal of Chemical Physics*, 18(2):162–170, 1950.

[11] C. Kittel and E. Abrahams. Dipolar broadening of magnetic resonance lines in magnetically diluted crystals. *Physical Review*, 90(2):238–239, 1953.

[12] D. Lathrop, D. Franke, R. Maxwell, T. Tepe, R. Flesher, Z. Zhang, and H. Eckert. Dipolar 31p nmr spectroscopy of crystalline inorganic phosphorus compounds. *Solid State Nuclear Magnetic Resonance*, 1(2):73–83, 1992.

[13] M. Meyer, P. Maass, and A. Bunde. Spin-lattice relaxation: Non-bloembergen-purcell-pound behavior by structural disorder and coulomb interactions. *Physical Review Letters*, 71(4):573–576, 1993.

[14] G. R. Miller and H. S. Gutowsky. Nmr study of the alkali hexafluorophosphates' dynamic structure. *The Journal of Chemical Physics*, 39(8):1983–1994, 1963.

[15] R. F. Moran, D. M. Dawson, and S. E. Ashbrook. Exploiting nmr spectroscopy for the study of disorder in solids. *International Reviews in Physical Chemistry*, 36(1):39–115, 2017.

[16] Y. Sun, B. Ouyang, Y. Wang, Y. Zhang, S. Sun, Z. Cai, V. Lacivita, Y. Guo, and G. Ceder. Enhanced ionic conductivity and lack of paddle-wheel effect in pseudohalogen-substituted li argyrodites. *Matter*, 5(12):4379–4395, 2022.

[17] H. C. Torrey. Nuclear spin relaxation by translational diffusion. *Physical Review*, 92(4):962–969, 1953.

[18] J. H. V. Vleck. The dipolar broadening of magnetic resonance lines in crystals. *Physical Review*, 74(9):1168–1183, 1948.

[19] M. Witschas, H. Eckert, D. Wilmer, R. D. Banhatti, H. Funke, J. Fitter, R. E. Lechner, G. Korus, and M. Jansen. Anion rotation and cation transport in the rotor phase α -sodium orthophosphate: Paddle-wheel mechanism redefined in view of new experimental results. *Zeitschrift für Physikalische Chemie*, 214(5), 2000.

[20] Z. Xu, H. Duan, Z. Dou, M. Zheng, Y. Lin, Y. Xia, H. Zhao, and Y. Xia. Machine learning molecular dynamics simulation identifying weakly negative effect of polyanion rotation on li-ion migration. *npj Computational Materials*, 9(1), 2023.

D

Appendix Chapter 6

D.1 X–ray Diffraction

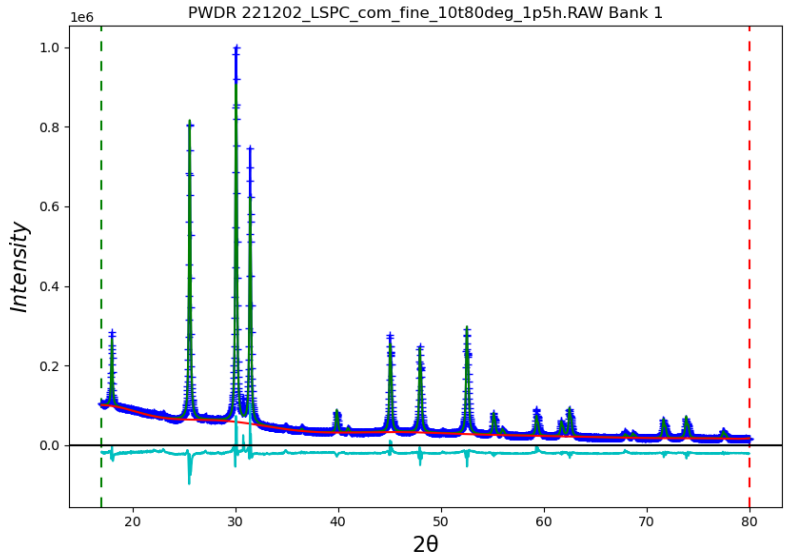

Figure D.1: XRD diffractogram of commercial Li_6PS_5Cl and fit obtained from Rietveld refinement.

Table D.1: Crystallographic data of commercial Li_6PS_5Cl obtained from Rietveld refinement. The uncertainty/error value is shown in brackets. a= 9.84923, Rwp=6.005%.

Atom	Wyckoff site	x	y	z	frac	U_{iso}
Li1	48h	0.1899(9)	0.1899(9)	0.0067(17)	0.371(26)	−0.034(12)
S2	16e	0.62056(23)	0.62056(23)	0.62056(23)	1	0.0405(10)
Cl1	4d	0.25	0.25	0.25	0.615	−0.0146(25)
S1	4d	0.25	0.25	0.25	0.385(22)	0.24(4)
P1	4b	0.5	0.5	0.5	1	0.0322(12)
S2	4a	0	0	0	0.615(9)	0.0365(23)
Cl2	4a	0	0	0	0.385(9)	0.032(3)

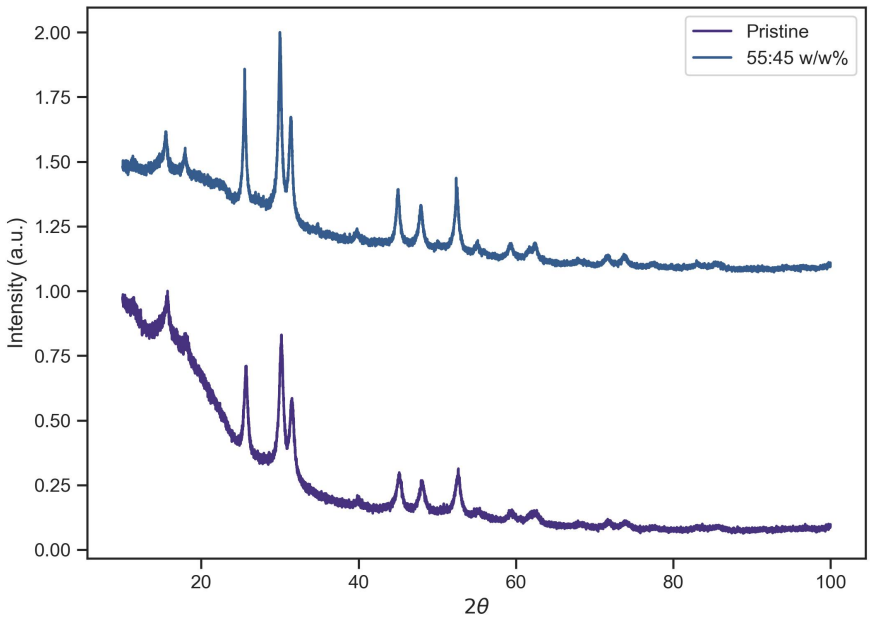

Figure D.2: XRD diffractogram of homemade Li_6PS_5Cl used in this chapter. The high background of the sample with EMIN TFSI is due to the airtight sample holder used.

D.2 NMR Spectra

To exclude degradation, approximately 20 mg of Li_6PS_5Cl and 1 ml of EMIN TFSI were mixed together and allowed to sit overnight. The following day, a small amount of EMIN TFSI was pipetted from the top to ensure no Li_6PS_5C was removed. This supernatant was yellow in colour. The ^{7}Li NMR spectrum (see Figures D.3 and D.4) show the presence of Li_2S, likely an unreacted precursor. No LiTFSI was observed.

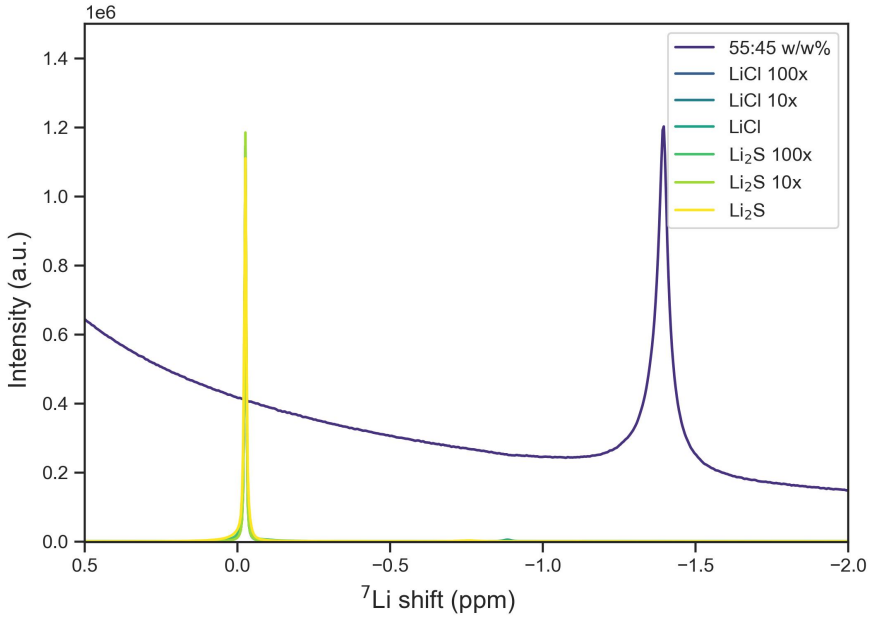

Figure D.3: The effect of dilution on the chemical shift of LiCl and Li_2S in EMIN TFSI compared to 55:45 w/w% Li_6PS_5Cl + EMIN TFSI. Spectra have been re-scaled for clarity. The change in chemical shift upon dilution is minor.

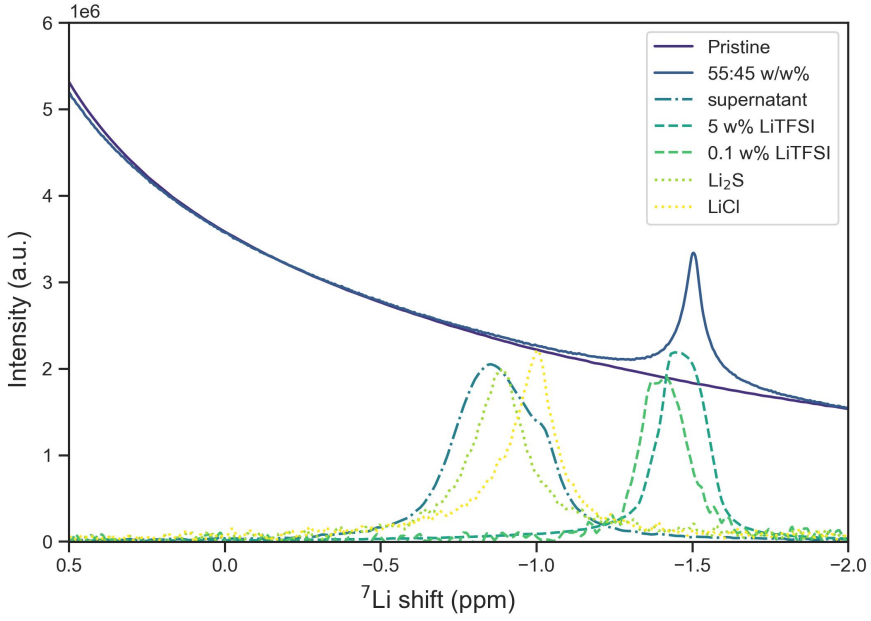

Figure D.4: The chemical shift of the supernatant in comparison with pristine Li6PS5Cl, 55:45 w/w% Li_6PS_5Cl and EMIN TFSI, LITFSI, Li_2S and LiCl. The figure shows that the filtrate has a similar chemical shift as Li_2S.

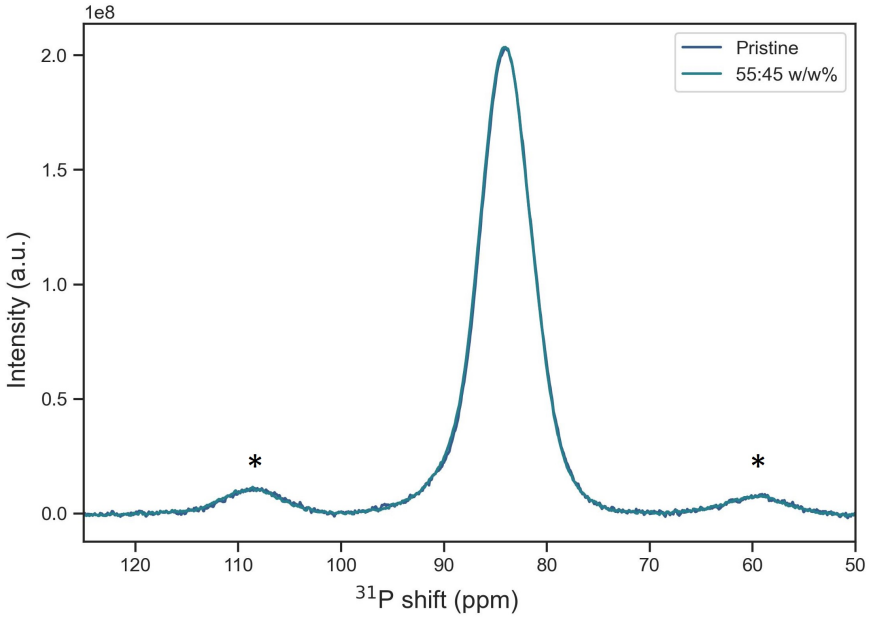

Figure D.5: The ^{31}P chemical shifts of pristine Li_6PS_5Cl and 55:45 w/w% Li_6PS_5Cl and EMIN TFSI. The spinning sidebands are indicated with astrices.

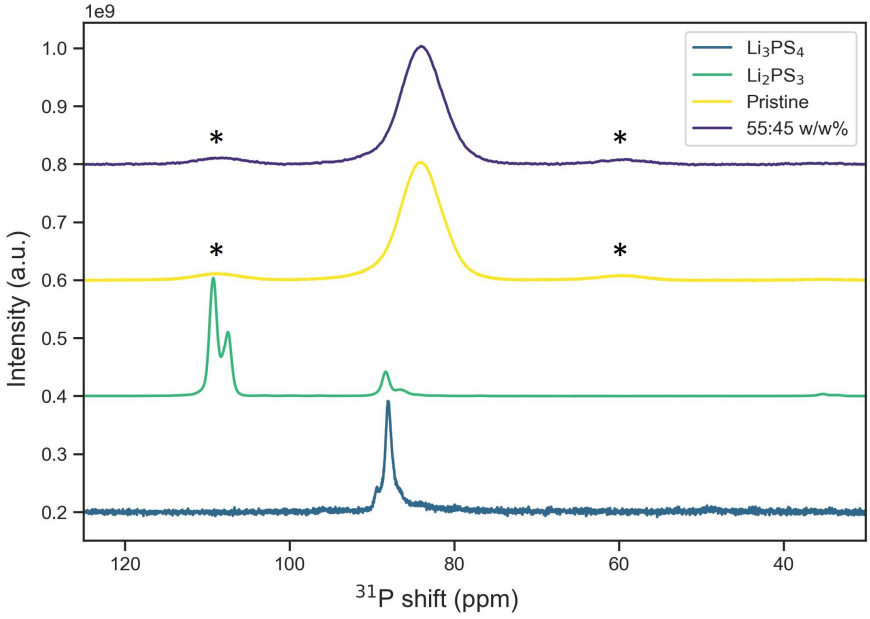

Figure D.6: Comparison of the ^{31}P NMR shifts of the pristine Li_6PS_5Cl and 55:45 w/w% Li_6PS_5Cl and EMIN TFSI to Li_3PS_4 and Li_2PS_3, showing that these compounds were not present. The spinning sidebands are indicated with astrices

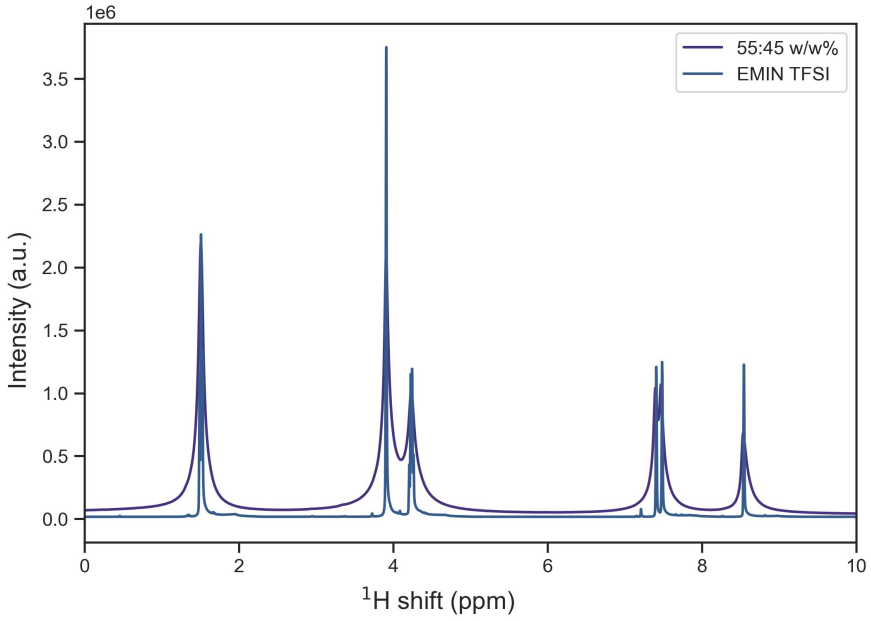

Figure D.7: Comparison of ^{1}H NMR spectra of EMIN TFSI and a 55:45 w/w% mixture of Li_6PS_5Cl and EMIN TFSI.

D.3 Raman Spectroscopy

Degradation of Li_6PS_5Cl, when coupled with the formation of H_2S and the loss of sulphur, could result in the formation of PS_3^- chains (~426 cm^{-1}), $P_2S_7^{4-}$ (~406 cm^{-1}), $Li_7P_3S_{11}$ (410 cm^{-1}), and $P_2S_6^{4-}$ (385 cm^{-1}).[1] As can be seen from Figures D.8, the corresponding vibrational modes appear to be absent.

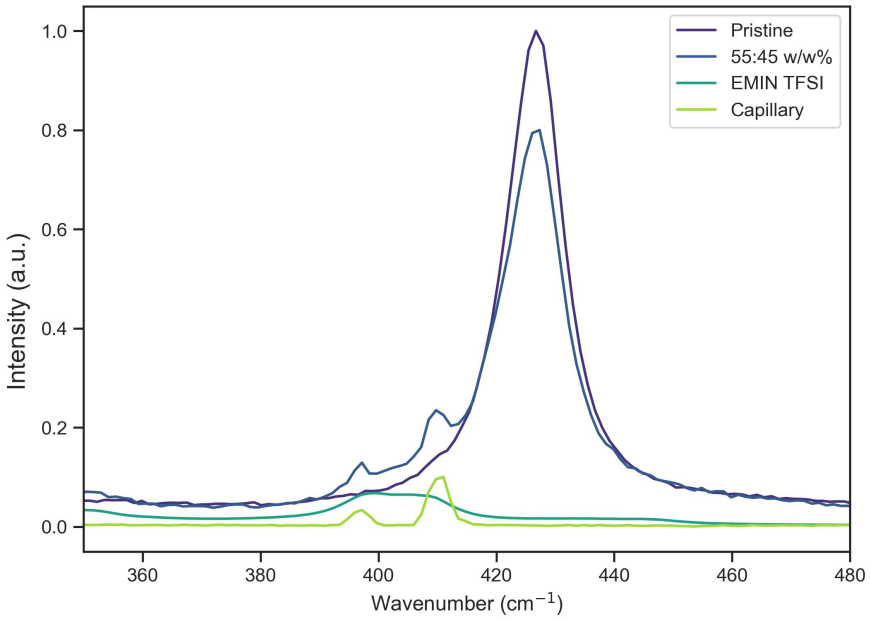

Figure D.8: Raman spectrum of pristine Li_6PS_5Cl, compared to 55:45 mixture of Li_6PS_5Cl and EMIN TFSI along with spectra of EMIN TFSI and the glass capillary used.

D.4 Exchange NMR

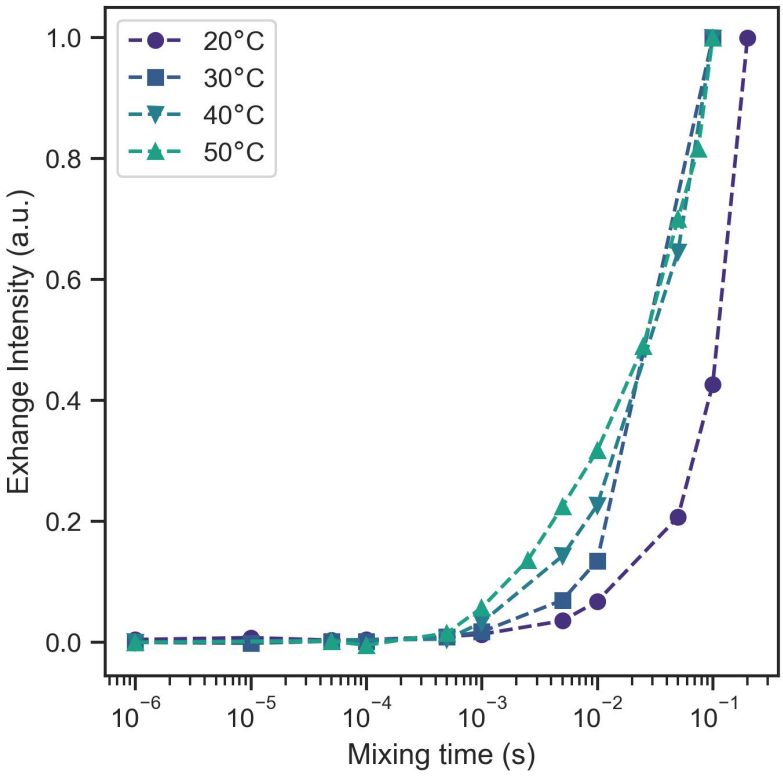

Figure D.9: Normalized ^{7}Li cross peak intensity as a function of mixing time at different temperatures for the 75:25 w/w% Li_6PS_5Cl + EMIN TFSI system.

D.5 BPP Fit

The ^{7}Li T_1 relaxation data were fitted using the Bloembergen–Purcell–Pound (BPP) model for homonuclear dipolar interactions (see 2 or a more detailed explanation) using the following formulas.

$$\frac{1}{T_1} = C\frac{\tau_c}{1+(\omega_0\tau_c)^{\beta}} \tag{D.1}$$

$$\tau_c = \tau_0 e^{E_a/kT} \tag{D.2}$$

The results are given in Tables D.2 and D.3.

Table D.2: Values obtained from the BPP fit for a 55:45 w/w% mixture of pristine commercial Li_6PS_5Cl and EMIN TFSI

	C (s^{-2})	τ_0 (s)	E_a (eV)	β
Value	8.132×10^9	8.137×10^{-14}	0.293	1.29
Error	1.74	2.74×10^{-14}	0.0126	0.0267
Error (%)	2.13	33.7	4.30	2.06

Table D.3: Values obtained from the BPP fit for pristine commercial Li_6PS_5Cl.

	C (s^{-2})	τ_0 (s)	E_a (eV)	β
Value	8.135×10^9	2.60×10^{-14}	0.332	1.26
Error	1.78	9.16×10^{-15}	0.013	0.022
Error (%)	2.13	35.2	3.97	1.79

D.6 EIS

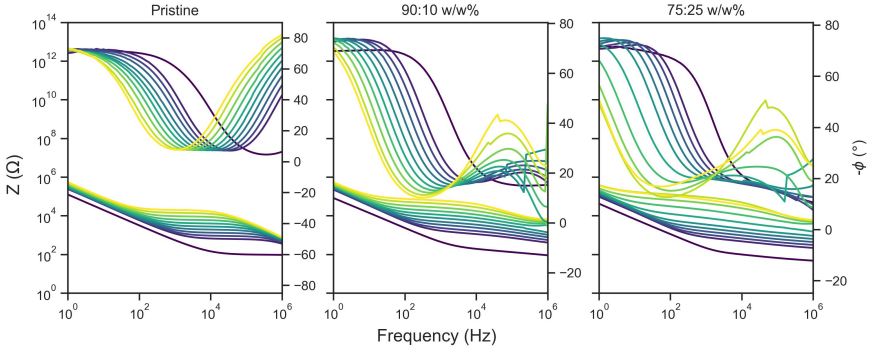

Figure D.10: Bode plot of pristine Li_6PS_5Cl and 90:10 and 75:55 w/w% mixtures of Li6PS5Cl and EMIN TFSI as a function of temperature. A discontinuity is observed at lower temperatures and higher frequencies for the phase angle.

Bibliography

[1] Y. Morino, H. Sano, K. Kawamoto, K. ichi Fukui, M. Takeuchi, A. Sakuda, and A. Hayashi. Degradation of an argyrodite-type sulfide solid electrolyte by a trace of water: A spectroscopic analysis. *Solid State Ionics*, 392:116162, 2023.

Acknowledgments

"If you wish to make an apple pie from scratch, you must first invent the universe."

Carl Sagan

The thesis you hold in your hands is the result of several years of research, woven together by countless moments of perseverance, patience, guidance, encouragement, happiness and a little bit of sadness. I will always be grateful to all those who made the good moments possible.

First I would like to thank my supervisors, Marnix and Swapna, for their scientific support. Without you there would not be a thesis. I am also grateful to the committee members for the time, care, and thoughtful consideration devoted to evaluating this work.

I would like to thank Frans, Boukje, Esther, Katarina, Nirmal, and Dan for their invaluable technical support and for keeping the laboratory a clean, safe, and functional place. My thanks also go to Kees, Robert, Anton, and Steven for their help with XRD, NMR, and the ovens, and to Jouke and Ernst for sharing their insights and expertise.

To the former and current members of the group: thank you for the laughter, conversations, and shared moments that made the journey lighter and richer. Thank you Tammo, Viola, and Angie for the joy of making music videos together. Thank you Chaofan, Pranav, Hao, and Pier for being such wonderful office mates. Thank you Katarina and Xavier for bringing the group together and always being ready for an adventure. And thank you Albert, Biffo, Bowei, Jan, Luca, Lucas, Mark, Mark, Meera, Meng Fu, Michi, Pedro, Peter, Rijk, Shengnan, Tim, Victor, Wenxuan, Xuehang, Zhu, Alexandros, Lars and many others for the many lunches, coffee breaks, and moments beyond the lab that made these years memorable. And of course, a big thank you to Kartik for all your hard work.

Thank you Remco for all your advice. May your family and business prosper. Thank you Ajay for your guidance, advice and supervision, both in science and in life.

My gratitude goes to my friends, whose unwavering support has carried me through this journey. Thank you Alain, Lucan, and Charlotte for filling my evenings with friendship and joy. Thank you Margo and Maureen for your friendship and constant inspiration. Thank you to Tjeerd, Stefan, and Ivy for the wonderful dinners and conversations.

Finally, to my parents, and to Zahra, my dearest sister: thank you for always being there, for your love and strength, and for standing by me when times were dark. To the love of my life, Federico, thank you for being my rock, for your unwavering support, and for the immeasurable light you bring into my life. And thank you to Marcelo, Cristina, Ricardo and Jade for accepting me into the family.

Hanan

Curriculum Vitæ

Hanan Ala Abdelamir Al-Kutubi

1991/01/06 Date of birth in Baghdad, Iraq

Like many people, Hanan Al-Kutubi was born in Baghdad, Iraq, on 6 January 1991. However, unlike many of those people she has lived in the Netherlands since 1996. After graduating from high school with excellent marks in Chemistry, she briefly studied Architecture at Delft University of Technology before coming to her senses and switching to Molecular Science and Technology, also at TU Delft.

It was during this time that she first dipped her toes into battery science, completing a bachelor thesis at the RID focused on the carbon coating of silicon nanoparticles. It was also then that she promised herself never to work with a glovebox again.

She continued her academic path with a Master's degree in Chemical Engineering at TU Delft. For her master's thesis, she explored electrochemical synthesis methods for metal–organic frameworks, resulting in several publications and awards, most notably the Best of TU Delft distinction, of which she remains particularly proud.

After graduating as an engineer, she moved to Groningen to work on electrochemical nanogap sensors. There, she became intimately familiar with chip fabrication techniques, theoretical electrochemistry, and the peculiar art of spending many hours staring at a line—hoping it would do what it was supposed to, while knowing deep down it would do precisely what it should not.

Eventually, she returned to Delft to pursue a PhD in battery research under the supervision of Professor Wagemaker. Here she found herself working with a glovebox once more. During her doctoral research, she focused on lithium argyrodite solid electrolytes, the results of which are presented in this thesis.

